
Extraction of Transport Coefficients in a Hybrid Approach for Heavy-Ion Collisions

Dissertation

zur Erlangung des Doktorgrades
doctor philosophiae naturalis
der Naturwissenschaften

Vorgelegt beim Fachbereich Physik (13)
der Johann Wolfgang Goethe-Universität
in Frankfurt am Main

von
Niklas Götz
aus Schweinfurt

Frankfurt am Main, 2025
(D 30)

vom Fachbereich Physik der
Johann Wolfgang Goethe-Universität als Dissertation angenommen.

Dekan: Prof. Dr. Roger Erb

Gutachter: Prof. Dr. Hannah Elfner
Prof. Dr. Carsten Greiner

Datum der Disputation:

NIKLAS GÖTZ

EXTRACTION OF TRANSPORT COEFFICIENTS IN A HYBRID
APPROACH FOR HEAVY-ION COLLISIONS

CONTENTS

List of Figures	vi
List of Tables	x
Zusammenfassung	xiii
1 Introduction	1
1.1 The Standard Model of Particle Physics	3
1.2 The Phase Diagram of QCD	8
1.3 Heavy-Ion Collisions	13
1.4 Modelling Heavy-Ion Collisions	16
1.5 Aim and Structure of This Thesis	26
2 The SMASH-vHLLE-Hybrid approach	29
2.1 The SMASH Hadronic Transport Approach	29
2.2 Viscous Hydrodynamics in the vHLLE Approach	43
2.3 Stages of the SMASH-vHLLE-Hybrid Approach	51
2.4 Technical Setup of a Modular Hybrid Approach	63
3 Observables of Heavy-Ion Collisions	67
3.1 Bulk Observables	67
3.2 Rapidity Spectra and Longitudinal Shape	69
3.3 Harmonic Flow Coefficients	70
3.4 Efficient Computation of Observables with SPARKX	75
4 Sensitivity of Hybrid Approaches on Initial State Models	79
4.1 Setup	79
4.2 Averaged Quantities	81
4.3 Event-by-event Distributions	84
4.4 Multiple Linear Regression	87
4.5 SMASH at Intermediate Energies	89
4.6 Discussion	90
5 Investigation of Viscosities in Hybrid Approaches	93
5.1 Exploring the Baryochemical Potential Dependence of Shear Viscosity . .	93
5.2 Bayesian Inference	104
5.3 Investigation of Temperature and Baryochemical Potential Dependent Viscosities	113
5.4 Summary	140
6 Summary, Conclusions, and Perspectives	143
A Appendix	147
A.1 Regression tables	147
A.2 MAP of Parameters	161
A.3 MAP Observable Predictions	161
Bibliography	165

LIST OF FIGURES

Figure 1.1	The elementary particles of the Standard Model. Adapted from [23].	4
Figure 1.2	The QCD coupling constant. One sees the running coupling due to the energy dependence. Figure adapted from [26].	7
Figure 1.3	Trace anomaly, entropy density, and pressure as a function of temperature, calculated by lQCD at $\mu_B = 0$. Figure from [37].	9
Figure 1.4	Schematic drawing of the QCD phase diagram.	11
Figure 1.5	Overview of temperature dependence of η/s and ζ/s for nuclear matter at $\mu_B=0$ for different groups and approaches. From [52]. . . .	12
Figure 1.6	Visualisation of a heavy-ion collision at high energies [107].	17
Figure 1.7	90% confidence interval of shear and bulk viscosity prediction from [54]. The different colors refer to different viscous correction schemes during particlization. Although this is only a detail at an interface of the hybrid model, the posterior shows substantial differences.	27
Figure 2.1	The spectral function of the vector mesons with dielectron decay mode. From [278].	31
Figure 2.2	Decay width of the $N^*(1440)^+$ resonance, as a function of the mass. The partial channels are depicted as colored lines, which sums up to the total decay width (in black). The figure is taken from [109]. . . .	32
Figure 2.3	Ratio of the current distribution function and the equilibrium Boltzmann distribution, for both SMASH and the exact solution. Figure from [282].	33
Figure 2.4	Total and partial cross sections of the reaction $p\pi^-$ as a function of the collision energy \sqrt{s} . The figure is taken from [286].	34
Figure 2.5	Upper row left: shear viscosity η . Upper row right: entropy density (circles) and enthalpy (triangles). Bottom: η/s (circles) or $\eta T/w$ (triangles) as a function of the temperature. Results are shown for different values of the baryochemical potential: $\mu_B = 0$ (blue), $\mu_B = 300$ MeV (red) and $\mu_B = 600$ MeV (green). The results for η/s from [266] are included as squares and the KSS bound $1/4\pi$ as a dotted line. From [267].	41
Figure 2.6	The equation of state of the SMASH hadron resonance gas for vanishing baryon, charge and strange density as a function of temperature: energy density ϵ , pressure p , and entropy density s (lines) compared to 2+1-flavor lattice QCD results [33] (bands). From [221].	42
Figure 2.7	Reduction of a three dimensional problem into a series of two dimensional problems for surface finding. The surface element is found by looking for its edges on the faces of the cube. From [224].	50

Figure 2.8	Process type of the last interaction of particles in the SMASH initial state as a function of collision energy. Clockwise from top-left: ratio of elastic processes n_{el} , ratio of resonance formations n_{res} , ratio of soft string processes n_{soft} and ratio of hard string processes n_{hard} . From [306].	52
Figure 2.9	Ratio of unformed particles in the initial state from SMASH as a function of collision energy with an impact parameter of $b = 2\text{fm}$. Adapted from [306].	52
Figure 3.1	Thermodynamic properties of the medium produced in Au+Au collisions at $\sqrt{s_{\text{NN}}} = 27\text{ GeV}$, extracted from measured yields as a function of number of participants. From [357].	70
Figure 3.2	Visualisation of the second flow coefficient (elliptic flow) and the third flow coefficient (triangular flow). From [358].	71
Figure 3.3	Simplified picture of a heavy-ion collision. The overlap region of two nuclei forms an almond shape for non-vanishing impact parameter. The spatial anisotropy in the fireball creates a pressure anisotropy, which can be detected as elliptic flow in the final state.	74
Figure 3.4	Execution time for a simple charged hadron transverse momentum analysis implemented in SPARKX 2.0.2 and Rivet 3.1.5.	76
Figure 4.1	Top: Energy density in single event transverse planes. Bottom: Average of 1000 events. From left to right: SMASH, T _R ENTo and IP-Glasma.	81
Figure 4.2	Eccentricities of the initial state for Au-Au collisions at $\sqrt{s_{\text{NN}}} = 200\text{ GeV}$ (top left), Pb-Pb collisions at $\sqrt{s_{\text{NN}}} = 5020\text{ GeV}$ (top right) and O-O collisions at $\sqrt{s_{\text{NN}}} = 7\text{ TeV}$ (bottom), each as a function of the impact parameter for the three models.	82
Figure 4.3	Initial state eccentricities (top left), final state flows (top right), and response functions v_n / ϵ_n (bottom) for all three models for Au-Au collisions at $\sqrt{s_{\text{NN}}} = 200\text{ GeV}$	83
Figure 4.4	Initial state eccentricity distributions. The normalized probability density distribution is shown on the top left and bottom right. The top right shows a 2D scatter plot of the ϵ_2 - ϵ_3 distribution, whereas the lower left plot visualizes the relationship of the two quantities, with the center of the ellipse at the mean of ϵ_2 and ϵ_3 , width and height are the variance of ϵ_2 and ϵ_3 , respectively, and the angle shows the covariance. Data at 0-5% centrality (left) and 20-30% centrality (right) for Au-Au collisions at $\sqrt{s_{\text{NN}}} = 200\text{ GeV}$	84
Figure 4.5	Final state flow distributions. The normalized probability density distribution is shown on the top left and bottom right. The top right shows a 2D scatter plot of the v_2 - v_3 distribution, whereas the lower left plot visualizes the relationship of the two quantities, with the center of the ellipse at the mean of v_2 and v_3 , width and height are the variance of v_2 and v_3 , respectively, and the angle shows the covariance. Data at 0-5% centrality (left) and 20-30% centrality (right) for Au-Au collisions at $\sqrt{s_{\text{NN}}} = 200\text{ GeV}$	85

Figure 4.6	Pearson correlation matrix at 0-5% centrality (top) and 20-30% centrality (bottom) for Au-Au collisions at $\sqrt{s_{NN}} = 200$ GeV for SMASH, IP-Glasma and T _{RENT} O (left to right).	85
Figure 4.7	Left: The difference between observed and fitted values (also known as residuals) for a fit on ϵ_2 on the one hand and ϵ_2 and $\langle p_T^{IC} \rangle$ on the other hand, for IP-Glasma at 0-5% centrality. Right: The same data for collisions in SMASH at 20-30% centrality, for the fit with v_3 on ϵ_3 (right) for Au-Au collisions at $\sqrt{s_{NN}} = 200$ GeV.	88
Figure 4.8	Pearson correlation matrix for SMASH at $\sqrt{s_{NN}} = 17.3$ GeV, at 0-5% centrality (left) and 20-30% centrality (right).	89
Figure 4.9	Hybrid evolution with SMASH IC at 0-5% centrality and $\sqrt{s_{NN}} = 17.3$ GeV: Residuals between observed and fitted values for a fit on ϵ_2 on the one hand and ϵ_2 and $\langle p_T^{IC} \rangle$ on the other hand.	90
Figure 5.1	Energy density and net baryon density dependent shear viscosity $\eta/s(\epsilon, \rho)$ for $S_\rho = 0.05$ fm ³ (left). The same quantity mapped to (T, μ_B) using a chiral equation of state (right).	94
Figure 5.2	Mean shear viscosity over entropy ratio (weighted with the energy density) throughout the whole hydrodynamic evolution. Top: Comparison between different parameterization choices for both central and off-central collisions. Bottom: effect of net baryon number density dependence for central and off-central collisions.	96
Figure 5.3	S_ρ -dependent data from fig. 5.2 normalized to the parameterization with $S_\rho = 0$. Deviation in percent.	97
Figure 5.4	Time evolution of the energy density weighted shear viscosity over entropy ratio for central collisions at $\sqrt{s_{NN}} = 39$ GeV.	98
Figure 5.5	Excitation function of $\langle p_T \rangle$ of charged hadrons at midrapidity ($ y < 0.5$) for different parameterization strategies (left) and different values of the net baryon number density dependence (right).	98
Figure 5.6	Excitation function of dN/dy ($ y < 0.5$) of charged hadrons for different parameterization strategies (left) and different values of the net baryon number density dependence (right).	99
Figure 5.7	Comparison of proton mean transverse momentum and midrapidity yield to data from NA49 [410] and STAR [411].	99
Figure 5.8	Integrated elliptic flow of charged hadrons at midrapidity ($ y < 0.5$) for different parameterization strategies (left) and different values of the net baryon number density dependence (right).	100
Figure 5.9	Comparison of charged hadron integrated event plane elliptic flow at midrapidity to STAR data [412].	101
Figure 5.10	Elliptic flow at the end of different stages of the hybrid simulation, for different values of the ϵ_{switch} . Top left: 0.1 GeV/fm ³ , top right: 0.3 GeV/fm ³ , bottom 0.5 GeV/fm ³	102
Figure 5.11	Integrated event plane elliptic flow of charged hadrons at midrapidity ($ y < 0.5$) depending on the parameterization strategy (top) and values of the net baryon number density dependence (bottom), for ϵ_{switch} set to 0.1 GeV/fm ³ (left) and set to 0.5 GeV/fm ³ (right).	102

Figure 5.12	Integrated event plane elliptic flow of charged hadrons at midrapidity ($ y < 0.5$) for different parameterization strategies and values of ϵ_{switch} . ¹⁰³	113
Figure 5.13	Schematic structure of a coupling layer. From [446].	111
Figure 5.14	Posterior for the μ_B -dependence of the shear viscosity and T-dependence of the bulk viscosity from [468].	115
Figure 5.15	Illustration of the shear viscosity parameterization.	116
Figure 5.16	Illustration of the bulk viscosity parameterization.	117
Figure 5.17	Temperature (top) and net baryochemical potential (bottom) shortly after fluidization in central Au–Au collisions at $\sqrt{s_{\text{NN}}} = 7.7$ GeV (left, fluidization at 3.29 fm) and 200 GeV (right, fluidization at 0.5 fm) [107]. ¹²¹	
Figure 5.18	The averaged root-mean-square error \mathcal{E} (top) and the uncertainty estimation metric \mathcal{H} (bottom) for both emulation strategies for all observables.	122
Figure 5.19	Probability distribution of the posterior observables for the full prior range, compared to the experimental data points used in this study. For mean transverse momenta, the width of the distribution is comparable to the size of the data markers.	123
Figure 5.20	Posterior of the technical parameters in the closure test. The red vertical line is the value of the parameter generating the pseudo-experimental data, whereas the golden vertical line represents the maximum-a-posteriori value.	125
Figure 5.21	Posterior of the viscosities in the closure test. From top to bottom: the shear viscosity as a function of temperature for vanishing baryochemical potential, the shear viscosity as a function of baryo-chemical potential at fixed temperature, and the bulk viscosity as a function of the energy density. The red line is the input parameterization, and the golden line represents the maximum-a-posteriori. The bands represent the 60% and 90% confidence interval of the posterior.	126
Figure 5.22	Normalized partial derivatives of observables with respect to parameters of the simulation (response matrix) averaged over multiple prior points. Positive values (red) mark an increase in the observable with the value of the parameter, negative values (blue) mark a decrease.	128
Figure 5.23	Posterior of the technical parameters. The golden vertical line represents the maximum-a-posteriori value.	130
Figure 5.24	Posterior of the viscosities. From top to bottom and left to right: the shear viscosity as a function of temperature for vanishing baryochemical potential, the shear viscosity as a function of baryo-chemical potential at fixed temperature, and the bulk viscosity as a function of the energy density. The golden line represents the maximum-a-posteriori. The bands represent the 60% and 90% confidence interval of the posterior.	131
Figure 5.25	Full posterior for all parameters. The diagonal shows the distribution for each parameter, whereas the off-diagonal shows the probability distribution for a combination of two parameters.	132

Figure 5.26	Shear viscosity over entropy ratio as a function of the critical temperature of $T_0=155$ MeV for different substances, with an overlay of the presented results as blue confidence bands. Adapted from [493]. . .	133
Figure 5.27	Comparison of predictions of observables from the posterior with experimental values (top). Residuals between predictions and experimental data in multiples of standard deviations (bottom).	134
Figure 5.28	MAP of the duration of the hydrodynamic evolution in the posterior.	135
Figure 5.29	Pearson correlation coefficients between the hydrodynamic evolution duration and observables used to train the fit. White squares signify observables which were not used at the respective energies/centralities. For spectra, the average over the data points is displayed.	136
Figure 5.30	Posterior of the technical parameters when including and excluding data at $\sqrt{s_{NN}}= 200$ GeV.	137
Figure 5.31	Posterior of the viscosities when including and excluding data at $\sqrt{s_{NN}}= 200$ GeV. From top to bottom and left to right: the shear viscosity as a function of temperature for vanishing baryo-chemical potential, the shear viscosity as a function of baryo-chemical potential at fixed temperature, and the bulk viscosity as a function of the energy density. The bands represent the 60% confidence interval of the posterior.	138
Figure 5.32	Posterior of the technical parameters depending on the rapidity cut.	139
Figure 5.33	Posterior of the viscosities depending on the rapidity cut. From top to bottom and left to right: the shear viscosity as a function of temperature for vanishing baryochemical potential, the shear viscosity as a function of baryochemical potential at fixed temperature, and the bulk viscosity as a function of the energy density. The bands represent the 60% confidence interval of the posterior.	140
Figure A.1	Comparison of predictions of observables from the posterior with experimental values for bulk observables.	162
Figure A.2	Comparison of predictions of observables from the posterior with experimental values for flow data.	162
Figure A.3	Comparison of predictions of observables from the posterior with experimental values for pseudorapidity yields.	163

LIST OF TABLES

Table 1.1	List of heavy-ion accelerators and their experiments at energies $E_{\text{lab}} > 1$ GeV. The operation time is given only for the heavy-ion period. Only accelerated projectile ions are listed; target ions are not.	15
Table 5.1	Priors for shear viscosity parameters.	118
Table 5.2	Priors for bulk viscosity parameters.	118

Table 5.3	Priors for technical parameters.	119
Table 5.4	The experimental measurements in Au–Au collisions used in this Bayesian Inference study.	120
Table A.1	Regression results for v_2 with SMASH IC at 0-5% centrality, $\sqrt{s_{NN}} = 200$ GeV.	149
Table A.2	Regression results for v_3 with SMASH IC at 0-5% centrality, $\sqrt{s_{NN}} = 200$ GeV.	150
Table A.3	Regression results for v_3 with SMASH IC at 20-30% centrality, $\sqrt{s_{NN}} = 200$ GeV.	151
Table A.4	Regression results for v_3 with SMASH IC at 20-30% centrality, $\sqrt{s_{NN}} = 200$ GeV.	152
Table A.5	Regression results for v_2 with IP-Glasma at 0-5% centrality, $\sqrt{s_{NN}} = 200$ GeV.	153
Table A.6	Regression results for v_3 with IP-Glasma at 0-5% centrality, $\sqrt{s_{NN}} = 200$ GeV.	154
Table A.7	Regression results for v_2 with IP-Glasma at 20-30% centrality, $\sqrt{s_{NN}} = 200$ GeV.	155
Table A.8	Regression results for v_3 with IP-Glasma at 20-30% centrality, $\sqrt{s_{NN}} = 200$ GeV.	156
Table A.9	Regression results for v_2 with SMASH IC at 0-5% centrality, $\sqrt{s_{NN}} = 17.3$ GeV.	157
Table A.10	Regression results for v_3 with SMASH IC at 0-5% centrality, $\sqrt{s_{NN}} = 17.3$ GeV.	158
Table A.11	Regression results for v_2 with SMASH IC at 20-30% centrality, $\sqrt{s_{NN}} = 17.3$ GeV.	159
Table A.12	Regression results for v_3 with SMASH IC at 20-30% centrality, $\sqrt{s_{NN}} = 17.3$ GeV.	160
Table A.13	MAP of all parameters of the model.	161

ZUSAMMENFASSUNG

Diese Arbeit basiert auf folgenden Publikationen:

- Niklas Götz und Hannah Elfner. „Temperature and net baryochemical potential dependence of η/s in a hybrid approach“. In: Phys. Rev. C 106.5 (2022), p.54904 [1]
- Niklas Götz, Lucas Constantin und Hannah Elfner. „Role of initial transverse momentum in a hybrid approach“. In: Phys. Rev. C 110.3 (2024), p.34901 [2]
- Nils Sass, Hendrik Roch, Niklas Götz, Renata Krupczak und Carl B. Rosenkvist. „SPARKX: A Software Package for Analyzing Relativistic Kinematics in Collision Experiments“. arXiv:2503.09415. Submitted to Computer Physics Communications [3]
- Niklas Götz, Iurii Karpenko und Hannah Elfner. „Bayesian analysis of a (3+1)D hybrid approach with initial conditions from hadronic transport“. arXiv: 2503.10181 Submitted to Phys. Rev. C [4]

Gegenstand dieser Arbeit ist die theoretische Beschreibung relativistischer Schwerionenkollisionen im Hinblick auf die Transportkoeffizienten der Kernmaterie. Eine der zentralen Fragen moderner Kernphysik ist die Untersuchung der Struktur und der Eigenschaften der Kernmaterie unter extremen Bedingungen von Temperatur und Dichte. Genau hier setzen relativistische Schwerionenkollisionen an: Sie bieten eine einzigartige Möglichkeit, die fundamentalen Bausteine unserer Materie zu untersuchen und Zustände nachzustellen, wie sie wenige Mikrosekunden nach dem Urknall geherrscht haben könnten. Indem man zwei schwere Ionen – in der Regel Atomkerne – auf Geschwindigkeiten nahe der Lichtgeschwindigkeit beschleunigt und miteinander kollidieren lässt, wird eine enorme Energiemenge freigesetzt. Diese Energie führt dazu, dass eine Vielzahl neuer Teilchen entsteht, die in einem kurzlebigen, extrem heißen und dichten „Feuerball“ interagieren. Während dieser Feuerball expandiert und abkühlt, kann in bestimmten Energiebereichen ein Zustand auftreten, in dem Quarks und Gluonen nicht mehr in Hadronen gebunden sind, sondern frei existieren können. Dieses Medium wird als Quark-Gluon-Plasma (QGP) bezeichnet.

Die Möglichkeit, die dabei entstehenden Teilchen am Ende im Detektor nachzuweisen, erlaubt Rückschlüsse auf das zuvor gebildete Medium. Unter anderem wird so versucht, das QCD-Phasendiagramm – also die Zustände stark wechselwirkender Materie in Abhängigkeit von Temperatur und Baryonendichte – experimentell und theoretisch zu erschließen. Bei niedrigen Temperaturen und Dichten liegt die Materie in Form gebundener Hadronen vor. Bei extremen Bedingungen hingegen brechen diese gebundenen Zustände auf, sodass die Quarks und Gluonen als Quark-Gluon-Plasma existieren können. Unterschiedliche Bereiche des QCD-Phasendiagramms werden durch eine Reihe großer internationaler Forschungsanlagen zugänglich gemacht. Beispiele sind das Conseil Européen pour la Recherche Nucléaire (CERN) in Genf, das Brookhaven National

Laboratory (BNL) in den USA oder die Gesellschaft für Schwerionenforschung (GSI) in Darmstadt.

Je nach Aufbau der Beschleunigeranlagen können Schwerionenkollisionen bei unterschiedlichen Energien durchgeführt werden. Dies ermöglicht gezielte Einblicke in verschiedene Temperatur- und Dichtebereiche. So werden etwa mit dem Large Hadron Collider (LHC) am CERN und dem Relativistic Heavy-Ion Collider (RHIC) am BNL sehr hohe Kollisionsenergien erzielt, die besonders hohe Temperaturen bei relativ geringen Baryonendichten erzeugen. Dieser Bereich ist essenziell, um zum Beispiel den Phasenübergang zwischen hadronischem Gas und Quark-Gluon-Plasma zu untersuchen, der bei niedriger Dichte als sogenannter Crossover erwartet wird. Bei höheren Dichten und mittleren Energien hingegen, wie sie unter anderem am BNL im Rahmen des Beam Energy Scan (BES), am CERN mit dem NA61/SHINE-Experiment oder zukünftig an der GSI (FAIR) erforscht werden, könnte ein Phasenübergang erster Ordnung auftreten. Die Entdeckung und genaue Lokalisierung eines möglichen kritischen Endpunktes im QCD-Phasendiagramm zählt derzeit zu den spannendsten Zielen vieler Experimente.

Um ein vollständiges Bild der zugrundeliegenden Prozesse und Eigenschaften zu erhalten, ist es notwendig, die gemessenen Daten aus diesen Experimenten mit theoretischen Modellrechnungen zu vergleichen. Auf diese Weise lassen sich bereits bestehende Annahmen über das QCD-Phasendiagramm verifizieren und potenzielle Lücken im theoretischen Verständnis erkennen. Da Schwerionenkollisionen sehr unterschiedliche Energiebereiche abdecken, kommen verschiedene Modelle zur Anwendung. Bei niedrigen Energien stellen Transportmodelle mit hadronischen Freiheitsgraden – etwa SMASH, UrQMD, PHSD, GiBUU oder JAM – eine bewährte Methode dar. In solchen Transportmodellen wird das Kollisionsintegral in der Boltzmann-Gleichung mithilfe von hadronischen Resonanzen abgebildet, die wiederum Formationen und Zerfälle durchlaufen können. Ein klarer Vorteil dabei ist die Möglichkeit, die vollständige Raum-Zeit-Impuls-Entwicklung jedes einzelnen Teilchens zu verfolgen und Interaktionsketten rückwirkend genau zu rekonstruieren. Allerdings stoßen rein hadronische Modelle an ihre Grenzen, sobald die relevanten Freiheitsgrade partonischer Natur sind und die Energien hoch genug sind, um ein Quark-Gluon-Plasma ausbilden zu können. Aus diesem Grund wenden einige dieser Transportmodelle auch ein String-Modell an, um partonische Prozesse besser beschreiben zu können.

In den hochenergetischen Bereichen, wie sie etwa am LHC und am RHIC realisiert werden, verwendet man häufig sogenannte Hybridmodelle. Diese kombinieren hydrodynamische Beschreibungen, die vor allem den heißen und dichten Teil der Feuerball-Evolution abdecken, mit Transportmodellen, welche die spätere, weniger dichte Expansionsphase simulieren. In der hydrodynamischen Phase wird das Medium üblicherweise mithilfe einer relativistischen, viskosen (3+1)-dimensionalen Hydrodynamik beschrieben, bis die Dichte so weit gefallen ist, dass eine Annahme lokaler thermischer Gleichgewichte nicht mehr gerechtfertigt ist. Dann erfolgt ein Übergang, bei dem die Fluid-Elemente zu Hadronen „gefroren werden“ und in ein Transportmodell überführt werden. Schließlich kann man damit den Ausfrierprozess der Teilchen weiterverfolgen. Derartige Hybridansätze sind in einem breiten Energiespektrum außerordentlich erfolgreich und erlauben eine detaillierte Beschreibung verschiedener beobachtbarer Größen wie zum Beispiel Teilchenspektren und den kollektiven Fluss.

Die hydrodynamische Beschreibung muss mit einer Verteilung der thermodynamischen Größen initialisiert werden, welche das Resultat der initialen Kollisionen ist. Die Beschreibung dieses Anfangszustands der Schwerionenkollision ist theoretisch anspruchsvoll, da sie experimentell kaum zugänglich ist. Aus diesem Grund gibt es eine Vielzahl an Modellen, unter anderem parametrischer Natur, aus effektiven Feldtheorien oder dem hadronischen Transport.

Ein wesentlicher Bestandteil dieser theoretischen Untersuchungen ist das Verständnis der Transportkoeffizienten im Quark-Gluon-Plasma. Dazu zählen insbesondere die Scherviskosität η/s und die Volumenviskosität ζ/s , die das Strömungsverhalten der Materie bestimmen und damit direkt in messbare Observablen wie kollektive Flusseigenschaften und Teilchenspektren eingehen. Die Bestimmung dieser Größen erfordert eine präzise Verbindung zwischen den theoretischen Beschreibungen – ob nun Transportmodelle oder (viskose) hydrodynamische Ansätze – und den experimentell ermittelten Daten. Erst durch diesen Abgleich lassen sich robuste Aussagen über den Zustand und die Eigenschaften des erzeugten Mediums gewinnen. Eine Übereinstimmung von Messungen und Simulationsergebnissen ist ein Indiz dafür, dass die Theorie das System korrekt beschreibt, während Abweichungen Hinweise auf unvollständige Modelle oder fehlende Prozesse liefern. Eine genaue Bestimmung dieser Transportkoeffizienten könnte es erlauben, wichtige Einblicke in die Prozesse zu erlangen, welche die komplexe Struktur des Phasendiagrams der QCD erzeugen.

Das zur Analyse verwendete SMASH-vHLLE-Hybridmodell kombiniert zwei verschiedene Ansätze, um die gesamte Dynamik der Kollision zu erfassen. In der anfänglichen Phase der Kollision, in der Prozesse außerhalb des Gleichgewichts auftreten, wird das hadronische Transportmodell SMASH verwendet, das eine mikroskopische Beschreibung der Hadron-Hadron-Wechselwirkungen ermöglicht. In diesem Stadium sind elastische und inelastische Streuprozesse sowie Resonanzbildungen von Bedeutung. Sobald das Medium thermodynamische Gleichgewichtsbedingungen erreicht, erfolgt ein Übergang zur relativistischen viskosen Hydrodynamik (vHLLE), welche die Expansion des Quark-Gluon-Plasmas unter Berücksichtigung der Transportkoeffizienten beschreibt. Diese Phase ist besonders wichtig, da die Viskositäten maßgeblich die hydrodynamische Entwicklung und die finalen Teilchenverteilungen beeinflussen. Schließlich kehrt das System zum hadronischen Transportmodell zurück, um den Übergang von einem hydrodynamischen Kontinuum zu einer kinetischen Beschreibung zu ermöglichen, bevor die Teilchen das Medium verlassen und gemessen werden können.

Zur Interpretation der Signaturen der Transportkoeffizienten im Endzustand, insbesondere der Impulsanisotropie, ist ein genaues Verständnis des Einflusses des Anfangszustands wichtig. Impulsanisotropien im Endzustand sind das Ergebnis einer Anisotropie der räumlichen Verteilung der Energie am Beginn der Kollision, d.h. der Exzentrizität der Kollisionszone. Diese kann experimentell aufgrund der kurzen Lebenszeit des Anfangszustands nicht beobachtet werden. Verschiedene Modelle sagen unterschiedliche Exzentrizitäten vorher, und manche von ihnen simulieren auch den Impuls des Anfangszustands, welcher die Evolution zusätzlich beeinflusst. Der Effekt dieser Unterschiede ist wichtig, um die anhand der Impulsanisotropie vorhergesagten Transportkoeffizienten korrekt zu interpretieren. In dieser Arbeit wurden drei verschiedene Modelle für

die Initialisierung untersucht: IP-Glasma, ein Modell, das die Gluonendynamik und Fluktuationen in der Energiedichte auf Grundlage von Farbfeldern beschreibt; T_{RENT}O, ein phänomenologisches Modell, das die Teilchendichteverteilungen aus einfachen Skalierungsrelationen ableitet; und SMASH, das eine hadronische Initialisierung erlaubt. Es konnte beobachtet werden, dass sich bei gleicher hydrodynamischer Entwicklung und bei gleichen Transportkoeffizienten signifikante Unterschiede ergeben. Die weit verbreitete Annahme, dass Exzentrizität und anisotroper Fluss linear zusammenhängen und der Koeffizient lediglich von Viskositäten abhängt, kann als Vereinfachung gesehen werden; allerdings spielte der Impuls im Anfangszustand gerade bei zentralen Kollisionen eine wichtige Rolle und sollte bei der Modellierung nicht vernachlässigt werden. Unterschiede zwischen Vorhersagen über die Transportkoeffizienten, welche unterschiedliche Anfangszustandsmodelle verwenden, können deshalb auch von Unterschieden im Anfangszustand herrühren.

In einem weiteren Schritt wurden wichtige Beiträge zur Bestimmung von Transportkoeffizienten geliefert. Dabei wurde anstatt eines Mittelwerts der Versuch unternommen, die Transportkoeffizienten abhängig von Dichte und Temperatur auszudrücken. Eine Untersuchung der Scherviskosität als Funktion der Energiedichte konnte zeigen, dass die hierdurch implizite Baryonendichteabhängigkeit der Scherviskosität die Abhängigkeit der Vorhersage des elliptischen Flusses vom Übergang zum hadronischen Transports reduziert. Dies legte eine Übereinstimmung mit der funktionalen Abhängigkeit im hadronischen Transport nahe und motivierte weitere Untersuchungen in diese Richtung.

Die Bestimmung der Viskositäten erfolgte daraufhin durch Bayessche Inferenz. Durch diese statistische Methode wurden experimentelle Daten mit theoretischen Modellen kombiniert, um die wahrscheinlichsten Werte der Transportkoeffizienten zu extrahieren. Die Analyse zeigte, dass die Scherviskosität in der Nähe der kritischen Temperatur des Phasenübergangs von hadronischer Materie zum Quark-Gluon-Plasma auf null fällt, während sie bei niedrigeren Temperaturen stark ansteigt. Die Abhängigkeit der Scherviskosität von der Baryonendichte kann bisher nur bedingt eingegrenzt werden und zeigt die Notwendigkeit weiterer experimenteller Daten. Für die Volumenviskosität konnten substantielle Werte gefunden werden. Die Untersuchung der Abhängigkeit der Vorhersagen von den verwendeten Datensätzen unterstrich die Notwendigkeit, sowohl ein breites Energieintervall als auch Daten aus einem möglichst breiten Rapiditätsintervall einzubeziehen. Beide konnten den Verlauf der Transportkoeffizienten einschränken. Dies unterstreicht, dass sowohl Theorie als auch Experiment bestrebt sein müssen, die vollständige Form von Events in einem breiten Energiebereich zu beschreiben.

Die Ergebnisse dieser Arbeit liefern neue Einblicke in die Transportkoeffizienten von Kernmaterie und deren Einfluss auf Schwerionenkollisionen. Durch die Kombination eines hybriden Simulationsansatzes mit modernen statistischen Methoden gelingt es, präzisere Aussagen über die Viskositäten zu treffen. Besonders hervorzuheben ist, dass sowohl die Temperatur- als auch die Dichteabhängigkeit von η/s und ζ/s wesentliche Einflussgrößen für die hydrodynamische Evolution der Materie darstellen. Diese Arbeit stellt die erste Bayessche Inferenz für relativistische Schwerionenkollisionen mit hadronischen Anfangszustand und temperatur- und baryonendichteabhängigen Transportkoeffizienten dar. Die Vorhersagen für die Scherviskosität unterscheiden sich substantiell von bisherigen

gen Ergebnissen in der Literatur und motivierten dadurch weitere Untersuchungen mit diesem Modell. Gleichzeitig konnte aber auch gezeigt werden, dass der Anfangszustand in Hybridmodellen eine zentrale Rolle spielt und die Vorhersagen stark beeinflussen kann, weshalb es notwendig ist, diesen in Zukunft besser zu verstehen.

Darüber hinaus könnten experimentelle Messungen in bisher weniger erforschten Bereichen des Phasendiagramms, insbesondere durch den geplanten Betrieb der FAIR-Anlage in Darmstadt, zusätzliche Informationen liefern. Die Kombination aus verbesserten Simulationen, präziseren experimentellen Daten und weiterentwickelten theoretischen Modellen wird dazu beitragen, das Verhalten von Kernmaterie unter extremen Bedingungen besser zu verstehen und das QCD-Phasendiagramm weiter zu kartieren. Diese Fortschritte sind nicht nur für das Verständnis fundamentaler Physikprozesse von Bedeutung, sondern haben auch Implikationen für astrophysikalische Objekte wie Neutronensterne, deren innere Struktur stark von den Eigenschaften der QCD-Materie abhängt.

INTRODUCTION

If a given science accidentally reached its goal, this would by no means stop the workers in the field, who would be driven past their goal by the sheer momentum of the illusion of unlimited progress.

— Hannah Arendt, *The Life of the Mind* (1971), p. 55

The 20th century profoundly transformed our understanding of the natural world, both around and within us, in ways unparalleled by any historical period before. At the dawn the 20th century, humanity's grasp of the universe was scarcely more advanced than when Goethe lent the famous words to his archetype of a scholar, Faust:

*Dass ich erkenne, was die Welt
Im Innersten zusammenhält*

("That I may perceive what holds the world together in its innermost essence") [5]. It was not the absence of a pact with the devil that had hindered scientific progress in previous centuries. Rather, while the scientific method had advanced significantly, technological developments lagged behind, limiting deeper insights into the true nature of matter.

At the turn of the 20th century, a synergy between the matured scientific method and rapidly advancing technological capabilities enabled revolutionary discoveries. Building upon earlier achievements like Maxwell's equations [6], the first breakthroughs came with the formulation of quantum mechanics and the theory of relativity. Max Planck's discovery of energy quantization [7] and Albert Einstein's explanation of the photoelectric effect [8] provided the foundation for understanding matter and light at atomic and subatomic scales. Simultaneously, Einstein's theories of special [9] and general relativity [10] redefined the understanding of space, time, and gravity, offering insights that remain cornerstones of modern physics. These advances were only possible through a deep interplay of theoretical ideas and technological progress.

One of the most transformative developments was the mastery of electricity. Innovations in electrical engineering not only electrified industries and cities but also powered the equipment indispensable for scientific inquiry. Early 20th-century technologies, such as vacuum tubes and later transistors, enabled the creation of increasingly sensitive and precise instruments. Spectrometers, powered by electrical systems, allowed for detailed atomic spectra analyses, while particle detectors like Geiger counters utilized electrical circuits to measure radiation. The invention of photography allowed Wilhelm Röntgen to not just discover X-rays, but also his successors to both understand the nature of radiation better, as well as to leverage it for application.

The coupling of advanced engineering and physics was particularly evident in the development of accelerators. Cyclotrons and synchrotrons, powered by high-voltage technologies, provided the energy required to delve deeper into matter's structure. High-energy collision studies with these machines revealed various subatomic particles, including the pion, confirming theoretical frameworks of nuclear forces.

Equally transformative was the advent of computation. Theoretical physics frequently requires solving complex equations describing particle and force interactions, equations

seldom solvable by hand. Early in the century, mechanical calculators facilitated this work, but the advent of digital computers during and after World War II revolutionized the field. The Manhattan Project, although focused on nuclear weapons, demonstrated computational modelling's potential for understanding atomic processes. These tools were later adapted for peacetime research, enabling simulations of phenomena like quantum field interactions and predicting particle properties before experimental discovery.

As the century advanced, the synergy between technology and theory became even more pronounced. Sensitive detectors, such as cloud chambers and later bubble chambers, enabled physicists to visualize particle paths. Electrical circuits processed these observations, while photographic techniques captured fleeting particle interactions. Each detector improvement brought new discoveries, from the positron to strange quarks.

The rapid advancement of technology not only transformed the way of life for humanity — disrupting traditions that had remained largely unchanged since the Neolithic Revolution until the Industrial Revolution — but also fundamentally altered the practice of science. The Renaissance ideal of the polymath and the image of the lone genius faded as scientific progress grew more collaborative and specialized. To this day, there is debate over who might be considered the last individual to excel across multiple scientific domains. Was it Alexander von Humboldt, the person for whom the greatest number of natural features, plants, and institutions are named [11]? Or Galileo Galilei, who constructed his own telescopes and used them to revolutionize our understanding of the universe [12]? Perhaps it was Bertrand Russell, who not only redefined the foundations of science but also extended his intellect to designing a vision for a more equitable society — fearlessly engaging in the political debates his peers often avoided [13]. Regardless of the candidate, few, if any, would propose a contemporary figure as their equal.

Even today, the idea of individual researchers making breakthroughs through brilliance and thought experiments captivates the imagination. Yet the reality is that the expansion of human knowledge since Einstein's time has grown far beyond what a single mind can encompass. While individuals such as Steven Weinberg [14] and Juan Maldacena [15] have made profound contributions, it is increasingly unlikely that any one person alone could both propose a radical new theory and independently test it. As in other areas of society, the division of labor has become indispensable. The rise of highly specialized disciplines and professionalization has propelled science forward but has also fragmented our understanding of the world. The dream of the German Idealists — figures like Kant and Hegel — that the universe might be contained, described, and comprehended in a single system [16], has long faded. Nevertheless, the pursuit of unified understanding within specific domains persists. It is a reflection of humanity's enduring ambition to seek coherence within the vastness of knowledge.

The division of labor within the scientific community has also led to a profound split between experimentalists and theorists in physics. However, it has also enabled the development of remarkable technological and mathematical expertise. While a foundational understanding of experimental methods for theorists — and of theoretical frameworks for experimentalists — is encouraged, deep specialization has become unavoidable. This evolution, as well as the ethical introspection following the destructive power demonstrated during the Manhattan Project, underscored the necessity for collaborative and peaceful scientific endeavors, ultimately leading to the founding of CERN, a symbol of international cooperation in physics.

At CERN, the Large Hadrons Collider (LHC) stands as one of the greatest achievements of engineering, incorporating superconducting magnets, cryogenic cooling systems, and a petabyte-scale data collection and analysis infrastructure [17, 18]. These feats were made possible by advances in materials science, computational technology, and electrical engineering, as well as the expertise of thousands of experimentalists who applied these innovations to scientific discovery. This technological marvel enabled the experimental confirmation of the Higgs boson in 2012 — a cornerstone of the Standard Model of particle physics [19, 20]. Though the Standard Model falls short of providing a complete understanding of nature, it offers at least a partial answer to the question, *“What holds the world together at its innermost essence?”*

In the 21st century, we reflect with awe upon past achievements, standing on the shoulders of giants in such heights that the air is getting too thin to breath. With a steadily growing community and knowledge base, but also more and more complex challenges, bridging the gap between theory and experiment is becoming increasingly difficult. The rise of phenomenology, a branch of physics aiming to make quantitative predictions from known theories, underscores the scientific method’s central step: falsification through comparison with experiment, as verification is inherently unattainable [21]. Advances in computational and numerical models, driven by decades of Moore’s law [22], gave us an ever increasing amount of computational power. With improving computational and numerical models, phenomenology stands up to the challenge to leverage experimental results in order to aid the development of new theories. Such an effort is fundamentally interdisciplinary and forces the practitioner to partially abandon ideas of specialization and division of labor in favor of a certain degree of a generalist approach, using results of many branches of physics, computer science and mathematics. Ultimately, the quest remains however to describe the fundamental constituents of matter. With this goal in mind, a brief overview of the current understanding of this issue is given. After a general overview of the field and its current state, an outline of the core problem at the heart of this work and its structure is provided.

1.1 The Standard Model of Particle Physics

The Standard Model of particle physics stands as one of the most successful theoretical frameworks in modern physics, describing the smallest known constituents of nature and their interactions via fundamental forces. Although we know that it is inherently incomplete, as it cannot describe phenomena like dark matter or gravity, no contradiction with experimental measurements has occurred in more than a decade after finding its last missing constituent. This presents both a great success as well as a major obstacle in the development of the field. The fundamental forces, in descending order of their strength, are the strong interaction, the weak interaction, the electromagnetic interaction and gravity. The Standard Model includes all but the gravity, as the latter is too weak to act on microscopic scales. Fundamental forces act on particles depending on associated charge, which are the color, weak and electric charge respectively, whereas gravity acts on the mass. This framework is rooted in quantum field theory, where particles are treated as excitations of underlying quantum fields, and their interactions are mediated by gauge bosons. Bosons carry integer spin, which is an intrinsic quantum mechanical property, akin to angular momentum, which determines their behavior under rotations.

Particles called fermions carry half-integer spins. Based on the charges of the particles mentioned above, fig. 1.1 summarizes the classification of the known elementary particles depending on their properties. The fermions split up in quarks and leptons. Quarks carry color charge, leptons do not. Leptons without electric charge are the neutrinos. The three generations of fermions have increasing mass. As their existence requires therefore a higher energy, and due to the fundamental observation that physical systems minimize the required energy, higher generations exist only rarely outside the most extreme of conditions. The gauge boson of electromagnetic interaction is the photon (γ), the W and Z boson transmit the weak interaction, whereas the gluons are responsible for the strong interaction. All of them are spin-1 particles. The Higgs boson, a spin-0 particle, is the mediator of the Higgs mechanism, which is responsible for the mass of particles via the Yukawa interactions with the Higgs field.

Standard Model of Elementary Particles

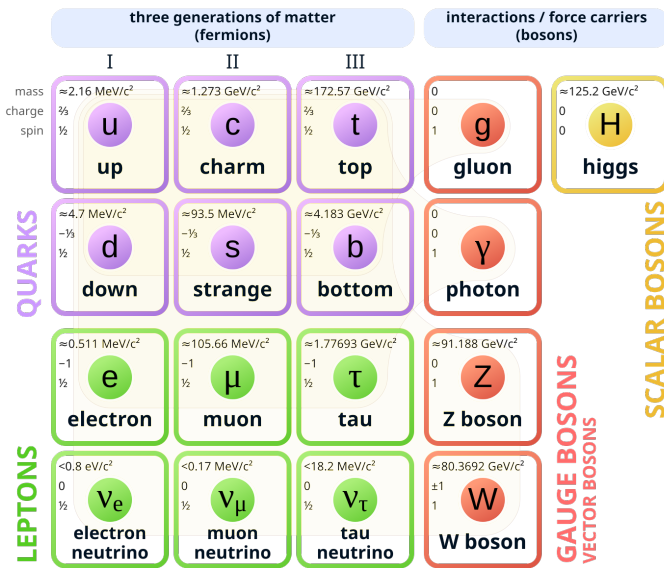


FIGURE 1.1: The elementary particles of the Standard Model. Adapted from [23].

1.1.1 The Lagrangian of the Standard Model

The dynamics of the Standard Model are encapsulated in its Lagrangian, which is expressed as:

$$\mathcal{L}_{\text{SM}} = \mathcal{L}_{\text{gauge}} + \mathcal{L}_{\text{fermion}} + \mathcal{L}_{\text{Higgs}}. \quad (1.1)$$

Here, $\mathcal{L}_{\text{gauge}}$ describes the self-interactions and dynamics of the gauge bosons, $\mathcal{L}_{\text{fermion}}$ accounts for the interactions of fermions with these gauge bosons, and $\mathcal{L}_{\text{Higgs}}$ introduces the mechanism responsible for generating particle masses through spontaneous symmetry breaking. In the following, we show the different terms contributing to the standard model Lagrangian sorted by the fundamental forces.

ELECTROMAGNETIC INTERACTION. The electromagnetic force acts on particles carrying electric charge and is mediated by photons, which are massless and do not self-interact. Quantum Electrodynamics (QED), an Abelian $U(1)$ gauge theory, provides the theoretical framework for this interaction. Its Lagrangian is given by:

$$\mathcal{L}_{\text{QED}} = \bar{\psi} (i\gamma^\mu (\partial_\mu - ieA_\mu) - m) \psi - \frac{1}{4} F_{\mu\nu} F^{\mu\nu}, \quad (1.2)$$

where ψ is the fermion wave function, A_μ is the photon field, and $F_{\mu\nu}$ is the electromagnetic field tensor.

WEAK INTERACTION. The weak force governs processes such as beta decay and neutrino oscillations. Mediated by the massive W^\pm and Z bosons, it is described by the electroweak theory, unifying the weak and electromagnetic interactions under the $SU(2)_L \times U(1)_Y$ gauge group. Its Lagrangian can be written as

$$\mathcal{L}_{\text{EW}} = -\frac{1}{4} W_{\mu\nu}^i W^{i\mu\nu} - \frac{1}{4} B_{\mu\nu} B^{\mu\nu} + \bar{\psi} \gamma^\mu (iD_\mu) \psi, \quad (1.3)$$

where:

- $W_{\mu\nu}^i$ and $B_{\mu\nu}$ are the field strength tensors of the W_μ^i and gauge B_μ gauge fields, respectively,
- $D_\mu = \partial_\mu - igT^i W_\mu^i - ig'YB_\mu$ is the covariant derivative,
- g and g' are the coupling constants for the $SU(2)_L$ and $U(1)_Y$ symmetries, respectively,
- T^i are the $SU(2)$ generators, and Y is the hypercharge.

The electroweak interaction couples differently to left-handed and right-handed fermions, reflecting the chiral nature of the weak force. The W and Z bosons acquire mass through the Higgs mechanism, breaking the underlying symmetry while preserving gauge invariance.

THE HIGGS MECHANISM The Higgs mechanism provides the Standard Model with a unified explanation for the masses of elementary particles through spontaneous symmetry breaking of the electroweak $SU(2)_L \times U(1)_Y$ symmetry. The Higgs field's quantum excitation, the Higgs boson, was experimentally confirmed by the ATLAS and CMS collaborations in 2012 [19, 20]. The Higgs Lagrangian is:

$$\mathcal{L}_{\text{Higgs}} = |D_\mu \Phi|^2 - V(\Phi), \quad (1.4)$$

where D_μ is the covariant derivative and $V(\Phi)$ is the potential responsible for symmetry breaking.

Although all of these interactions give rise to many interesting and challenging physics phenomena, the focus of this work is on the physics associated with the strong interaction.

1.1.2 The Strong Interaction and Quantum Chromodynamics (QCD)

Among the forces in the Standard Model, the strong interaction is unique due to its remarkable strength of around 10^{38} times the strength of gravity, while having short range of around 1 fm, or the radius of a proton. It binds quarks into protons, neutrons, and other hadrons, and holds atomic nuclei together. As almost all the mass of the measurable universe is realized by these hadrons, the strong interaction is pivotal for its description. The theoretical framework describing the strong interaction is Quantum Chromodynamics (QCD), a non-Abelian $SU(3)$ gauge theory where gluons, the force carriers, interact among themselves due to their color charge.

The QCD Lagrangian is expressed as:

$$\mathcal{L}_{\text{QCD}} = \bar{\Psi}_i (i\gamma^\mu (D_\mu)_{ij} - m\delta_{ij}) \Psi_j - \frac{1}{4} G_{\mu\nu}^a G_a^{\mu\nu}, \quad (1.5)$$

where Ψ_i are the quark fields, γ^μ are the Dirac matrices, $(D_\mu)_{ij} = \partial_\mu \delta_{ij} - ig_s(T^a)_{ij} A_\mu^a$ is the $SU(3)$ covariant derivative, A_μ^a represents the gluon fields, and $G_{\mu\nu}^a$ is the gluon field strength tensor:

$$G_{\mu\nu}^a = \partial_\mu A_\nu^a - \partial_\nu A_\mu^a + g_s f^{abc} A_\mu^b A_\nu^c, \quad (1.6)$$

with f^{abc} being the structure constants of $SU(3)$. The self-interaction of gluons, a consequence of the non-Abelian nature of the $SU(3)$ gauge group, leads to the emergence of key phenomena such as confinement and asymptotic freedom. This also means that gluons carry color charge themselves, allowing self-interaction. As a result of this self-interaction, the strength of the strong coupling reduces with the energy scale.

ASYMPTOTIC FREEDOM. Asymptotic freedom, discovered by Gross, Wilczek, and Politzer [24, 25], is the property that the QCD coupling constant α_s decreases at high momentum transfers (short distances), as can be seen from fig. 1.2. This implies that quarks and gluons interact weakly at high energies, enabling perturbative calculations in this regime. It is this phenomenon that, on the one hand, allows precision calculations for hadron collisions at the LHC. QCD interactions can be perturbatively expanded here, allowing to test the Standard Model to very high degrees of certainty. On the other hand, in less energetic situations, like in a nucleus at rest, the coupling constant becomes very large, leading to bound states.

CONFINEMENT. Confinement is the property that quarks and gluons cannot exist freely in the low energy regime; they are always confined within color-neutral hadrons. Color neutral combinations are in nature primarily achieved in two ways—*mesons*, a combination of a quark with a quark having the anti-color of the other quark, and *baryons*, which are a combination of one quark of each color ("red", "blue" or "green", or the respective anti-colors), such that they achieve together color neutrality. If one were to attempt to split a meson and separate the quarks, the QCD potential would grow linearly with the separation distance between quarks. This would continue until there is enough energy to create two new quarks, such that one ends up with two color neutral mesons. This severely restricts our ability to study the structure of hadrons from first principles. On the other hand, given a high temperature or a dense medium, the confinement to

hadrons would cease. Such a process of deconfinement gives rise to a new phase of matter, referred to as quark-gluon plasma (QGP). This "parton soup"¹ is a fundamentally different state than a gas of color-neutral hadrons, predominant at low-energy regimes.

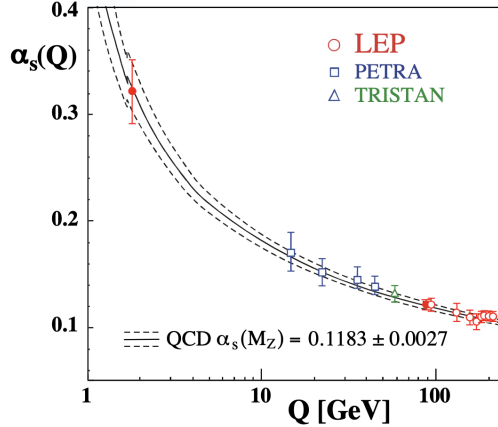


FIGURE 1.2: The QCD coupling constant. One sees the running coupling due to the energy dependence. Figure adapted from [26].

CHIRAL SYMMETRY AND ITS BREAKING. Another essential property of QCD is chiral symmetry. This symmetry is explicitly and spontaneously broken. Chirality is a property determining the behavior of the fermion spinor under chiral transformations, often interpreted as the "left- or right-handedness" of a fermion. The fermion wave function Ψ , which describes quarks in the QCD Lagrangian eq. (1.5), is represented as a spinor that can be decomposed into left-handed and right-handed components:

$$\Psi = \Psi_L + \Psi_R, \quad (1.7)$$

where

$$\Psi_L = P_L \Psi = \frac{1}{2}(1 - \gamma^5) \Psi \quad \text{and} \quad \Psi_R = P_R \Psi = \frac{1}{2}(1 + \gamma^5) \Psi, \quad (1.8)$$

with P_L and P_R being projection operators and γ^5 defined in the Dirac basis as $\gamma^5 = i \gamma^0 \gamma^1 \gamma^2 \gamma^3$.

QCD, as an $SU(3)$ gauge theory, has a chiral symmetry representation of $SU(3)_R \times SU(3)_L$. Left- and right-handed components of the spinor transform differently under this symmetry, governed by:

$$\Psi \rightarrow e^{-i \theta^a T^a} \gamma^5 \Psi \quad \text{for } a \in \{1, \dots, 8\}, \quad (1.9)$$

where T^a are the $SU(3)$ generators expressed as $T^a = \frac{\lambda^a}{2}$ using the Gell-Mann matrices λ^a [27].

In the chiral limit of massless quarks, the QCD Lagrangian is chirally symmetric. In reality, however, the quarks have non-zero masses. This leads to this symmetry being explicitly broken. Nevertheless, as quark masses are much smaller than those of hadrons,

¹ Partons refer to the constituents of a nucleon, in general quarks and gluons.

chiral symmetry remains an approximate symmetry of QCD [28]. Furthermore, although QCD exhibits an invariance under chiral transformations, the vacuum expectation value $\langle \bar{\psi} \psi \rangle$ is not invariant, leading to spontaneous chiral symmetry breaking [29]. This breaking arises because chiral transformations mix left- and right-handed components of the ground state:

$$\bar{\psi} \psi = (\bar{\psi}_L + \bar{\psi}_R) (\psi_L + \psi_R) = \psi_R \bar{\psi}_L + \psi_L \bar{\psi}_R. \quad (1.10)$$

At extreme temperatures and densities, chiral symmetry is expected to be restored, marking a transition in the properties of strongly interacting matter.

As a result of the running coupling and chiral symmetry breaking, matter governed by the strong interaction is expected to show highly different behavior depending on the energy and density scales. Just as regular molecular matter shows different properties as a function of temperature and density, a similar property can be defined for nuclear matter as well, leading to the definition of a phase diagram.

1.2 The Phase Diagram of QCD

The investigation of nuclear matter at different temperatures and densities is at the core of this work. We want to give an overview of the current understanding of this topic before we proceed in describing the aims of this work in greater detail.

The phase diagram of QCD provides a theoretical framework to understand the behavior of strongly interacting matter across varying temperatures (T) and baryochemical potential (μ_B). The latter is defined as the excess of baryons over anti-baryons. It includes key phenomena such as confinement, chiral symmetry breaking, and the transition to a deconfined quark-gluon plasma (QGP) phase. Despite the complexity of QCD, significant progress has been made in mapping the phase diagram through both first-principles calculations and effective models, taking into account our knowledge about QCD from the Standard Model.

1.2.1 First Principles and Field Theory Approaches to the Phase Diagram

Theoretical exploration of the QCD phase diagram employs a combination of approaches which start from the Lagrangian of QCD:

LATTICE QCD. Lattice QCD (lQCD, [30]) remains the most reliable first-principles approach for $\mu_B = 0$ and regions of small μ_B . lQCD calculations non-perturbatively solve QCD. This is achieved by discretizing the space-time on a lattice and afterwards extrapolating it to the continuum. It provides accurate predictions of the crossover transition at $\mu_B \approx 0$ from a hadron gas to a QGP [31] at a critical temperature of $T_C \approx 155$ MeV [32], as well as thermodynamic equilibrium properties. Figure 1.3 shows an example for this. Additionally, lQCD allows to calculate an equation of state (including the mentioned phase transition) [33–35] for small μ_B . The reason for this restriction is that the sign problem limits its applicability to larger μ_B values, necessitating alternative methods. Results for physical quark masses are limited to a chemical potential of $\mu_B = 0$, and small finite μ_B values are only accessible by Taylor expansions around $\mu_B = 0$ [36].

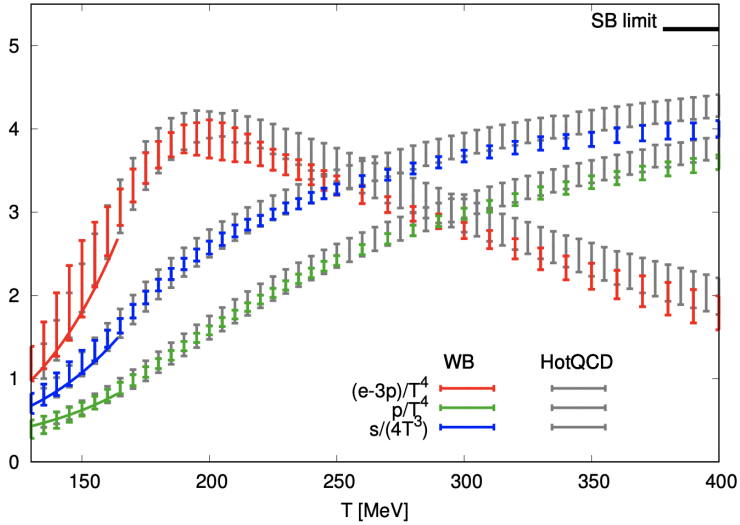


FIGURE 1.3: Trace anomaly, entropy density, and pressure as a function of temperature, calculated by lQCD at $\mu_B = 0$. Figure from [37].

EFFECTIVE MODELS. Effective theories such as the Nambu–Jona-Lasinio (NJL) model [38, 39], Chiral Effective Field Theory [40] or Color Glass Condensate (CGC) [41] each capture some key features of QCD. This is achieved by integrating out specific degrees of freedom and restricting the description to certain regimes, like regimes of high density or temperature. NJL, for example, is an approximation for the low-energy regime. As it predicts for certain regimes a first-order phase transition between a hadron gas and the QGP, whereas lQCD predicts a crossover, this is one of the hints for the existence of a critical end point (CEP), a point in the phase diagram where the line of first-order phase transition ends [42].

FUNCTIONAL METHODS. Non-perturbative approaches such as the Functional Renormalization Group (FRG) [43] and the Dyson-Schwinger Equations (DSE) [44] offer a complementary perspective to lattice QCD, particularly at finite baryochemical potential. Both frameworks start from the fundamental QCD action and derive infinite hierarchies of coupled integral equations for Green’s functions. The FRG follows the evolution of these Green’s functions under changes of an infrared (IR) cutoff scale, integrating out momentum modes step by step to capture fluctuations across all scales. Similarly, the DSE approach leverages integral equations that directly relate quark and gluon propagators and vertices, enabling the computation of correlation functions beyond the perturbative regime.

One key advantage of functional methods is their ability to treat finite μ_B without encountering the severe sign problem that plagues lattice calculations. Thus, they can explore phases of QCD matter at large baryon densities, where the existence of exotic states (such as color-superconducting phases) and a possible critical end point are anticipated. However, these methods come with specific challenges: since both FRG and DSE generate infinitely many coupled equations, practical studies rely on controlled truncation schemes to render the problem tractable. The choice of truncation and the

inclusion of relevant interaction channels critically influence the reliability and stability of results. As a consequence, a continuous effort to improve truncation strategies, benchmark calculations against lattice data at low densities, and incorporate state-of-the-art vertex functions is necessary to enhance predictive power.

PERTURBATIVE QCD AND HIGH-DENSITY REGIONS. At asymptotically high densities and energies, perturbative QCD (pQCD) becomes a suitable tool to analyze the behavior of strongly interacting matter. This applicability arises from asymptotic freedom, where the QCD coupling constant decreases at short distances, making quark and gluon interactions effectively weak. Under these conditions, perturbative expansions in the strong coupling constant α_s become reliable, enabling first-principle calculations of observables in regimes characterized by large momentum transfers. Such calculations have provided insight into the color-superconducting phases predicted to appear at extreme baryon densities, where quark matter may pair analogously to electrons in superconductors [45]. Although these exotic phases are of substantial theoretical interest, they remain far beyond current experimental reach.

Moreover, pQCD has proven essential for understanding processes involving high momenta, such as jet production in heavy-ion collisions, where high-energy jets serve as probes of the quark-gluon plasma [46]. However, while pQCD is well-suited for these high-energy regimes, it cannot be applied directly to the low-energy sector, where confinement and the rich structure of hadrons dominate. This is the domain in which lattice QCD and effective models take precedence. To bridge the gap between the perturbative and strongly coupled regimes, new theoretical ideas have emerged, most notably the application of the AdS/CFT correspondence [15], where a strongly coupled quantum field theory can be mapped to a weakly coupled gravitational theory in higher dimensions. Although the correspondence was initially established for conformal theories, it provides valuable qualitative insights into the behavior of strongly coupled QCD matter, especially in understanding properties such as viscosity and other transport coefficients [47].

1.2.2 Structure of the QCD Phase Diagram

From the aforementioned theoretical approaches, the following understanding of the nature of nuclear matter has emerged: At low temperatures and baryochemical potentials, the strongly interacting matter exists as a hadron gas, where quarks and gluons are confined within hadrons. At vanishing temperature and a net baryon density close to 1, one has nuclei in the ground state, as they exist in everyday nature. In the low temperature regime, we also observe a phase transition between nuclear gas and nuclear liquid. As the temperature increases, a transition into the QGP occurs. Lattice QCD (lQCD) calculations have established that at $\mu_B \approx 0$, this transition is a smooth crossover, occurring at a critical temperature $T_C \approx 155$ MeV [31, 32].

At finite baryochemical potential ($\mu_B > 0$), the phase structure is less well understood. Effective models predict the existence of a first-order phase transition at higher μ_B , which terminates at a critical end point (CEP) in the phase diagram [48–51]. Identifying this CEP is a major goal of both theoretical and experimental studies. A schematic drawing of the structure of the phase diagram can be seen in fig. 1.4.

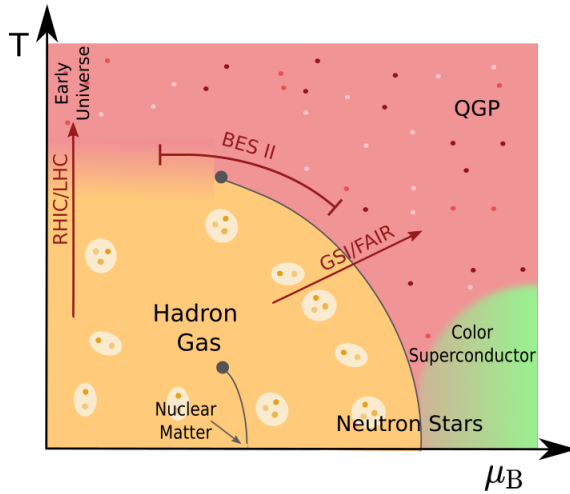


FIGURE 1.4: Schematic drawing of the QCD phase diagram.

At extremely high baryon densities, beyond the reach of current experiments, exotic phases such as color-superconducting states are theorized to exist. These phases are characterized by pairings between quarks analogous to Cooper pairs in conventional superconductors.

1.2.3 Viscosity in the Phase Diagram

The QCD phase diagram encapsulates how strongly interacting matter transitions between a hadron-dominated phase at low temperatures/densities and the quark-gluon plasma (QGP) phase at sufficiently high temperatures or densities. The thermodynamic and transport properties of QCD matter can vary markedly across this diagram, especially near the critical or crossover region.

Transport coefficients, such as shear (η) and bulk (ζ) viscosities, characterize the system's response to velocity gradients or volume changes, respectively. To facilitate comparisons across widely varying conditions in the phase diagram, these viscosities are often normalized by the entropy density s , defining the dimensionless ratios η/s and ζ/s . This normalization reduces the dependence on the absolute scale of energy density or temperature, making it easier to gauge how dissipative the medium is under different conditions. Below, we discuss how these transport coefficients impact the dynamics of heavy-ion collisions and, correspondingly, the manifestation of the QCD phase structure in experimental observables.

1.2.3.1 Shear Viscosity

Shear viscosity, in broad terms, acts to reduce local velocity differences in the expanding fluid, thereby smoothing out steep velocity gradients. Physically, if one region of the fireball flows faster than a neighboring region, shear viscosity works to equalize these velocities by transporting momentum between them. Consequently, this damping of velocity gradients modifies the anisotropies in the expansion and thus influences final observables such as elliptic flow. In a high-energy nuclear collision, a small shear viscosity

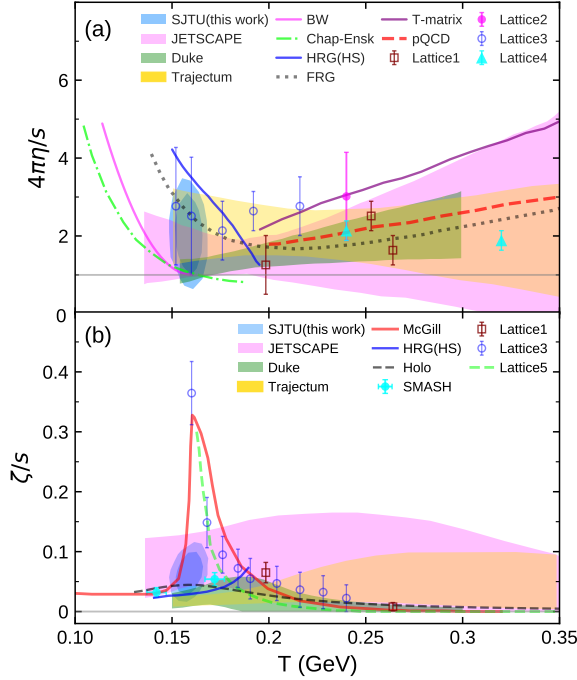


FIGURE 1.5: Overview of temperature dependence of η/s and ζ/s for nuclear matter at $\mu_B = 0$ for different groups and approaches. From [52].

means the expanding quark-gluon matter responds almost like a perfectly flowing fluid; a larger viscosity implies more dissipation, resulting in lower flow harmonics and more moderate velocity profiles across the fireball. However, in general viscosities are dependent on temperature and net-baryochemical potential, and strong hints for such a relationship, especially for the temperature, have already been found [53–68]. This can also be seen in fig. 1.5, where many predictions propose a temperature-dependent behavior. Such temperature dependence has mostly been parameterized as a piecewise-linear $\eta/s(T)$, with a minimum near the temperature of the phase transition. The density dependence has, however, been studied considerably less so far. This motivates the study of such a dependence in the upcoming chapters.

1.2.3.2 Bulk Viscosity

Bulk viscosity influences how the fireball responds to uniform expansion or compression by relating changes in the fireball's volume to its internal pressure. Whenever the medium's density or temperature evolves non-uniformly, bulk viscosity can either enhance or retard local compression or rarefaction. In practical terms, a positive bulk viscosity dampens isotropic expansion by transforming some of the collective flow energy into heat, thus reducing the system's tendency to expand freely. As a result, a sizeable bulk viscosity can visibly modify the evolving radial flow and particle spectra, particularly at intermediate beam energies, where the system's equation of state is more susceptible to thermal and density variations. Current constraints on experimental data show that it is not vanishing and must be included to provide a full picture of the evolution [53, 54, 68]. However, there is considerable disagreement about the magnitude of the bulk viscosity,

as can be seen in fig. 1.5. Bulk viscosity is assumed to be very large around the transition temperature, but small at considerably higher or lower temperatures, motivating an asymmetric Gaussian shape [69, 70].

In the chapters that follow, we will explore in more detail how the transport coefficients η/s and ζ/s vary across the QCD phase diagram and how these variations influence the bulk evolution of heavy-ion collisions.

1.2.4 QCD Phase Diagram in Nature

The QCD phase diagram is central to our understanding of strongly interacting matter in the cosmos. The deconfined QGP phase is believed to have permeated the early universe shortly after the Big Bang, when the temperatures were on the order of several hundred MeV. Under these extreme conditions, the previously confined quarks and gluons transitioned into a nearly perfect fluid state. Understanding this transition provides valuable insights into the dynamics of the early universe, matter-antimatter asymmetry, and the formation of the first hadrons [71].

The QCD phase diagram is also highly relevant for understanding matter in neutron stars. These compact stellar objects, formed from the gravitational collapse of massive stars after supernova explosions, contain matter at densities that can greatly surpass normal nuclear density. In this regime, the nature of dense matter and the role of QCD degrees of freedom become paramount for determining the stability and structure of neutron stars. For instance, whether the equation of state transitions from a hadronic description to one involving deconfined quarks has profound implications for the star's maximum mass and radius, as well as the existence of hypothetical hybrid stars containing both hadronic and quark matter phases [72].

Neutron star mergers, which are now accessible through multimessenger astronomy by the simultaneous detection of gravitational waves and electromagnetic signals, probe regions of the QCD phase diagram at even higher densities and temperatures. The gravitational wave signals emitted during the inspiral, merger, and post-merger phases encode information about the star's internal composition and equation of state. By comparing these signals to theoretical predictions derived from various QCD-inspired models, constraints on the phase structure of dense matter can be extracted. In this way, neutron star mergers serve as natural laboratories that offer an indirect window into regions of the QCD phase diagram far beyond the reach of terrestrial experiments or current first-principle calculations [73].

1.3 Heavy-Ion Collisions

Technological progress has not just enabled us to study the nature of nuclear matter by observing its high-density behavior in celestial objects; instead, we can produce high densities and temperatures in the lab too, albeit at much smaller scales. This study is crucial for tracing the effects of shear and bulk viscosities at different temperatures and densities. Due to this, we want to outline both the experimental programs for heavy-ion collisions, as well as the advances of theoretical modelling.

1.3.1 Overview of Experiments

Exploring the QCD phase diagram in the laboratory is realized through relativistic heavy-ion collisions, in which large nuclei are accelerated to high energies and then collided. By varying the collision energy and system size, different temperatures and net-baryon densities can be achieved, mapping out distinct regions of the phase diagram. Several facilities around the world have been dedicated to heavy-ion research, each covering different energy ranges and offering unique insights into strongly interacting matter.

At low-to-intermediate beam energies, where the baryon density is relatively high, facilities like the *Super Proton Synchrotron* (SPS) at CERN, *SchwerIonenSynchrotron 18* (SIS18) and the future *Facility for Antiproton and Ion Research* (FAIR) at GSI probe regions of the phase diagram potentially close to a first-order phase transition and a possible critical end point [74, 75]. The NA61/SHINE experiment at the SPS [76, 77] also contributes crucial data to this energy regime, where the onset of deconfinement and the search for the CEP remain key objectives. Fixed-target setups provide high luminosities at very low beam energies, allowing for precise measurements of rare probes such as dileptons, as conducted by the HADES experiment at SIS18 [78]. Other important experiments are the NA49 program [77] and the future *Compressed Baryonic Matter* (CBM) experiment at GSI [79]. The latter is expected to provide results at extremely high baryon density and give more insights into sections of the phase diagram relevant for astrophysics.

At higher energies, such as those accessible at *Relativistic Heavy Ion Collider* (RHIC) at BNL and the LHC at CERN, the produced matter exhibits very high temperatures but small net-baryon densities, facilitating the formation of a nearly net-baryon-free quark-gluon plasma [80]. Detectors like *Solenoid Tracker at RHIC* (STAR), *Pioneering High Energy Nuclear Interaction eXperiment* (PHENIX), *Particle Hunting Observatory for Baryons and Other Studies* (PHOBOS), and *Brookhaven Relativistic Almost Hadronic Momentum Spectrometer* (BRAHMS) at RHIC observe collisions up to $\sqrt{s_{NN}} = 200$ GeV, whereas *A Large Ion Collider Experiment* (ALICE), *A Toroidal LHC Apparatus* (ATLAS), *Compact Muon Solenoid* (CMS), and LHCb at the LHC, are designed to measure a broad range of observables, from bulk particle production to high- p_T jets and heavy-flavor hadrons [81–83] up to $\sqrt{s_{NN}} = 5.4$ TeV. These experiments have confirmed the existence of a strongly coupled QGP phase and continue to refine our knowledge of its properties, including its equation of state, viscosity, and parton energy loss mechanisms [84–87].

A special role is assigned RHIC Beam Energy Scan (BES) program [88] and its continuation BES II due to the wide range of collision energies from $\sqrt{s_{NN}} = 3$ GeV to $\sqrt{s_{NN}} = 200$ GeV. This allows to use the same experimental setup for wide sections of the phase diagram, which delivers highly comparable data for different scenarios.

Overall, the international network of heavy-ion collision facilities provides a complementary set of conditions and observables, covering a broad range of the QCD phase diagram. This allows for a systematic exploration of strongly interacting matter and ongoing improvements in our understanding of its fundamental properties. The regions of the phase diagram studied by the most important experimental facilities have been marked in fig. 1.4, whereas a table of all important heavy-ion experiments can be found in table 1.1.

Accelerator	Place	Lab.	Time	$\sqrt{s_{NN}}$ [GeV]	Projectile	Experiment	Refs.
Bevalac	Berkeley	LBL	1971-1993	2-2.7	O, C, Ne, Fe, Xe, U	Plastic Ball, Streamer chamber, EOS, DLS	[89, 90]
Synchro- Phasotron Nuclotron	Dubna Russia Dubna	JINR	1970-2003	1.9-3.5	d-Si	FOPI, HADES, KaoS	[91]
SIS18	Darmstadt	GSI	1990-now	1.9-2.7	d-Au, π	BM@N	[92, 93]
SIS100(300)	Darmstadt	GSI/FAIR	2025-(planned)	< 5.5 (9.2)	d-U, π	CBM, PANDA, NUSTAR	[94]
AGS	Brookhaven	BNL	1980-1999	2.7-5.5	O, Si, Au	E802, E859, E866, E917, E814, E877, E810, E891, E895, E910	[94, 95]
RHIC	Brookhaven	BNL	2000-now	7.7-200	Au, Cu, U, d	STAR, PHENIX, PHOBOS, BRAHMS	[96]
SPS	Geneva	CERN	1983-now	6.3-19.4	O, S, In, Pb	NA35, CERES(NA45), NA49, NA57, NA60, WA98, NA61 (SHINE)	[94, 97]
LHC	Geneva	CERN	2008-now	2760, 5020, 5400 (PbPb) 5400, 8160, 8800 (pPb) 5440 (Xe) 7000 (O) 9900 (pO)	p, Pb, Xe, O	ALICE, ATLAS, CMS, LHCb	[80, 98-100]

TABLE 1.1: List of heavy-ion accelerators and their experiments at energies $E_{\text{lab}} > 1 \text{ GeV}$. The operation time is given only for the heavy-ion period. Only accelerated projectile ions are listed; target ions are not.

1.3.2 Phenomenological Picture of Heavy-Ion Collisions

Heavy-ion collisions provide a dynamic view of the QCD phase diagram, where the system evolves through various stages, each characterized by distinct properties and degrees of freedom. Depending on the collision energy, these trajectories probe different regions of the phase diagram, offering insight into the behavior of strongly interacting matter under extreme conditions. In this section, we want to summarize the current picture of the processes occurring during a heavy-ion collision.

At high collision energies, the initial state consists of Lorentz-contracted nuclei dominated by partonic degrees of freedom [41], primarily gluons. After the collision, the system transitions into a pre-equilibrium state [101], characterized by a high energy density but with significant deviations from thermal equilibrium. This stage is dominated by hard partonic interactions, which eventually drive the rapid thermalization of the medium. The thermalized phase forms a QGP, where quark and gluon degrees of freedom become deconfined. The QGP exhibits nearly ideal hydrodynamic behavior [102], expanding and cooling over time. As the temperature drops, the system transitions through

the confinement region of the phase diagram, where quarks and gluons recombine into hadrons during hadronization. The chemical freeze-out fixes particle abundances, and subsequent elastic scatterings drive the system toward kinetic freeze-out, where momentum distributions are finalized [103, 104]. A visualization of a heavy-ion collision at high energies is given in fig. 1.6. It is important to stress that each single event does not refer to a point in the QCD phase diagram, but rather a blurry line, as the temperature and baryon density continuously evolve.

At intermediate collision energies, the baryochemical potential μ_B increases, and the trajectory through the phase diagram shifts to regions where baryonic density plays a more prominent role. The initial state involves a significant degree of baryon stopping [105], resulting in a higher net baryon density in the central region. The pre-equilibrium phase in this regime is less dominated by gluonic interactions, and the transition to thermalization may occur more slowly. The thermalized medium exhibits a mix of partonic and hadronic properties, depending on the local energy density. As the system cools, it may pass through the coexistence region of the QCD phase diagram, where the degrees of freedom are partonic in some domains and hadronic in others, reflecting a potential first-order phase transition or critical phenomena.

At low collision energies, the system predominantly explores the high-density, low-temperature region of the phase diagram. The initial state is strongly influenced by hadronic interactions, with baryonic matter playing a dominant role. The medium does not reach the conditions necessary for a fully deconfined partonic phase; instead, it remains confined throughout its evolution [106]. The trajectory through the phase diagram involves regions where dense baryonic clusters interact in a hadronic environment. The chemical and kinetic freeze-out occur relatively close together, as the hadronic medium does not sustain prolonged elastic scatterings due to lower energy densities and shorter lifetimes.

Across all collision energies, the evolution follows a general sequence: an initial state dominated by the properties of the colliding nuclei, a dynamic and rapidly changing pre-equilibrium phase, thermalization to some degree (depending on energy), and an expanding medium that transitions through hadronic and partonic degrees of freedom before freezing out. The properties of the system — whether dominated by partons or hadrons, whether in equilibrium or far from it, and whether confined or deconfined — vary markedly with collision energy, reflecting the rich complexity of QCD matter. The detector itself can only measure the debris of the collision, that is, confined color neutral states reaching the detector at timescales orders of magnitude greater than the collision process. Due to this, insights in the initial state are very difficult to obtain.

1.4 Modelling Heavy-Ion Collisions

In order to interpret the complex dynamics observed in heavy-ion collision experiments, a detailed modelling of the medium's space-time evolution is essential. Such modelling connects measured observables to the underlying microscopic and macroscopic properties of matter at extreme conditions. As demonstrated above, a heavy-ion collision is dominated by vastly different degrees of freedom and dynamics depending on the stage, collision energy and system. It is therefore extremely challenging to describe such a process in a single theory or from field theory alone. No single theoretical framework can accurately



FIGURE 1.6: Visualisation of a heavy-ion collision at high energies [107].

capture the entire evolution from the initial out-of-equilibrium stage to the late dilute hadronic phase across all collision energies. Instead, various theoretical tools have been developed, each tailored to a particular kinematic regime and degree of freedom. These approaches differ in their assumptions about equilibration, their underlying particle content, and the physics incorporated into their dynamical equations.

Broadly, three classes of approaches have proven most influential: *transport models*, *hydrodynamic models*, and *hybrid frameworks* that combine features from both. Transport models are indispensable at lower and intermediate collision energies, where the medium remains relatively dilute and the mean free path is not negligible. At very high energies, hydrodynamic descriptions, which assume near-local-equilibrium conditions and treat the medium as a fluid, have been remarkably successful. Hybrid strategies, in which transport and hydrodynamics are sequentially or concurrently applied, aim to describe the entire evolution from early non-equilibrium stages to final hadronic rescattering. In what follows, we outline these three modelling paradigms and connect them to commonly employed numerical implementations and associated physical assumptions.

1.4.1 Transport Models

Transport models rely on a microscopic description of the medium, tracking the phase-space distributions of hadrons, and sometimes partons, through Boltzmann-type equations. The classical Boltzmann equation reads as

$$\frac{\partial f}{\partial t} + \frac{\vec{p}}{m} \nabla f + \vec{F} \frac{\partial f}{\partial \vec{p}} = \left(\frac{\partial f}{\partial t} \right)_{\text{coll}}, \quad (1.11)$$

where $f = f(\vec{r}, \vec{p}, t)$ is the phase-space probability density function, meaning that the number of particles inside a differential phase space volume $d^3\vec{r}d^3\vec{p}/(2\pi)^3$ is given as $dN = f(\vec{r}, \vec{p}, t)d^3\vec{r}d^3\vec{p}/(2\pi)^3$. \vec{F} is a force field. The right hand side is called the *collision integral*. In the classical case, it is written as:

$$I_{\text{coll}} = \int \frac{d^3 p_2}{E_2} \frac{d^3 p'_1}{E_1} \frac{d^3 p'_2}{E'_2} \times W(p, p_2 \rightarrow p'_1, p'_2) \times (f'_1 f'_2 - f f_2). \quad (1.12)$$

which encodes particle creation and annihilation. It is assumed that only decays and collisions change the number of particles. The Boltzmann equation can easily be extended to the relativistic case:

$$p_\mu \partial^\mu f + m \partial_{p_\mu} (F^\mu f) = C(f). \quad (1.13)$$

The first term describes a linear propagation of particles according to their momenta, and the second term describes changes of the propagation due to external force fields. Lastly, the collision integral contains gains and losses of distribution functions due to interactions:

$$C(f) = I_{\text{coll}} = \int \frac{d^3 p_2}{E_2} \frac{d^3 p'_1}{E'_1} \frac{d^3 p'_2}{E'_2} \times W(p, p_2 \rightarrow p'_1, p'_2) \times (f'_1 f'_2 (1 + \alpha f)(1 + \alpha f_2) - f f_2 (1 + \alpha f'_1)(1 + \alpha f'_2)). \quad (1.14)$$

Here $\alpha = 1$ for bosons and $\alpha = -1$ for fermions. In the quantum case, the Boltzmann equation was first formulated by Uehling and Uhlenbeck and therefore the equation is called BUU (Boltzmann-Uehling-Uhlenbeck). It differs from the classical Boltzmann only by factors that account for quantum statistics in the collision term. The intuitive interpretation is that during the time interval dt , the number of particles in a phase-space cell has changed by the difference of particles entering it from other cells via interactions minus the ones escaped by other interactions. Commonly, theories based on the Boltzmann equation are referred to as *kinetic theories*. They do not assume that the medium is in equilibrium, however, the nonlinear integro-differential equations are usually not analytically solvable. This is related to the fact that although we have only written one equation, in reality, there are hundreds of different hadrons with many different forms of interactions (elastically, inelastically, decays, resonance formation) which creates a formidable challenge, as this couples all equations. The collision integral encodes elastic and inelastic collisions, resonance formations, and decays. The medium is thus modeled as a collection of particles whose dynamics are governed by known or parameterized cross sections and interactions.

Another limitation is the fact that this equation is only applicable for dilute systems, meaning that the mean-free path should substantially exceed the Compton wavelength:

$$\lambda_{\text{Compton}} \ll l_{\text{mfp}}. \quad (1.15)$$

This limitation is a result of the derivation of the Boltzmann equation from the more fundamental BBGKY hierarchy [108]. As a result of this, transport approaches are usually applied for $\sqrt{s_{\text{NN}}} \leq 10 \text{ GeV}$, or for the late dilute stages of a more energetic heavy-ion collision, after the fluid picture has broken down.

Numerical Monte-Carlo transport approaches effectively solve these equations by propagating the particles according to an equation of motion, which is equivalent to the left hand side of eq. (1.11), whereas the collisions in the model realize the right hand side.

At very low energies, where the system often consists predominantly of hadrons, transport approaches capture nuclear mean fields, baryon currents, and resonance excitation, which are relevant for $\sqrt{s_{\text{NN}}} \leq 4 \text{ GeV}$. Codes following the Boltzmann-Uehling-Uhlenbeck (BUU) approach—such as SMASH [109], GiBUU [110], HSD [111], or pBUU [112, 113]—treat the medium with test particles in local density fields, retaining

a one-body distribution function. By contrast, quantum molecular dynamics (QMD) methods, such as UrQMD [114], IQMD [115], JAM [116], AMD [117], or RQMD [118], represent particles as wave packets, incorporating particle correlations more explicitly. As SMASH was used in this work, a dedicated section on it will follow in the form of section 2.1.

The differences between BUU and QMD stem mainly from how potentials and correlations are modelled. While BUU-type models are built on local densities, QMD approaches emphasize particle-particle correlations and can yield richer many-body dynamics. As such differences are mainly relevant for potentials in the low energy regime, they are not crucial for this work due to its focus on intermediate and high energy regimes. Both frameworks can be extended to higher energies by including string degrees of freedom or even partonic phases, leading to so-called multiphase transport models. Examples include PHSD [119] and AMPT [120], as well as purely partonic transport codes like BAMPS [121] and ZPC [122], which are capable of describing partonic scatterings at RHIC and LHC energies.

Transport approaches are not completely parameter free, but rely on input from experiments and theoretical calculations. Most importantly, the cross sections are a pivotal input to these models. They can either be drawn from a field theory calculation, which provides the scattering matrix S , or from experimental measurements.

The strength of transport models lies in their ability to trace every particle's trajectory and its interactions in detail, offering a direct link between microscopic interactions and final-state observables. This makes them valuable for investigating non-equilibrium phenomena, baryon-rich matter, and transition regions where local equilibrium may not be well established.

Hadronic transport approaches have a long history [123–127] of being employed to model nucleus-nucleus collisions. This is due to the fact that the beam energies of older experiments were low in comparison to modern accelerators, leading to experiments which primarily observed confined phenomena. However, even in modern times, hadronic transport approaches are crucial as a baseline, as they cannot model deconfined matter. Therefore, they played a crucial role in the identification of QGP signatures: It was concluded that no QGP signatures are seen in the experimental data from AGS [128], as transport models could reproduce the observations. While the inability of transport approaches to reproduce the strangeness measurement at SPS was seen as a clear indication of a QGP formation [129].

1.4.2 Hydrodynamics

At sufficiently high collision energies, heavy-ion collisions create a hot and dense medium—the quark-gluon plasma (QGP)—that behaves as an almost perfect fluid with extremely low shear viscosity over entropy density η/s [71, 130]. This finding, one of the major achievements in the field, was realized through the application of relativistic hydrodynamic models that incorporate viscous corrections and successfully describe a multitude of bulk observables such as multiplicities, momentum distributions, and flow coefficients [131]. Remarkably, signs of hydrodynamic behavior have also been observed in small systems such as proton-proton or proton-nucleus collisions at high

multiplicities [132–134], raising important questions about the early onset of collective phenomena and the rapid thermalization of the system [135, 136].

FOUNDATIONS OF RELATIVISTIC HYDRODYNAMICS Relativistic hydrodynamics provides a macroscopic, effective description of the medium by evolving energy-momentum tensors and conserved currents under the assumptions of local thermal equilibrium and a mean free path much smaller than a macroscopic length scale:

$$l_{\text{mfp}} \ll L. \quad (1.16)$$

Formally, the fundamental equations are the conservation laws of energy-momentum and charges:

$$\partial_\mu T^{\mu\nu} = 0, \quad (1.17)$$

$$\partial_\mu J_i^\mu = 0. \quad (1.18)$$

Here, $T^{\mu\nu}$ is the energy-momentum tensor, and J_i^μ are the conserved currents corresponding to, for example, baryon number, strangeness, or electric charge. In practice, these equations represent the conservation of the first and second moments of the Boltzmann equation [137] and encode the conservation of energy, momentum, and quantum numbers. In the ideal case, the energy momentum tensor can be written as

$$T_{\text{ideal}}^{\mu\nu} = \begin{pmatrix} \epsilon & 0 & 0 & 0 \\ 0 & p & 0 & 0 \\ 0 & 0 & p & 0 \\ 0 & 0 & 0 & p \end{pmatrix}, \quad (1.19)$$

with ϵ , the local energy density and p the pressure. Here, the local fluid velocity is called $\vec{\beta}$. Then the four-velocity takes the following form

$$u^\mu = (\gamma, \gamma \vec{\beta}), \quad (1.20)$$

where $\gamma = (1 - \beta^2)^{-1/2}$. The energy-momentum tensor is boosted to the laboratory frame with the Lorentz-matrices:

$$T^{\mu\nu} = \Lambda_a^\mu \Lambda_b^\nu T^{ab} \quad (1.21)$$

$$\Lambda_\nu^\mu = \begin{pmatrix} \gamma & -\gamma \vec{\beta} \\ -\gamma \vec{\beta} & \delta_{ij} + (\gamma - 1) \frac{\vec{\beta}_i \vec{\beta}_j}{\beta^2} \end{pmatrix} = \begin{pmatrix} u^0 & -u^i \\ -u^i & \delta^{ij} + (1 + u^0)^{-1} u^i u^j \end{pmatrix} \quad (1.22)$$

Therefore, in the laboratory frame

$$T_{\text{ideal}}^{\mu\nu} = \epsilon u^\mu u^\nu - p(g^{\mu\nu} - u^\mu u^\nu), \quad (1.23)$$

where $g^{\mu\nu} = \text{diag}(1, -1, -1, -1)$. In ideal hydrodynamics the four-current is a vector $(n, 0, 0, 0)$, where n is the density. Again, this is boosted to the laboratory frame:

$$j^\mu = n u^\mu \quad (1.24)$$

In the context of heavy-ion collisions, it is crucial to apply this relativistic form of hydrodynamics, as the expansion velocity is comparable to the speed of light. It was initiated in 1953 by Landau [138, 139] in order to describe multiparticle production in proton and nucleus collisions. These partial differential equations cannot be solved analytically and require advanced numerical treatment.

To close the system of equations, it is necessary to supply an equation of state (EoS) relating the thermodynamic quantities such as energy density, pressure, and charge densities:

$$p = p(\epsilon, n_i). \quad (1.25)$$

The EoS plays a crucial role in hydrodynamics as it directly incorporates the properties of the medium and the underlying physics of nuclear matter. This is one of the great advantages of hydrodynamics, as it allows very advanced modeling, like including a phase transition into the equation of state [140], which is challenging for dynamic approaches like transport. Different regions of the QCD phase diagram, due to the different dominating physical processes, require different approaches under different assumptions to determine the EoS. In the case of vanishing chemical potentials, the EoS can be extracted directly from first-principle lattice QCD (lQCD) calculations [141]. Here, (2+1)-flavor results are provided by the HotQCD [33] and Wuppertal-Budapest [35] collaborations. Their result is a smooth crossover transition between hadronic and quarks degree of freedom in this region of the phase diagram.

At finite baryon densities, lQCD calculations are hampered by the fermion sign problem, limiting their applicability. Various extrapolation techniques, such as Taylor expansions [142–144], reweighting methods [145, 146], or simulations at imaginary chemical potentials [147, 148], extend lattice predictions to small but finite μ_B , albeit with increasing systematic uncertainties [149]. At larger baryon densities, effective models must be employed. Examples include chiral models relying on chiral symmetry restoration [150], PNJL models [151], quasiparticle approaches [152], the 3D Ising model universality class [153], or the VDF model [154]. These models can incorporate a first-order phase transition and a critical end point.

In the hadronic regime, one may construct an EoS directly from hadron resonance gas models, which can be obtained from solutions of the coupled thermodynamic equations if the hadrons are considered as point particles. More sophisticated approaches include excluded-volume corrections [155–158], the inclusion of a Hagedorn mass spectrum [159–161], or a combination of both [162]. Such hadronic EoSs characterize QCD matter at low temperatures and low baryon densities, complementing the lattice-based EoSs at low μ_B . At the opposite corner of the phase diagram—high baryon densities and low temperatures, relevant for neutron stars—approaches based on holographic QCD [163] or chiral perturbation theory combined with perturbative QCD [164] are employed. A unified framework that satisfies constraints from lQCD, nuclear matter, and neutron stars can be found in [165].

VISCOUS, ANISOTROPIC AND FLUCTUATING HYDRODYNAMICS Equation (1.19) assumes strict local thermodynamic equilibrium. However, realistic systems show devia-

tions from equilibrium. These deviations are treated by introducing viscous corrections (shear and bulk viscosities) and relaxations times, forming the basis of viscous hydrodynamics [130, 135, 166–171]. The equations of dissipative relativistic fluid dynamics were first found by Eckart [172] and subsequently by Landau and Lifshitz [173]. Both represent relativistic generalizations of Navier-Stokes theory and are often referred to as first-order theories. However, it was quickly realized that these generalizations are acausal. This means that the speed of sound can exceed the speed of light. As a consequence, this motivated the development of second-order hydrodynamics in the form of Israel-Stewart theory [166]. An improvement of this was recently developed in the form of a systematic expansion in Knudsen number Kn [174]. This extension allows describing anisotropic flow harmonics and constraining transport coefficients such as η/s and ζ/s from experimental data [175–177]. Besides the EoS, transport coefficients such as shear and bulk viscosities, as well as relaxation times, govern the dissipative properties and evolution of the fluid. They determine how strongly the medium resists to anisotropies in pressure, and by this affects the evolution of the system. As a result, their values influence the development of flow and other observables [130]. More details on viscosities are presented in section 2.3.2.2. As it is on the one hand very challenging to infer transport coefficients from first principle, but on the other hand, they encode properties of nuclear matter, it is one of the central aims of the field to infer the values of the transport coefficients from experimental data. Section 5.2 is dedicated to this cause.

Further improvements have led to anisotropic hydrodynamics [178, 179], where the expansion is performed around an already anisotropic momentum distribution rather than around equilibrium. This approach is particularly useful in the early, highly non-equilibrium stages of heavy-ion collisions when large momentum anisotropies are present.

It is also noteworthy that hydrodynamics, derived under the assumption of local equilibrium, may describe systems slightly out of equilibrium and that solutions can converge towards so-called attractor solutions [180]. This partially explains the success of hydrodynamics in describing even small systems where full thermal equilibrium is questionable. Nevertheless, it is expected that heavy-ion collisions thermalize very rapidly, even if the exact reasons for this remain unknown [135, 136].

Fluctuations and critical phenomena remain challenging for hydrodynamic simulations. Near a critical point, correlations and the correlation length grow, making the system deviate from the $\text{Kn} \ll 1$ regime and breaking some assumptions underlying hydrodynamics. The emerging framework of fluctuating hydrodynamics [181] aims to incorporate thermal fluctuations, but it remains an open and ongoing field of research.

INITIAL CONDITIONS AND APPLICABILITY CRITERIA Hydrodynamics becomes applicable only if the system is sufficiently large and close to local equilibrium, ensuring that the mean free path λ_{mfp} is much smaller than the system size L , i.e., $\text{Kn} = \lambda_{\text{mfp}}/L \ll 1$ [182]. As a result, hydrodynamics is fundamentally a macroscopic description of the system. Initially, after the nuclei collide, the system might not be equilibrated, and different models must be employed to generate suitable initial conditions. Historically, it was assumed that for high collision energies, the nuclei are flat discs due to Lorentz contraction, which stop rapidly during the collision [138, 139]. The thus predicted Gaussian rapidity spectrum of final state particles was observed by AGS and SPS. For

even higher collision energies, this model started failing as the stopping weakens, leading to a flat rapidity distribution at midrapidity. This lead to the development of the Bjorken model [183], which assumes boost invariance near midrapidity. Modern approaches incorporate increasingly sophisticated initial condition models, which can be categorized into three broad classes [184, 185]:

- **Glauber-based models:** They use a geometric picture of the nucleus-nucleus overlap, often combined with a Woods-Saxon density profile, to determine the initial energy density distribution [186–188].
- **Color Glass Condensate (CGC)-based models:** Here, the initial state is governed by the strong color fields (gluon saturation) at small Bjorken- x . Popular implementations are IP-Glasma [189, 190], MC-KLN [191, 192], and Lappi’s approach [193].
- **Transport-based models:** Partonic or hadronic transport codes such as SMASH [194], UrQMD [114, 195], EPOS [196], or AMPT [197] evolve the early system microscopically. Their output can be converted into energy and charge densities to initialize hydrodynamics.

More details into initial conditions will be provided in a dedicated section of this work section 2.3.1.

Lumpy, event-by-event initial conditions are crucial to reproduce higher flow harmonics v_n [198–200]. Because hydrodynamic equations are nonlinear, averaging initial conditions before evolution is not equivalent to event-by-event simulations. State-of-the-art hydrodynamic simulations commonly combine realistic initial conditions with viscous hydrodynamics and carefully tuned transport coefficients to describe experimental data at RHIC and LHC energies.

THREE FLUID DYNAMICS Another approach for modelling heavy-ion collisions at intermediate energies is *three-fluid hydrodynamics* (3FD) [201, 202]. In contrast to conventional single-fluid or two-phase descriptions, 3FD considers the dynamical evolution of three distinct fluids representing the projectile nucleons, target nucleons, and newly produced, excited matter (often called the "fireball") separately. Each fluid evolves with its own hydrodynamic equations, while interacting through mutual friction terms that facilitate the exchange of energy, momentum, and conserved charges.

This explicit separation allows the model to naturally incorporate non-equilibrium effects and delayed thermalization. As a result, it offers a more flexible framework to explore the dynamics of baryon stopping, the formation and equilibration of hot and dense matter, as well as the development of collective flow patterns in regimes where local equilibrium may be questionable. The 3FD approach has been employed extensively to describe collisions from SIS up to SPS energies and to make predictions for future FAIR experiments [202–205].

Recent studies have used 3FD simulations to investigate various equations of state, including purely hadronic ones and as well as such featuring a phase transition to a deconfined phase. These investigations help to pinpoint where and how signatures of QCD phase transitions, such as a first-order transition or a critical endpoint, could emerge in the evolution of the nuclear fireball. They also provide insights into the sensitivity of

observables like particle yields, rapidity distributions, and flow harmonics to the choice of the EoS and the interaction between the three fluids. The results indicate that 3FD calculations can reproduce key experimental observables at intermediate energies. This helps to constrain the EoS and transport properties in a region of the phase diagram where standard hydrodynamics may not yet be fully applicable [205–207].

The three-fluid hydrodynamics approach serves as a valuable tool to study heavy-ion collisions in an energy range that bridges the purely hadronic regime and the full QGP domain. By providing a more nuanced treatment of early-stage, non-equilibrium dynamics and offering a testbed for different EoSs and phase transition scenarios, it complements and enriches the standard hydrodynamic modelling toolbox.

NUMERICAL IMPLEMENTATION OF HYDRODYNAMICS Solving the hydrodynamic equations involves advanced numerical techniques. Commonly used algorithms include the HLLE scheme [208–210] as employed in [211, 212], the SHASTA algorithm [213–216] as used in [175, 217], or the Kurganov-Tadmor (KT) algorithm [218] applied in [219]. These methods solve the Riemann problem associated with the hydrodynamic equations (1.17) and (1.18), ensuring stable and accurate solutions. Modern hydrodynamics codes in the heavy-ion community include vHLLE [211], MUSIC [219, 220], and CLVisc [217], among others. A more detailed description of the HLLE scheme in vHLLE is given in section 2.2.

As the system expands and cools, it eventually becomes too dilute for hydrodynamics to remain valid and the equilibrium assumption to hold. A common criterion is when the energy density or temperature falls below a critical value, such as $e_{\text{crit}} = 0.5 \text{ GeV/fm}^3$ or $T_{\text{crit}} = 0.15 \text{ GeV}$ [221, 222]. At this so-called freeze-out or particlization stage, the fluid description is converted into hadrons using the Cooper-Frye formula [223], which samples particles from the freeze-out hypersurface. This is necessary in order to compare predictions from hydrodynamics with the spectra measured in experiment, as hydrodynamics represents the system in the form of an energy-momentum tensor. In practice, various sampling methods exist, relying on grand-canonical ensembles and oversampling techniques [177, 224–227], or even micro-canonical ensembles [228] to ensure strict conservation of quantum numbers event-by-event.

Furthermore, while the standard Cooper-Frye approach uses a grand-canonical ensemble, this does not guarantee exact global conservation of baryon number, strangeness, or charge on an event-by-event basis. Some observables, especially those related to fluctuations, may require stricter charge conservation prescriptions. Due to this, canonical hadron samplers have been developed, which preserve quantum numbers on an event-by-event basis [229].

2D VS 3D HYDRODYNAMICS The numerical implementation of hydrodynamics can be performed in either two (2+1D) or three (3+1D) spatial dimensions, depending on the assumed symmetries of the system.

In the simplest case, the system is considered boost-invariant along the longitudinal direction, effectively reducing the problem to two dimensions in the transverse plane. This approximation, first introduced by Bjorken [183], works well at very high collision energies near mid-rapidity, where longitudinal dynamics are approximately uniform. Boost-invariant hydrodynamics is computationally efficient, requiring fewer grid points

and simplifying the numerical treatment. However, it neglects longitudinal fluctuations and rapidity-dependent structures, which become increasingly relevant at lower collision energies and for non-central collisions.

In contrast, full 3D hydrodynamic simulations allow for a detailed treatment of the longitudinal dynamics, including rapidity-dependent flow and decorrelations. This comes at the cost of increased computational complexity and resource requirements. Modern event-by-event hydrodynamic codes such as MUSIC [219, 220], vHLLE [211, 212], and CLVisc [217] provide 3D implementations capable of describing the full space-time evolution of the system, including longitudinal and transverse fluctuations.

The choice between 2D and 3D implementations depends on the collision energy, system size, and the desired level of precision. While 2D simulations remain useful for high-energy collisions with approximate boost invariance, 3D hydrodynamics is essential for accurately modeling systems with strong longitudinal structure, such as those encountered in lower-energy collisions or in small systems with significant rapidity dependence. Recent studies incorporating realistic initial conditions and full 3D hydrodynamics have shown that longitudinal effects play a critical role in the development of flow harmonics and in reproducing experimental observables [189, 225].

In summary, relativistic hydrodynamics is a cornerstone of theoretical modeling in heavy-ion collisions, capturing the nearly ideal fluid behavior of the QGP and providing invaluable insight into the properties of hot and dense nuclear matter. By incorporating increasingly sophisticated equations of state, initial conditions, viscous corrections, and advanced numerical techniques, hydrodynamic simulations have achieved quantitative agreement with a broad range of experimental data at RHIC and LHC energies. However, lower energies as well as the late stage of the evolution remain a challenge, as non-equilibrium features are more pronounced here and assumptions of local equilibrium may break down.

1.4.3 Hybrid Approaches

Hybrid frameworks have been developed to bridge the gap between the microscopic and macroscopic regimes, capitalizing on the strengths of both transport and hydrodynamics [230–233]. The general procedure is to start with a transport model or parametric approach to generate fluctuating initial conditions, evolve the dense deconfined stage hydrodynamically, and then switch back to a hadronic transport description once the system becomes dilute. This can be seen in the visualisation fig. 1.6, where individual particles are modeled in the early and late stages, and in between, a hydrodynamic description is applied. The motivation for this approach comes from the fact that due to applicability conditions for transport approaches (Eq. 1.15) and hydrodynamics (Eq. 1.16), transport is better applicable at lower densities, whereas hydrodynamics is applicable at higher densities. Additionally, as the hydrodynamical equations can be derived from the Boltzmann equation, the regions of applicability of hydrodynamics and transport overlap, and switching is to be done in regions where both are valid.

Such hybrid models have succeeded in describing a wide array of observables at top RHIC and LHC energies [177, 230, 232–243], including flow coefficients, particle yields, and spectra of various hadron species. They allow for the incorporation of realistic

EoSs, fluctuating initial states, and dissipative effects, while maintaining a connection to microscopic degrees of freedom during the non-equilibrium or dilute phases.

A part of their success is the fact that both hydrodynamics and transport are used in their applicability ranges. Additionally, late stage rescattering (commonly referred to as "afterburner") in hadronic transport consistently improves observables with respect to particlization from hydrodynamics without rescattering. Other than pure transport, a complex equation of state can be incorporated and studied. The challenging dynamics of hadronization, that means the formation of bound states from a deconfined state, does not have to be modelled explicitly but can be condensed in the equation of state.

At lower beam energies, where the fireball created in the collision may not be as extended or as dense, and the timescale for reaching equilibrium may be longer, the applicability of such hybrid frameworks becomes more subtle [233]. It is not immediately clear when hydrodynamics is justified or whether hydrodynamical assumptions fail near the boundary of the system, where mean-free paths are large. Moreover, the question of properly modeling partial local equilibration is pressing, as is the possibility that hadrons could scatter back into dense regions and temporarily re-thermalize. It is also not clear if a single fireball, or rather many smaller drops of fluids are formed. Such behavior motivates an ongoing effort to refine the interface between hydrodynamics and transport [244–248]. Indeed, some formulations propose a continuous emission scheme, while others focus on dynamical domain-decomposition methods [249], which solve hydrodynamic and kinetic equations simultaneously [120, 250].

For intermediate collision energies, a variety of strategies have thus been explored. One option is to modify a hadronic transport model by enforcing local thermalization in high-density regions and thereby mimicking a hydrodynamic-like evolution [251], though realizing a phase transition in such a scheme remains challenging. Another possibility is the core–corona picture [252], where the densest region is described by hydrodynamics and the surrounding more dilute corona is treated with transport, albeit with limited interaction between the two domains. Anisotropic hydrodynamics [178, 179] has also been advocated, aiming to mitigate the strong momentum anisotropies present at intermediate timescales. Another approach tries to couple transport and hydrodynamics throughout the whole evolution, by running them in parallel and allow particles to enter and exit the fluid [253]. However, this refinement shares the challenge of dynamically coupling the macroscopic and microscopic descriptions in a unified way.

Nevertheless, the most commonly employed and currently state-of-the-art strategy is to initialize collisions on an event-by-event basis using a specified model, deposit the resulting energy density into a two- or three-dimensional viscous relativistic hydrodynamics framework, then perform the Cooper-Frye procedure to convert the fluid cells into hadrons, and finally evolve those hadrons within a dedicated transport code. This general scheme has been successfully realized in several hybrid approaches, such as UrQMD-vHLLE-hybrid [211], JETSCAPE [54], Trajectum [58], and SMASH-vHLLE-Hybrid [221]. The latter is employed in the present work and will be introduced in detail in chapter 2.

1.5 Aim and Structure of This Thesis

Although these hybrid approaches have been very successful in describing a variety of observables and dynamical features of heavy-ion collisions, there remain significant

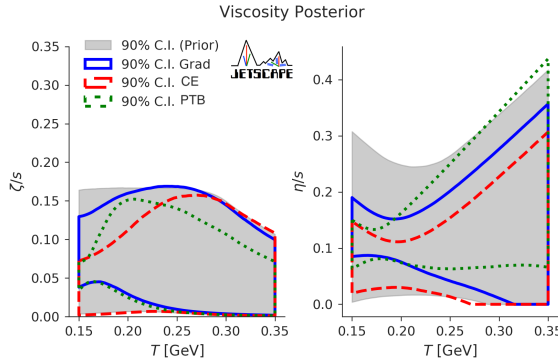


FIGURE 1.7: 90% confidence interval of shear and bulk viscosity prediction from [54]. The different colors refer to different viscous correction schemes during particlization. Although this is only a detail at an interface of the hybrid model, the posterior shows substantial differences.

limitations. As discussed above, many key properties of nuclear matter can only be calculated from first-principles under restrictive conditions. This is especially true for the transport coefficients which are to be studied here. A viable alternative is therefore to determine these properties, including transport coefficients, in a data-driven fashion. One of the strengths of hybrid approaches is that they encode the complex features of nuclear matter in a relatively concise way, allowing model predictions to be compared directly to experimental data. By optimizing agreement with these data, one hopes to extract meaningful constraints on fundamental input parameters.

In practice, this strategy encounters critical barriers. A striking illustration was provided by the JETSCAPE collaboration, which applied Bayesian inference (see section 5.2) in order to extract transport coefficients from experimental data within their hybrid framework [54]. They found that modifying the viscous corrections entering the Cooper-Frye particlization altered the inferred transport coefficients significantly, as can be seen in fig. 1.7. This demonstrates a strong dependence on the details of the model implementation.

Such findings exemplify the crucial issue often referred to as model dependence. They underscore the theoretical uncertainties built into hybrid frameworks. These can arise for various reasons, including open questions about the most appropriate viscous corrections in the particlization scheme, ambiguity in selecting the equation of state, incomplete knowledge of how transport coefficients evolve with temperature and density, and the inherent uncertainties in the initial state. The latter is especially critical: one must disentangle effects of the initial state from those of the transport coefficients when comparing model output to experimental observables. Due to the short lifetime of the fireball, there are comparatively few measurements that constrain the initial state, making it a major source of theoretical uncertainty (see chapter 4).

The goal of this thesis is to help elucidate these uncertainties, thereby improving our understanding of the inherent limitations within state-of-the-art hybrid simulations and advance the understanding of shear and bulk viscosities. The focus lies on two of the most critical sources of model sensitivity in such approaches: the choice of initial state models and the specific parameterization of viscosities. We aim to compare different

initial state models and understand better how their differences affect predictions of final state momentum anisotropies, which are often used to determine transport coefficients. Additionally, we study different parameterizations of transport coefficients, and include baryochemical potential dependence, in order to study the effect of such an inclusion as well as the constraints we can gain on this dependence. Furthermore, we investigate how the SMASH-vHLLE-Hybrid framework predicts certain properties of nuclear matter and compare these predictions to those obtained from other commonly used hybrid approaches.

The structure of this thesis is as follows. In chapter 2, the SMASH-vHLLE-Hybrid model is presented in detail. This includes a thorough description of the hadronic transport approach SMASH (section 2.1), the hydrodynamic code vHLLE (section 2.2), and a discussion of how the different stages of the hybrid approach are interfaced (section 2.3). In chapter 3, we summarize the primary observables used to compare model output with experimental data, emphasizing their importance in tuning simulations to a data-driven framework.

The investigation of initial-state models begins in chapter 4. The study two-dimensional initial conditions is based on [2]. The variations in the initial state itself are analyzed as well as the impact these differences can have on the subsequent dynamical evolution, providing a deeper insight into the role of momentum in the initial state.

Then, in chapter 5, the role of transport coefficients in the hydrodynamic evolution is investigated. Section 5.1, studies the changes in the functional dependence of the shear viscosity on temperature and baryon density, building on the study presented in [1]. Next, the framework of Bayesian inference is introduced, which is a powerful statistical learning approach to constrain physical parameters from experimental data. It is applied to the SMASH-vHLLE-Hybrid model, resulting in estimates of various transport coefficients in section 5.2.

In chapter 6, the findings are summarized and avenues for future research are outlined, highlighting the aspects that remain crucial in advancing the precision and reliability of hybrid approaches for heavy-ion collision studies.

THE SMASH-VHLLE-HYBRID APPROACH

*If you think you see both
Destruction and becoming,
Then you see destruction and becoming
Through impaired vision.*

— Nāgārjuna, Mūlamadhyamakārikā, § 20.11

The central model employed in this work is the SMASH-vHLLE-Hybrid approach [221], a versatile framework that provides a unified description of heavy-ion collisions over a broad range of energies. At its core, this is a modular hybrid scheme: the model components for different stages of the collision can be interchanged or refined without disrupting other stages. Such modularity constitutes a key benefit and underpins many of the results presented in the following.

In its default mode, the SMASH-vHLLE-Hybrid leverages the hadronic transport code SMASH to generate the initial state. SMASH’s capability to accurately model baryonic degrees of freedom and baryon stopping at moderate and lower energies effectively broadens the energy domain in which the hybrid framework remains valid. Once the hot and dense phase is reached, the system transitions to the vHLLE hydrodynamics code for a fluid-dynamic treatment of strongly interacting matter. Subsequently, the Cooper-Frye sampling of the hydrodynamic freeze-out surface is carried out by the SMASH-hadron-sampler, which hands hadrons back to the SMASH transport description for final-stage rescattering and decays. This cycle of (i) initial transport, (ii) hydrodynamics, (iii) sampling, and (iv) final transport extends the approach’s applicability to intermediate collision energies, where purely hydrodynamic or purely transport-based methods may face limitations.

This chapter gives a concise overview of each component in the SMASH-vHLLE-Hybrid, focusing on its default configuration. Relevant references are provided in each section for readers seeking a deeper understanding of the underlying theoretical and technical details.

2.1 The SMASH Hadronic Transport Approach

The present work employs the SMASH (Simulating Many Accelerated Strongly-interacting Hadrons) transport model [109] to describe the non-equilibrium hadronic dynamics in heavy-ion collisions. SMASH provides an effective solution to the relativistic Boltzmann equation eq. (1.14), treating each hadron as a point-like particle undergoing formations, scatterings, and decays. It is implemented as a thoroughly tested C++ code [254], openly accessible for external reviews. Detailed documentation, including extensive validation studies, is publicly available [255, 256]. The specific SMASH version used is stated in each result section to ensure reproducibility.

Over the years, transport approaches of this type have successfully captured the hadronic phase of ultra-relativistic collisions, as well as the full evolution at lower collision

energies. SMASH, in particular, has been developed by building on experience with prior transport approaches [110, 114, 116, 119–121, 123–127, 257] and has been applied to study a wide range of observables. Examples include hadronic flow [258], strange-particle production [259, 260], baryon stopping [261], deuteron production [262, 263], photon and dilepton emission [264, 265], and critical phenomena using a density-functional EoS [154]. It has also served to determine transport coefficients (e.g., shear [266, 267], bulk [70], electrical conductivity [268], cross-conductivity [269]) and to study fluctuations [270]. Benchmark comparisons with other transport models [271–273] have revealed strong consistency, and SMASH has been integrated into the JETSCAPE framework for hybrid studies [53].

In what follows, the main components of SMASH are reviewed: its hadronic degrees of freedom, its treatment of cross sections, the formation and decay of resonances, and several numerical details. Unless otherwise noted, we focus on the default cascade configuration (i.e. no potentials), which is particularly suited to the collision energies addressed in this study.

2.1.1 Degrees of Freedom

SMASH simulates a comprehensive set of hadrons up to masses of about 2.35 GeV, focusing on species with 3- or 4-star ratings from the Particle Data Group (PDG) [274]. This set covers pions, kaons, η -type mesons, heavier scalar, vector, and pseudoscalar resonances (e.g., ρ , ω , f_0 , a_0), as well as baryons such as N , Δ , Λ , Σ , Ξ , Ω , and their excited states. An up-to-date particle list is included with each SMASH release [275]. The full list is not quoted here because many resonance properties will be modified in the near future, as they are tuned to experimental cross sections using a genetic algorithm [276]. Masses and decay widths are typically taken from the PDG, within their allowed uncertainties, and small mass differences among isospin partners are neglected by assuming isospin symmetry. Any hadron whose width is below 10 keV is designated stable. Hadrons with higher decay width are considered to be unstable resonances.

Since SMASH-3.2, also charmed particles are included with elastic interactions from the additive quark model as well as resonance production and decays for inelastic collisions. Beyond ordinary hadrons, SMASH also includes a point-like description of deuterons [262, 263]. Each deuteron is treated as an on-shell stable particle that can form or break up in catalysis reactions involving nucleons and pions. This microscopic description, motivated by cluster formation at intermediate energies, reproduces data for light-nucleus production in heavy-ion collisions reasonably well [277].

2.1.1.1 Spectral Functions

A large fraction of particles created in heavy-ion collisions are resonances. All resonances in SMASH carry vacuum spectral functions, with any in-medium modifications arising solely from dynamical scattering. This effectively shortens lifetimes by increasing the probability of inelastic collisions before a resonance can decay. The spectral function of a resonance is given by the relativistic Breit-Wigner form

$$\mathcal{A}(m) = \frac{2N}{\pi} \frac{m^2 \Gamma(m)}{(m^2 - M_0^2)^2 + m^2 \Gamma(m)^2}, \quad (2.1)$$

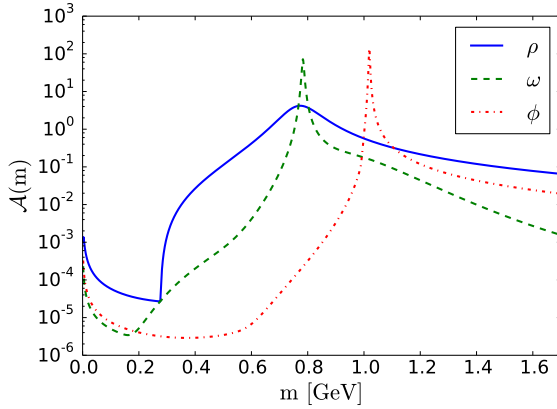


FIGURE 2.1: The spectral function of the vector mesons with dielectron decay mode. From [278].

where m is the actual mass of the resonance, M_0 its pole mass, $\Gamma(m)$ the mass-dependent decay width, and \mathcal{N} a normalization constant ensuring

$$\int_0^\infty dm \mathcal{A}(m) = 1. \quad (2.2)$$

Since $\Gamma(m)$ varies with m , \mathcal{N} can differ from unity. SMASH enforces energy-momentum conservation during formation and decay by sampling m from $\mathcal{A}(m)$ and treating the resonance as on-shell throughout its lifespan. The spectral function vanishes below the sum of the lightest final-state masses.

2.1.1.2 Decay Widths

In fig. 2.1, we see that the spectral function shows a non-trivial shape. This originates from the mass dependent decay width $\Gamma(m)$. The rising $\mathcal{A}(m)$ at low masses originates from a dilepton channel, because it is below twice of the pion mass from the default hadronic channel. The lifetime of the resonances is given as $\tau = 1/\Gamma(m)$. The total decay width of a resonance is the sum of its partial widths:

$$\Gamma(m) = \sum_i \Gamma_i(m). \quad (2.3)$$

Figure 2.2 shows total and partial widths for the $N^*(1440)^+$ resonance [109], illustrating how different channels combine to yield an m -dependent width. SMASH employs the Manley-Saleski procedure [279], whereby each two-body decay $R \rightarrow ab$ scales with the ratio

$$\Gamma_{R \rightarrow ab}(m) = \Gamma_{R \rightarrow ab}^0 \frac{\rho_{ab}(m)}{\rho_{ab}(M_0)}, \quad (2.4)$$

where $\Gamma_{R \rightarrow ab}^0 = \Gamma_{R \rightarrow ab}(M_0)$ and

$$\rho_{ab}(m) = \int dm_a \int dm_b \mathcal{A}_a(m_a) \mathcal{A}_b(m_b) \frac{|\vec{p}_f|}{m} B_L^2(|\vec{p}_f| R) \mathcal{F}_{ab}^2(m). \quad (2.5)$$

$\mathcal{A}_{a(b)}$ are the spectral functions of $a(b)$; $|\vec{p}_f|$ is the momentum in the center-of-mass frame, B_L is a Blatt-Weisskopf factor [280], and \mathcal{F}_{ab} is a form factor [281]. SMASH disallows decays that require $m < M_a + M_b$ at the pole, as they yield imaginary $|\vec{p}_f|$.

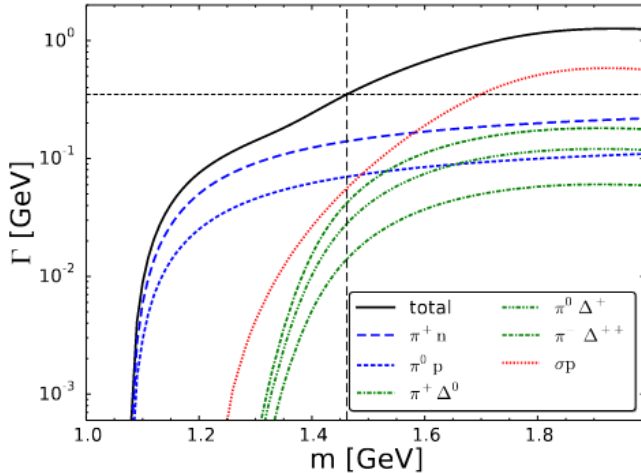


FIGURE 2.2: Decay width of the $N^*(1440)^+$ resonance, as a function of the mass. The partial channels are depicted as colored lines, which sums up to the total decay width (in black). The figure is taken from [109].

2.1.2 Effective Solution of the Boltzmann Equation

Transport approaches like SMASH aim to realize an effective numerical solution of the Boltzmann or Boltzmann-Uehling-Uhlenbeck equation,

$$\frac{\partial f}{\partial t} + \frac{\vec{p}}{E} \cdot \nabla f + \vec{F} \frac{\partial f}{\partial \vec{p}} = \left(\frac{\partial f}{\partial t} \right)_{\text{coll}}, \quad (2.6)$$

where f denotes the phase-space distribution of hadrons. Indeed, as mentioned before, the great number of degrees of freedom realized by the hadron resonance gas would turn such a Boltzmann equation analytically untrackable. Therefore, only an effective numerical treatment is possible. The time evolution of the particle distribution function in the absence of collisions is contained in the first term on left side of the equation¹. The second term on the left side is known as the free streaming term, which accounts for particles propagating along straight lines according to their momenta. The third term, on the other hand, describes the effect of an external force field on the particle trajectories. Finally, the right-hand side, the collision term, represents the interaction of the particles. The SMASH implementation has been verified against analytically solvable test cases, notably an expanding Friedmann–Robertson–Walker metric setup where a known solution of the Boltzmann equation exists [282].

Figure 2.3 shows the comparison of the exact solution of the Boltzmann equation with the one obtained by SMASH in the case of an expanding metric. This result shows that SMASH effectively provides a correct solution of the Boltzmann equation in this setup.

2.1.2.1 Propagation and Potentials

In SMASH’s default cascade mode, hadrons move along straight-line trajectories from one collision or decay to the next, which avoids limiting each particle to at most one

¹ Without the collision term, the equation is referred to as the Vlasov equation.

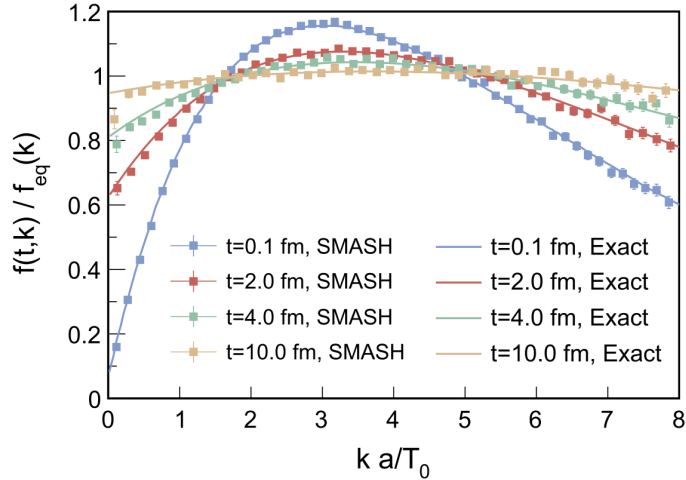


FIGURE 2.3: Ratio of the current distribution function and the equilibrium Boltzmann distribution, for both SMASH and the exact solution. Figure from [282].

interaction per time step [109, 114]. Indeed, this was a major limitation in a fixed-time step approach. The algorithm identifies the nearest upcoming event, updates the system to that time, performs the interaction, then repeats for the subsequent events. If, however, the stochastic collision criterion (section 2.1.2.3) is used, one must revert to time steps Δt to define collision probabilities, briefly restoring the single-collision-per-time step assumption.

A more sophisticated mean-field mode is also available, in which particles feel attractive and repulsive nuclear forces. These potentials enter the Boltzmann equation as an additional term on the left-hand side. In SMASH, the Skyrme potential [109, 283] is a commonly used option, taking the form

$$U(\rho, \rho_{13}) = a \left(\frac{\rho}{\rho_0} \right) + b \left(\frac{\rho}{\rho_0} \right)^\tau \pm 2 S_{\text{pot}} \left(\frac{\rho_{13}}{\rho_0} \right), \quad (2.7)$$

where ρ denotes the local baryon density, ρ_{13} is the isospin- I_3 density, and $\rho_0 = 0.168 \text{ fm}^{-3}$ is the nuclear saturation density. The potentials modify particle trajectories via relativistic equations of motion that depend on $\partial H^*/\partial x^\mu$ and $\partial H^*/\partial p^\mu$, where H^* is the Hamiltonian in the local rest frame. Only baryons experience these nuclear forces, which can be crucial at lower collision energies to describe effects such as the nuclear equation of state and collective flow in heavy-ion collisions [154].

In this work, the collision energies are sufficiently high that potentials have a marginal effect. Consequently, all reported results use the cascade mode without mean fields, causing baryons and mesons to move on straight-line trajectories between collisions. At lower energies, however, the inclusion of these potentials can be essential to reproduce nuclear binding and the stiffening of the hadronic equation of state in dense matter.

2.1.2.2 Interactions and Cross Sections

The interactions among the hadronic degrees of freedom in SMASH span a wide range of processes that are implemented through distinct partial cross sections, which can belong

to (in)elastic collisions, string fragmentation, as well as resonance formation and decay. All partial contributions together determine the total hadron-hadron cross section,

$$\sigma_{\text{tot}} = \sum \sigma_{\text{partial}}, \quad (2.8)$$

which serves as the foundation for deciding whether two hadrons collide. There are two approaches: a bottom-up strategy, where each individual resonance channel contributes to the total cross section in a way that reproduces measured hadron-hadron cross sections [109, 114, 284]. More recently, an alternative top-down approach has been made available as well, in which an overall cross section fit is performed first, and subsequent partial contributions are assigned afterward [285]. For measured processes, SMASH uses the top-down approach, and bottom-up for the rest.

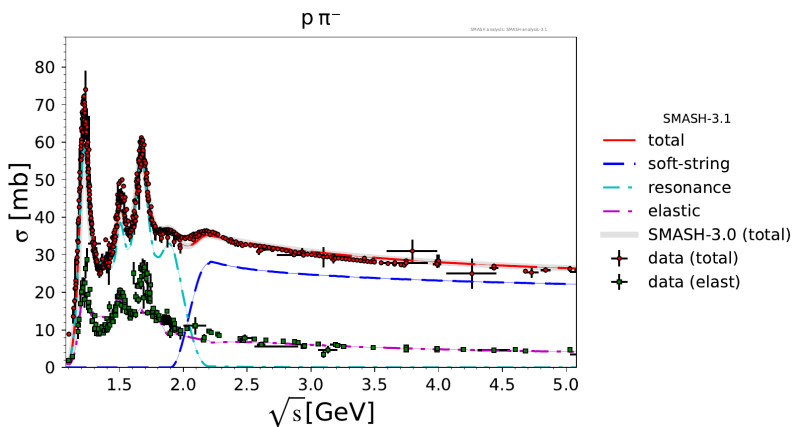


FIGURE 2.4: Total and partial cross sections of the reaction $p\pi^-$ as a function of the collision energy \sqrt{s} . The figure is taken from [286].

Figure 2.4 shows as an example the cross section of a proton pion reaction. The total and elastic were also measured, and they are well reproduced by SMASH. Additionally, one can see the dominance of resonance contributions at low energies, whereas soft string interactions quickly take over. At even higher collision energies, one would also observe hard strings. Since there are many more possible reactions between the constituents, the interested reader is referred to [255], where a wide collection of results calculated with SMASH is publicly available for each version. In these examples, one observes the interplay of multiple channels (resonance excitations, elastic scattering, etc.) that collectively reproduce the total measured cross section.

RESONANCE FORMATION. At low and intermediate energies, resonances dominate the dynamics through their formation and decay. Elastic and inelastic channels both play a role. Elastic processes for many combinations of nucleons, pions, kaons, or deuterons are guided by experimentally known cross sections, whereas the Additive Quark Model (AQM) [287] is employed when data are sparse. Inelastic processes include, among others, Δ and N^* excitation in NN collisions, hyperon production in KN interactions, and baryon-antibaryon annihilation channels such as $N\bar{N} \rightarrow \text{multi-pion}$. A subset of multi-particle reactions (e.g., $N\bar{N} \leftrightarrow 5\pi$) can be modeled via sequential two-body collisions or—if all particles lie within the same local volume—through an explicit multi-particle collision

approach using the stochastic collision criterion. The cross section of resonance formation ($ab \rightarrow R$) can be calculated from the forward decay process ($R \rightarrow ab$). Therefore, the cross section is given in terms of the decay width as [110]

$$\sigma_{ab \rightarrow R}(s) = \frac{2J_R + 1}{(2J_a + 1)(2J_b + 1)} S_{ab} \frac{2\pi^2}{\vec{p}_i^2} \Gamma_{ab \rightarrow R}(s) \mathcal{A}_R(\sqrt{s}). \quad (2.9)$$

It is important to stress that $\Gamma_{ab \rightarrow R}(s)$ only equals $\Gamma_{R \rightarrow ab}(s)$ for stable particles. However, for unstable incoming particles, a modified width is employed in the so-called Manley resonance treatment. The form of this modification is

$$\Gamma_{ab \rightarrow R}(m) = \Gamma_{R \rightarrow ab}^0 \frac{|\vec{p}_{ab}| B_L^2(|\vec{p}_{ab}| R) \mathcal{F}_{ab}(m)}{m \rho_{ab}(M_0)}, \quad (2.10)$$

with the same notation as in eq. (2.5).

DECAY TREATMENT AND COLLISIONAL BROADENING. Besides scatterings, resonances also decay. In SMASH, the probability that a resonance decays in its rest frame over a small time interval Δt is

$$P_{\text{decay}} = \frac{\Delta t}{\tau}, \quad (2.11)$$

where τ is the inverse of the total decay width. The probability is the input for the Monte-Carlo simulation of the decay at each time step, giving in average the correct lifetime. Each partial decay channel has a branching ratio proportional to its partial width.

Vacuum decay widths are consistently applied, but since hadrons in a dense medium may scatter inelastically before decaying, their effective lifetimes can be shortened, a phenomenon termed collisional broadening. This dynamical effect is naturally captured in transport simulations without modifying vacuum widths [288]. Therefore, the different processes influencing the lifetimes of resonances can be disentangled out-of-the-box.

ELASTIC COLLISIONS Well-established experimental measurements exist for many crucial elastic processes, notably NN, $N\bar{N}$, NK, (anti)deuteron-nucleon, and (anti)deuteron-pion scattering. These are encoded in parametrized cross sections [114, 259, 262, 284]. Other channels, such as baryon-baryon or meson-meson scattering that lack precise data, rely on the AQM prescription. In the resonance-rich region of moderate energies, so-called “quasi-elastic” scattering proceeds via intermediate resonances, for example $\pi\pi \rightarrow \{\sigma, \rho\} \rightarrow \pi\pi$. Elastic channels can incorporate nontrivial angular dependencies (e.g., for NN scattering) [289].

INELASTIC COLLISIONS. Inelastic collisions $2 \rightarrow 2$ in SMASH comprise single and double resonance excitations (NN \rightarrow NR or NN \rightarrow RR), resonance absorption (NR \rightarrow NN), strangeness exchange (KN \rightarrow πY), charge exchange (e.g., $K^- p \leftrightarrow \bar{K}^0 n$), and other production or annihilation channels.

The cross section for inelastic scattering can often be expressed in terms of matrix elements $|\mathcal{M}|^2$ that depend on the Mandelstam variable s . For instance, double resonance

excitations are calculated by integrating over resonance spectral functions in the final state, as illustrated by

$$\sigma_{ab \rightarrow R_1 R_2}(s) = \frac{(2J_{R_1} + 1)(2J_{R_2} + 1)}{s |\vec{p}_i|} \sum_I \left(C_{ab}^I C_{R_1 R_2}^I \right)^2 \frac{|\mathcal{M}|_{ab \leftrightarrow R_1 R_2}^2(s, I)}{16\pi} \times \int_{m_1^{\min}}^{\sqrt{s} - m_2^{\min}} dm_1 \mathcal{A}_1(m_1) \int_{m_2^{\min}}^{\sqrt{s} - m_1^{\min}} dm_2 \mathcal{A}_2(m_2) |\vec{p}_f|(\sqrt{s}, m_1, m_2), \quad (2.12)$$

with C_{ab}^I denoting isospin Clebsch-Gordan factors, $|\vec{p}_{i(f)}|$ the center-of-mass momentum in the initial (final) state, and $\mathcal{A}_{1(2)}$ being the spectral functions of the formed resonances. Various parameterizations exist for the matrix elements (e.g., one-boson-exchange fits for $NN \rightarrow N\Delta$), and the resonance widths (both forward and backward processes) obey the principle of detailed balance.

STRING FRAGMENTATION. At higher collision energies, where resonances above masses of around 2 GeV are not well known, SMASH models inelastic interactions using string fragmentation. If two strongly interacting particles are separated, a string is formed, which is also known as a color flux tube. As seen before, the nature of the strong coupling constant results in its strength increasing with the distance. Therefore, the energy of the string rises with the separation scale. This continues until enough energy for a new quark-anti-quark pair is available. At this point, the string fragments, which means that the newly formed quarks and gluons are confined into new hadrons. In this way, string fragmentation models the complex multi-particle production at high-energy hadron collisions. This approach relies on the Lund string model [290] as implemented in PYTHIA [291], and includes the distinction between single-diffractive, double-diffractive, and non-diffractive processes. In practice, a transition region is set up to ensure a smooth handover between the resonance-dominated regime and the string-dominated one. Soft or hard string fragmentation may be activated depending on the collision energy [114, 261, 292]. Hard strings are modeled using cross sections calculated from pQCD [291]. As a result, they are only applicable for highly energetic collisions. An interpolation between resonances and hard string cross sections for the intermediate energy range is given in the soft string routine. It is tuned to match the total cross section. This approach is inspired by the logic employed in UrQMD [114, 292]. In the common case that the inelastic cross section for a particle pair is not known, the Additive Quark Model (AQM) [287] is used. Along similar lines, since PYTHIA only fragments (anti-) nucleons, pions and other particle species are mapped onto the known fragmentations.

In a dynamical picture pair production does not happen simultaneously but at different points in time. In the yoyo model, the created particles are assigned a formation time. This is mirrored in SMASH by assigning the particles a formation time. Until this time has passed, the cross section is scaled down, proportional to the amount of non-leading string fragments. The cross section continuously increases till formation time for high collision energies. At lower collision energies, a step function is used [261].

DETAILED BALANCE. SMASH enforces exact conservation of baryon number, strangeness, and electric charge for every interaction. Additionally, time-reversal symmetry is respected for any channel with an explicit back-reaction, thus satisfying detailed balance

in resonance production and absorption. Therefore, the probability of a reaction from an initial phase space distribution Γ_i to the final phase space distribution Γ_f has to follow

$$p(\Gamma_i, \Gamma_f) = p(\Gamma_f, \Gamma_i). \quad (2.13)$$

This principle of ergodicity ensures the ability to reach thermal equilibrium from any accessible state [293]. String-based processes lacking reverse fusion channels partially violate detailed balance but remain necessary at high energies.

PAULI BLOCKING Fermionic quantum statistics is partially realized via Pauli blocking for baryons. In the BUU framework, the collision integral carries factors $(1 - f)$ for the final states of fermions to reflect the Pauli exclusion principle. Numerically, SMASH implements this by rejecting collisions into fully occupied states according to the local phase space densities. In the present work, Pauli blocking is turned off, as it has a diminished impact at high collision energies [109].

All these mechanisms, from resonance formation and decay to string fragmentation and multi-particle channels, constitute the collision term for the transport dynamics of SMASH. In this manner, the model provides an effective solution of the Boltzmann (or BUU) equation across a broad range of energies and collision systems.

2.1.2.3 Collision Criteria and Test Particle Method

Interactions among point-like particles in SMASH can only occur when the particles come sufficiently close. This seemingly simple notion of “closeness” must be defined consistently to decide both whether a scattering event happens and at what time it is realized in the simulation. In SMASH, two conceptually different classes of collision criteria exist: geometric criteria and a stochastic criteria. Both are compatible with the Boltzmann or BUU framework, but they differ in how the effective cross section is mapped onto possible collisions, and in how easily they generalize to multiple incoming particles.

GEOMETRIC CRITERIA. A traditional geometric approach [114, 123] interprets the total cross section σ as an effective area. Two hadrons collide if their transverse distance at closest approach d_T is less than

$$d_{\text{int}} = \sqrt{\frac{\sigma}{\pi}}, \quad (2.14)$$

where σ is the total cross section for the relevant process. When a collision is accepted, one must then decide which channel actually occurs, weighting different partial cross sections by $\sigma_{\text{partial}}/\sigma_{\text{tot}}$. Originally, SMASH employed a non-covariant version of this criterion, similar to UrQMD [114], in which positions and momenta were evaluated in a preferred frame, and the collision time was computed as

$$t_{\text{coll}} = -\frac{(\vec{r}_a - \vec{r}_b) \cdot (\frac{\vec{p}_a}{E_a} - \frac{\vec{p}_b}{E_b})}{(\frac{\vec{p}_a}{E_a} - \frac{\vec{p}_b}{E_b})^2}, \quad (2.15)$$

supplemented by

$$d_T^2 = (\vec{r}_a - \vec{r}_b)^2 - \frac{[(\vec{r}_a - \vec{r}_b) \cdot (\vec{p}_a - \vec{p}_b)]^2}{(\vec{p}_a - \vec{p}_b)^2}. \quad (2.16)$$

Such a prescription can introduce frame dependence in deciding the sequence of collisions, since time-ordering of interactions is not covariant. To mitigate this, a fully covariant geometric criterion was implemented in SMASH-2.0 [294], which employs the Lorentz-invariant generalization of d_T and a covariant procedure for collision times. Nonetheless, geometric criteria—whether covariant or not—describe instantaneous interactions over a finite range. This inevitably introduces some residual non-locality and potential causality issues that are alleviated by using test particles to reduce the reaction range.

Although geometric criteria work efficiently for two-particle collisions, they are difficult to extend to processes with more than two incoming particles. One can simulate multi-particle reactions via a chain of successive $2 \rightarrow 2$ or $2 \rightarrow n$ scatterings, but only if suitable intermediate states exist. Alternatively, SMASH offers a stochastic collision criterion, which provides a more direct handle on $3 \rightarrow 2$, $3 \rightarrow 1$, $5 \rightarrow 2$, and other multi-particle processes.

STOCHASTIC COLLISION CRITERION The stochastic criterion departs from the geometric interpretation of cross sections as physical areas. Instead, space is divided into small cells of volume $\Delta^3 x$, and for each pair (or group) of particles inside a cell, the collision probability is computed over a small time interval Δt . For a $2 \rightarrow m$ channel, for instance, the probability can be expressed as

$$P_{2 \rightarrow m} = \frac{\Delta t}{\Delta^3 x} v_{\text{rel}} \sigma_{2 \rightarrow m}, \quad (2.17)$$

where v_{rel} is the relative velocity between the two particles and $\sigma_{2 \rightarrow m}$ is the corresponding cross section. If the number thus obtained lies below a random number generated in $(0, 1)$, the collision is accepted. This approach is then generalized to multiple incoming (and outgoing) particles, making it ideal for baryon-antibaryon annihilation with $N\bar{N} \leftrightarrow 5\pi$ or catalysis reactions for deuteron production [295].

An obvious advantage is that multi-particle processes require only knowledge of the total cross section and no ad hoc geometric notion of “closeness” for more than two particles. A disadvantage is that large numbers of particles in each cell greatly increase the combinatorial cost of calculating probabilities for every possible collision. Moreover, for stable results, $\Delta^3 x$ and Δt must be chosen such that particles do not significantly change their distribution within a cell during the interval. Practically, a large test particle number N_{test} is often used to ensure smoother phase-space densities. This makes this approach very costly at high collision energies and densities. Therefore, for the rest of this work, the geometric covariant criterion is used and as a result no multiparticle interactions.

TEST PARTICLE METHOD AND SCALING OF CROSS SECTIONS. SMASH can operate in a Boltzmann-Uehling-Uhlenbeck (BUU) spirit, meaning that each physical particle

is represented by N_{test} *test* particles. The total number N of physical particles thus is replaced by $N \mapsto N N_{\text{test}}$, while the cross section must be scaled down according to

$$\sigma \mapsto \sigma N_{\text{test}}^{-1}, \quad (2.18)$$

so that the physical scattering rate is unchanged. In cascade mode (i.e. no mean fields), increasing N_{test} reduces spurious fluctuations and narrows the effective interaction region, thereby mitigating non-locality issues inherent to instantaneous collisions. At the same time, one must keep in mind that raising N_{test} increases the number of collision checks, which can be computationally expensive—particularly when employing the stochastic approach that examines all possible particle combinations within each cell.

In summary, SMASH offers both geometric and stochastic formulations of the collision criterion. The geometric approach is fast and simple for $2 \rightarrow 2$ scatterings but struggles with multi-particle processes, while the stochastic approach provides a covariant, cell-based collision probability that cleanly accommodates higher-order processes at the price of greater computational overhead. Through these complementary strategies—and the flexibility of the test particle method—SMASH can effectively tackle a wide variety of hadronic collision dynamics.

2.1.3 Initialization Scenarios

SMASH provides several distinct initialization modes, each suited to a particular physical situation and energy regime [109]. In particular, it may simulate either the full evolution of a low- or intermediate-energy heavy-ion collision, or only a particular stage of a higher-energy scenario (e.g., an afterburner for the hadronic freeze-out). The following subsections highlight the main ways to set up the hadronic system.

COLLIDER (TWO NUCLEI). For collisions of nuclei at low and intermediate energies, SMASH initializes the nucleons (protons and neutrons) according to a Woods-Saxon density profile,

$$\frac{dN}{d^3r} = \frac{\rho_0}{\exp[(r - r_0)/d] + 1}, \quad (2.19)$$

where $\rho_0 = 0.168 \text{ fm}^{-3}$ is the ground-state nuclear density, r_0 is the effective radius, and d is the diffuseness of the nucleus [109]. Certain special nuclei demand specific (r_0, d) values, and deformations can be introduced by allowing r to depend on the angles (θ, ϕ) [296]. Once the nucleons are placed, they can optionally be assigned Fermi motion up to a local Fermi momentum

$$p_F(\vec{r}) = \hbar c [3\pi^2 \rho(\vec{r})]^{1/3}, \quad (2.20)$$

accounting for the Pauli principle. Because such initial momenta might cause spurious expansion of the nucleus, one may either use a mean-field potential to bind the nucleons or freeze the Fermi motion for propagation purposes, applying it only during collisions [109, 297]. After the setup, the two nuclei (or more exotic systems) are boosted to the desired beam energy and arranged at an impact parameter b , which is defined as the perpendicular distance between the trajectories of the two nuclei, measured in the

plane transverse to the beam direction ². This mode covers the entire evolution of the collision within SMASH, from initial nuclear overlap through final-state scatterings.

INFINITE MATTER (BOX). A second mode simulates infinite nuclear or hadronic matter by imposing periodic boundary conditions in a cubic box. Particles that leave one face of the box reappear on the opposite face with unchanged momentum. Hadrons and their momenta can be prescribed from grand-canonical thermal distributions, quantum statistical distributions or set manually. This periodic “box” scenario is valuable for investigating equilibrium properties such as transport coefficients, chemical relaxation, and thermalization. One can also initialize resonances at their pole masses, or sample them with the corresponding spectral functions as needed.

SPHERE. An alternative, spherically symmetric initial condition places hadrons uniformly in a sphere of radius R . Their momenta may again be drawn from thermal or manual distributions. This setup mimics an expanding fireball without boundary conditions and can be employed to study radial flow, expansion dynamics, or to embed high-energy test particles (e.g., jets) in a controlled environment [298].

AFTERRUNNER (LIST MODE). At higher collision energies, the QCD medium undergoes early partonic or hydrodynamic evolution, after which the system transitions into a hadron gas phase. SMASH can serve as an afterburner to handle the final hadronic rescattering stage. In this mode, SMASH reads a particle list obtained, for instance, from a Cooper-Frye sampling on a hydrodynamic freeze-out hypersurface. Each hadron is then propagated through any further collisions and decays until the medium becomes dilute. Some of these hadrons may appear at different formation times, so SMASH rewinds or “scrolls back” their positions to the earliest relevant time and starts the simulation from that point, prohibiting interactions before a hadron is actually produced.

These complementary initialization modes make SMASH flexible across a wide range of energies and applications: from collisions of stable or exotic nuclei in the low-energy regime, to thermalized boxes for equilibrium studies, up to high-energy collisions where SMASH provides either the post-hydrodynamic rescattering stage or the pre-hydrodynamic initial conditions.

² This is based on the assumption of antiparallel movement of the nuclei, which is in general approximately true.

2.1.4 Viscosities in SMASH

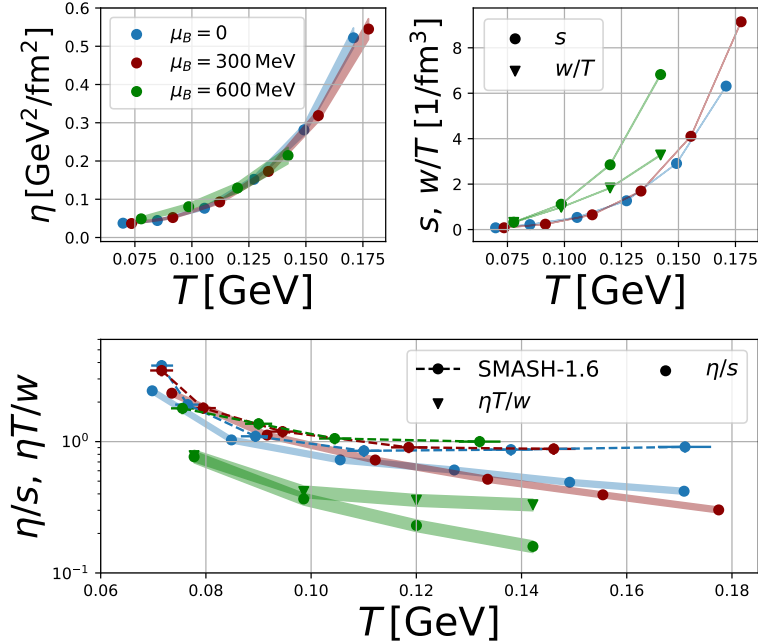


FIGURE 2.5: Upper row left: shear viscosity η . Upper row right: entropy density (circles) and enthalpy (triangles). Bottom: η/s (circles) or $\eta T/w$ (triangles) as a function of the temperature. Results are shown for different values of the baryochemical potential: $\mu_B = 0$ (blue), $\mu_B = 300$ MeV (red) and $\mu_B = 600$ MeV (green). The results for η/s from [266] are included as squares and the KSS bound $1/4\pi$ as a dotted line. From [267].

The aim of this work is to study transport coefficients in the QCD phase diagram in regions sufficiently hot and dense to use hydrodynamics as an effective description. For more dilute systems, hadronic transport can be used to deliver predictions for viscosities. This is in general performed using the Green-Kubo formalism [267]. Figure 2.5 shows the prediction for both temperature and baryochemical potential dependence, which suggests in this region of the phase diagram a decrease both with temperature and density. This fits the expectations, as we are in a region with a smaller energy density than the transition line.

2.1.5 Equation of State from SMASH

Although SMASH primarily operates at the microscopic level by propagating hadrons and their interactions, it also supplies a hadronic equation of state (EoS) that can be utilized in hybrid modeling [109, 268]. One starts by describing the ensemble of mesons and baryons in a grand-canonical framework at given temperature T and chemical potentials μ_B , μ_S , and μ_Q . Various equilibrium thermodynamic observables (e.g., the energy density ϵ , the net particle densities n_B , n_S , n_Q , and the pressure p) then follow from momentum-space integrals over relativistic distributions. When tabulated at discrete points in (ϵ, n_B, n_Q) or (T, μ_B, μ_Q) , this EoS can be matched to a hydrodynamic description, ensuring a consistent

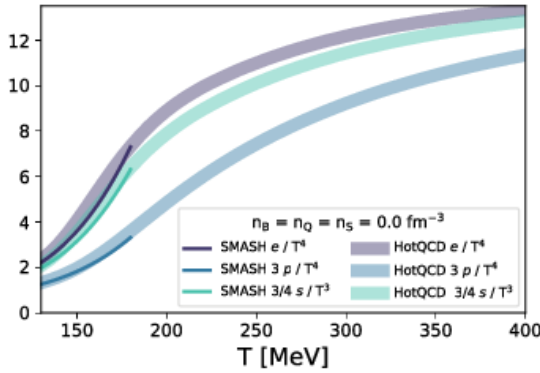


FIGURE 2.6: The equation of state of the SMASH hadron resonance gas for vanishing baryon, charge and strange density as a function of temperature: energy density ϵ , pressure p , and entropy density s (lines) compared to 2+1-flavor lattice QCD results [33] (bands). From [221].

switch (particlization) between fluid cells in hydrodynamics and the microscopic hadron-resonance gas in SMASH [221].

MOTIVATION FOR THE SMASH EOS. At high energy densities, a transition to a quark-gluon phase is eventually required because purely hadronic degrees of freedom become insufficient. Nevertheless, for moderate and low energies, the SMASH EoS serves as a valuable baseline in numerous hybrid approaches. Near thresholds where partial densities of light hadrons (pions, nucleons) vanish, specialized interpolations are necessary to ensure numerical smoothness in solving for T and μ_B .

In general, the EoS maps the thermodynamic variables $(\epsilon, n_B, n_Q, n_S)$ to the temperature T , the pressure p , and chemical potentials (μ_B, μ_Q, μ_S) . Because heavy-ion collisions typically conserve net strangeness to zero, one often omits an explicit dependence on n_S by setting $n_S = 0$. Moreover, for the hydrodynamic stage in a hybrid setup, local net strangeness is usually chosen to be zero initially and remains so throughout its evolution. Hence, the SMASH EoS employed here effectively provides:

$$(\epsilon, n_B, n_Q) \rightarrow (T, p, \mu_B, \mu_Q, \mu_S), \quad (2.21)$$

with $n_S = 0$ enforced.

DERIVATION VIA A GRAND-CANONICAL BOLTZMANN GAS. The hadronic EoS is found by solving a system of coupled equations that express ϵ, n_B, n_Q, n_S in terms of T, μ_B, μ_Q, μ_S under the assumption of an ideal Boltzmann gas in the grand-canonical ensemble [251]:

$$\begin{aligned} \epsilon &= \epsilon(T, \mu_B, \mu_Q, \mu_S), \\ n_B &= n_B(T, \mu_B, \mu_Q, \mu_S), \\ n_Q &= n_Q(T, \mu_B, \mu_Q, \mu_S), \\ n_S &= n_S(T, \mu_B, \mu_Q, \mu_S). \end{aligned} \quad (2.22)$$

A root-finding algorithm obtains T , p , μ_B , μ_Q and μ_S for a given $(\epsilon, n_B, n_Q, n_S)$. Unfortunately, the solver can be highly sensitive to initial guesses, especially at low energy densities or near kinematic thresholds.

Consequently, the tabulated SMASH EoS is most reliable at sufficiently large ϵ and moderate baryon/charge densities. The final table covers ϵ from 0.01 up to $1.0 \text{ GeV}/\text{fm}^3$ and includes all SMASH hadronic degrees of freedom. It is publicly available in tabular form [299].

COMPARISON WITH LATTICE QCD A standard validation is to compare the SMASH EoS to lattice QCD at $\mu_B = \mu_Q = \mu_S = 0$. Figure 2.6 shows the pressure p , energy density ϵ , and entropy density s (all divided by appropriate powers of T) versus temperature, in comparison to 2+1-flavor lattice data [33]. The SMASH curves (lines) and the lattice results (bands) agree rather well at low T , confirming the hadron-resonance-gas description in that regime.

RELEVANCE FOR HYBRID APPROACHES In a hydrodynamics-plus-transport (hybrid) framework, this SMASH EoS is key. During the particlization step, one maps each fluid cell at temperature T and baryon chemical potential μ_B onto a hadron-resonance gas. If the macroscopic EoS underlying the hydrodynamic phase does not match the microscopic EoS used by SMASH, quantum number conservation and consistency at freeze-out become problematic. Therefore, the SMASH equation of state is extensively employed in hybrid modeling [221], particularly at moderate or lower collision energies.

With these considerations in mind, we now shift to describing the second major component of the hybrid approach, namely the hydrodynamic code vHLLE.

2.2 Viscous Hydrodynamics in the vHLLE Approach

The hydrodynamic code vHLLE belongs to the class of viscous relativistic hydrodynamics. As explained earlier, using viscous hydrodynamics relaxes the requirement of equilibrium for the nuclear matter, which is a more appropriate description for the quickly expanding fireball. vHLLE is built to solve second-order (Israel-Stewart) relativistic viscous hydrodynamics in full three spatial dimensions plus time. This framework addresses shortcomings of the simpler first-order Navier-Stokes approach, incorporates relaxation-type equations for dissipative stresses, and uses Godunov/HLLE-type algorithms to handle large velocity gradients and potential shock waves. In the following, we describe the underlying algorithm in a quick overview. More details are provided in the relevant paper [211] and in the original papers about the Israel-Stewart approach [166, 300].

2.2.1 From Basic Conservation Laws to Relativistic Navier-Stokes

Starting from the fundamental conservation laws eq. (1.17) and eq. (1.18) the total energy-momentum tensor $T^{\mu\nu}$ is written as a sum of an *ideal* part and a small *dissipative* correction:

$$T^{\mu\nu} = T_{\text{ideal}}^{\mu\nu} + \Delta T^{\mu\nu}. \quad (2.23)$$

In the Navier-Stokes tradition (both non-relativistic and relativistic), one usually posits that in a near-equilibrium regime, the leading dissipative corrections are first order in gradients of the fluid velocity or thermodynamic fields. Physically, this is motivated by a Taylor expansion about local equilibrium. If deviations from equilibrium are small, then to first order, shear and bulk stresses respond proportionally to local gradients:

$$\Delta T^{\mu\nu} \propto (\partial u).$$

Hence, in a relativistic setting, one splits:

$$\Delta T^{\mu\nu} = \pi^{\mu\nu} + \Pi g^{\mu\nu}, \quad (2.24)$$

where $\pi^{\mu\nu}$ captures the *shear* contributions and Π the *bulk* pressure correction.

SHEAR STRESS $\pi^{\mu\nu}$ AND BULK PRESSURE Π In an isotropic but near-equilibrium fluid, the viscous stress can be separated into:

- **Shear-stress tensor** $\pi^{\mu\nu}$, which is transverse, symmetric, and traceless. This accounts for anisotropic momentum transport when velocity gradients deform the fluid shape.
- **Bulk pressure** Π , a scalar correction that captures expansion or compression modes uniform in all directions.

Note that with these definitions, the energy-momentum tensor is symmetric, just like in the ideal case. The shear-stress tensor and the bulk pressure can be expressed in linear-gradient form (Navier-Stokes limit) as:

$$\pi_{\text{NS}}^{\mu\nu} = 2\eta\sigma^{\mu\nu} = \eta \left(\Delta^{\mu\alpha}\partial_\alpha u^\nu + \Delta^{\nu\alpha}\partial_\alpha u^\mu - \frac{2}{3}\Delta^{\mu\nu}\partial_\alpha u^\alpha \right), \quad (2.25)$$

$$\Pi_{\text{NS}} = -\zeta\partial_\alpha u^\alpha. \quad (2.26)$$

Here, $\sigma^{\mu\nu}$ is the symmetric and traceless velocity-gradient tensor, η is the shear viscosity coefficient, ζ is the bulk viscosity coefficient and $\Delta^{\mu\nu} = g^{\mu\nu} - u^\mu u^\nu$. These forms represent:

- $\pi_{\text{NS}}^{\mu\nu}$ is linear in the symmetrized velocity gradient $\sigma^{\mu\nu}$. The subtraction of $\frac{2}{3}\Delta^{\mu\nu}(\partial_\alpha u^\alpha)$ ensures tracelessness.
- Π_{NS} depends on the local expansion rate $\partial_\alpha u^\alpha$, contributing an isotropic stress shift for expansions or compressions.

This first-order prescription is valid near equilibrium when gradients are small. Higher-order terms are neglected, implying that the system's departure from equilibrium is mild enough for a linear-approximation.

2.2.2 Problems of First-Order Navier-Stokes and the Israel-Stewart Solution

Althoug the dissipative corrections above yield a straightforward way to incorporate viscous effects, doing so, one encounters two major problems:

- *Causality violation*: Propagation speeds for disturbances exceed the speed of light.
- *Instability*: In strongly relativistic flows, the equations can become ill-posed numerically and physically.

These issues arise because one tries to force the shear-stress tensor $\pi_{\text{NS}}^{\mu\nu}$ and bulk pressure Π_{NS} to be instantaneously proportional to local velocity gradients. In many realistic situations, there is a finite relaxation time for establishing dissipative corrections.

Israel-Stewart theory [166, 300] overcomes these deficiencies by treating $\pi^{\mu\nu}$ and Π as independent degrees of freedom with their own relaxation-type evolution equations. For example, instead of forcing $\pi^{\mu\nu} = \eta \sigma^{\mu\nu}$ at each moment in time, one writes

$$u^\gamma \partial_\gamma \pi^{\mu\nu} = -\frac{\pi^{\mu\nu} - \pi_{\text{NS}}^{\mu\nu}}{\tau_\pi} - \frac{4}{3} \pi^{\mu\nu} \partial_\gamma u^\gamma + \dots \quad (2.27)$$

where $\pi_{\text{NS}}^{\mu\nu}$ is the Navier-Stokes term, τ_π is a relaxation time, and \dots includes possible vorticity or geometrical source corrections. Similarly, one finds

$$u^\gamma \partial_\gamma \Pi = -\frac{\Pi - \Pi_{\text{NS}}}{\tau_\Pi} - \frac{4}{3} \Pi \partial_\gamma u^\gamma + \dots \quad (2.28)$$

This formalism ensures that the dissipative currents do not exceed physical bounds and approach the Navier-Stokes form only exponentially over a relaxation timescale τ_π . A similar logic applies to the bulk pressure Π . Consequently, causality is preserved, and instabilities are reduced [167]. $\pi_{\text{NS}}^{\mu\nu}$ and Π_{NS} are the Navier-Stokes forms (the combination of velocity gradients with η or ζ), while τ_π and τ_Π are relaxation times controlling how fast $\pi^{\mu\nu}$ and Π approach their Navier-Stokes limits. Thus, these equations are of the relaxation-type because each non-equilibrium component evolves toward its asymptotic (Navier-Stokes) form on timescales set by τ_π or τ_Π . Physically, that timescale arises from kinetic considerations: dissipative currents cannot instantly track changing velocity gradients but must relax from their previous values. For the Navier-Stokes limits,

$$\pi_{\text{NS}}^{\mu\nu} = 2\eta \sigma^{\mu\nu}, \quad \Pi_{\text{NS}} = -\zeta \nabla_\lambda u^\lambda, \quad (2.29)$$

with shear viscosity η and bulk viscosity ζ . These equations reduce to first-order Navier-Stokes if $\tau_\pi, \tau_\Pi \rightarrow 0$. A typical assumption is that viscosity corrections remain small relative to ideal parts, though the formalism can (in principle) handle moderate departures.

2.2.3 Numerical Implementation

The evolution of the viscous fluid in vHLLE is numerically realized through mirroring the splitting of ideal and viscous parts, following ideas from [301]. The code separates the contributions from the ideal (inviscid) part of the energy-momentum tensor and the viscous part, updating them sequentially within each time step Δt . In broad strokes, the code does the following at each time step:

1. Solve the ideal (non-dissipative) hydrodynamic equations, ignoring any shear or bulk viscous terms.

2. Update the dissipative quantities themselves, such as $\pi^{\mu\nu}$ and Π , by integrating their Israel-Stewart relaxation equations.
3. Re-insert the viscous flux corrections into the full hydrodynamic conservation laws for a final update.

Below, we outline why this decomposition is advantageous, how each step is performed, and how stability is preserved if the relaxation times are small.

2.2.3.1 *Splitting of Ideal and Viscous Parts*

We write the fundamental conservation laws eq. (1.17) and eq. (1.18) in Minkowski coordinates for clarity:

$$\frac{\partial Q^\mu}{\partial t} + \frac{\partial F^{\mu i}}{\partial x^i} = 0, \quad (2.30)$$

$$\frac{\partial N^0}{\partial t} + \frac{\partial N^i}{\partial x^i} = 0, \quad (2.31)$$

where $Q^\mu \equiv T^{0\mu}$, $F^{\mu i} \equiv T^{\mu i}$, and N^i is the flux of net baryon number (or other conserved charges). In a fully viscous treatment, $T^{\mu\nu} = T_{id}^{\mu\nu} + \delta T^{\mu\nu}$, and the flux $F^{\mu i}$ likewise splits into $F_{id}^{\mu i} + \delta F^{\mu i}$. Following [301], one can rewrite the resulting equations so that the total update can be achieved by two simpler subsystems:

1. **Ideal step:** evolve the system only with $T_{id}^{\mu i}$ (and ignore $\delta T^{\mu\nu}$). Denote the result after a full Δt as $Q_{id}^{*(n+1)}$.
2. **Viscous step:** incorporate the effects of the dissipative fluxes and the Israel-Stewart relaxation equations for the shear/bulk variables. That corrects $Q_{id}^{*(n+1)}$ to $Q_{full}^{n+1} = Q_{id}^{n+1} + \delta Q^{n+1}$, and also updates $\pi^{\mu\nu}$, Π .

2.2.3.2 *Substep 1: Ideal Update*

In the first substep, eq. (2.30) and eq. (2.31) are solved while ignoring any $\pi^{\mu\nu}$, Π . In other words, $T_{id}^{\mu\nu}$ acts like a perfect fluid. This leads to (see [301] for details)

$$\frac{1}{\Delta t} (Q_{id,i}^{*(n+1)} - Q_{id,i}^n) + \frac{1}{\Delta x_i} (\Delta F_{id}) + S_{id,i} = 0, \quad (2.32)$$

where S_{id} are any geometric source terms (as in Milne coordinates). The code employs a Godunov-type finite-volume procedure with an approximate Riemann solver, specifically the HLLE approach [209, 210, 302]. The Godunov's scheme [303] works by first assuming a piecewise constant approximation of the solution. In the following time step, a local solution for the Riemann problem at the cell interfaces is obtained by resolving discontinuities there with the help of a superposition of waves satisfying the conservation equations. Then, after a time interval Δt , the state is averaged and a new piecewise constant approximation is defined. The time step is limited by the CFL condition [304] of $c_s \Delta t < \Delta x / 2$, as otherwise the Riemann problems interact. The approximate solution to the Riemann problem above is constructed with a relativistic extension of the HLLE solver.

APPROXIMATE RIEMANN SOLVER. At each cell boundary, a local Riemann problem is formed by two states, $Q_l = Q_i$ and $Q_r = Q_{i+1}$. The HLLE solver estimates the left/right wave speeds b_l, b_r , solves for the single uniform intermediate state (bounded by shock or rarefaction waves). The properties of the intermediate state follow the algebraic relations:

$$Q_{lr}^\kappa(Q_l, Q_r) = \frac{b_r Q_r^\kappa - b_l Q_l^\kappa - F^\kappa(Q_r) + F^\kappa(Q_l)}{b_r - b_l}, \quad (2.33)$$

$$F_{lr}^\kappa(Q_l, Q_r) = \frac{b_r F^\kappa(Q_l) - b_l F^\kappa(Q_r) + b_l b_r (Q_r^\kappa - Q_l^\kappa)}{b_r - b_l}, \quad (2.34)$$

where κ runs over the component indices (e.g., Lorentz and charge), and $b_{l,r}$ represent the left and right signal (wave) velocities bounding the intermediate state. They can be estimated in various ways; following [305], one uses:

$$b_r = \max \left\{ 0, \frac{\bar{v} + \bar{c}_s}{1 + \bar{v} \bar{c}_s}, \frac{v_r + c_{s,r}}{1 + v_r c_{s,r}} \right\}, \quad (2.35)$$

$$b_l = \min \left\{ 0, \frac{\bar{v} - \bar{c}_s}{1 - \bar{v} \bar{c}_s}, \frac{v_l - c_{s,l}}{1 - v_l c_{s,l}} \right\}, \quad (2.36)$$

where $c_{s,l}, c_{s,r}$ are the local sound speeds (function of ϵ_l, ϵ_r), $v_{l,r}$ are the flow velocities, and \bar{v}, \bar{c}_s are suitable averages of these quantities. The time update is done dimensionally-split in x, y, η directions, repeatedly applying the HLLE solver. For second-order spatial accuracy, the slopes (ΔQ) in each cell are reconstructed by a slope limiter (e.g., the minmod or MUSCL algorithms). For second-order time accuracy, a predictor-corrector step is done:

- First, evolve for half Δt using F_i^n to get $Q_i^{*(n+\frac{1}{2})}$ (predictor).
- Then, recalculate fluxes $F_i^{(n+\frac{1}{2})}$ from these half-step states, and update for the full Δt (corrector) to obtain $Q_i^{*(n+1)}$.

After finishing all coordinate directions, we obtain $Q_{id}^{*(n+1)}$ for that substep.

Cells at domain edges are ghost cells that enforce outflow boundary conditions:

$$Q_{\text{ghost}}^n = Q_{\text{near}}^n,$$

ensuring no inflow from outside, with Q_{near} being the contributions from cells near the boundaries. If the code encounters vacuum ($\epsilon = 0$) in a neighbor cell, wave speeds are set to $b_l = -1$ or $b_r = 1$ to reflect that the fluid can expand into vacuum with nearly no resistance.

2.2.3.3 Substep 2: Relaxation of Viscous Variables

Once the ideal portion $Q_{id}^{*(n+1)}$ is known, vHLLE updates the shear tensor $\pi^{\mu\nu}$ and bulk pressure Π via the Israel-Stewart equations eq. (2.27) and eq. (2.28). This amounts to the integration of equations of motion. The code does this in two phases:

(A) SOURCE INTEGRATION (PREDICTOR-CORRECTOR). The partial derivatives of u^μ and thus $\pi_{NS}^{\mu\nu}, \Pi_{NS}$ are estimated at half time steps or half-locations. Then $\pi^{\mu\nu}$ (or Π) is relaxed towards its Navier-Stokes limit over Δt . If the relaxation time is big enough, this is performed as

$$\pi^{\dagger n+1/2} = \pi^n + I_{\text{full}}(\pi^n) \quad (2.37)$$

$$\pi^{\dagger n+1} = \pi^n + I_{\text{full}}(\pi^{n+1/2}) \quad (2.38)$$

where $I_{\text{full}}(\pi) = -(\pi - \pi_{NS})/\tau_\pi + I_\pi(\pi)$, the viscous source terms (see [211] for more details). For the case $\tau_\pi \ll \Delta t$ [301], a formal solution with only the relaxation part is chosen, thus ensuring stability:

$$\pi_{n+1}^\dagger = (\pi_n - \pi_{NS}) \exp\left(-\frac{\Delta t}{\gamma \tau_\pi}\right) + \pi_{NS}.$$

Integration of the source term $I_\pi(\pi)$ is done separately.

(B) ADVECTION OF $\pi^{\mu\nu}$. The dissipative fields themselves must be advected with the local velocity. vHLL-E uses a first-order upwind approach here, which takes the following form:

$$\pi_{ijk}^{n+1} = \sum_{\Delta i} \sum_{\Delta j} \sum_{\Delta k} w_{\Delta i} w_{\Delta j} w_{\Delta k} \pi_{i+\Delta i, j+\Delta j, k+\Delta k}^{\dagger n+1}$$

where $\Delta i, \Delta j, \Delta k = -1, 0, +1$, and

$$w_{\Delta i} = \{-a_x^-, 1 - |a_x|, a_x^+\}$$

$$a_x^- = \min(v_x \Delta t / \Delta x, 0), \quad a_x^+ = \max(v_x \Delta t / \Delta x, 0)$$

with similar expressions for a_y^\pm and a_η^\pm . This yields π^{n+1}, Π^{n+1} after a single step. An important issue arises here if the viscous corrections are not small, usually due to high gradients of u^μ . Indeed, this can cause instabilities in the hydrodynamical solution. Therefore, clamping or rescaling $\pi^{\mu\nu}$ is performed [301]:

$$\max_{\mu, \nu} |\pi^{\mu\nu}| < C \max_{\mu, \nu} |T_{id}^{\mu\nu}|, \quad |\Pi| < C p, \quad (2.39)$$

where C is of order one but less than unity. It is assumed that such corrections only appear in dilute regions of the medium. Although this implies that in these regions, the assumptions of hydrodynamics are violated, this is only of small concern as due to the diluteness, only a small fraction of energy is bound in these regions and therefore the effect on observables is small.

2.2.3.4 Substep 3: Viscous Flux Correction

Finally, one must incorporate the explicit viscous fluxes (δF) into the momentum/energy conservation. The code solves:

$$\frac{1}{\Delta t} \left((Q_{id,i}^{n+1} + \delta Q_i^{n+1}) - (Q_{id,i}^{*(n+1)} + \delta Q_i^n) \right) + \frac{1}{\Delta x_i} \Delta \delta F + \delta S = 0. \quad (2.40)$$

This is the evolution equation for the viscous part, whereas the ideal evolution equation eq. (2.32) was already solved in substep 1. Here, $Q_{\text{ini}} = Q_{\text{id}}^{*(n+1)} + \delta Q^n$ are the states before flux correction, and $Q_{\text{full}}^{n+1} = Q_{\text{id}}^{n+1} + \delta Q^{n+1}$ is the final result. Because the newly updated π^{n+1}, Π^{n+1} from substep 2 are known, one can compute $\delta F, \delta S$ consistently. The half step results of the viscous fluxes are saved, allowing for a stepwise solving of this equation as well. If the relaxation times are extremely small, this step remains stable because the largest wave speeds were already handled in the ideal flux step, and the local changes in δQ do not propagate extremely fast. After each major or minor update, the code must revert from conservative variables $\{T^\mu, N^\mu\}$ to $\epsilon, p, \vec{v}, \dots$. A standard 1D root search ensures $u^\mu u_\mu = 1$, solves for ϵ and n_B , and checks that $|\vec{v}| < 1$.

After propagating the medium through a sufficient number of time steps, the expansion causes the density to sink rapidly. Eventually, the medium becomes too dilute to fulfill the requirements of a hydrodynamic description. A common condition for switching out hydrodynamics and starting particlization is a limit on the local energy density. Therefore, one has to find at each time step the fluid elements which reached this limit, and save their hydrodynamic quantities. They will form a hypersurface in 4D, as at each time step, new elements will be included. The content of the fluid elements is not removed from the hydrodynamic evolution, but their effect on the medium is assumed to be small. The hypersurface finding is performed using the CORNELIUS procedure [224], which is integrated into vHLLE.

2.2.4 Hypersurface Detection with CORNELIUS

The challenge of constructing a freezeout hypersurface results from the requirements of Cooper-Frye sampling for particlization [223]. It is not sufficient to find only the location of the surface σ , but also its normal. Additionally, although the surface will have in general a complex structure, holes or double counting have to be avoided in order to respect conservation laws.

INITIAL GRID TRAVERSAL. One regards the computational domain as a 4D grid of cells (sometimes called “hypercubes”), each cell bounded by 16 corner points. The fluid variables, including $\epsilon(x)$, are stored at these corner nodes. Once a cell is located where some corners have $\epsilon > \epsilon_{\text{switch}}$ and other corners $\epsilon < \epsilon_{\text{switch}}$, we know the isosurface crosses that cell.

FINDING EDGE INTERSECTIONS. Within a cell that encloses part of the isosurface, CORNELIUS checks all the edges for the location where a linear interpolation of ϵ equals ϵ_{switch} . This procedure is illustrated schematically in 3D in fig. 2.7 but generalized to 4D. Each identified intersection point is recorded as a piece of the boundary.

SORTING INTERSECTION POINTS INTO POLYGONS OR POLYHEDRA. In a 3D slice, the intersection of a cube with an isosurface is typically a polygon (fig. 2.7). In 4D it becomes more intricate, forming a polyhedron with faces that themselves can be polygons. The key challenge is to consistently assemble these intersection points into connected surface patches without leaving holes or accidentally duplicating patches. CORNELIUS accomplishes this by systematically:

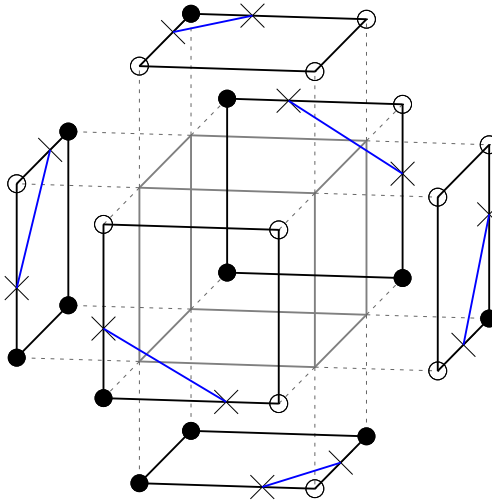


FIGURE 2.7: Reduction of a three dimensional problem into a series of two dimensional problems for surface finding. The surface element is found by looking for its edges on the faces of the cube. From [224].

1. Reducing the problem dimension-by-dimension (e.g., going from edges to faces, then to volumes).
2. Resolving ambiguities in diagonal connections by sampling whether the interior is above/below ϵ_{switch} at carefully chosen center points.
3. Checking for disconnected patches or multiple surface components in a single cell and grouping them appropriately.

This ensures that if the isosurface loops back or separates into multiple fragments, CORNELIUS will detect all such fragments, building a coherent manifold.

COMPUTING NORMAL VECTORS AND HYPERAREAS. Once a polyhedron is found, CORNELIUS needs the 4D oriented surface element $d\sigma_\mu$ which is applied in the Cooper-Frye formula. Analogous to polygons in 3D, each face is subdivided (triangulated) so that the polyhedron can be decomposed into tetrahedra. Summing the oriented volumes of these tetrahedra yields the net hyperarea vector:

$$\Delta\sigma_\mu = \sum_i \epsilon_{\mu\alpha\beta\gamma} \frac{1}{6} f_i a_i^\alpha b_i^\beta c_i^\gamma, \quad (2.41)$$

where a_i, b_i, c_i are vectors from the approximate centroid to the vertices of each tetrahedron face, and $f_i = \pm 1$ chooses the outward direction (i.e. decreasing ϵ). Similarly, the fluid variables ($u^\mu, \epsilon, n_B, \dots$) are linearly interpolated at the centroid of the polyhedron, ensuring the correct local velocity and densities are associated with that surface patch.

2.3 Stages of the SMASH-vHLLE-Hybrid Approach

With both the hadronic transport simulation and the hydrodynamic modeling in place, and the construction of the particlization hypersurface clarified, we now turn to describing how the SMASH-vHLLE-Hybrid is arranged in its default configuration. We follow the successive evolution of each stage in chronological order.

2.3.1 Initial Condition

The initial step of a hybrid approach represents the early, highly energetic collisions between the incoming nuclei. Whereas the initial shape of the nuclei can be inferred from our knowledge about cold nuclei, leading to the Woods-Saxon-distribution, the processes involved in the collision of heavy nuclei are less accessible due to the short lifetime of the initial matter.

2.3.1.1 Hadronic Initial Condition

As explained in section 2.1.3, SMASH initializes the colliding nuclei via a Woods-Saxon density distribution. These nuclei are then propagated in the cascade mode at the specified beam energy, allowing collisions to occur in a purely hadronic manner. We explicitly disregard potentials and Pauli blocking due to the elevated collision energies. However, rather than letting SMASH evolve the collision to its final low-density state, the transport simulation is ended at an isochronous hypersurface in proper time τ_0 . This τ_0 is estimated by

$$\tau_0 = \frac{R_p + R_t}{\sqrt{\left(\frac{\sqrt{s_{NN}}}{2m_N}\right)^2 - 1}}, \quad (2.42)$$

where R_p and R_t are the respective nuclear radii, and $\sqrt{s_{NN}}/(2m_N)$ describes the Lorentz boost of each nucleus [177, 237]. Geometrically, the passing time is the earliest moment when all nucleons of both nuclei have had a chance to interact, thus setting a plausible limit for forming an approximately thermalized fluid. In practice, we also impose a minimum $\tau_0 = 0.5$ fm/c to prevent unreasonably early switching at high energies.

Once a particle crosses $\tau = \tau_0$, it is recorded into an output file for vHLLE and is removed from the SMASH simulation. After all particles have left SMASH in this way, the transport run terminates. Because most collisions in these high-energy systems produce short-lived string interactions, subsequent rescatterings are rare. Hence, removing the crossing particles does not strongly affect the initial-state cascade.

The reason for this is the formation time outlined in section 2.1.2.2. The initial collisions are hard and are, especially at high collisions, dominated by hard string fragmentations, as can be seen in fig. 2.8. This results into a creation of a large amount of unformed particles, as can be seen in fig. 2.9. These have initially very small cross sections and do not interact.

Spectators, that means initial nucleons which not collide, are extracted separately and later introduced again to the system for the late stage rescattering.

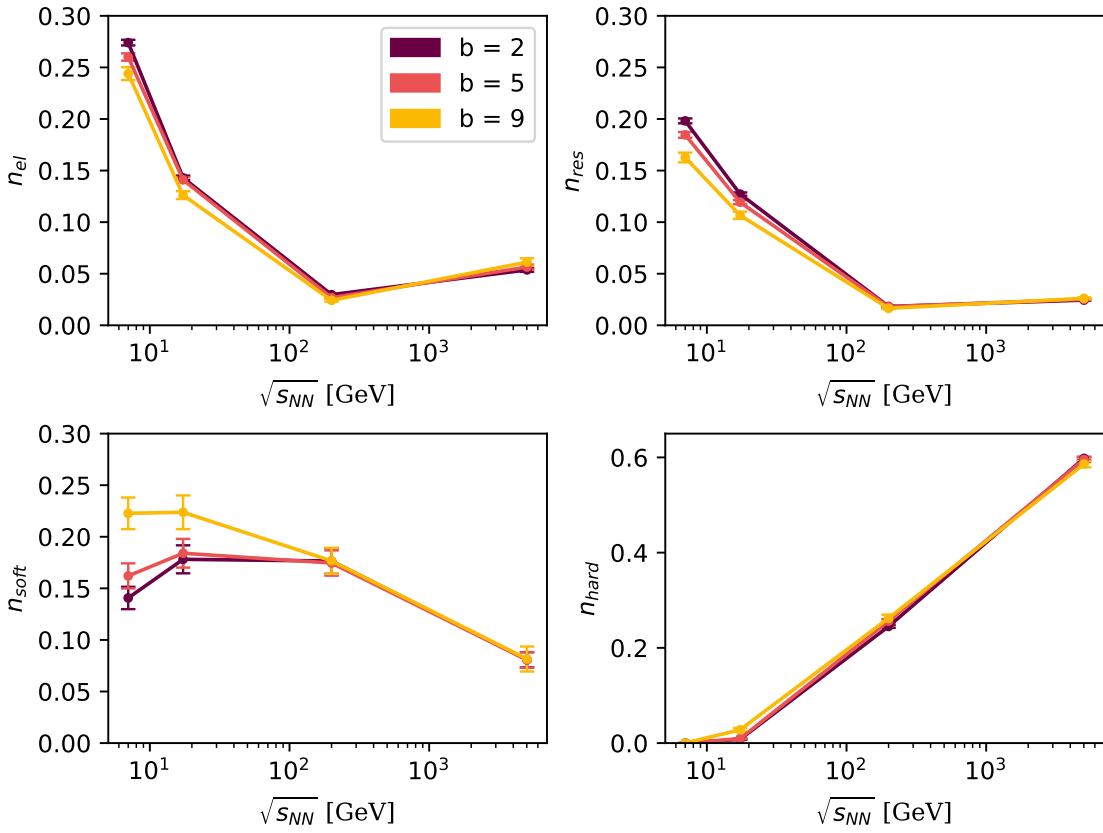


FIGURE 2.8: Process type of the last interaction of particles in the SMASH initial state as a function of collision energy. Clockwise from top-left: ratio of elastic processes n_{el} , ratio of resonance formations n_{res} , ratio of soft string processes n_{soft} and ratio of hard string processes n_{hard} . From [306].

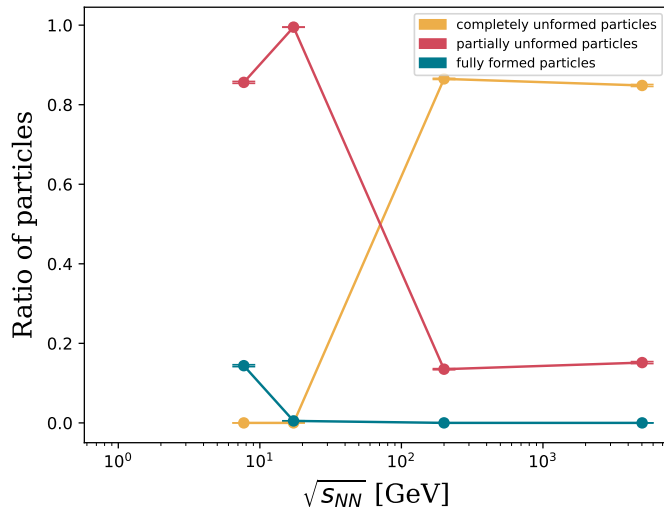


FIGURE 2.9: Ratio of unformed particles in the initial state from SMASH as a function of collision energy with an impact parameter of $b = 2$ fm. Adapted from [306].

CONSTRUCTING THE FLUID INITIAL STATE. At the τ_0 switching surface, each hadron's distribution is very localized in coordinate space, and feeding these point-like momenta directly into vHLLE could produce large velocity gradients and shocks in the fluid. Two principal strategies exist:

1. *Event-averaging*: Summing many hadron-based initial states, then computing mean densities for each fluid cell. This smooths out fluctuations and discards event-by-event structure.
2. *Event-by-event smearing*: Keeping each single event's actual hadrons, but spatially smearing them with a kernel to obtain continuous energy, momentum, and baryon densities.

In our default approach, we adopt a Gaussian kernel:

$$\Delta Q_{ijk}^\alpha = Q^\alpha C \exp\left(-\frac{\Delta x_i^2 + \Delta y_j^2}{R_\perp^2} - \frac{\Delta \eta_k^2}{R_\eta^2} \gamma_\eta^2 \tau_0^2\right), \quad (2.43)$$

where Q^α denotes either a component of the four-momentum or a conserved quantum number (like baryon charge). Here, $(\Delta x_i, \Delta y_j, \Delta \eta_k)$ is the offset from the hadron's coordinates in Milne space to the cell center, R_\perp and R_η control the smearing widths in transverse and longitudinal (rapidity) directions, $\gamma_\eta = \cosh(y_p - \eta)$ is the relevant Lorentz factor, and C is a normalization ensuring total energy and charge are exactly preserved. The parameters R_\perp and R_η crucially tune how strongly the fluctuations are smoothed; large values yield more equilibration and gentler flow fields, whereas small values preserve local irregularities but can cause shocklike structures. In practice, R_\perp and R_η must be chosen consistently with data and with the system size [177, 221]. The ambiguity of this choice reflects the core problem that by construction, hybrid approaches have discontinuities when switching descriptions between the initial state and hydrodynamics. Although controlling the isotropization and avoiding shocks can avoid violating the boundaries of applicability of hydrodynamics, there is no easy remedy for the fact that the physics at these boundaries does not exactly match. As an example, the equation of state of the hadronic gas will not fit precisely the one employed in hydrodynamics. In practice, however, the hadronic initial state has been employed very successfully, which shows that the discontinuities are either small or of very small impact for the evolution.

An alternative criterion is the covariant smearing. Here, the prescription reads

$$K(\Delta \vec{r}) = \frac{\gamma}{(2\pi\sigma^2)^{2/3}} \exp\left(-\frac{\Delta \vec{r}^2 + \gamma^2(\Delta \vec{r} \cdot \vec{\beta})^2}{2\sigma^2}\right) \quad (2.44)$$

After the SMASH outputs have been Gaussian-smeared onto the vHLLE grid, we obtain a continuous fluid initial condition (energy density, flow velocity, baryon density, etc.), ready for hydrodynamic evolution.

Before delving into this topic, we want to outline two alternative ways to initialize the fluid, representative of two classes of initial condition models. The effect of switching the SMASH initial condition model with these will be studied in chapter 4.

2.3.1.2 Parametric Initial Conditions with $T_{\text{RENT}}\text{o}$

The first class are parametric initial condition models, of which $T_{\text{RENT}}\text{o}$ is a prominent example. Unlike the fluidization of a hadronic cascade (as previously discussed), these parametric models provide an ansatz for mapping participant geometry into an energy-density (or entropy-density) distribution, thus circumventing the explicit pre-equilibrium dynamics or microscopic propagation. Here, we sketch the core idea of $T_{\text{RENT}}\text{o}$ to illustrate how a universal, simplified initial-state prescription can be deployed and then fed into hydrodynamical evolution.

T_{RENT} basics. Originally introduced in [307] (see also [54, 308–310]), $T_{\text{RENT}}\text{o}$ postulates a “reduced thickness” approach. In a high-energy collision of two nuclei A and B, one first defines thickness profiles T_A and T_B that specify the transverse densities of the participant matter. A simple, yet flexible, functional form is used to combine these densities:

$$T_R(p; T_A, T_B) = \left(\frac{T_A^p + T_B^p}{2} \right)^{1/p}, \quad (2.45)$$

where p is a dimensionless parameter that interpolates between different limiting behaviors (e.g. $p = 1$ approximates a wounded-nucleon scaling, $p \rightarrow 0$ emulates certain saturation-based or EKRT-like models [311]). The function T_R is then taken as proportional to the local entropy or energy density. One commonly writes:

$$s(\mathbf{x}_\perp) \propto T_R(p; T_A(\mathbf{x}_\perp), T_B(\mathbf{x}_\perp)). \quad (2.46)$$

The parameter p allows for a continuous interpolation between geometrical extremes, making $T_{\text{RENT}}\text{o}$ a powerful and generic tool for investigating how variations in the initial geometric profile translate into observable flow patterns in the subsequent hydrodynamics.

Specifically, $p = 1$ yields

$$T_R = \frac{1}{2}(T_A + T_B), \quad (2.47)$$

which is reminiscent of a wounded nucleon Glauber model [187], while $p \rightarrow 0$ corresponds to the geometric mean,

$$T_R = \sqrt{T_A T_B}, \quad (2.48)$$

which is known to mimic the energy density distributions of the saturation based models discussed in the following. Equation (2.48) can be derived from performing the limes while rewriting eq. (2.45) with the natural logarithm.

Other values such as $p = -1$ (harmonic mean) and large positive or negative p produce even more scalings. Because $T_{\text{RENT}}\text{o}$ does not assume separate binary-collision contributions, its resultant multiplicities do not scale with the number of binary collisions once nucleons have participated.

IMPLEMENTATION DETAILS. One typically samples fluctuating nucleon positions (or quark substructure, if desired), computes the local participant densities $T_A(\mathbf{x}_\perp)$ and $T_B(\mathbf{x}_\perp)$ in transverse plane cells, and then obtains T_R from eq. (2.45). Next, one converts T_R to an entropy density s at the formation (or thermalization) time τ_0 :

$$s(\mathbf{x}_\perp) \propto [T_A^p(\mathbf{x}_\perp) + T_B^p(\mathbf{x}_\perp)]^{1/p}. \quad (2.49)$$

A global normalization is fixed by matching final-state charged-hadron yields to experimental data, or by external constraints such as an overall dS/dy if known. Additionally, local fluctuation models—most commonly gamma-distributed prefactors—are applied to each participating nucleon to mimic the wide multiplicity fluctuations observed in small systems. This yields negative binomial-like total multiplicity distributions that can be tuned to match $p+p$ baseline data.

PARAMETERS AND BAYESIAN INFERENCE. In practice, T_RENTo is frequently embedded in Bayesian analyses [54, 308] as it smoothly spans various physically motivated assumptions about the nuclear collision geometry via p , the nucleon width and nucleon fluctuations. By exploring the posterior distribution of these parameters against an array of final hadronic observables, one can systematically constrain both initial-state and medium properties. The downside is that the wide range and strength of input parameters—the parameter p , the minimum nucleon distance, the nucleon width, the fluctuation parameter as well as the normalization—make T_RENTo so powerful that it allows to overfit the initial condition in a Bayesian context. This is a shared problem with many parametric initial conditions, which have to find a balance between expressibility and allowing for only physically motivated initial states.

NO INITIAL MOMENTA OR CHARGES FROM T_RENTO. One should note that, in its standard usage, T_RENTo only furnishes the density (or entropy) distribution. It does not provide initial flow velocities or local net-baryon profiles unless those are augmented externally. One can, for example, set the fluid velocity to zero or treat the system as initially at rest, ignoring pre-equilibrium flow. This approach is often deemed acceptable at LHC energies or high collision energies, but it is recognized that a true dynamic pre-hydrodynamic stage might impart nontrivial initial flows. For the present purpose, T_RENTo may serve as a convenient baseline to compare with SMASH-based or other dynamic initializations, given its robust track record in describing large classes of experimental data when combined with viscous hydrodynamics [54]. Additionally, T_RENTo only describes a transversal plane and can therefore only offer a description at very high energies, although most recently, a 3D extension was developed [312]. Saturation based models on the other hand derive their motivation from effective field theories, which greatly reduces their parameter space.

2.3.1.3 *Saturation-based Modelling with IP-Glasma*

The Color-Glass-Condensate (CGC) framework [41] offers a first-principle-inspired approach for generating fluctuating initial conditions by unifying the color-charge distributions of large nuclei with classical Yang-Mills (CYM) solutions for the soft gluon fields. One widely used realization of these ideas is the so-called IP-Glasma model [184, 189, 190], which combines the Impact-Parameter dependent Saturation (IP-Sat) approach [313, 314] for nucleon- or proton-level color distributions with the Glasma picture of classical gluon fields.

MOTIVATION FROM THE CGC. At very high energies, the parton densities in the nuclear wavefunction become large, so that the light-cone wavefunction can be described

by classical background fields. Physically, the large occupation numbers of soft gluons make them amenable to an effective classical treatment, while harder partons appear as classical color charges that generate those fields. The starting point is the CGC effective action [315]

$$S_{\text{CGC}} = \int d^4x \left(-\frac{1}{4} F_{\mu\nu}^a F^{a\mu\nu} + J^{a\mu} A_\mu^a \right), \quad (2.50)$$

where $F_{\mu\nu}^a$ denotes the non-Abelian field strength tensor, and $J^{a\mu}$ is the color-current of the large- x (hard) degrees of freedom (valence partons). In the presence of two highly boosted nuclei, each moving along a light-cone direction, one obtains large color sources ρ_A^a , ρ_B^a , whose typical transverse distribution is characterized by the saturation scale $Q_s(x_\perp)$, which grows with energy and local nuclear thickness.

COLOR-CHARGE FLUCTUATION AND IP-SAT. To incorporate realistic fluctuations of color charges at nucleon scale, IP-Glasma uses the IP-Sat (impact-parameter saturation) model [313, 314]. This model fits small- x HERA data (inclusive and diffractive deep inelastic scattering) by representing the proton (or nucleon) as an eikonalized gluon distribution with a known b_\perp (impact-parameter) dependence. Each nucleon carries a local color-charge density $g^2 \mu^2(x_\perp)$ related to $Q_s^2(x_\perp)$ in IP-Sat. For a nucleus, one obtains the net color source by superimposing the nucleon-level $g^2 \mu^2$ contributions at each transverse point, plus random fluctuations in nucleon positions. This yields an event-by-event realization of color charges $\rho_A^a(x_\perp)$ and $\rho_B^a(x_\perp)$ for the two colliding nuclei.

CLASSICAL YANG-MILLS EVOLUTION. Once these color densities are specified, one solves the classical Yang-Mills field equations

$$[D_\nu, F^{\mu\nu}]^a = J^{a\mu}, \quad \text{where} \quad D_\mu = \partial_\mu - i g A_\mu^a t^a, \quad (2.51)$$

subject to the appropriate boundary conditions imposed by the two colliding sheets of color charge along x^\pm . At very early proper time $\tau \rightarrow 0$, the resulting soft gluon fields in the future light cone form the Glasma, a dense plasma of gluons. Concretely, one implements the matching of (boost-invariant) pure gauge fields from nucleus A and nucleus B to get initial gauge fields in the overlap region [316]. Numerically, these classical fields are discretized on a transverse lattice, and one samples random color charges in each nucleon according to IP-Sat. Finally, the initial energy density

$$\varepsilon(\tau = 0, x_\perp) = \varepsilon_E + \varepsilon_B$$

combines contributions from longitudinal electric (E_η) and magnetic (B_η) fields at $\tau = 0$. Notably, the small-distance fluctuations induced by $Q_s(x_\perp)$ lead to finer structures in the energy-density profile than in many simpler Glauber- or k_\perp -factorized-based models. As discussed earlier the total (integrated) energy in each event fluctuates in a manner well fit by a negative binomial distribution [190, 317], consistent with the Glasma flux-tube picture [318].

INPUT TO HYDRODYNAMICS. After computing the classical fields at $\tau \approx 0$, one can (optionally) evolve these fields for a short time in classical Yang-Mills up to $\tau_0 \sim$

0.2–0.5 fm/c, or directly use the $\tau = 0$ result as an initial condition. We will see later that it provides large eccentricities and, due to the short-wavelength structure imparted by Q_s can also lead to harder p_T spectra due to radial flow generated by “hot spots.”

With the initial condition in place, we can now proceed to the hydrodynamic stage.

2.3.2 Hydrodynamic Stage

Following the initialization, the fluid dynamics in vHLLE proceed in Milne coordinates following the procedure outlined in section 2.2. Here, further details on additional aspects of the input are given.

2.3.2.1 Equation of State

The EoS is a crucial input for the hydrodynamic stage of a hybrid approach, as it has to represent relevant physics over a large area of the QCD phase diagram. It must handle hadronization (which is not to be confused with the particlization in the Cooper-Frye procedure, which only changes the way of describing the medium), but also physics of regions of high net-baryon density as well as the physics at LHC-like energies, where the net-baryon density is low but temperature is high. This need arises as the EoS is necessary to close the equations of hydrodynamics for every fluid cell at every time step. Differences in the EoS can therefore have substantial effects on the evolution of the medium [319]. Therefore, one needs to interpolate between predictions of many different sources and combine them in a consistent way. This is achieved by a chiral mean-field equation of state [165, 320, 321], matched to a hadron resonance gas at lower energy densities.

In this approach, the thermodynamics of hadrons (including strange species) is governed by a Lagrangian that respects $SU(3)$ chiral symmetry and incorporates parity-doubled baryon fields, ensuring that chiral symmetry is restored continuously at high densities and/or temperatures. A small, chirally invariant mass term allows for realistic nucleon masses and nuclear binding at saturation density, while scalar and vector couplings to the baryons yield self-consistent mean fields driving the transition. At lower temperatures and densities, the model seamlessly matches a hadron-resonance-gas description, ensuring that nuclear ground-state properties such as binding energy per nucleon and the nuclear liquid-gas transition are reproduced. In the high-density, hot regime, quark degrees of freedom are also included in the CMF approach, yielding a smooth crossover transition for vanishing or moderate net-baryon densities at around 150 to 160 MeV, in qualitative agreement with lattice-QCD thermodynamics. At finite baryon chemical potentials, the EoS can exhibit a rapid crossover. These properties have been extensively compared to nuclear data at low densities (e.g., binding energies and compressibility) and lattice-QCD data at small baryon chemical potentials, with the result that the CMF EoS shows good quantitative agreement in both regimes. Thus, the chiral mean-field EoS spans a wide range of densities and temperatures, providing a consistent description of hadronic and partonic matter and enabling a physically motivated evolution of the medium in the hydrodynamic stage.

A crucial point arises upon the earlier described construction of the freezeout hypersurface, which in the default setting is constructed at $\epsilon_{\text{switch}} = 0.5 \frac{\text{GeV}}{\text{fm}^3}$. Although the equation of state is matched to a hadronic resonance gas, it is not identical to the equation of state of the SMASH resonance gas described in section 2.1.5. However, this is the equation of state of the hadronic gas formed for the late state rescattering. Therefore, although the chiral-mean field equation of state is used for the evolution of the medium, upon construction of the particlization surface, the quantities of the medium are calculated according to the SMASH EoS, which produces a discontinuity in the evolution.

2.3.2.2 Viscosities

vHLLE uses the 14-moment approximation [322, 323]. In Boltzmann-based kinetic theory, one begins with the relativistic Boltzmann equation,

$$k^\mu \partial_\mu f_k = C[f_k],$$

where $f_k \equiv f(x, k)$ is the single-particle distribution function at spacetime point x and momentum k^μ . By multiplying both sides of this equation by powers of k^μ and integrating over momenta, one obtains an infinite series of moment equations: each new moment involves one higher power of k^μ . Physically, these integrals represent increasingly detailed information about how the nonequilibrium system departs from local equilibrium. As long as there is no intrinsic cutoff, the hierarchy of moment equations never truncates by itself.

Israel and Stewart's 14-moment approximation [166] is a practical solution to this "infinite hierarchy" problem. It posits that the deviation from local equilibrium $\delta f_k \equiv f_k - f_{0k}$ can be approximated by expanding in a finite set of orthonormal basis functions. Specifically, they chose a linear combination of fourteen basis functions to capture all dissipative contributions to the energy-momentum tensor (and any conserved currents, if needed) at first and second order in gradients [174, 322, 324]. This truncation implies that nonequilibrium effects on fluid dynamics can be encoded in only two tensor structures: the shear-stress tensor $\pi^{\mu\nu}$ and the bulk viscous pressure Π . Higher-rank moments of δf_k (beyond bulk and shear) are algebraically eliminated via constraints that express them in terms of Π and $\pi^{\mu\nu}$. This leads to relaxation-type equations for Π and $\pi^{\mu\nu}$, such as

$$\tau_\Pi \dot{\Pi} + \Pi = -\zeta \theta - \delta_{\Pi\Pi} \Pi \theta + \lambda_{\Pi\pi} \pi^{\mu\nu} \sigma_{\mu\nu}, \quad (2.52)$$

$$\tau_\pi \dot{\pi}^{\langle\mu\nu\rangle} + \pi^{\mu\nu} = 2\eta \sigma^{\mu\nu} - \delta_{\pi\pi} \pi^{\mu\nu} \theta + \dots, \quad (2.53)$$

where the ellipsis can include other allowed second-order terms (e.g., $\varphi_7 \pi_\alpha^{\langle\mu} \pi^{\nu\rangle\alpha}$, $\lambda_{\pi\Pi} \Pi \sigma^{\mu\nu}$, etc.). Crucially, once bulk and shear viscosities (ζ and η) have been specified, the 14-moment closure provides algebraic formulas for the second-order transport coefficients τ_Π , τ_π , $\delta_{\Pi\Pi}$, $\delta_{\pi\pi}$, ... in terms of thermodynamic integrals and the chosen viscosities. Hence, in fluid-dynamical codes employing Israel-Stewart-like formalisms, one only needs to supply (i) the equation of state, (ii) $\zeta(T, \mu)$, and (iii) $\eta(T, \mu)$. The 14-moment approach then defines how the second- and higher-order coefficients enter the evolution, thereby closing the system of equations while retaining causal and stable dynamics at moderate departures from equilibrium.

These transport coefficients are not just necessary for a correct fluid-dynamic simulation, but give potentially also insight into the nature of the medium. The shear viscosity, as an example, was argued to be sensitive to the phase transition of the QGP medium. The motivation behind this statement is the fact that on the one hand, all liquids in nature exhibit a minimum in the shear viscosity to entropy ratio η/s near a phase transition [61, 325–327]. On the other hand, a similar behavior has also been observed so far from experimental constraints for the shear viscosity of nuclear matter [53–60]. Therefore, there is a strong interest in determining transport coefficients. However, they are very challenging to predict from first principles. Lattice QCD calculations face numerical challenges [328–330]. Nevertheless, many theoretical predictions support a non-vanishing shear viscosity over entropy ratio η/s [47, 331, 332], although many lQCD approaches have to limit themselves to pure gluon systems [332–335]. On the other hand, many phenomenological studies have succeeded in showing that the hadronic observables measured from heavy-ion collisions are sensitive to the viscosities in the QGP [177, 239, 242, 323, 336–338]. In the default approach, collision energy dependent constant values for η/s are chosen, the value of which can be found in [221]. This is in general a legitimate choice, as the main sensitivity of observables is to the effective, event averaged shear viscosity [339]. As has been outlined before however, in general, a dependence on temperature and baryochemical potential is expected. Bulk viscosity, on the other hand, has not been study before in the SMASH-vHLLE-Hybrid approach. It shall be stressed, however, that one of the central contributions of this work is the modification of this viscosities and the study of its effect, which is presented in chapter 5.

With these considerations in place, we can continue to look at particlization in the hybrid approach.

2.3.3 Particlization

Upon reaching sufficient diluteness, hybrid approaches assume that the medium has already hadronized. As an equation of state is employed which is matched to the hadron resonance gas, hydrodynamics can also successfully describe systems which are dominated by hadrons, as long as they are close enough to an equilibrium. As a result, there is a range in which both hadronic transport and hydrodynamics can successfully describe the system. This range of agreement is crucial for the applicability of hybrid approaches, and the particlization is to be performed inside this range.

2.3.3.1 Multiplicity Sampling

In the SMASH-vHLLE-Hybrid approach, the particlization is performed per default with the SMASH-hadron-sampler [340]. It assumes a grand-canonical ensemble, which allows each fluid element to be sampled individually. In the procedure, the total thermal multiplicities, which include all degrees of freedom of the hadron resonance gas, are calculated for the fluid element i on the hypersurface as

$$N_i^{\text{tot}} = V_i \sum_{k=1}^{N_{\text{dof}}} \frac{(2J_k + 1)m_k^2 T_i}{2\pi^2} \sum_{i=1}^{11} \frac{s_k^{i+1}}{i} K_2\left(\frac{im_k}{T_i}\right) \exp\left(\frac{im_k}{T_i}\right), \quad (2.54)$$

with J_k and m_k spin and mass of the k -th degree of freedom, s_k quantifying Bose/Fermi statistics and μ_k is the total chemical potential

$$\mu_k = B_k \mu_{B,i} + Q_k \mu_{Q,i} + S_k \mu_{S,i} \quad (2.55)$$

with B_k , Q_k and S_k the baryon number, electric charge and strangeness of the degree of freedom and $\mu_{B,i}$, $\mu_{Q,i}$ and $\mu_{S,i}$ the respective potentials of the hypersurface element. Similarly T_i and V_i are temperature and effective volume of the hypersurface element.

The actual number of particles sampled results from a Poisson distribution around this value. One quickly sees that this breaks conservation of quantum numbers, energy and momentum. Indeed, in order to preserve them, one in practice samples many particle lists from the same hypersurface. This restores on average conservation and additionally improves statistics. A balance has to be found in the number of hypersurfaces generated, which provides access to fluctuations, and oversampling, which improves statistics and conservation of quantum numbers.

2.3.3.2 Momenta Sampling

Lastly, one needs to generate the momenta of the particles. This follows the Cooper-Frye formula [223]

$$\frac{dN}{d\vec{p}} = \frac{g}{(2\pi)^3} \int_{\sigma} [f_0(x, \vec{p}) + \delta f_{\text{shear}}(x, \vec{p}) + \delta f_{\text{bulk}}(x, \vec{p})] \frac{p^{\mu} d\sigma_{\mu}}{E_{\vec{p}}} \quad (2.56)$$

with $\frac{dN}{d\vec{p}}$ the momentum distribution of a particle species, g its degeneracy factor, p^{μ} and $E_{\vec{p}}$ is momentum and energy and $d\sigma_{\mu}$ the normal vector of the hypersurface. Crucially, f_0 is the equilibrium distribution function of the particle species, which is corrected by the shear stress and bulk pressure on the hypersurface.

Despite the inclusion of shear and bulk viscous effects via δf corrections in the Cooper-Frye prescription, there is no universal consensus on their precise functional form. Each prescription, whether linear (Grad or Chapman-Enskog) or exponential (PTM, PTB), operates under different theoretical assumptions and regimes of applicability, and each encounters inconsistencies when the viscous corrections become large.

LINEAR VISCOS CORRECTIONS: GRAD & CHAPMAN-ENSKOG. The two linearized approaches introduce viscous corrections δf in a manner strictly proportional to the dissipative currents $\pi^{\mu\nu}$ and Π . Both methods rely on an assumption of small deviations from local equilibrium, so their functional forms become questionable once $\delta f \gtrsim f_{\text{eq}}$. A more in-depth discussion can be found in Ref. [341].

In the Grad (or 14-moment) method [166, 168, 174, 300, 342–344], one writes the off-equilibrium distribution as a polynomial expansion in the particle momenta. Focusing on a system without net charges, the leading term may be expressed as

$$\delta f_i = f_{\text{eq},i} \bar{f}_{\text{eq},i} c_{\mu\nu} P^{\mu} P^{\nu} \quad (2.57)$$

where $\bar{f}_{\text{eq},i} \equiv 1 - \Theta f_{\text{eq},i}$, and Θ is 1 for fermions and -1 for bosons. Often, one assumes that the coefficients $c_{\mu\nu}$ are species-independent, which yields the following for the viscous correction in terms of the dissipative currents:

$$\delta f_i^{\text{Grad}} = f_{\text{eq},i} \bar{f}_{\text{eq},i} [\Pi (A_T m_i^2 + A_E (u \cdot P)^2) + A_\pi \pi^{\mu\nu} P_{\langle\mu} P_{\nu\rangle}] \quad . \quad (2.58)$$

Here A_T , A_E , and A_π are combinations of thermodynamic moments of the equilibrium distribution described in Ref. [341]

The Chapman-Enskog technique solves the Boltzmann equation in the Relaxation-Time Approximation (RTA) [325, 345–347]:

$$P^\mu \partial_\mu f = - \frac{u \cdot P}{\tau_{\text{rel}}} [f - f_{\text{eq}}], \quad (2.59)$$

by expanding f in powers of the Knudsen number. Truncating at first order yields

$$\delta f_i^{\text{CE}} = -\tau_{\text{rel}} \frac{P^\mu \partial_\mu f_{\text{eq}}}{(u \cdot P)}. \quad (2.60)$$

Using $\Pi = -\zeta \theta$ and $\pi^{\mu\nu} = 2\eta \sigma^{\mu\nu}$ in Navier-Stokes form, one again obtains a linearized ansatz,

$$\delta f_i^{\text{CE}} = f_{\text{eq},i} \bar{f}_{\text{eq},i} [\alpha_\Pi \Pi \Omega(P, u^\mu) + \alpha_\pi \pi^{\mu\nu} P_{\langle\mu} P_{\nu\rangle}], \quad (2.61)$$

where α_Π and α_π are species-independent coefficients determined by thermodynamic integrals of f_{eq} , and Ω is a scalar function encoding bulk corrections. We refer the reader to Ref. [341] for explicit forms.

Both Grad and Chapman-Enskog expansions assume $\delta f \ll f_{\text{eq}}$. Numerically, one often encounters δf comparable to or exceeding f_{eq} in certain phase-space regions near freeze-out. This can yield negative total distributions, $f_{\text{eq}} + \delta f < 0$, or otherwise unphysical results. In practice, many codes therefore impose a local condition

$$\delta f \rightarrow \text{sign}(\delta f) \min(|\delta f|, f_{\text{eq}}), \quad (2.62)$$

simply “clamping” the correction whenever $\delta f \sim f_{\text{eq}}$. Although not fully consistent theoretically, such a regulator mitigates the largest pathologies in the linear approach.

EXPONENTIATED VISCOS CORRECTIONS: PTM & PTB. To address the breakdown of linear expansions, exponentiated methods attempt to incorporate large viscous corrections in a more self-consistent, “resummed” fashion. We briefly describe here two representative models, the Pratt-Torrieri-McNelis (PTM) [341, 348] and Pratt-Torrieri-Bernhard (PTB) [348, 349] prescriptions.

The PTM approach defines

$$f_{\text{PTM}} = z \left[\exp\left(\frac{\sqrt{p'^2 + m^2}}{1 + \beta_\Pi^{-1} \Pi \mathcal{F}}\right) + a \right]^{-1}, \quad (2.63)$$

where p' is the transformed momentum: $p_i = A_{ij} p'_j$, with

$$A_{ij} = \left(1 + \frac{\Pi}{3\beta_\Pi}\right) \delta_{ij} + \frac{\pi_{ij}}{2\beta_\pi}. \quad (2.64)$$

Expanding for small $\pi^{\mu\nu}$ and Π recovers the linear Chapman-Enskog corrections. However, at moderate or large viscous stresses, the exponentiated form can avoid unphysical negative distribution functions. Still, if $\pi^{\mu\nu}$ or Π become very large, pathologies such as $\mathcal{Z} < 0$ or negative determinants can appear [341].

The PTB correction is formulated as

$$f_{\text{PTB}} = \frac{\mathcal{Z}_{\Pi}}{\det(\Lambda)} \left[\exp\left(\frac{\sqrt{p'^2 + m^2}}{T}\right) + a \right]^{-1}, \quad (2.65)$$

with $p_i = \Lambda_{ij} p'_j$ and

$$\Lambda_{ij} = (1 + \lambda_{\Pi}) \delta_{ij} + \frac{\pi_{ij}}{2\beta_{\pi}}. \quad (2.66)$$

Here, one has $\lambda_{\Pi} \neq \Pi/(3\beta_{\Pi})$. Instead, it is tuned to satisfy local matching of energy-momentum, so that \mathcal{Z}_{Π} and $\det(\Lambda)$ regulate bulk and shear simultaneously. Although the PTB scheme handles bigger gradients than the linear expansions, in practice extremely large stresses again can yield unphysical transformation Jacobians [341].

SPECIES DEPENDENCE AND MATCHING DIFFICULTIES. Beyond the question of how to incorporate shear and bulk corrections is the issue of which species (pions, protons, kaons, etc.) or resonances receive which corrections. Some codes use the same δf for all hadrons, while others attempt partial re-summations or mass-dependent adjustments. Matching the off-equilibrium components of the stress-energy tensor $T^{\mu\nu}$ across the fluid-to-particle transition is also complicated. Indeed, the definition of $(\epsilon + \mathcal{P})u^{\mu} - T^{\mu\nu}$ near freeze-out may involve various assumptions about partial chemical equilibrium, hadronic widths, and residual scattering. Dropping the ansatz of "democratic" corrections is however of great importance, as this approach ignores the dynamics of the processes which keep the medium in equilibrium completely, thus introducing a discontinuity between the stages of a hybrid approach. It is expected that such an improvement would have substantial effects on observables [350].

SMASH-HADRON-SAMPLER IMPLEMENTATION. The approach chosen by the SMASH-hadron-sampler belongs to the Chapman-Enskog class of corrections, without any species dependence [351]:

$$\delta f^{\text{shear}}(P, X) = f_{\text{eq}}(P)(1 + \Theta f_{\text{eq}}(P)) \frac{\pi^{\mu\nu} P^{\mu} P^{\nu}}{2T^2(\epsilon + \mathcal{P})} \quad (2.67)$$

and

$$\delta f^{\text{bulk}}(P, X) = -f_{\text{eq}}(P)(1 + \Theta f_{\text{eq}}(P)) \left[\frac{1}{3} \frac{m^2}{T^2} \frac{1}{P \cdot u/T} - \frac{P \cdot u}{T} \left(\frac{1}{3} - c_s^2 \right) \right] \Pi \frac{\tau_{\Pi}}{\zeta}, \quad (2.68)$$

where τ_{Π}/ζ is set according to [322]. A regulator is applied to ensure the stability of the approach.

With this in place, the hadron sampler generates a list of particles from the particlization hypersurface which is provided as an initialization for the final hadronic transport.

2.3.4 Afterburner

In the final state rescattering, the hadronic transport evolves the medium until complete freezeout, both chemically and kinetically, is achieved. This is performed by propagating the particles until all interactions cease. Consistency is reached by applying all settings of the transport approach identically to the ones used to generate the initial condition.

2.4 Technical Setup of a Modular Hybrid Approach

Due to the high statistics needed to provide good comparisons with experimental data on the one hand, and the high CPU and memory cost of 3+1D hybrid approaches on the other hand, a very efficient computational setup is required to maximize scientific output while minimizing the input of resources. This does not solely mean improving the performance of the different software involved, but also enhancing the infrastructure and handling of the approach. After all, failed runs and corrupted output files often lead to a significant loss of runtime. Additionally, it is crucial that such software is intuitive to handle. Scientific open-source software is used by many researchers all over the world, with varying degrees of knowledge about software development and the specific components at hand. It is desirable to minimize the learning curve to enable users to become productive as quickly as possible and to produce results.

For SMASH-vHLLE-Hybrid, this is an especially important challenge. It consists of different software components that were originally developed independently and follow different coding paradigms. Additionally, the aim of modularity requires a high flexibility of the approach. The original setup of the hybrid approach relied on hard-coded computation targets using CMake. Although this was sufficient for the original publication, in practice, it became clear that such a setup severely restricts the flexibility necessary to support the multitude of projects that would make use of this approach.

Therefore, one of the contributions of this thesis was to improve the infrastructure of the hybrid approach in collaboration with other users. The CMake setup was completely removed in favor of a Bash-based handler structure.

The new hybrid handler is a collection of Bash scripts designed to streamline the execution of the various stages of the SMASH-vHLLE-Hybrid model. Its primary function is to manage the workflow of simulations, ensuring that each component operates in harmony with the others. The handler is structured to be user-friendly. It requires minimal setup and does not necessitate installation. Once the repository is cloned, the ‘Hybrid-handler’ script can be executed directly, provided that the necessary software dependencies are installed [352].

The handler operates through a configuration file written in YAML syntax, allowing users to customize the execution of different stages of the model. This configuration file is divided into sections corresponding to each stage. Each section specifies the executable path, configuration files, and any software-specific parameters. This modular configuration enhances flexibility and allows for easy adjustments to individual components without affecting the overall workflow. An important feature is the automatic validation of configurations. On the one hand, this ensures that each stage receives a configuration which is valid. This avoids, for example, the execution of the hydrodynamic simulation if the configuration given for the particle sampling would be invalid, and therefore ensures

that there is no waste of computation time. On the other hand, consistency between the different stages is enforced. This prevents, for example, that the particlization energy density ϵ_{switch} ³ differs between the hydrodynamic stage and the particle sampler.

A further feature is the structured storage of output files. The handler automatically ensures that no existing files are overwritten and stores the output of each stage in a transparent way. Moreover, reproducibility is ensured by retaining the configurations for each file and also saving git-hashes of the used software, so that the version used can be exactly tracked.

Furthermore, the execution of all stages at once is not required. Already existing output files can be read in by the hybrid handler, allowing external input as well as the processing of existing input with different parameters in further stages.

The handler was developed following state-of-the-art principles of software developing, with a special focus on modularity. This is achieved following the integration-operation segregation principle (IOSP) [353]. In a nutshell, this principle dictates that a method either contains logic, which means transformations, control structures and I/O—it is then called an operation. Otherwise, it combines the call to multiple operations, and is then referred to as integration. A typical integration function looks like this:

LISTING 2.1: Main execution logic of a stage in the hybrid handler.

```

1  function Do_Needed_Operations_For_Given_Software()
2  {
3      local software_section
4      for software_section in "${HYBRID_given_software_sections[@]}"; do
5          Prepare_Software_Input_File "${software_section}"
6          Ensure_All_Needed_Input_Exists "${software_section}"
7          Ensure_Run_Reproducibility "${software_section}"
8          Run_Software "${software_section}"
9      done
10 }

```

From the transparent naming of the operations, it becomes immediately clear what the code does here. The high encapsulation of the functions ensures a good readability as well. Both contribute to the effect that new developers can easily understand the code and debug or extend it, which guarantees a high maintainability, making the code valuable for future generations of users. The IOSP also enables a trivial extension of the code to support new modules for the different stages. Often, only one of the operations needs to be modified. This helps restricting changes to only a few places in the code.

One of the benefits of this is that supporting a different software for one of the stages requires only very limited changes. As an example, supporting a different hadron sampler software, like the FIST-sampler [354], required only minimal changes to the framework, underling its easy and stable extendability. This is valuable for testing the effect of using different implementations and models for the different stages, which is a major source of theoretical uncertainty.

Additionally, the encapsulation of operations into several small functions enables efficient testing. The SMASH-vHLL-E-Hybrid approach is extensively tested. This not only ensures that all features behave as expected. It also guarantees that future modifications

³ We use the term "particlization energy density" and "switching energy density" interchangeably in this work.

can be done without the risk of unintended side effects hampering existing functionalities, as this would immediately cause existing tests to fail.

To facilitate the onboarding of new users, predefined configuration files are provided for various collision systems and energies. These configurations are based on setups from previous studies and can be executed with minimal modification, primarily requiring the user to specify the paths to the necessary executables. This feature significantly reduces the learning curve for new users and ensures that simulations can be performed without deep insight into the codebase.

The hybrid handler also supports parameter scans, enabling users to perform simulations over a range of parameter values systematically. This is particularly useful for studies requiring extensive exploration of the parameter space. The handler's design ensures that such scans are straightforward to set up and execute, further enhancing the tool's utility for research purposes. Several scan strategies, like combinations of parameter lists or latin hypercube sampling, are supported. This was leveraged for the Bayesian inference of the hybrid approach (see section 5.2).

In summary, the development of the hybrid handler has substantially improved the usability, flexibility, and efficiency of the SMASH-vHLLE-Hybrid model. By replacing the rigid CMake setup with a dynamic Bash-based framework, the handler accommodates a wider range of research projects and user expertise levels, thereby maximizing scientific output while minimizing resource input. SMASH-vHLLE-Hybrid was transformed from a proof-of-concept to a fully functional, integrated approach, which can easily be extended and maintained by future generations of researchers.

OBSERVABLES OF HEAVY-ION COLLISIONS

I shut my eyes and all the world drops dead; I lift my lids and all is born again.

— Sylvia Plath, Mad Girl’s Love Song

The study of transport coefficients in heavy-ion collisions requires the comparison of the results of simulations with experimental measurements. This is done by comparing observables, quantities which can be computed from the measurements. In the following, the most important observables in heavy-ion collisions are collected and introduced. The selection is not exhaustive, but restricted to observables that are discussed within the scope of this thesis. This will form the basis for reflections upon results in the upcoming chapters.

3.1 Bulk Observables

In high-energy heavy-ion collisions, the term bulk observables usually refers to inclusive quantities that characterize the global properties of the collision system. They serve as a foundation for understanding how the medium evolves from its initial state, through a possible quark-gluon plasma phase, and eventually hadronizes into the multitude of final-state particles. Of particular interest are observables such as particle multiplicities, mean transverse momentum, mean transverse mass, and transverse momentum spectra. These observables contain information both of the thermodynamic conditions and the collective flow patterns that emerge during the system’s expansion.

3.1.1 Multiplicity

Particle multiplicity is often the first observable analyzed in heavy-ion collisions, as it provides a straightforward measure of the overall particle production in each event. In particular, due to the simpler experimental access, the charged-particle multiplicity density at midrapidity, denoted $dN_{ch}/d\eta$, is commonly used, where midrapidity is defined via the pseudorapidity. The preference for midrapidity has multiple reasons: 2D hydrodynamics was for a long time preferred due to the smaller computational cost, and from an experimental perspective, measurements are easier to take here. Additionally, due to Bjorken-scaling, there is a plateau around midrapidity, and a measurement here reveals a substantial amount of information about the event. In a thermalized system of temperature T and volume V , the integrated particle yield for species i can be expressed within the grand-canonical ensemble as [355]

$$N_i = g_i V \int \frac{d^3 p}{(2\pi)^3} \frac{1}{\exp[(E_i - \mu_i)/T] \pm 1}, \quad (3.1)$$

where g_i is the degeneracy factor, $E_i = \sqrt{p^2 + m_i^2}$ is the on-shell energy, and μ_i is the chemical potential (for instance, baryon or strangeness chemical potential). The sign in

the denominator corresponds to the Fermi-Dirac or Bose-Einstein statistics. In practice, non-equilibrium corrections or partial chemical equilibrium can modify the multiplicity distribution, but this thermal expression remains a useful reference.

More advanced measurements can also identify specific particle species. Although this reduces statistics, it can give valuable information about the nature of the matter. For example, the multiplicity of protons and antiprotons approach each other with increasing collision energy, as a result of decreasing net-baryon density.

3.1.2 Mean Transverse Momentum and Mean Transverse Mass

The mean transverse momentum, $\langle p_T \rangle$, characterizes the average momentum of particles in the transverse plane relative to the beam axis, with $p_T = \sqrt{p_x^2 + p_y^2}$. It is computed by averaging the transverse momentum distribution:

$$\langle p_T \rangle = \frac{\int_0^\infty p_T \frac{dN}{dp_T} dp_T}{\int_0^\infty \frac{dN}{dp_T} dp_T}. \quad (3.2)$$

This quantity is sensitive to both thermal motion (governed by the temperature at kinetic freeze-out) and collective radial flow induced by the pressure gradients in the medium. A larger value of $\langle p_T \rangle$ typically signals stronger radial flow or higher freeze-out temperatures.

A related observable is the mean transverse mass,

$$m_T = \sqrt{p_T^2 + m^2}, \quad \langle m_T \rangle = \frac{\int m_T \frac{dN}{dm_T} dm_T}{\int \frac{dN}{dm_T} dm_T}, \quad (3.3)$$

where m is the rest mass of the particle. Heavier hadrons usually exhibit a larger $\langle m_T \rangle$, because their spectra are significantly modified by radial flow. Consequently, comparing $\langle p_T \rangle$ or $\langle m_T \rangle$ across different species sheds light on the mass hierarchy of flow: heavier particles gain more momentum from the collective expansion. Average transverse momentum and multiplicity are not independent—indeed, both are connected by the conservation of energy.

3.1.3 Transverse Momentum Spectra

A more differential view is offered by the transverse momentum spectra

$$\frac{d^2N}{d^2p_T dy} = \frac{d^2N}{2\pi p_T dp_T dy}, \quad (3.4)$$

which directly reflect the freeze-out distribution in both thermal and collective degrees of freedom. For a boost-invariant and purely thermal source at temperature T , one could approximate these spectra by a Boltzmann-like distribution. However, to account for collective flow, an effective flow-boost factor modifies the exponential slope. From low to high collision energies, the spectra harden, reflecting both increased final temperatures and stronger radial flow. These features directly connect to the initial conditions and

subsequent hydrodynamic expansion, thus making transverse momentum spectra an important benchmark for theory [356]. Not all regions of the transverse momentum spectra are equally relevant. At very low momentum, particles are hard to detect experimentally. At high transverse momentum, jets and hard QCD dominate, which is not covered in the hybrid approach at hand.

3.2 Rapidity Spectra and Longitudinal Shape

Although more challenging for experimental measurements, data from forward and backward rapidity allow important insights into the evolution of the nuclear matter and the mechanisms of baryon number deposition.

3.2.1 Rapidity and Pseudorapidity Distributions

In relativistic collisions, measuring how particle yields are distributed along the beam axis is vital for uncovering the longitudinal dynamics and baryon transport mechanisms. Two commonly employed rapidity variables are:

$$y = \frac{1}{2} \ln \left(\frac{E + p_z}{E - p_z} \right), \quad (3.5)$$

$$\eta = -\ln \tan(\theta/2). \quad (3.6)$$

The first is the *energy-based* rapidity y , used in theoretical analyses, while the second is the *pseudorapidity* η , which depends only on the polar angle θ and simplifies massless kinematics. Experimentally, $dN/d\eta$ is more readily measured, since tracking detectors typically measure angles rather than energies.

The shape of dN/dy or $dN/d\eta$ reveals whether the system forms a midrapidity plateau, characteristic of partial boost invariance at LHC energies, or a peaked structure. At lower SPS or RHIC energies, stronger baryon stopping leads to more compact dN/dy distributions centered around midrapidity.

3.2.2 Longitudinal Evolution and Baryon Stopping

The concept of baryon stopping refers to the extent to which incoming nucleons are slowed down (or “stopped”) in the collision. Net baryon density distributions (dN_B/dy) measure how many baryons, minus antibaryons, remain at lower rapidities compared to their initial ultrarelativistic velocities. A higher baryon stopping typically produces a rapidity distribution with peaks closer to $y = 0$, as is seen at moderate energies. Conversely, at top RHIC and LHC energies, baryons barely decelerate, resulting in fewer net baryons at midrapidity [356].

In phenomenological terms, one often distinguishes a single-peaked shape for lower energies and a broader, double-peaked structure at higher energies, where the projectile and target remnants remain at large positive or negative rapidities. The interplay between baryon transport and partonic degrees of freedom thus shapes the final 3D structure of collisions. The Bjorken picture, which posits boost-invariant longitudinal expansion, is

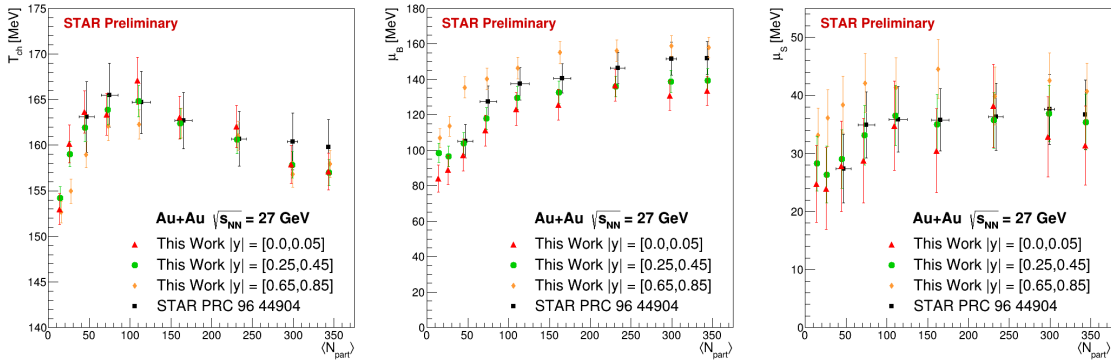


FIGURE 3.1: Thermodynamic properties of the medium produced in Au+Au collisions at $\sqrt{s_{\text{NN}}} = 27$ GeV, extracted from measured yields as a function of number of participants. From [357].

realized approximately only near midrapidity at very high energies. Away from midrapidity or at modest $\sqrt{s_{\text{NN}}}$, the full rapidity dependence reveals significant deviations from that simple scenario.

Due to this, the full longitudinal structure of an event can only be captured when a 3D initial state approach is used. Alternative approaches, such as distributing the energy from the transverse plane by using a Bjorken picture, reach limits at intermediate energies. Measurements away from midrapidity are also of increased interest due to giving access to a wider range of the QCD phase diagram. Due to the baryon stopping, which decreases with increasing collision energies, baryon charge is deposited preferably away from midrapidity regions at high collision energies. Therefore, studying observables both at midrapidity and at forward and backward rapidities gives access to a broader range of the QCD diagram and allows to study the effect of baryochemical potential on the evolution [357]. This can be seen in fig. 3.1. At the same energy and centrality, the further one measures at forward rapidity, the higher μ_B and μ_S become, whereas the temperature remains mostly constant.

3.3 Harmonic Flow Coefficients

Anisotropic flow, or the azimuthal momentum-space anisotropy observed in relativistic heavy-ion collisions, is typically characterized via harmonic flow coefficients v_n . These coefficients appear in the Fourier decomposition of the azimuthal distribution of the particles:

$$\frac{dN}{d\phi} = \frac{1}{2\pi} \left[1 + \sum_{n=1}^{\infty} 2 v_n \cos [n (\phi - \Psi_{\text{RP}})] \right] \quad (3.7)$$

This basically means that the complex momentum distribution of final state particles can be decomposed in different modes, each of which can be assigned an intuitive interpretation. Such modes are often called "(anisotropic) flow modes". Figure 3.2 shows the intuitive interpretation for coefficient 2 and 3, which are called elliptic and triangular flow, respectively. They are of great interest, as they provide insights into the collective expansion of the quark-gluon plasma or hadronic matter. Notably, each v_n is defined

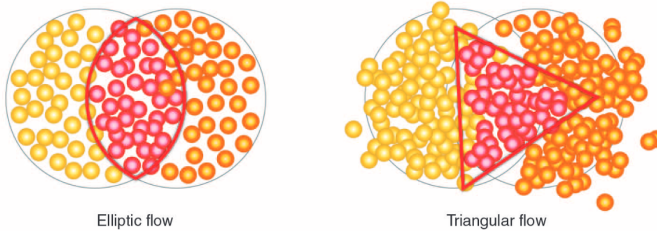


FIGURE 3.2: Visualisation of the second flow coefficient (elliptic flow) and the third flow coefficient (triangular flow). From [358].

with respect to an estimated *event plane*, itself determined from measured particles in the final state. This section presents three widely used methods to infer v_n from experimental or simulated data: (i) the Event Plane (EP) method, (ii) the Scalar Product (SP) method, and (iii) the Cumulant method (Q-cumulants). We highlight differences among these methods, discussing their respective strengths and weaknesses.

3.3.1 Event Plane Method

The starting point for the Event Plane (EP) method [359, 360] is that the initial geometry of a non-central nucleus-nucleus collision singles out a preferred plane: the *reaction plane*, spanned by the impact parameter vector and beam axes. However, this true plane is unknown experimentally, so an *event plane* is reconstructed from particle momenta using flow correlations themselves.

Let ϕ_i be the azimuthal angle of the i^{th} particle, measured in the laboratory frame around the beam axis. For a chosen harmonic n , one defines a flow vector,

$$Q_{n,x} = \sum_{i=1}^M w_i \cos(n \phi_i), \quad Q_{n,y} = \sum_{i=1}^M w_i \sin(n \phi_i),$$

where M is the number of particles used for the event plane reconstruction, and w_i is a weight (often $w_i = p_{t,i}$ or simply 1). From these, the event plane angle Ψ_n follows by

$$\Psi_n = \frac{1}{n} \arctan(Q_{n,y}, Q_{n,x}).$$

The weight factor w_i can be chosen to maximize the statistics, or to favor contributions from different components of the event.

Once Ψ_n is known, any subset of particles can be binned in $\phi - \Psi_n$. One then expands the azimuthal distribution in a Fourier series about Ψ_n :

$$\frac{dN}{d(\phi - \Psi_n)} = \frac{N_{\text{tot}}}{2\pi} \left(1 + \sum_{m=1}^{\infty} 2v_m^{\text{obs}} \cos[m(\phi - \Psi_n)] \right),$$

with $v_m^{\text{obs}} = \langle \cos[m(\phi - \Psi_n)] \rangle$ the observed elliptic flow due to the orthogonality of the cosine. $\langle \dots \rangle$ refers to the average over events. Because Ψ_n itself has finite resolution, the observed coefficient v_m^{obs} is related to the true v_m by

$$v_m = \frac{v_m^{\text{obs}}}{\langle \cos[m(\Psi_n - \Psi_r)] \rangle} = \frac{v_m^{\text{obs}}}{R},$$

where Ψ_r denotes the exact reaction plane. The crucial factor $\langle \cos[m(\Psi_n - \Psi_r)] \rangle$ is the *resolution* of the event plane. This resolution can be estimated by subdividing the event into two (or more) independent subevents A and B, and examining

$$\langle \cos[m(\Psi_n^A - \Psi_n^B)] \rangle = \langle \cos[m(\Psi_n^A - \Psi_r)] \rangle \langle \cos[m(\Psi_n^B - \Psi_r)] \rangle.$$

Because Ψ_n^A and Ψ_n^B are uncorrelated aside from their mutual correlation to Ψ_r , one extracts the plane resolution in each subevent as $R = \sqrt{\langle \cos[m(\Psi_n^A - \Psi_n^B)] \rangle}$. Corrections from the subevent resolution to the full event resolution can be applied using known analytical formulae [359, 361].

The EP method is straightforward conceptually: one literally constructs an approximate reaction plane and measures azimuthal anisotropies relative to it. It delivers direct access to differential flow $v_n(p_T)$ or $v_n(\eta)$ by correlating each particle in a bin with Ψ_n . It can suffer however from “non-flow” correlations that affect the event plane resolution. An example of this are the effects of jets, which also contribute to momentum anisotropy. Additionally, the resolution factor must be well estimated; if the multiplicity is small, or if v_n is small, the resolution can degrade significantly.

3.3.2 Scalar Product Method

The Scalar Product (SP) method [362] is another pairwise correlation technique that does not require explicit angle-subtraction as in $\phi - \Psi_n$. Instead, one partitions an event into two disjoint groups (subevents A and B), constructs flow vectors

$$Q_n^A = \sum_{i \in A} w_i e^{i n \phi_i} = \sum_{i \in A} w_i u_{n,i} \quad , \quad Q_n^B = \sum_{j \in B} w_j e^{i n \phi_j} = \sum_{j \in B} w_j u_{n,j},$$

where $u_{n,i}$ is a unit vector associated with the i -th particle and Q_n is the flow vector. The flow can be then calculated using the scalar product:

$$v_n(\eta, p_t) = \frac{\langle \langle Q_n u_{n,i}^*(\eta, p_t) \rangle \rangle}{2 \sqrt{\langle Q_n^A Q_n^B \rangle}}. \quad (3.8)$$

Here, the numerator is both averaged over particles and events. For a large number of particles in each subevent this yields an estimate of v_n . Again, one can use a differential formulation of this method to get an insight into the flow as a function of rapidity or transverse momentum.

The scalar product method is simpler in some implementations: no explicit event plane is constructed, yet $\langle Q_n^A \cdot Q_n^B \rangle$ directly links to $\langle v_n^2 \rangle$. A further advantage is that it can yield smaller statistical errors compared to the standard EP method, especially in high-multiplicity environments. However, it suffers as well from non-flow correlations, potentially biasing $\langle Q_n^A \cdot Q_n^B \rangle$.

3.3.3 Cumulant (Q-Cumulant) Method

While the EP and SP methods employ pairwise correlations, genuine multiparticle correlations can help disentangle flow-related physics from “non-flow” backgrounds. In particular, the cumulant method [363–365] was introduced to systematically isolate

the collective flow contribution by combining multi-particle correlation moments into cumulants. For example, the second-order cumulant $c_n\{2\}$ recovers essentially the pair-correlation measure

$$c_n\{2\} = \langle e^{in(\phi_1 - \phi_2)} \rangle,$$

but the fourth-order cumulant

$$c_n\{4\} = \langle e^{in(\phi_1 + \phi_2 - \phi_3 - \phi_4)} \rangle - 2 \langle e^{in(\phi_1 - \phi_2)} \rangle^2$$

removes spurious two-particle correlations from the net four-particle correlation. In other words, higher orders remove more and more non-flow effects, originating for example from particle decays, and give better access to collective effects. Typically, if flow is truly collective, the four-particle cumulant is insensitive to low-level non-flow effects that scale like $1/N$. One obtains

$$v_n\{2\} = \sqrt{c_n\{2\}}, \quad v_n\{4\} = \sqrt[4]{-c_n\{4\}}.$$

One further generalizes to differential cumulants to get $v_n\{2\}(p_T)$ or $v_n\{4\}(p_T)$. In an event-by-event approach, the unintegrated correlation can be systematically extracted. Especially high-order cumulants (like fourth order) effectively reject non-flow two-particle correlations, providing a “pure flow” measurement. The approach is systematically improvable by adding terms of higher order ($\{6\}$, $\{8\}$, etc.), which provide further insights into the nature of collective effects. However, the statistical uncertainties rise with the order of the cumulant. In data sets with limited statistics, $v_n\{4\}$ or higher might become unfeasible or too noisy. This is especially problematic for extractions from theoretical models. In general, the implementation is more mathematically involved and the computation is considerably more costly.

3.3.4 Eccentricities and the Creation of Anisotropic Flow

The final state momentum anisotropy, expressed in the flow coefficients, is intimately connected to the spatial anisotropy, or *eccentricities*, of the initial state. These eccentricities, commonly denoted by ε_n , are defined in terms of moments of the transverse energy (or entropy) density profile of the collision zone in the transverse plane. They quantify the shape of the overlap region produced when two nuclei collide at a non-zero impact parameter or when local density fluctuations occur [366, 367].

DEFINITION OF ECCENTRICITIES. The complex eccentricity ε_n is often defined in polar coordinates (r, ϕ) as

$$\varepsilon_n \equiv -\frac{\int r^n e^{in\phi} \epsilon(r, \phi) r dr d\phi}{\int r^n \epsilon(r, \phi) r dr d\phi}, \quad (3.9)$$

where $\epsilon(r, \phi)$ is the transverse energy density in the initial state, and the coordinate system is shifted so that $\int r e^{i\phi} \epsilon(r, \phi) dr d\phi = 0$. The event-plane angle of ε_n is determined by the phase of this integral, and its magnitude quantifies the strength of the spatial anisotropy in harmonic n . In a non-central heavy-ion collision, for instance, ε_2 captures the elliptic shape (“almond-like” overlap), while ε_3 and higher orders represent more subtle geometric or fluctuational features [368, 369].

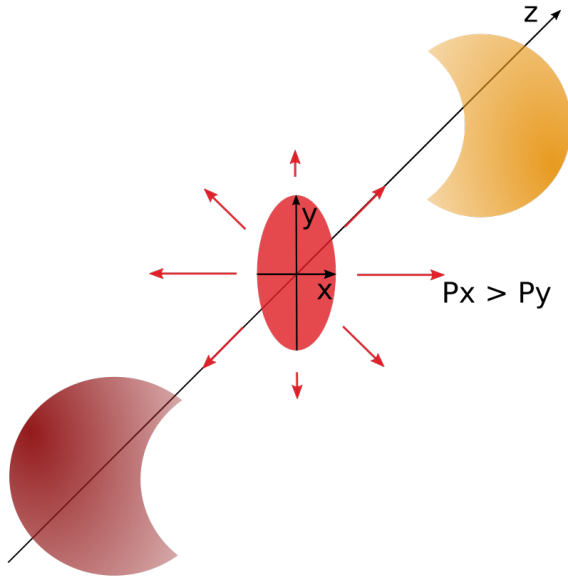


FIGURE 3.3: Simplified picture of a heavy-ion collision. The overlap region of two nuclei forms an almond shape for non-vanishing impact parameter. The spatial anisotropy in the fireball creates a pressure anisotropy, which can be detected as elliptic flow in the final state.

LINEAR RESPONSE AND HIGHER-ORDER CONTRIBUTIONS. Within relativistic hydrodynamics, one typically assumes that the anisotropic flow coefficients v_n are proportional to the corresponding initial eccentricities ε_n , i.e.,

$$v_n = \kappa_n \varepsilon_n. \quad (3.10)$$

This linear response works well in central and midcentral collisions and is supported by numerous event-by-event hydrodynamic simulations [198, 370, 371]. However, at higher eccentricities (peripheral collisions), clear deviations from the purely linear picture have been observed [311, 372, 373]. These deviations can be quantified by introducing a cubic-response term in ε_n , giving

$$v_n = \kappa_n \varepsilon_n + \kappa'_n |\varepsilon_n|^2 \varepsilon_n + \delta_n, \quad (3.11)$$

where κ'_n is the cubic-response coefficient and δ_n denotes the residual (uncorrelated) part of v_n [374, 375]. The key result is that κ'_n systematically grows in more peripheral collisions, compensating for the smaller linear coefficient κ_n in that regime [371]. Hence, the total v_n arises from both the well-known linear scaling and a non-negligible cubic contribution once $|\varepsilon_n|$ becomes large.

PHYSICAL ORIGIN OF ECCENTRICITIES AND FLOW. The spatial anisotropies ε_n encode the initial-state geometry of the quark-gluon plasma. In non-central collisions, the “almond shape” drives a larger pressure gradient in one direction than in the one orthogonal to it, leading to an anisotropic expansion, as is sketched in fig. 3.3. In the case of elliptic flow ($n = 2$), the elliptic eccentricity ε_2 is the dominant driver of v_2 , while local fluctuations (even in central events) provide non-zero triangularity ε_3 and

other higher harmonics. Each harmonic in ε_n translates into a corresponding v_n via the hydrodynamic evolution. Note, however, that this picture gets more complex for orders starting at 4, which lie outside the scope of this thesis [376]. The final anisotropic flow is thus predominantly determined by:

- (i) The medium's equation of state and the temperature and density dependence of its transport coefficients [168, 342].
- (ii) The interplay between linear and possible higher-order response terms in eq. (3.11).
- (iii) Additional noise (short-range structure in the initial state) that leads to a residual δ_n uncorrelated with ε_n [198].

It is important to note that, while the final state flow can be measured, initial state eccentricities are not accessible experimentally. They can be only quantified in theoretical initial state models, but otherwise remain out of reach. This is a challenge, as it restricts experimental constraints on theoretical modelling of the emergence of harmonic flows.

3.4 Efficient Computation of Observables with SPARKX

One of the contributions of this work is the development of SPARKX (*Software Package for Analyzing Relativistic Kinematics in Collision eXperiments*) [3, 377], an open-source Python library designed to simplify analysis workflows for data from heavy-ion collision simulations. SPARKX addresses the longstanding issue that existing analysis tools often exhibit steep learning curves and limited extensibility, forcing many researchers to write ad-hoc, untested scripts that are difficult to maintain and validate. By contrast, SPARKX seeks to bridge this gap and provide a robust, maintainable codebase that can be easily extended to meet the evolving needs of the heavy-ion theory community.

The overall design is centered around simplicity and cleanliness in both usage and implementation. SPARKX adopts a modular, object-oriented architecture, guided by the SOLID design principles of object-oriented programming [378]. The Single-Responsibility Principle is evident in the way that each module focuses on a dedicated task; for instance, data loading is handled by specialized loader classes, while flow calculations or jet-finding routines remain in modules dedicated to analysis. This approach avoids tightly coupling logic for reading data with logic for physics observables. The Open-Closed Principle allows abstract interfaces, such as `BaseLoader` for file reading, to remain stable while new classes extending these abstractions can be created without altering the original interfaces. Users can incorporate new file formats or specialized analysis routines without breaking existing parts of the codebase. Adhering to the Liskov Substitution Principle, all derived classes can stand in for their respective base classes without causing runtime errors or unexpected behaviors. This allows, for example, specialized OSCAR loaders and JETSCAPE loaders to be used interchangeably, since both satisfy the same interfaces and can be called from the same analysis methods. Furthermore, the Interface Segregation Principle guides SPARKX to define specialized interfaces—for loaders, storers, or analysis modules—instead of forcing large, monolithic ones, reducing needless code dependencies for end users. Finally, the Dependency Inversion Principle prevents high-level modules, such as flow analyses, from depending on the intricate details of lower-level modules.

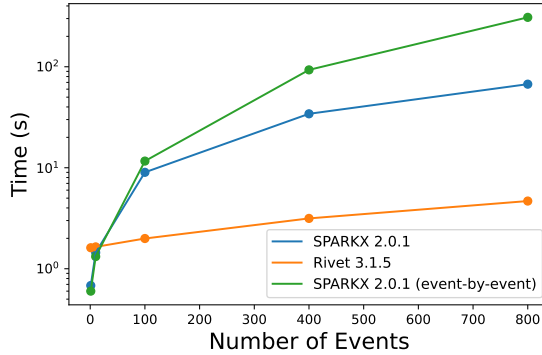


FIGURE 3.4: Execution time for a simple charged hadron transverse momentum analysis implemented in SPARKX 2.0.2 and Rivet 3.1.5.

Instead, the flow classes depend only on abstract contracts (for instance, `BaseStorer`), so that switching from one file format to another entails minimal alterations to the analysis code.

Beyond design principles, SPARKX simplifies the overall workflow by neatly partitioning data-loading logic (including reading input files and applying user-defined filters) from the physics analysis logic. Data are extracted into Python objects with well-defined attributes (like momenta, particle IDs, or event metadata), then passed to specialized modules that compute bulk observables, anisotropic flow quantities, or jet-related properties. Supported flow methods include the Q-cumulant approach [365, 379], the reaction-plane method [380], and the Lee-Yang Zero formalism [381, 382]. These methods allow SPARKX to cover a broad range of standard flow analyses within the heavy-ion community.

A fundamental aspect of SPARKX is its focus on reliability, embodied by a comprehensive automated test suite and strict static typing. Tests, written with `pytest`, span from unit checks (for instance, verifying that Q-cumulant routines or histogramming classes work as expected) to integration tests (ensuring that the entire pipeline—loader, filtering, and flow computations—produces consistent results for known inputs). Whenever new features are introduced or existing functionalities are updated, continuous integration pipelines verify that these tests pass, reducing the likelihood of regressions. Alongside testing, the use of static typing (via `mypy`) brings clarity and consistency to the Python codebase. Type annotations ensure that developers understand the expected structure and data types at each interface, catching potential type mismatches before they cause issues at runtime. This practice significantly enhances maintainability and debugging.

This careful attention to design principles and testing regimes ensures that SPARKX is both accessible to novice users and robust enough for large-scale HPC analyses. By minimizing code complexity, reducing the need for elaborate custom scripts, and maintaining high standards of software engineering, SPARKX aims to streamline the computation of key observables in heavy-ion collisions and promote confidence in the resulting scientific inferences.

SPARKX is under active development, aiming both at extending the coverage of physics analysis scenarios as well as performance. Currently covered observables include bulk observables like yields and transverse momenta, anisotropic flows from different algorithms, eccentricities, density calculations, jet analyses and p_T -correlations. A complete

overview can be found in [383]. Future extensions include improved centrality class and HBT-radii calculations. However, incoming releases will focus on improved performance. Current benchmarks show substantial weaknesses in this metric with respect to more performance-focused codebases like Rivet [384], as can be seen in fig. 3.4. By implementing parallelized analysis routines and online observable calculations as well as moving core calculations to C++ using Python bindings, this gap can be reduced, resulting in a fast, reliable, and easy-to-use analysis package.

SENSITIVITY OF HYBRID APPROACHES ON INITIAL STATE MODELS

Movement is the origin of all existence. Therefore, no stillness can reside within it, for if being were motionless, it would return to its source—and that source is nothingness.

— Ibn Arabi, *Kitâb Al-Isfâr*

As explained before, one of the main observables relevant to the study of transport coefficients in heavy-ion collisions are anisotropic flows. This observable is also strongly affected by the initial state due to the impact of initial state eccentricities and other initial state properties. One can gain further insights into this by studying both the properties of selected initial state models and how they contribute to the observed final state flows. This contributes to disentangling different sources of anisotropic flows and therefore establishing a clearer connection between flow and transport coefficients. Future predictions of transport coefficients can then take the impact on the chosen initial state model into account.

4.1 Setup

Based on [2], this study is performed by exchanging the initial state model in the SMASH-vHLLE-Hybrid approach. For this comparison SMASH IC, IP-Glasma, and T_RENTo are studied in the transverse plane, which requires a restriction to events at high collision energies. The reason for this is that we have only at high energies an extensive Bjorken plateau, which allow extrapolating results from the transverse plane to a midrapidity region.

The properties of the initial condition extracted from SMASH, IP-Glasma, and T_RENTo were outlined in section 2.3.1. As a dataset to compare these three approaches, we generate 750 events per centrality class from each model. We run the Yang-Mills evolution for IP-Glasma till $\tau = 0.5$ fm, the same end time as SMASH IC at high energies. We generate the initial conditions from SMASH with SMASH-2.2, and use the default parameters for IP-Glasma initial states [385]. For T_RENTo, we use parameters extracted from a recent Bayesian inference [54] without the use of nuclear substructure. We rescale the transverse planes produced by IP-Glasma and T_RENTo to the correct energy by the number of participants provided. We want to stress that the presented results depend of course on the choice of parameters. However, parameter sets were chosen which reproduce experimental data well and give comparable results.

There are several properties of the initial state compared in the following. For all initial state models, the eccentricity is studied, as introduced in section 3.3.4. SMASH and IP-Glasma provide access to momenta, and therefore one can define a radial flow in the initial state, $\langle p_T^{\text{IC}} \rangle$, which is the mean transverse flow of the initial state. This can be calculated on the basis of particles for SMASH, and from the energy momentum

tensor for IP-Glasma as $\epsilon_p = \sqrt{T^{xx^2} + T^{yy^2}}$. Lastly, one can also look at the anisotropies of momenta in the initial state for SMASH and IP-Glasma. For SMASH, due to the descriptions as particles, we can directly calculate v_2^{IC} and v_3^{IC} . For IP-Glasma, we have to again choose a related quantity from the energy momentum tensor. As proposed in [386], we choose $\epsilon_p e^{i2\psi_2^p} = \frac{\langle T^{xx} - T^{yy} \rangle + i\langle 2T^{xy} \rangle}{\langle T^{xx} + T^{yy} \rangle}$. Eccentricities and flows were calculated using SPARKX-1.1, employing the scalar product method.

Furthermore, we investigate the effect on the whole hydrodynamic evolution when exchanging the initial state model. In order to achieve this, we perform a completely identical simulation except for the initial state used. As the SMASH IC is 3D, we have to extend the 2D transverse plane initial condition models into the longitudinal direction and distribute the missing charges. This is performed according to the prescription proposed in [387–389]. It is based on the assumption of an approximately triangular shape of the space-time rapidity distribution of the energy deposition from the forward-going (+) and backward-going (-) participant nucleons. In order to realise this, a smearing kernel of the following form is used:

$$f_{\pm}(\eta_s) = \frac{\eta_M \pm \eta_s}{2\eta_M} H(\eta_s) \quad \text{for } |\eta_s| < \eta_M \quad (4.1)$$

with the beam pseudorapidity η_M . $f_{\pm}(\eta_s)$ is then limited to the range $[0, 1]$ so that the deposition does not become locally negative, and the finiteness of the shape in rapidity is ensured by the profile function H :

$$H(\eta_s) = \exp\left(-\frac{(|\eta_s| - \eta_0)^2 \Theta(|\eta_s| - \eta_0)}{2\sigma_{\eta}^2}\right). \quad (4.2)$$

η_0 represents the energy-dependent width of the midrapidity plateau. Such a rapidity profile of the energy deposition from the participant nucleons has been successfully used in a variety of studies. These include, for example, transverse momentum correlations in Au-Au collisions at the top RHIC energy [387] or even Pb-Pb collision at the LHC energies [390]. Apart from this, it was also applied for collective flow in small systems [391], or longitudinal decorrelation of flow harmonics in Pb-Pb collisions at the LHC energies [392].

For the rest of the evolution of the system, the aforementioned SMASH-vHLLE-Hybrid approach was used in the versions SMASH-vHLLE-Hybrid :298ebfa, vHLLE:oa1od56, vhllle-params:4bfe48a¹ and SMASH-hadron-sampler-1.1. This includes all aforementioned default setups, except for the shear viscosity. Here, a parameterization was used which will be presented in section 5.1.

¹ As pre-release versions were employed, the references to the commits were given here.

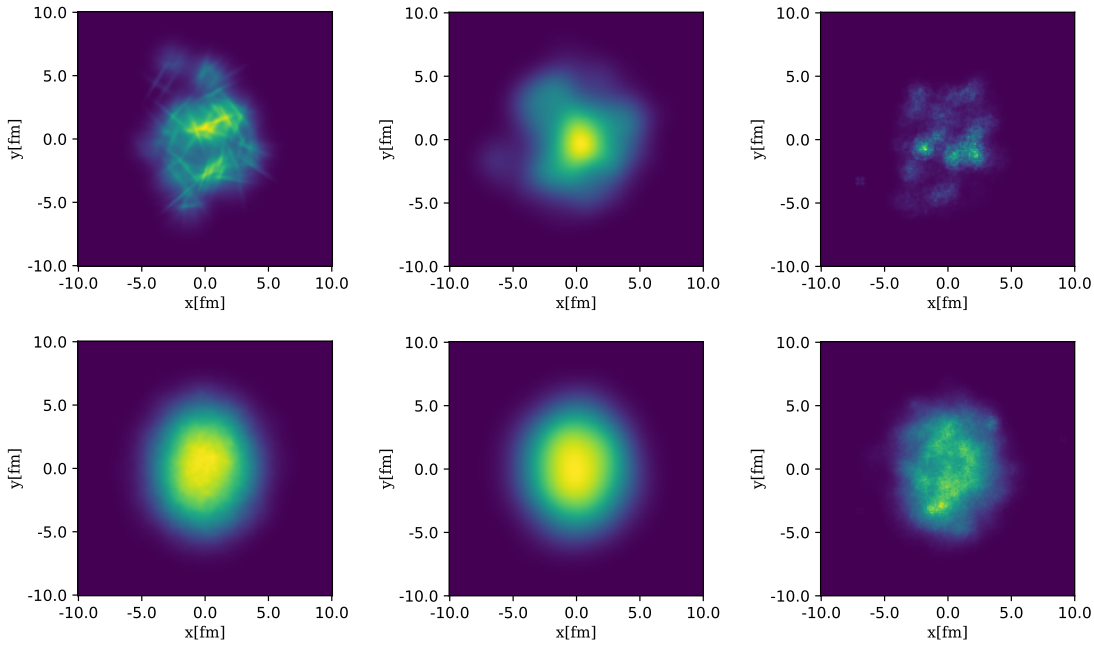


FIGURE 4.1: Top: Energy density in single event transverse planes. Bottom: Average of 1000 events. From left to right: SMASH, T_RENTo and IP-Glasma.

4.2 Averaged Quantities

We start with the investigation of event-averaged quantities. It is very instructive to look at the energy density distribution in the transverse plane, as can be seen in fig. 4.1. Here, for SMASH we use the smearing kernel according to eq. (2.44). The covariant nature of this smearing kernel results in a tube-like structure in the single event transverse plane for SMASH. T_RENTo, on the other hand, shows very smooth structures, while for IP-Glasma, a high granularity remains. For each single event, fluctuations are introduced due to different Woods-Saxon-sampled positions of the nuclei. However, once quantities are averaged out, the differences largely disappear. The average transverse plane of SMASH and T_RENTo are practically identical, and the IP-Glasma transverse plane is approaching the same elliptical gaussian form. If one were to average over even more events, all three models would provide almost identical initial states.

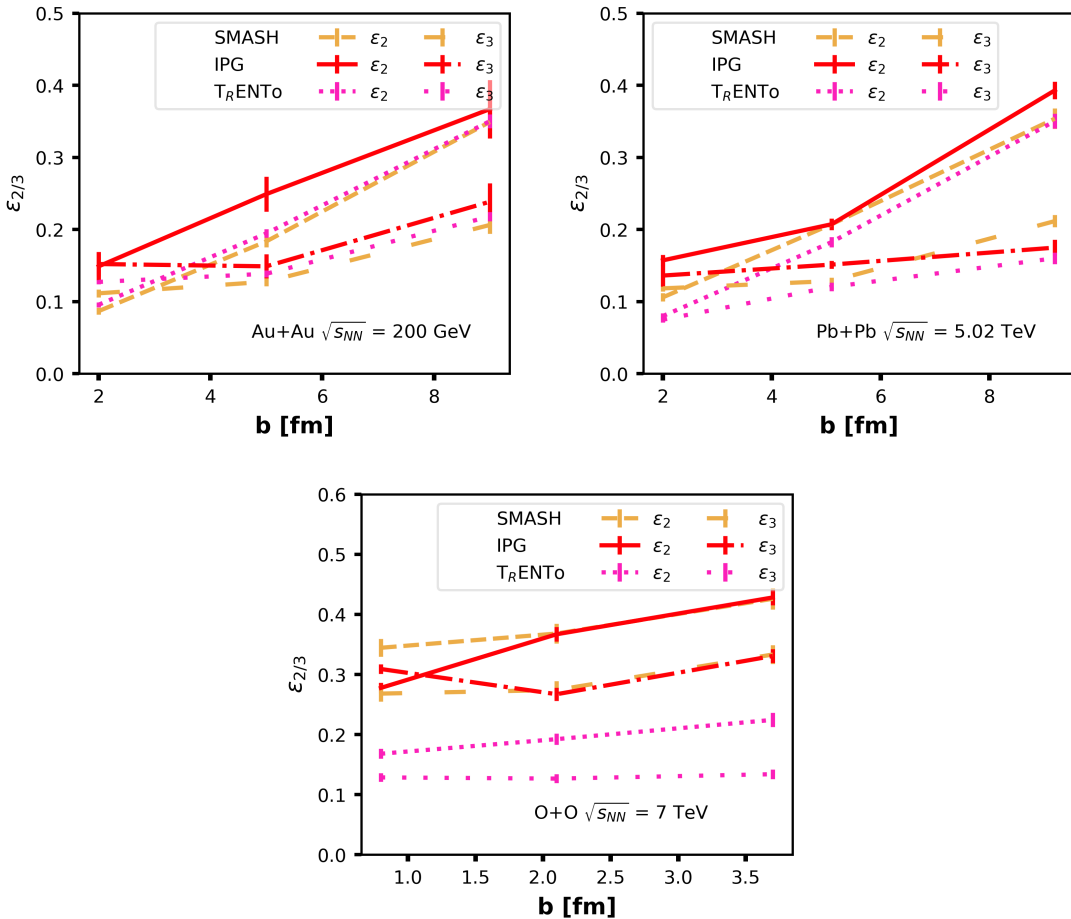


FIGURE 4.2: Eccentricities of the initial state for Au-Au collisions at $\sqrt{s_{NN}} = 200$ GeV (top left), Pb-Pb collisions at $\sqrt{s_{NN}} = 5020$ GeV (top right) and O-O collisions at $\sqrt{s_{NN}} = 7$ TeV (bottom), each as a function of the impact parameter for the three models.

Figure 4.2 shows the eccentricities ϵ_2 and ϵ_3 as functions of the impact parameter for three experimentally relevant systems: Au-Au collisions at $\sqrt{s_{NN}} = 200$ GeV, Pb-Pb collisions at $\sqrt{s_{NN}} = 5020$ GeV, and O-O collisions at $\sqrt{s_{NN}} = 7$ TeV. Since TRENTo does not provide oxygen configurations, those employed here are taken from Ref. [393]. In all cases, the passing time (see section 2.3.1.1) is set to $0.5\text{fm}/c$.

For the large systems (Au-Au and Pb-Pb), the three models exhibit similar trends: the eccentricities increase comparably with the impact parameter. In both systems, IP-Glasma generally gives the highest values for ϵ_2 and ϵ_3 , except in very peripheral collisions at high energies where SMASH produces slightly higher ϵ_3 . Similar behavior was reported in Ref. [394], and a good overall agreement among different models has also been noted in Ref. [395].

By contrast, for collisions involving smaller ions (O-O), the models differ more significantly. While SMASH and IP-Glasma remain in reasonable agreement, TRENTo predicts much more spherical profiles with virtually no dependence on the impact parameter. Furthermore, even in nearly central collisions, the eccentricity does not vanish, a feature particularly pronounced in IP-Glasma.

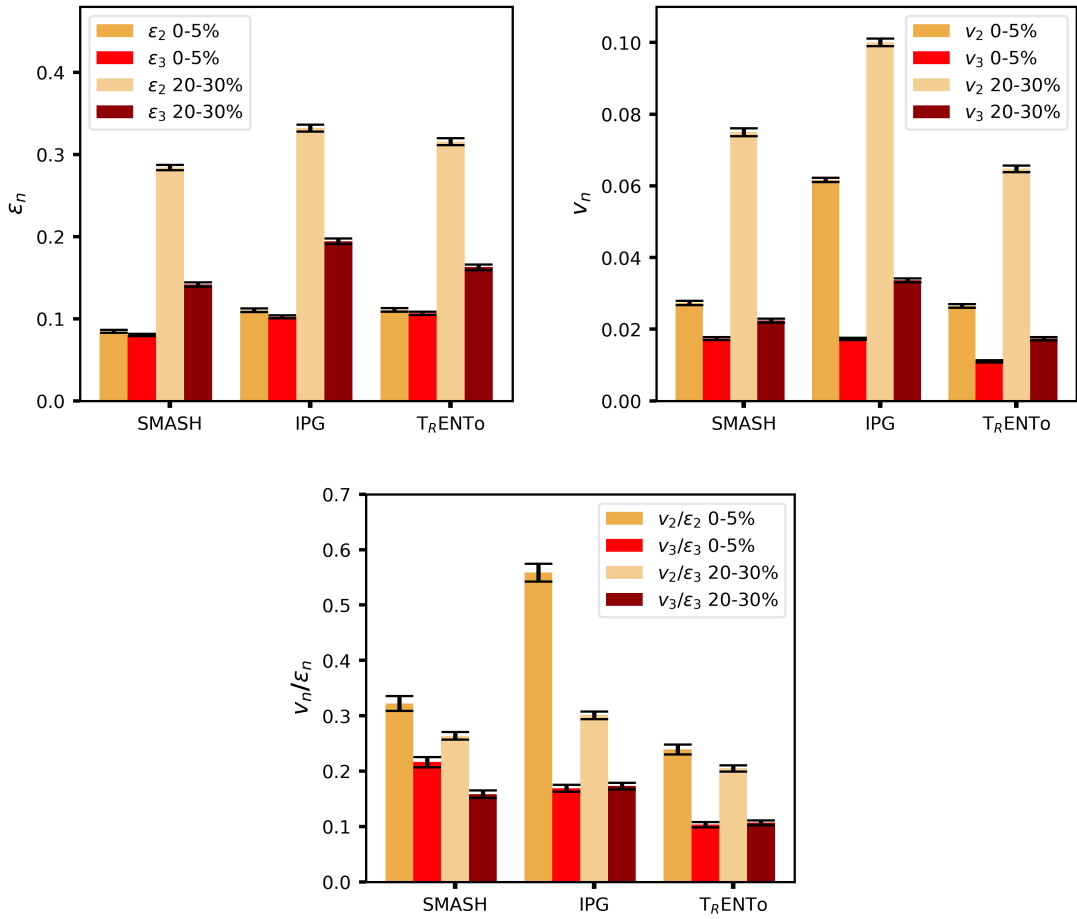


FIGURE 4.3: Initial state eccentricities (top left), final state flows (top right), and response functions v_n/ϵ_n (bottom) for all three models for Au-Au collisions at $\sqrt{s_{\text{NN}}} = 200$ GeV.

It is instructive to see how the rather small differences at $\sqrt{s_{\text{NN}}} = 200$ GeV translate into the final state observables. We restrict ourselves to this energy as it reduces computational cost, and the validity of the hybrid approach has been most thoroughly established here. Figure 4.3 shows the averaged values of ϵ_2 , ϵ_3 , v_2 , and v_3 for the three models for Au-Au collisions at $\sqrt{s_{\text{NN}}} = 200$ GeV at 0-5% and 20-30% centrality, respectively. The centrality class was selected here by defining a mapping between impact parameters and multiplicities based on the Glauber model, and only taking into account collisions within this specified interval of impact parameters. In agreement with earlier results, the eccentricities of the models have similar values in both centrality classes. Especially T_RENTo and the transport initial state are close in the values of their eccentricities. We see a considerably better agreement for the eccentricities here than between UrQMD and T_RENTo for earlier comparisons at lower energies [389]. It is noteworthy that we observe a systematically slightly increased flow with SMASH in comparison to T_RENTo, although the eccentricities are smaller. Nevertheless, we observe both the highest eccentricities and flows with IP-Glasma. Although the differences between the models seem only moderate, they become more pronounced when looking at the response function. The response

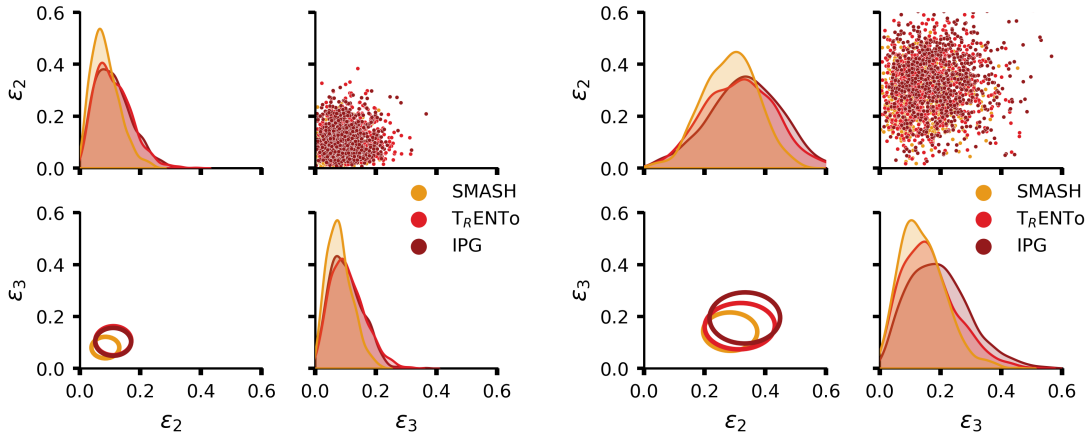


FIGURE 4.4: Initial state eccentricity distributions. The normalized probability density distribution is shown on the top left and bottom right. The top right shows a 2D scatter plot of the ϵ_2 - ϵ_3 distribution, whereas the lower left plot visualizes the relationship of the two quantities, with the center of the ellipse at the mean of ϵ_2 and ϵ_3 , width and height are the variance of ϵ_2 and ϵ_3 , respectively, and the angle shows the covariance. Data at 0-5% centrality (left) and 20-30% centrality (right) for Au-Au collisions at $\sqrt{s_{NN}} = 200$ GeV.

function encodes the proposed proportionality factor between flow and eccentricity in eq. (3.10). The only change in the three setups is the choice of the initial condition model, but the response to initial state eccentricities differs, especially for central collisions. A clear hierarchy between the models and their response functions seems to emerge. This is however contrary to the naive believe that the response is mainly governed by the properties of the hydrodynamic medium.

We want to gain insights into this by looking into the distribution of the variables in an event-by-event basis. Existing research shows that while the average eccentricities between different models might agree, this is not necessarily given for the distribution of eccentricities [395].

4.3 Event-by-event Distributions

Figure 4.4 and fig. 4.5 illustrate the event-by-event distributions of eccentricities and flows, respectively. In terms of eccentricities, SMASH exhibits a significantly more peaked distribution, particularly in central collisions where the IP-Glasma and T_RENTo distributions are very similar. This behavior changes slightly for off-central collisions: SMASH remains more peaked but IP-Glasma shows a substantially broader spread in both centralities classes compared to T_RENTo. For all three models and both centralities, there is no strong ϵ_2 - ϵ_3 correlation, and the variation in ϵ_2 exceeds that of ϵ_3 .

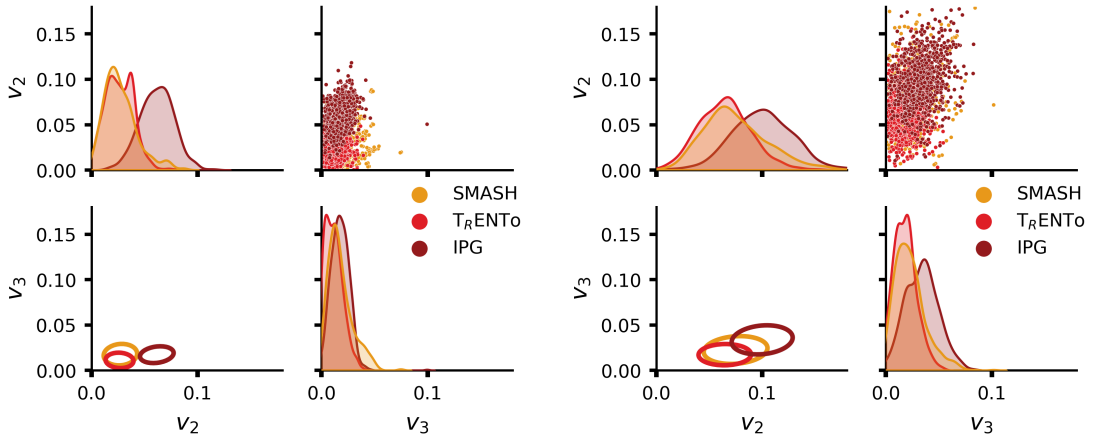


FIGURE 4.5: Final state flow distributions. The normalized probability density distribution is shown on the top left and bottom right. The top right shows a 2D scatter plot of the v_2 - v_3 distribution, whereas the lower left plot visualizes the relationship of the two quantities, with the center of the ellipse at the mean of v_2 and v_3 , width and height are the variance of v_2 and v_3 , respectively, and the angle shows the covariance. Data at 0-5% centrality (left) and 20-30% centrality (right) for Au-Au collisions at $\sqrt{s_{NN}} = 200$ GeV.

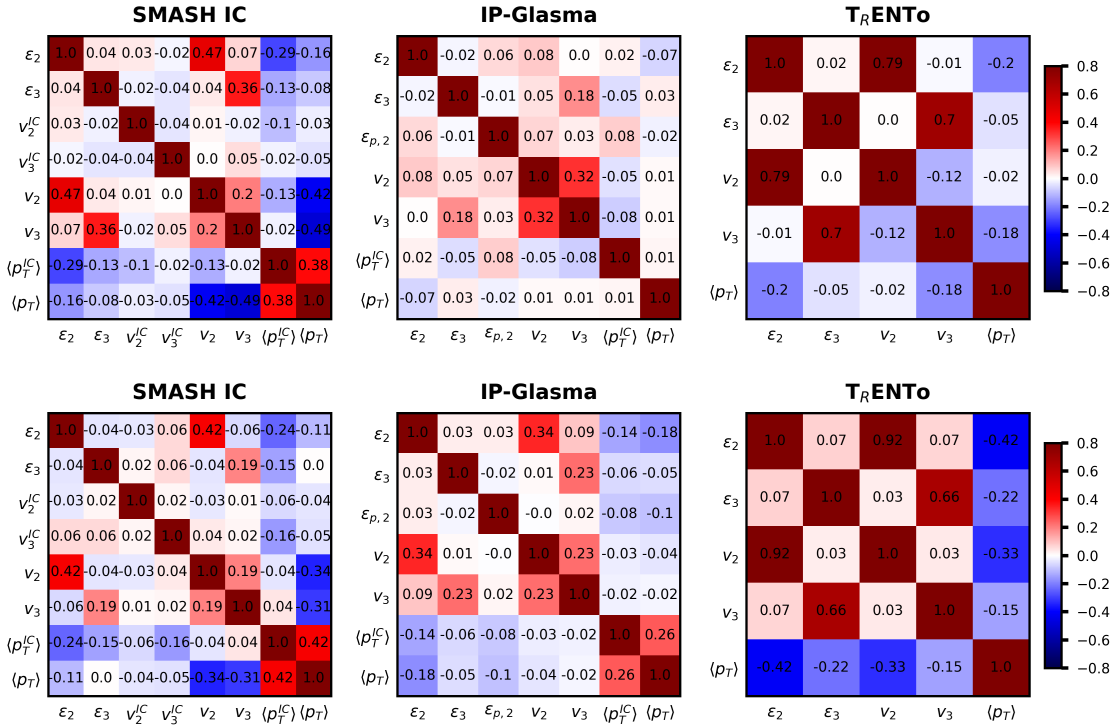


FIGURE 4.6: Pearson correlation matrix at 0-5% centrality (top) and 20-30% centrality (bottom) for Au-Au collisions at $\sqrt{s_{NN}} = 200$ GeV for SMASH, IP-Glasma and T_RENTo (left to right).

An additional observation that challenges a simple linear or higher-order response of flows to eccentricities is the pronounced difference in the shapes of final state flow distributions compared to initial state eccentricity distributions. For both centrality classes, the T_{RENT}o distributions are more peaked than those of SMASH and IP-Glasma. A simpler response model would have preserved the original hierarchy of peaks, but here we observe significant correlations, visible in the orientations of the ellipses in the lower-left corner. SMASH and IP-Glasma show a positive correlation between v_2 and v_3 , whereas T_{RENT}o exhibits a negative correlation for central events. Although all three distributions were initially very similar, IP-Glasma now stands apart, shifted toward higher flow values.

These findings indicate that the properties of final state flow cannot be solely attributed to initial state eccentricities, even when other components of the hybrid approach are held fixed. In what follows, we explore possible factors that may account for these differences among the models.

Figure 4.6 presents the Pearson correlation matrix for all relevant quantities across the three models and the centrality classes under study, encoding the Pearson correlation coefficient between each pair of variables. The Pearson correlation coefficient is a measure of the linear relationship between two continuous variables, labeled X and Y. Its values range from -1 to 1 , where values near ± 1 indicate a strong linear dependence, and values close to 0 indicate no relationship. Formally, it is given by

$$r = \frac{\sum_{i=1}^n (x_i - \bar{x})(y_i - \bar{y})}{\sqrt{\sum_{i=1}^n (x_i - \bar{x})^2} \sqrt{\sum_{i=1}^n (y_i - \bar{y})^2}}, \quad (4.3)$$

where \bar{x} and \bar{y} are the sample means of X and Y, respectively.

Concerning the $\epsilon_n - v_n$ correlations, these are generally strongest for T_{RENT}o and SMASH. In contrast, they become particularly weak for IP-Glasma in central collisions, likely due to its higher initial state granularity, which increases the effect of fluctuations. Even if the entire event can be approximated by an elliptical shape, the pressure gradient from granular structures exerts a more substantial influence on the final flows. Whereas these correlations grow for both T_{RENT}o and IP-Glasma in more off-central collisions, they decrease in SMASH. This implies that in off-central SMASH events, the eccentricity serves as a less reliable predictor of the flow.

These findings stand in opposition to earlier results in Ref. [198], where it was noted (using NeXus events) that the $\epsilon_n - v_n$ correlation grows with increasing off-centrality. Hence, we see that this behavior does not hold universally across all initial condition models.

In SMASH, the initial state flows do not reveal any significant correlation with either the final state observables or other initial state quantities. The situation is somewhat less clear for central IP-Glasma events, where the correlation between ϵ_p and v_2 reaches a magnitude comparable to the $\epsilon_2 - v_2$ correlation, though both remain small. Reference [396] demonstrated that classifying the initial state by eccentricities, the average square radius, and the total energy per unit rapidity can accurately predict final state flows, consistent with our observation of no correlation between initial and final state momentum anisotropies. It appears that initial state momentum anisotropy does not persist through hydrodynamic evolution to influence the final state momentum anisotropy.

For SMASH in particular, this contradicts earlier assumptions that the substantial initial flow directly contributes to the final flow [199].

Examining the final state transverse momentum, we find marked differences among the three models. In T_RENTo, there is a slight anti-correlation with all initial and final state properties in central collisions, which grows stronger at off-central collisions. In SMASH, a strong anti-correlation emerges only in relation to the final flows, whereas IP-Glasma shows no significant correlation at all. On the other hand, for SMASH we find a significant correlation between radial flow and the final transverse momentum. It is notably stronger than that observed in IP-Glasma. Additionally, SMASH also shows a slight anti-correlation between the initial eccentricities and the radial flow, whereas the initial ellipticity is negatively correlated with the inverse root-mean-square radius. This can be seen as a result of the fact that smaller, more compact sources lead to larger transverse momenta but lower deformation. This effect is less pronounced in T_RENTo, which produces a smoother source, and in IP-Glasma, where granular fluctuations play a larger role.

4.4 Multiple Linear Regression

The assumption of a linear relationship between the initial eccentricities and the final state flow can be viewed as applying a linear regression model. As we have access to additional initial state properties, we can also test whether other aspects of the initial state contribute to the development of final state flow, beyond the relevant eccentricity mode. In other words, we can check whether additional independent variables help explain the observed final state flow. It is important to stress that merely examining pairwise correlations is insufficient for this purpose, because such correlations only capture relationships between two variables, while our aim is to explore a multivariate relationship. Indeed, owing to the strong connection between flow and eccentricity, the influence of other independent variables may not be evident through correlation analyses alone.

A simple example helps illustrate this point. Suppose two initial state properties both contribute to v_q via the relation

$$v_q = 2 \epsilon_p + \epsilon_q, \quad (4.4)$$

and further assume that ϵ_p and ϵ_q are perfectly anti-correlated. Even though ϵ_q is an independent source of v_q , the Pearson correlation between v_q and ϵ_q can appear negative, because the much larger contribution from ϵ_p masks the effect of ϵ_q .

In the appendix, we present a series of linear regressions involving different initial state properties to predict v_2 and v_3 , based on SMASH and IP-Glasma initial conditions in both centrality classes. For each regression variable, we report the coefficient and the corresponding p-value, the latter indicating the probability of observing the result under the null hypothesis. As a rule of thumb, a p-value below 0.05 is necessary (though not sufficient) to consider the inclusion of a dependent variable as statistically significant. In addition, we report r^2 . It tells us what fraction of the total variation in y is explained by our regression line. Both concepts are explained in more detail in the appendix.

Adding more independent variables generally improves r^2 (or at least does not decrease it), because additional linearly independent information helps account for statistical

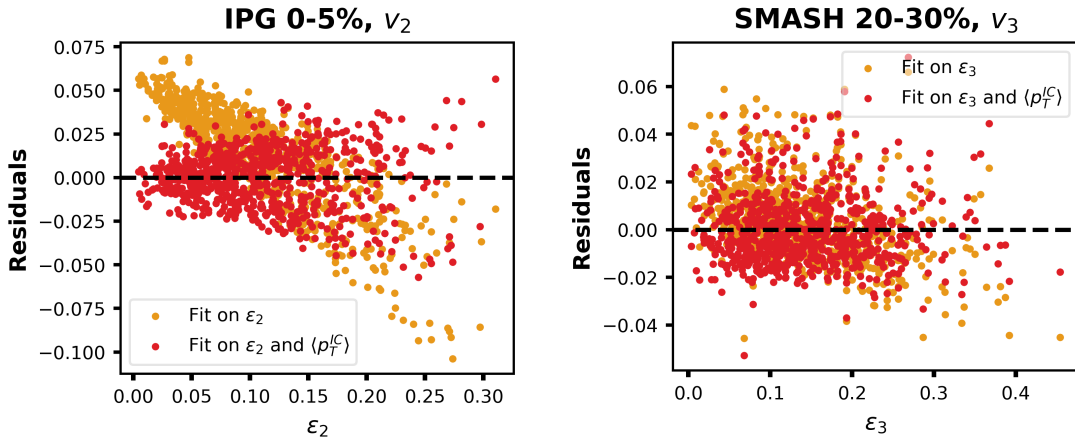


FIGURE 4.7: Left: The difference between observed and fitted values (also known as residuals) for a fit on ϵ_2 on the one hand and ϵ_2 and $\langle p_T^{IC} \rangle$ on the other hand, for IP-Glasma at 0-5% centrality. Right: The same data for collisions in SMASH at 20-30% centrality, for the fit with v_3 on ϵ_3 (right) for Au-Au collisions at $\sqrt{s_{NN}} = 200$ GeV.

fluctuations. In the cases examined here, the inclusion of $\langle p_T^{IC} \rangle$ in particular is statistically significant and yields a greater improvement in r^2 than any other variable. From tables A.5 to A.8, we see this effect is especially strong for IP-Glasma, which contains a substantial amount of transverse momentum. Nonetheless, tables A.1 to A.4 illustrate a qualitatively similar, though less pronounced, effect in SMASH.

Because IP-Glasma is known to include more initial transverse momentum, it is reasonable that its initial $\langle p_T^{IC} \rangle$ stands out as a stronger and more significant predictor. This consistent and significant improvement clarifies that radial flow in the initial state constitutes a next-to-leading-order contribution to the final state flows. A stronger transverse push leads to a stronger hydrodynamic response to the initial azimuthal deformation.

These findings help to interpret the differences observed in the response functions earlier: depending on the initial condition model, the presence of initial state transverse flow modifies the response to initial state eccentricities. Consequently, eccentricity is not the only feature of the initial state that influences the initial flow, but can rather be seen as the leading contribution.

The effect of including radial flow in the predictor of final state flow becomes clear in fig. 4.7. Here the residuals of the prediction of the linear regression model with respect to the observed value is shown in two cases. In other words, one can see the difference between prediction and true value based on the predictive model. The systems were chosen as they demonstrate strong improvement when including a second independent variable. We see that in both systems the inclusion of the additional independent variable compensates too high predictions of flow for small eccentricities and too small predictions for the flow at high eccentricities. It becomes clear that for events with small eccentricities, initial radial flow is an important factor in the emergence of final state flow harmonics.

4.5 SMASH at Intermediate Energies

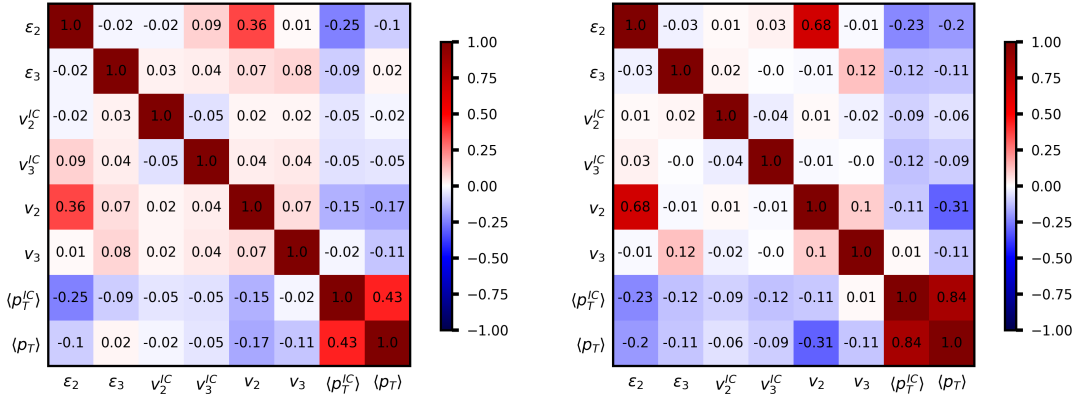


FIGURE 4.8: Pearson correlation matrix for SMASH at $\sqrt{s_{NN}} = 17.3$ GeV, at 0-5% centrality (left) and 20-30% centrality (right).

As the SMASH IC is a three-dimensional initial condition model, one can also apply it to lower collision energies. Therefore, we can extend the study of this initial condition model also to the case of Pb–Pb collisions at an energy of $\sqrt{s_{NN}}=17.3$ GeV, where the passing time is 1.44 fm/c.

The correlation matrix in Fig. 4.8 shows a weaker dependence between ϵ_3 and v_3 in comparison to the high-energy case. Additionally, the correlation between the flow modes is also reduced, hinting at a stronger role of non-flow for v_3 , but not v_2 . We observe a greatly increased relationship between radial flow and final transverse flow, whereas the relationship between eccentricities and radial flow remains roughly unchanged. It seems that, due to the shorter lifetime of the medium, the average radial flow itself is hardly changed, whereas the flow harmonic again do not survive the fireball evolution. Tables of different linear regression models can be found in the appendix in tables A.9 to A.12. Due to the weak ϵ_3 - v_3 -correlation, linear regression with v_3 as dependent variable fails to appropriately describe the data. The inclusion of radial flow in the linear fit again improves the regression. This effect is however more relevant at high energies, although its consequence for the residuals remains unchanged, as can be seen in fig. 4.9.

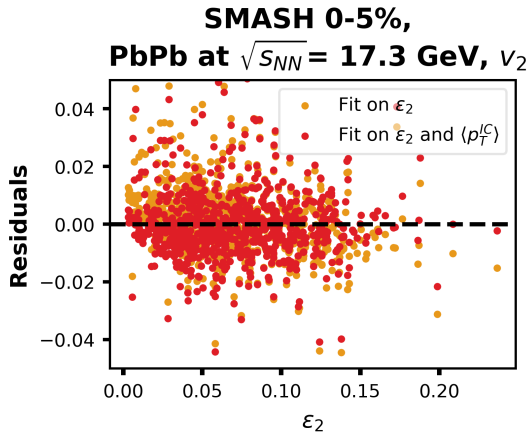


FIGURE 4.9: Hybrid evolution with SMASH IC at 0-5% centrality and $\sqrt{s_{NN}} = 17.3$ GeV: Residuals between observed and fitted values for a fit on ϵ_2 on the one hand and ϵ_2 and $\langle p_T^{IC} \rangle$ on the other hand.

4.6 Discussion

We observe substantial differences in eccentricity and final state flow distributions across various models, with T_RENTo exhibiting the most pronounced peaks. Consequently, relying on average values alone does not fully capture the discrepancies among initial state models. Indeed, the correlation between initial eccentricities and final flows is conspicuously model-dependent, featuring the strongest correlation in T_RENTo and the weakest in IP-Gasma, particularly in central collisions. Moreover, even though the same hydrodynamic evolution was applied in each case, the system's response to initial eccentricities differed among the initial condition models.

The underlying cause stems from the transverse momentum in the initial state, as provided by SMASH IC and IP-Gasma, which exerts a non-negligible influence on the final flows. Including this component alongside eccentricity in a linear regression model improves predictions of the final flows. This contribution from initial radial flow constitutes a relevant second-order effect in shaping final anisotropic flows, thereby challenging the assumption of a universal linear hydrodynamic response. Extending the study to lower energies with SMASH IC showed weaker correlations overall, yet initial radial flow continued to benefit final flow predictions.

In contrast, anisotropies in the initial state momentum do not significantly affect the final state, since they rapidly isotropize during the hydrodynamic phase and do not influence the momentum distribution of the final state. This could potentially be related to forced regularization in hydrodynamics, which suppresses terms which are too far from equilibrium.

In summary, our detailed event-by-event analysis demonstrates marked differences among commonly used initial state models, which bear critical implications for predicting final state observables. Even though averaged results appear similar, the event-by-event distributions, correlations, and hydrodynamic response differ substantially. These findings underscore the importance of initial transverse momentum as a key contributor to final

flows, indicating that comprehensive characterization of the initial conditions requires more than just eccentricity when correlating with final state observables.

Future studies could extend this analysis to further initial condition models. Most importantly, IP-Glasma can be combined with alternative approaches for the pre-equilibrium dynamics. The pre-equilibrium can have a substantial effect on the initial state transverse momentum [397–400]. Alternatively, the study could also be performed in an anisotropic hydrodynamics setup [401], which could potentially improve model uncertainties at the point of fluidization. Additionally, it would be worthwhile to extend the statistical toolset employed in this study. Instead of just comparing the results of different setups of multiple linear regression, one could employ more strict schemes like LASSO regression. This has the advantage of better and more systematically estimating the true importance of independent variables, especially in the presence of multicollinearity, which is expected to affect results here, too [402].

INVESTIGATION OF VISCOSITIES IN HYBRID APPROACHES

The more we learn about the world, and the deeper our learning, the more conscious, specific, and articulate will be our knowledge of what we do not know, our knowledge of our ignorance. For this, indeed, is the main source of our ignorance — the fact that our knowledge can be only finite, while our ignorance must necessarily be infinite.

— Karl Popper, *Conjectures and Refutations: The Growth of Scientific Knowledge*

After studying the substantial difference in the existing initial state models and their effect on observables, we want to proceed with studying the existing uncertainties in the hydrodynamic stage. Here, we want to focus on the form and values of viscosities. In a first step, based on [1], we study the effect of the inclusion of a baryochemical potential dependence in the parameterization of the shear viscosity. With the results of this in mind, we proceed to perform a full Bayesian analysis of the SMASH-vHLLE-Hybrid approach, based on [4].

5.1 Exploring the Baryochemical Potential Dependence of Shear Viscosity

As mentioned previously, there is theoretical support for a dependence on the net baryochemical potential [62–65]. Although studies including a non-constant $\eta/s(T, \mu_B)$ in hydrodynamic simulations exist [403], the effect on the observables is largely unexplored. Previous studies focus on a temperature dependence or even a constant effective shear viscosity [53, 54, 58, 233, 237, 311, 331, 404, 405]. Thus, in the following, we want to investigate in the following the effect of including a dependence on the net baryochemical potential.

5.1.1 Selection of the Parameterization and Choice of Comparison Models

A common approach for exploring a combined temperature and net baryochemical potential dependence of the shear viscosity in the fireball is to start with a direct parameterization of η/s in terms of the temperature T , then add terms proportional to μ_B . However, parameterizing the shear viscosity in terms of the local rest-frame energy density ϵ and the net baryon number density ρ benefits from the fact that these are the hydrodynamic fields actually evolved in time. Consequently, the parameterization becomes less sensitive to the EoS, though η/s itself still depends on the EoS via the entropy density in the denominator. An additional advantage is the observation that the shear viscosity is expected to have a minimum near the cross-over transition between the

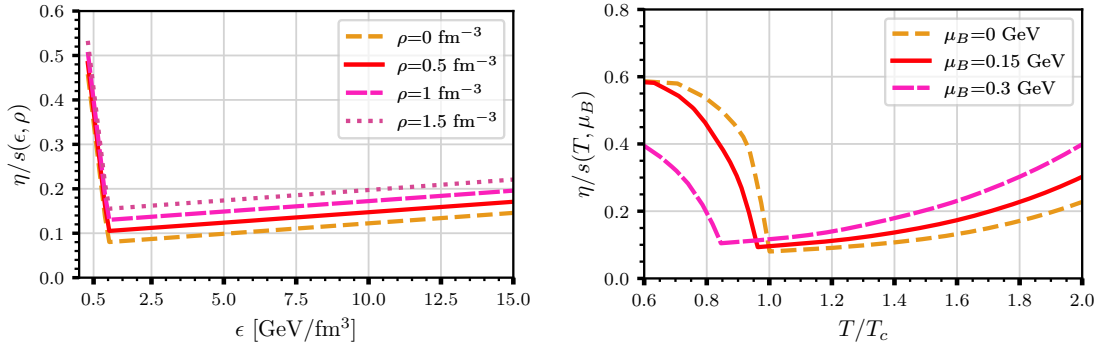


FIGURE 5.1: Energy density and net baryon density dependent shear viscosity $\eta/s(\epsilon, \rho)$ for $S_\rho = 0.05 \text{ fm}^3$ (left). The same quantity mapped to (T, μ_B) using a chiral equation of state (right).

quark–gluon plasma and the hadronic phase. This transition line approximately follows a constant-energy-density contour [406]. Therefore, it is more straightforward to reproduce this feature with a parameterization in ϵ .

Since our objective is primarily qualitative, we adopt several simplifications. First, although the more accurate measure of fluidity at finite μ_B is $\eta T/w$, with $w = \epsilon + p$ denoting the enthalpy [407], we use η/s for convenience, noting that both expressions coincide in the limit of small μ_B .

Next, to reflect the expected minimum of η/s near the transition, we enforce that $\eta/s(\epsilon)$ approximately reproduces the typical $\eta/s(T)$ behavior in the limit $\mu_B \rightarrow 0$, exploiting the fact that $\epsilon \sim T^4$. Observables are known to be more sensitive to the overall magnitude of the shear viscosity than to its detailed functional form [339], so we opt for a piecewise linear dependence in both the high- ϵ and low- ϵ regimes. This choice inherently introduces a μ_B -dependence: the minimum of $\eta/s(\epsilon)$ is shifted to lower temperatures for increasing μ_B (see fig. 5.1). Although it may seem counterintuitive that a higher baryochemical potential could reduce the shear viscosity in the low-temperature regime, this follows directly from fixing the minimum of η/s along a constant- ϵ line. Increased baryochemical potential raises the energy density, thus driving the system closer to the transition region.

Nonetheless, we wish to study the explicit μ_B -dependence in more detail, and therefore include a term linear in the net baryon number density ρ . We choose the net baryon density because it is the relevant quantity evolved in hydrodynamics. Although negative net baryon densities are not formally excluded, in practice, smoothing the initial condition together with the baryon rich collision energies under consideration ensures $\rho \geq 0$ throughout the fluid. Imposing positivity on the shear viscosity then leads us to the following functional form:

$$\eta/s(\epsilon, \rho) = \max \left(0, (\eta/s)_{\text{kink}} + \begin{cases} S_{\epsilon, H}(\epsilon - \epsilon_{\text{kink}}) + S_\rho \rho, & \epsilon < \epsilon_{\text{kink}} \\ S_{\epsilon, Q}(\epsilon - \epsilon_{\text{kink}}) + S_\rho \rho & \epsilon > \epsilon_{\text{kink}} \end{cases} \right) \quad (5.1)$$

This choice of parameterization introduces five fit parameters, out of which all but S_ρ are fixed by constraints. We set ϵ_{kink} , the position of the minimum at vanishing net baryochemical potential, to 1 GeV/fm^3 , guided by lattice QCD results [35] and

experimental data [408]. The value of the shear viscosity at this minimum is set according to the Kovtun-Son-Starinets (KSS) bound [47]. The slope in the high-energy-density region is adjusted to reproduce perturbative QCD calculations [55] at a temperature of 400 MeV and vanishing μ_B . For the low-energy-density region, we match the shear viscosity extracted from box calculations in SMASH at vanishing μ_B at the particlization temperature¹, thereby reducing discontinuities at the switch from hydrodynamics to the hadronic transport description. It is, however, essential to note that this correspondence is only approximate. The hadronic transport in box calculations used to extract transport coefficients differs significantly from an expanding medium, where scatterings occur in an environment that can be less isotropic. Moreover, we emphasize that, in general, this parameterization permits η/s to take any positive value, potentially violating the KSS bound because values smaller than $\frac{1}{4\pi}$ are allowed. This is not a strict bound for non-conformal theories [409].

With these constraints set, only one free parameter remains, S_ρ . We will vary this parameter to assess its impact on observables, as it determines how strongly η/s scales with ρ . Figure 5.1 displays the parameterization for $S_\rho = 0.05 \text{ fm}^3$ in both (ϵ, ρ) and (T, μ_B) coordinates. The mapping is performed using the same equation of state employed in vHLLE. A characteristic kink structure appears in both representations. Even for $S_\rho = 0$, the minimum of η/s shifts to lower temperatures with growing μ_B because it is placed along a contour of constant energy density, as discussed above. The value of η/s at the minimum, however, changes only if S_ρ is non-zero.

In what follows, we compare our parameterization to other existing options for η/s , namely constant or temperature-dependent functional forms. The first comparison uses constant η/s values, which differ by collision energy (see Table 1 in Ref. [221]). These values constitute the default settings in the SMASH-vHLLE-Hybrid, originally taken from UrQMD+vHLLE to match experimental data optimally. Such constant- η/s choices often prove sufficient because many observables depend predominantly on the effective shear viscosity [339], rather than its detailed variations at different stages of the fireball evolution.

The second form of the shear viscosity for comparison exemplifies the growing interest in extracting $\eta/s(T)$ from experimental data via Bayesian analyses. We use the $\eta/s(T)$ parameterization from JETSCAPE [54], with a set of parameters near the center of their 60% confidence interval. While tuned to reproduce high-energy data and featuring a minimum close to the transition temperature, it lacks both implicit and explicit dependence on μ_B .

5.1.2 Insights on Shear Viscosity in Hybrid Approaches

Our investigation targets the intermediate-energy regime, specifically Au–Au collisions at $\sqrt{s_{NN}} = 7.7 \text{ GeV}$ and 39 GeV , as well as Pb–Pb collisions at $\sqrt{s_{NN}} = 17.3 \text{ GeV}$. In this range, the baryochemical potential μ_B is sufficiently large to be impactful, and the fireball’s lifetime remains considerable, making the system notably sensitive to modifications of the shear viscosity during the hydrodynamic phase. We examine both central (0–5% centrality) and mid-central (20–30% centrality) collisions.

¹ This particlization temperature is defined as the temperature equivalent to the particlization or switching energy density ϵ_{switch} at vanishing μ_B in the SMASH hadron gas EoS.

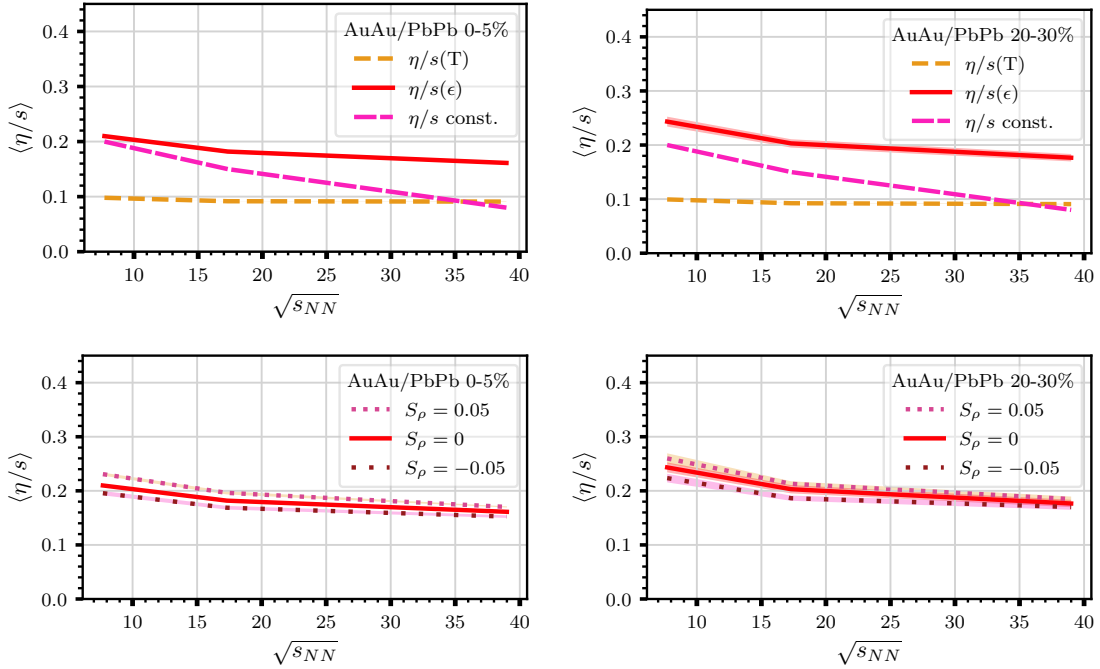


FIGURE 5.2: Mean shear viscosity over entropy ratio (weighted with the energy density) throughout the whole hydrodynamic evolution. Top: Comparison between different parameterization choices for both central and off-central collisions. Bottom: effect of net baryon number density dependence for central and off-central collisions.

For each simulation configuration, we run 100 event-by-event viscous-hydrodynamics events, each initialized from a single SMASH initial condition. The smearing parameters for transitioning from transport to hydrodynamics follow Table 1 of Ref. [221], which demonstrated compatibility with experimental data. From the resulting freeze-out hypersurface, we sample 1000 events for the hadronic afterburner to ensure, on average, quantum-number conservation. We neglect bulk viscosity in all cases, whereas the choice of shear viscosity will be described in the following sections.

For this project, SMASH-vHLLE-Hybrid:03232b2, SMASH-2.1.4, vhle-params:99ef7b4, vHLLE:ef9e28 and SMASH-hadron-sampler-1.0 were employed².

In what follows, we examine the qualitative impact of our proposed η/s parameterization and various values of S_ρ on the dynamical evolution and selected observables of heavy-ion collisions. We focus on the midrapidity yields and mean transverse momentum in central collisions. These observables display only weak sensitivity to the shear viscosity. Their advantage, however, is that they can be accurately computed even with relatively low statistics. Additionally, we study the integrated elliptic flow v_2 in the 20–30% centrality region, an observable known to be highly sensitive to the shear viscosity. Under the conditions of our simulations, the temperature throughout the hydrodynamic evolution spans values between 108 and 407 MeV, while the net baryochemical potential reaches values between 0 and 583 MeV.

² As pre-release versions were employed, the references to the commits were given here.

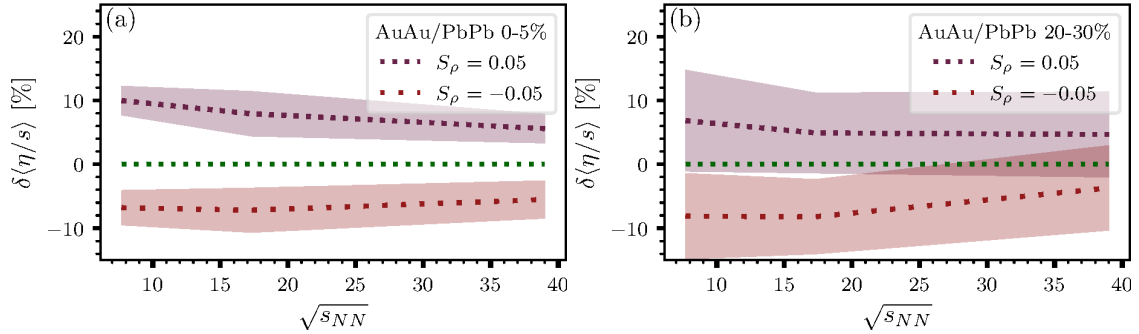


FIGURE 5.3: S_ρ -dependent data from fig. 5.2 normalized to the parameterization with $S_\rho = 0$. Deviation in percent.

We compare observables across two sets of shear-viscosity configurations. First, we contrast our $\eta/s(\epsilon)$ parameterization (with $S_\rho = 0$) against both constant- η/s and temperature-dependent forms, thereby relating our results to common prior choices in the literature. Second, we assess the explicit net baryon number dependence of η/s by comparing $S_\rho = 0$, $S_\rho = 0.05 \text{ fm}^3$, and $S_\rho = -0.05 \text{ fm}^3$. These values were chosen to be significant enough to have a substantial impact on the evolution without leading to excessive values for the viscosity.

5.1.2.1 Effective η/s and Time Evolution

An instructive way of comparing different non-constant shear-viscosity parameterizations is via the effective shear viscosity, which is calculated as a weighted average throughout the hydrodynamic evolution. Various schemes exist for assigning weights to the shear viscosity in a single fluid cell at any given time, but in this work, we focus on the energy density as our weighting factor. The results of this comparison are shown in fig. 5.2, where the deviation of the shear viscosity when including a ρ -dependent term is shown in percent, and standard statistical error is indicated by the shaded bands.

We find that the parameterization based on energy density attains higher shear-viscosity values than the alternative scenarios considered, particularly in peripheral collisions and at larger collision energies. This difference arises mainly because SMASH has a higher shear viscosity than the purely temperature-dependent parameterization, thereby elevating the weighted average via cells situated near the particlization energy density. In contrast, the temperature-dependent parameterization shows only a modest sensitivity to collision energy, reflecting a relatively small slope in the Bayesian posterior for its parameters combined with a similar minimal value. Finally, the constant- η/s setup agrees well with the effective values at lower collision energies but diminishes more sharply at higher energies. Its strong decline displays a qualitative difference to the other parameterizations.

Turning to the ρ -dependence of η/s , fig. 5.3 shows that the overall effect remains moderate and diminishes with increasing collision energy. A smaller effect is also observed when transitioning from central to peripheral collisions. In both instances, the effective baryon density is reduced: either due to a lower net baryochemical potential at higher energies or because the reaction zone is more peripheral. Note, however, that a small

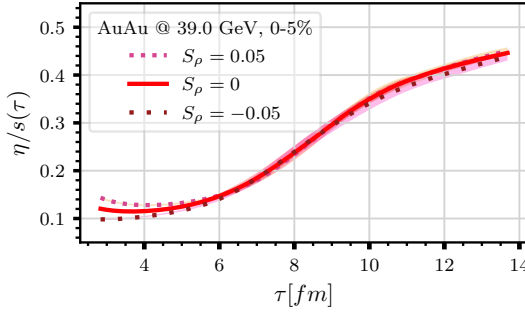


FIGURE 5.4: Time evolution of the energy density weighted shear viscosity over entropy ratio for central collisions at $\sqrt{s_{NN}} = 39$ GeV.

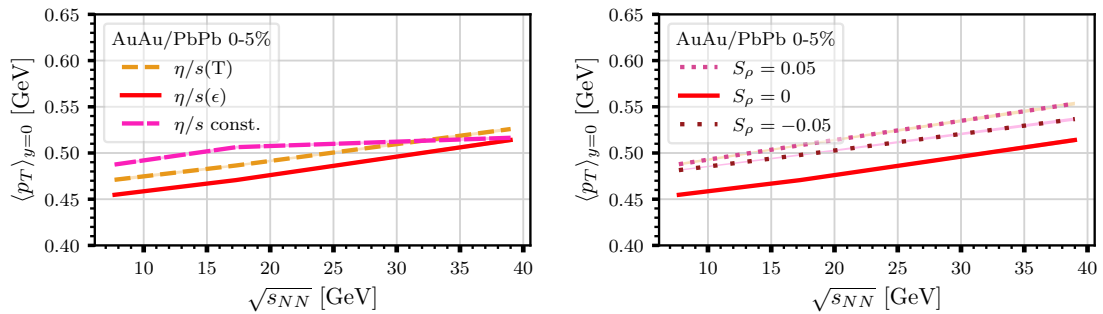


FIGURE 5.5: Excitation function of $\langle p_T \rangle$ of charged hadrons at midrapidity ($|y| < 0.5$) for different parameterization strategies (left) and different values of the net baryon number density dependence (right).

difference in the effective shear viscosity does not necessarily imply a negligible impact on observables; variations in the viscosity across distinct regions of the fireball could still modify measured quantities, even if the overall effective viscosity remains the same, as the fireball evolution is influenced by the anisotropy of the shear viscosity.

Further insight is provided by fig. 5.4, which depicts the effective shear-viscosity-over-entropy ratio over time for central collisions at $\sqrt{s_{NN}} = 39$ GeV. The most pronounced effect of S_ρ appears in the early stages of hydrodynamic evolution, when the fireball volume is still small and densities are correspondingly high. Generally, the $\eta/s(\epsilon)$ parameterization exhibits a strong time dependence. At these energies, numerous fluid cells begin their evolution near or slightly above ϵ_{kink} and thus have initially low shear viscosities, which then rise rapidly as the system cools and dilutes.

5.1.2.2 Bulk Observables

An initial perspective on the influence of the net baryochemical potential dependence emerges from examining bulk observables in central collisions. In fig. 5.5, we compare the mean transverse momentum at midrapidity for charged hadrons under various shear-viscosity parameterizations. At lower collision energies, the $\eta/s(\epsilon)$ parameterization leads to a reduced mean p_T , yet it converges slowly toward the values obtained from other parameterizations as the collision energy grows, in line with the trend of the shear

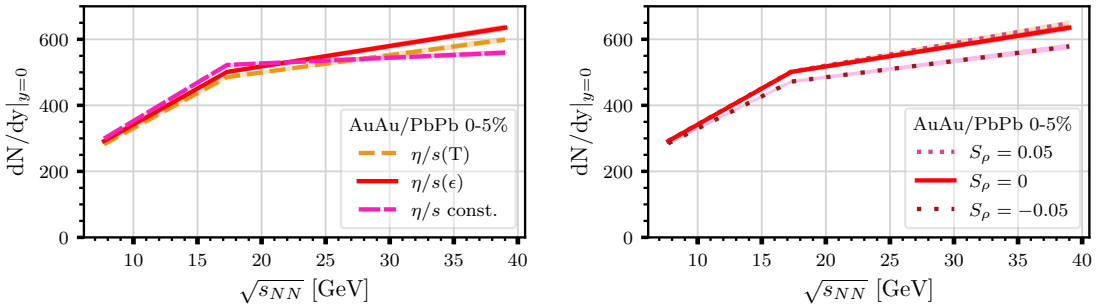


FIGURE 5.6: Excitation function of dN/dy ($|y| < 0.5$) of charged hadrons for different parameterization strategies (left) and different values of the net baryon number density dependence (right).

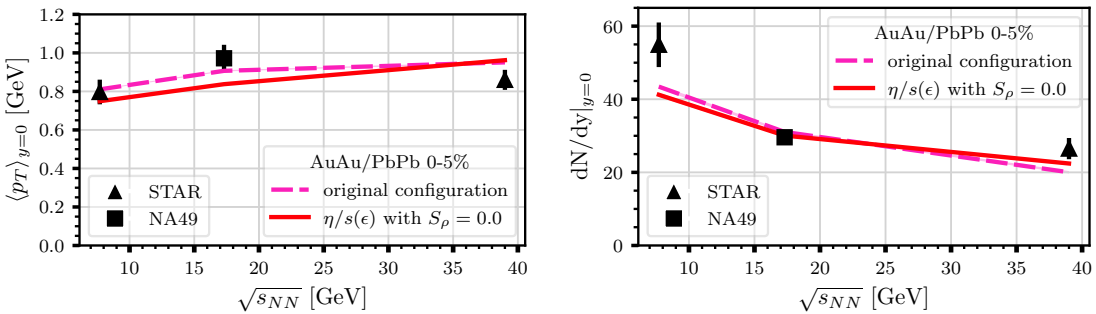


FIGURE 5.7: Comparison of proton mean transverse momentum and midrapidity yield to data from NA49 [410] and STAR [411].

viscosity itself. Introducing an explicit ρ -dependence—whether positive or negative—increases the transverse momentum. Notably, this indicates that the fireball evolution exhibits a non-linear response to changes in the viscosity, as a purely linear effect would require changes in the observables to be either correlated or anticorrelated with S_ρ .

In fig. 5.6, we plot the charged-hadron yield at midrapidity as a function of beam energy. Marked differences among the various parameterization strategies appear only at higher collision energies, where the energy-density-based parameterization leads to an increased yield. Regarding the explicit net baryon number dependence, the inclusion of S_ρ also has a stronger impact at higher energies. However, once again the effect is non-linear: increasing the shear viscosity with growing net baryon density has almost no influence on the yield, whereas decreasing it significantly reduces the yield.

Although our aim is to provide only a qualitative analysis of how a net baryochemical-potential dependence in the transport coefficients impacts heavy-ion collisions, it is still instructive to compare selected results to experimental data. In fig. 5.7, we contrast our model predictions for the mean transverse momentum and midrapidity yield of protons—obtained from the energy-density-based parameterization with $S_\rho = 0$, the original constant- η/s scenario, and the temperature-dependent parameterization—with experimental measurements. Protons serve as a convenient reference because data for them are readily available.

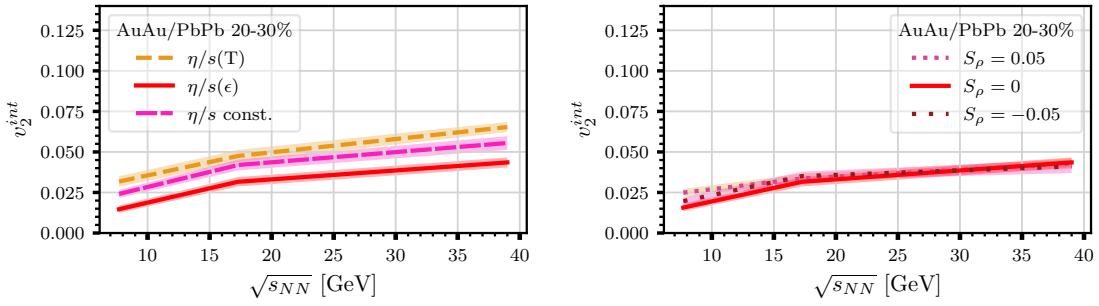


FIGURE 5.8: Integrated elliptic flow of charged hadrons at midrapidity ($|y| < 0.5$) for different parameterization strategies (left) and different values of the net baryon number density dependence (right).

In both observables, the agreement among the various parameterizations and the experimental results is comparably good. This outcome is not surprising given that fig. 5.5 and fig. 5.6 already showed the observable differences among all parameterizations to be on the order of 10% at most.

5.1.2.3 Elliptic Flow

The anisotropic flow coefficients are highly sensitive to the shear viscosity [404], particularly at higher orders. However, these measurements typically require substantial statistics, which is why we focus on the integrated v_2 in 20–30% central collisions for our exploratory study. The scalar product method (see section 3.3.2) is employed for the v_2 analysis, as it both gives reliable errors without too high requirements in statistics.

Figure 5.8 displays the excitation function of the average $\langle v_2 \rangle$. Most notably, the energy-density-based parameterization yields a considerably lower elliptic flow compared to the other scenarios, attributable to its higher effective shear viscosity. By contrast, varying S_ρ has only a minor impact on elliptic flow, and this impact is predominantly seen at lower collision energies.

This outcome points to two complementary observations. On the one hand, our bulk observables proved more sensitive to S_ρ at higher collision energies, but on the other hand, elliptic flow appears to be influenced by it primarily at lower energies. Since the average net density ρ is larger in the lower-energy collisions, the flow is more easily modified in those systems. Conversely, while higher collision energies do produce larger net densities at early stages, our results suggest that bulk observables are influenced most strongly by early-time physics, whereas flow—largely unaffected by S_ρ at higher collision energies—reflects late-time dynamics. A likely explanation is the out-of-equilibrium correction δf_{shear} in the sampling procedure, which can substantially alter observables and depends on the shear stress at particlization [339].

When comparing the integrated charged-hadron flow to experimental data, we find that the flow reduction caused by $\eta/s(\epsilon)$ results in a larger discrepancy with the measurements. An exception appears at low energies, where the default SMASH-vHLL-E-Hybrid configuration also fails to reproduce the data point due to a shorter hydrodynamic evolution. Otherwise, the original configuration generally shows better agreement than $\eta/s(\epsilon)$. Nevertheless, this does not imply that the net baryon chemical-potential dependence can

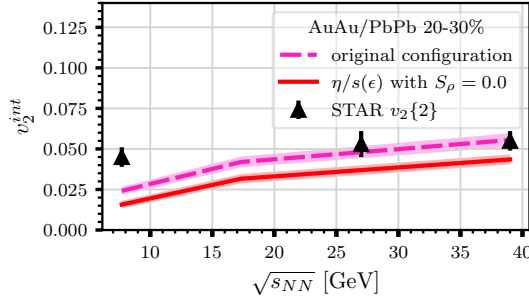


FIGURE 5.9: Comparison of charged hadron integrated event plane elliptic flow at midrapidity to STAR data [412].

be neglected entirely; rather, it reflects our qualitative approach, which did not include simultaneously tuning other parameters. Indeed, as we demonstrate later in this chapter, many different parameterizations can achieve compatibility with data, provided the initial-state parameters are also optimized. Despite the reduced agreement at higher energies, we remain within a 2σ range of the experimental results.

5.1.2.4 Impact of Switching Energy Density

As noted above, the duration of the hydrodynamic phase crucially influences how η/s parameterizations impact observables, given that viscous corrections operate on the system for a longer or shorter interval. We define the hydrodynamic lifetime as the time until the last fluid cell falls below ϵ_{switch} . Depending on the value of ϵ_{switch} , the system spends more or less time in the hydrodynamic stage and correspondingly less or more time in the transport phase, thereby dictating the portion of flow developed under each description.

Figure 5.10 extends a study from Ref. [199], comparing three different elliptic flow contributions: the elliptic flow in the initial conditions, the elliptic flow at the end of the hydrodynamic phase (approximated only allowing decays and not scattering in the final hadronic transport stage), and the total flow after the hadronic transport stage. These calculations were done with the default constant shear viscosity and varying $\epsilon_{\text{switch}} \in \{0.5, 0.3, 0.1\} \text{ GeV/fm}^3$. We assume that the flow directions at the end of hydrodynamics and the end of rescattering are approximately aligned, such that the flow generation effectively shifts between the hydrodynamic and transport stages. This assumption is justified because the initial momentum distribution becomes isotropic during hydrodynamics, while the pressure gradient from spatial anisotropies generates new momentum, as shown in the last chapter. Note that the flow originating from the initial state is not necessarily aligned with the final flow, since it arises from initial particle momenta and fluctuating anisotropies.

When comparing the contributions of the different stages of this hybrid model, we see that with increasing ϵ_{switch} and decreasing collision energy, a larger fraction of the total elliptic flow originates from the hadronic transport evolution. For $\epsilon_{\text{switch}} = 0.5 \text{ GeV/fm}^3$, hydrodynamic evolution meaningfully contributes to the final flow starting around $\sqrt{s_{\text{NN}}} = 20 \text{ GeV}$. By contrast, for $\epsilon_{\text{switch}} = 0.1 \text{ GeV/fm}^3$, the afterburner stage no longer imparts a noticeable effect on the observed elliptic flow.

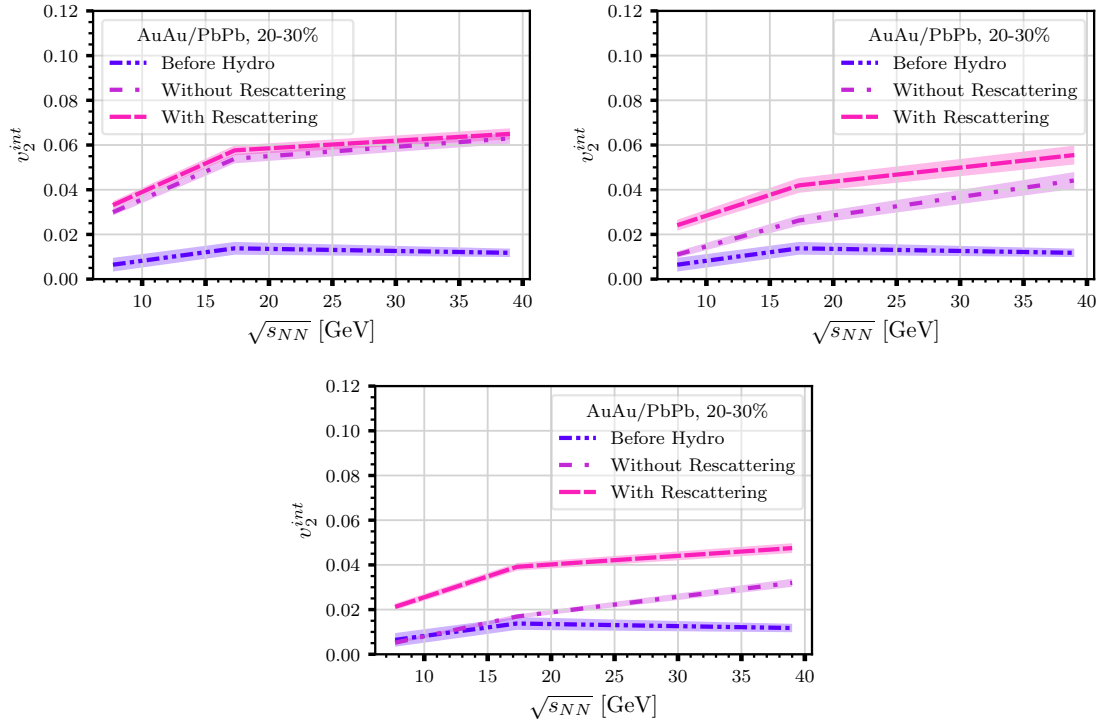


FIGURE 5.10: Elliptic flow at the end of different stages of the hybrid simulation, for different values of the ϵ_{switch} . Top left: 0.1 GeV/fm^3 , top right: 0.3 GeV/fm^3 , bottom 0.5 GeV/fm^3 .

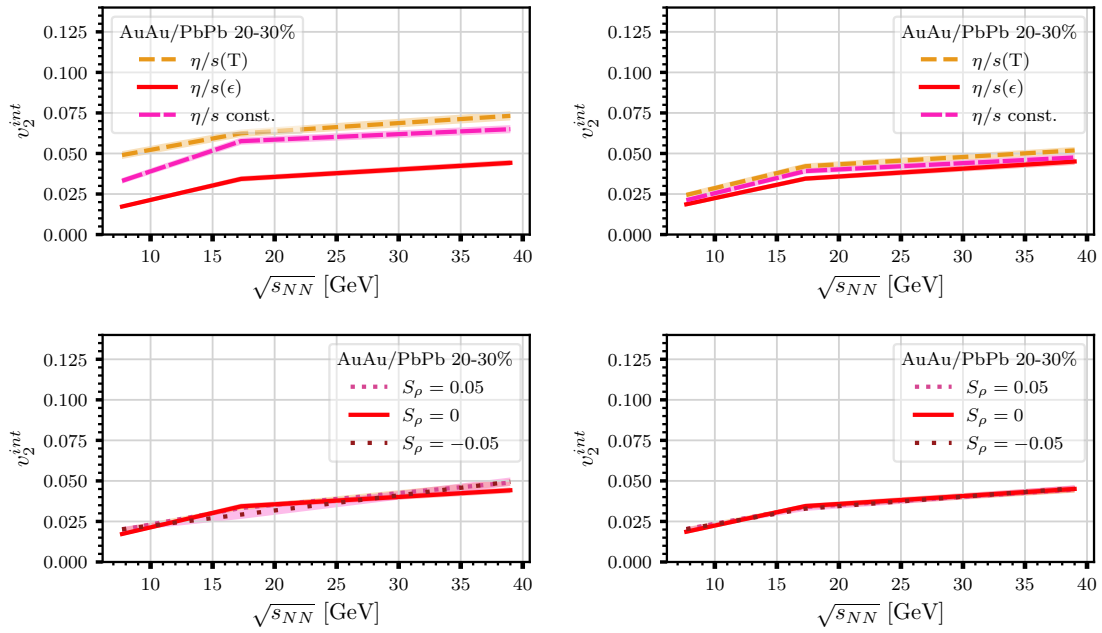


FIGURE 5.11: Integrated event plane elliptic flow of charged hadrons at midrapidity ($|y| < 0.5$) depending on the parameterization strategy (top) and values of the net baryon number density dependence (bottom), for ϵ_{switch} set to 0.1 GeV/fm^3 (left) and set to 0.5 GeV/fm^3 (right).

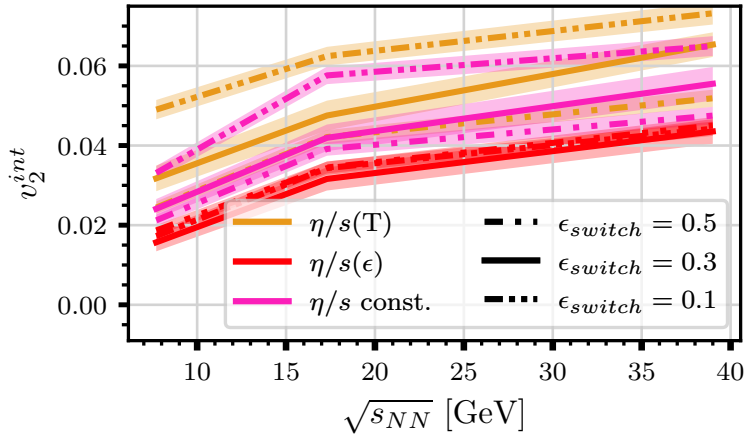


FIGURE 5.12: Integrated event plane elliptic flow of charged hadrons at midrapidity ($|y| < 0.5$) for different parameterization strategies and values of ϵ_{switch} .

Based on these observations, fig. 5.11 compares the integrated charged-hadron elliptic flow at two different particlization energy densities, $\epsilon_{\text{switch}} = 0.5 \text{ GeV/fm}^3$ and 0.1 GeV/fm^3 . These results should be viewed alongside fig. 5.8. Notably, the influence of S_p remains essentially the same irrespective of ϵ_{switch} . By contrast, both the temperature-dependent $\eta/s(T)$ and constant η/s scenarios exhibit substantial changes when ϵ_{switch} is varied, whereas $\eta/s(\epsilon)$ does not show a similar level of sensitivity.

This observation is even clearer in fig. 5.12, where we plot the integrated charged-hadron elliptic flow for all three investigated values of ϵ_{switch} , comparing the default constant- η/s scenario to both $\eta/s(T)$ and $\eta/s(\epsilon)$. We see that the curves for constant η/s and $\eta/s(T)$ vary substantially with different ϵ_{switch} . As ϵ_{switch} decreases, the flow grows significantly. In contrast, for $\eta/s(\epsilon)$, all curves nearly coincide, indicating that in this range of ϵ_{switch} , the integrated elliptic flow remains unaffected by changes in the particlization energy density.

Because elliptic flow is highly sensitive to the shear viscosity, raising ϵ_{switch} transfers part of the late-time evolution from the hydrodynamic phase (where η/s is prescribed) to the hadronic-transport phase (where η/s is not directly controlled). Consequently, the fact that $\eta/s(\epsilon)$ yields an invariant flow across a range of ϵ_{switch} values strongly suggests that $\eta/s(\epsilon)$ closely approximates the effective shear viscosity in the non-equilibrium hadronic transport. Put differently, the insensitivity of the final flow to ϵ_{switch} indicates that the viscous hydrodynamic and transport descriptions are largely equivalent in this segment of the phase diagram.

5.1.3 Discussion

Our qualitative analysis shows that although the net baryon number density dependence of η/s has little impact on the elliptic flow (largely because its influence occurs during the early stages of the hydrodynamic evolution), it does substantially affect the particle yield and mean transverse momentum. Relative to the other parameterizations considered, the chosen constraints for $\eta/s(\epsilon)$ allow for a good description of the proton midrapidity yield and $\langle p_T \rangle$, but it underestimates the elliptic flow. The effect of baryochemical potential on

the shear viscosity and its observables is therefore for anisotropic flow mainly relevant due to its contribution to the energy density, whereas other observables are more sensitive to n_B .

We further observe that, depending on the particlization energy density ϵ_{switch} , a significant fraction of the final state elliptic flow can be generated in the hadronic rescattering phase. While constant or temperature-dependent η/s shows a clear sensitivity to the particlization energy density, $\eta/s(\epsilon)$ remains almost unaffected by this choice. This indicates that the energy-density-based parameterization effectively reproduces the shear viscosity in a non-equilibrium hadronic transport regime over the range $\epsilon = 0.1\text{--}0.5 \text{ GeV/fm}^3$ of the particlization energy density. This approach offers a novel way to study viscosity in out-of-equilibrium conditions, complementing the usual box-based Green–Kubo method for hadronic transport [267]. Next to a direct calculation from transport, the viscosity could be along these lines studied by minimizing the effects of switching from hydrodynamics to transport at different points.

Moreover, our findings suggest that an (implicit) dependence on the baryochemical potential can reduce the influence of purely technical parameters (such as ϵ_{switch}) in hybrid approaches, potentially increasing their consistency and reliability.

However, this study remains limited in scope. Besides its qualitative focus and restricted set of observables, we have neglected bulk viscosity, which can significantly impact observables. Since bulk viscosity is expected to peak near the phase transition, an energy-density-based parameterization thereof also warrants exploration. In addition, the modifications introduced by non-constant viscosities alter the fireball evolution, affecting the effective shear viscosity. As an example, larger bulk viscosity slows down the medium’s expansion, raising the average energy density and thus lowering the effective shear viscosity.

Lastly, the collision energies investigated here extend only up to $\sqrt{s_{\text{NN}}} = 39 \text{ GeV}$ to ensure a sufficiently high μ_B . Although the difference in the effective shear viscosity from a non-zero S_ρ diminishes with rising collision energy, notable changes in the midrapidity yield and $\langle p_T \rangle$ persist due to longer fireball lifetimes. Including higher beam energies may therefore be a promising avenue for future studies. Increased statistics would also allow access to higher-order flow observables such as v_3 , known for its heightened sensitivity to η/s .

In light of these insights, we now move toward a more systematic and quantitative Bayesian Inference approach. The next section introduces this method, outlines widely used inference algorithms, and presents the state-of-the-art algorithms employed in the present work.

5.2 Bayesian Inference

One of the core problems of phenomenological modeling is the correct choice of parameters. As we have only limited access to first principle predictions, there is an inherent uncertainty in our models, which is represented by parameters. Just as we do not have exact knowledge about the correct values for the shear viscosity in the last section and incorporated lack of constraints in different possible values for S_ρ , it is our intention to fit all model parameters which we can not determine from physical grounds alone. This is performed by comparison with experimental data. However, observables in experiments

are not known exactly, but with a limited precision. The same is true for predictions from theoretical models. Hence, we must derive insights by comparing model predictions (with their inherent uncertainties) against experimental data (with its own uncertainties), all while incorporating theoretical constraints that also carry uncertainties. This can be achieved by applying Statistical Inference.

5.2.1 Statistical Inference

Statistical Inference is a cornerstone of modern data analysis, enabling researchers and practitioners to draw conclusions about a population based on a representative sample. "Population" refers to the complete set of possible outcomes, whereas "sample" is a finite set of observations obtained from experiments or simulations. This field provides the theoretical and practical foundation for making decisions and predictions under uncertainty [413].

Statistical Inference as a field can be divided along different paradigms, although often, different methods from different paradigms are combined. In this thesis, we encounter two schools of Statistical Inference. The first is the frequentist approach. It interprets probability as the long-run frequency of events. From this perspective, parameters are fixed and the data is drawn randomly. Typical tools of frequentist inference are confidence intervals, and the concept of p-value, as we have seen before. Usually, one decides on a certain measure for coming to a conclusion before the experiment is conducted. An example encountered earlier is the rule of having a p-value of less than 0.05 in order to assume statistical significance.

The Bayesian approach differs notably. Here, beliefs are encoded in probabilities. As a result, they are positive, integrate into one and obey the probability axioms. This concept of belief as probability allows to define beliefs before taking into account data, and after seeing the data—these are represented by prior and posterior probability distributions. The option to include prior knowledge comes at the cost of the necessity to investigate a wide parameter space to construct meaningful distributions.

5.2.2 Bayesian Model Calibration

Bayesian model calibration is performed by choosing a model which has an associated set of hypotheses, which is a vector of parameters $\theta = (\theta_1, \dots, \theta_m)$. They will govern the simulation. Depending on the field, they can be for example the mutation rate in the genome of bacteria, the correlation between income and political views or, in our case, the parameters of our hybrid approach. These parameters are not drawn randomly, but within theoretical constraints, the prior, which we will discuss later on. A central objective of Bayesian calibration is to systematically incorporate uncertainty when fitting theoretical models to data. The model maps θ to an output vector $\mathbf{y}_{\text{sim}} \in \mathbb{R}^d$. Comparing this simulation result to experimental data $\mathbf{y}_{\text{exp}} \in \mathbb{R}^d$ can be formalized by a statistical model:

$$\mathbf{y}_{\text{exp}} = \mathbf{y}_{\text{sim}}(\theta) + \epsilon, \quad (5.2)$$

where the residual ϵ typically follows a multivariate normal (MVN) distribution with zero mean and covariance matrix Σ .

The Bayesian formulation interprets probability as a degree of belief informed by observed data as well as prior knowledge [414]. According to Bayes' theorem, the posterior distribution of parameters, $\mathcal{P}(\boldsymbol{\theta} | \mathbf{y}_{\text{exp}})$, is given by

$$\mathcal{P}(\boldsymbol{\theta} | \mathbf{y}_{\text{exp}}) = \frac{\mathcal{P}(\mathbf{y}_{\text{exp}} | \boldsymbol{\theta}) \mathcal{P}(\boldsymbol{\theta})}{\mathcal{P}(\mathbf{y}_{\text{exp}})}, \quad (5.3)$$

where $\mathcal{P}(\mathbf{y}_{\text{exp}} | \boldsymbol{\theta})$ is the likelihood function of observing \mathbf{y}_{exp} with a given parameter set, $\mathcal{P}(\boldsymbol{\theta})$ is the prior, and $\mathcal{P}(\mathbf{y}_{\text{exp}})$ is the evidence (a normalization constant). Note the Bayesian paradigm incorporated here: our prior knowledge of the system is a probability distribution over the parameter space. In reality, our parameters describe not the whole system. Simulations usually incorporate fluctuations, and detectors are imperfect, hampering the comparison between model and experiment. These factors can be incorporated into nuisance parameters $\boldsymbol{\psi}$. This nuisance has to be integrated out in order to construct our posterior, leading to

$$\mathcal{P}(\boldsymbol{\theta} | \mathbf{y}_{\text{exp}}) \propto \int \mathcal{P}(\mathbf{y}_{\text{exp}} | (\boldsymbol{\theta}, \boldsymbol{\psi})) \mathcal{P}(\boldsymbol{\theta}, \boldsymbol{\psi}) d\boldsymbol{\psi}. \quad (5.4)$$

Commonly, one assumes a multivariate normal distribution in order to describe the likelihood function. Then, the likelihood that the observed data can be produced by a model with a given parameter set takes the form

$$\mathcal{P}(\mathbf{y}_{\text{exp}} | \boldsymbol{\theta}) = \frac{1}{\sqrt{|2\pi\Sigma|}} \exp\left[-\frac{1}{2}(\mathbf{y}_{\text{sim}}(\boldsymbol{\theta}) - \mathbf{y}_{\text{exp}})^T \Sigma^{-1} (\mathbf{y}_{\text{sim}}(\boldsymbol{\theta}) - \mathbf{y}_{\text{exp}})\right]. \quad (5.5)$$

In most practical scenarios, the posterior distribution in eq. (5.3) lacks a closed-form solution. Markov Chain Monte Carlo (MCMC) algorithms, which will be discussed later, then become the primary tool for traversing the parameter space and approximating the posterior. However, they require repeatedly evaluating $\mathbf{y}_{\text{sim}}(\boldsymbol{\theta})$ for numerous proposed $\boldsymbol{\theta}$. This can be computationally untenable when the simulations require extensive run times. As an example, evaluating a 3D hybrid approach at a single parameter point over sufficient events in order to produce predictions with a comparable precision as experiments can take thousands of CPU hours.

To mitigate this issue, surrogate models (or emulators) approximate $\mathbf{y}_{\text{sim}}(\boldsymbol{\theta})$ with significantly lower computational cost. A Gaussian Process (GP) emulator [415–417], for instance, is trained on a finite set of parameter configurations and their corresponding simulation outputs. Once trained, the GP predictor yields a mean $\boldsymbol{\mu}(\boldsymbol{\theta})$ and a covariance $\mathbf{C}(\boldsymbol{\theta})$ that characterize the emulator's estimate of $\mathbf{y}_{\text{sim}}(\boldsymbol{\theta})$. If we then denote the total uncertainty by $\mathbf{V}(\boldsymbol{\theta}) = \mathbf{C}(\boldsymbol{\theta}) + \Sigma$, we can write an approximate likelihood:

$$\mathcal{P}_{\text{approx}}(\mathbf{y}_{\text{exp}} | \boldsymbol{\theta}) = \frac{1}{\sqrt{|2\pi\mathbf{V}(\boldsymbol{\theta})|}} \exp\left[-\frac{1}{2}(\boldsymbol{\mu}(\boldsymbol{\theta}) - \mathbf{y}_{\text{exp}})^T \mathbf{V}(\boldsymbol{\theta})^{-1} (\boldsymbol{\mu}(\boldsymbol{\theta}) - \mathbf{y}_{\text{exp}})\right]. \quad (5.6)$$

Replacing the exact likelihood with $\mathcal{P}_{\text{approx}}$ reduces the computational load during MCMC and makes Bayesian calibration feasible for high-dimensional, multi-stage event simulations.

5.2.3 Gaussian Process Emulation

At this point, a few details will be given on the construction of surrogate models using GPs. Although using such emulators greatly improves performance when performing the MCMC, training them to represent true model predictions results in a trade-off between precision and speed. The more training data one uses, the better the surrogate but also the higher the computation time. It is therefore crucial to employ emulation algorithms which represent the model as faithfully as possible, in order to reduce the cost of exploring the parameter space while maintaining acceptable accuracy in predictions.

A significant challenge is posed by the high-dimensionality of the model output. Often, the information can be condensed to a lower-dimensional space, greatly decreasing noise in the data. A common strategy for handling this involves applying Principal Component Analysis (PCA) to project the full set of observables onto a lower-dimensional space [418]. More concretely, suppose each training parameter configuration θ_i^{tr} produces an averaged simulation output vector $\tilde{\mathbf{y}}_{\text{sim}}(\theta_i^{\text{tr}})$ of dimension d . In a first step, the data is standardized, that means, centered around zero and rescaled to give a variance of 1. Then, the vectors are arranged into a $d \times n$ data matrix, with n the number of sampled parameter points. PCA yields a reduced set of p principal components (with $p \ll d$) that capture the bulk of the output variance [419–422]. Each principal component is then independently emulated by a GP, preserving flexible, nonparametric modeling for each reduced-dimensional coordinate.

Specifically, let $\mathbf{S} \in \mathbb{R}^{d \times p}$ be the PCA transformation matrix. For each principal component $t_l(\theta) = \mathbf{s}_l^T \tilde{\mathbf{y}}_{\text{sim}}(\theta)$, where $\tilde{\mathbf{y}}_{\text{sim}}$ is the standardized output, a GP model provides a predictive mean $m_l(\theta)$ and variance $s_l^2(\theta)$. In other words, each principle component is drawn from a Gaussian distribution with mean $m_l(\theta)$ and standard deviation $s_l^2(\theta)$, where $m_l(\theta) = \mathbf{k}_l^T \mathbf{K}_l^{-1} \mathbf{t}_l$ and $s_l^2(\theta) = k_l(\theta, \theta) - \mathbf{k}_l^T(\theta) \mathbf{K}_l^{-1} \mathbf{k}_l(\theta)$. Here, $\mathbf{k}_l(\theta) = [k_l(\theta, \theta_i^{\text{tr}})]_{i=1}^n$ denotes the covariance vector between n training parameters $\{\theta_1^{\text{tr}}, \dots, \theta_n^{\text{tr}}\}$ and any chosen parameter θ , and $\mathbf{K}_l = [k_l(\theta_i^{\text{tr}}, \theta_j^{\text{tr}}) + \delta_{i,j} r_{l,i}]_{i,j=1}^n$ represents the covariance matrix between the n training parameters. The covariance function $k_l(\theta, \theta')$ depends on the choice of the kernel function in the GP. The choice of covariance kernel (e.g., Matérn or Radial Basis Function) plays a key role in capturing correlations between distinct regions of the parameter space.

The emulators used in this work follow the PCGP (Principal Component Gaussian Process) and PCSK (Principal Component Stochastic Kriging) prescription [423], provided by the BAND collaboration's `surmise` package [424]. They both use the above described PCA-decomposition and the Matérn kernel. However, the core difference is the Kronecker delta in the definition of \mathbf{K}_l . $r_{l,i}$ is the square of the statistical uncertainty of the l -th principal component at the training point i . Including this term does not only account the mean of the model predictions in the emulation, but also its uncertainty. Within each reduced dimension, the covariance matrix \mathbf{K} of training outputs captures smooth variations in parameter space, while additional diagonal terms model the statistical uncertainties from event-by-event fluctuations.

The Gaussian emulator fitting has to find hyperparameters such that $k_l(\theta, \theta')$ optimizes the emulation. One common way to achieve this is to minimize the difference between the probability distribution realized by each t_l and by a multivariate normal distribution

centered at zero with variance K_l . This can be performed by maximising the log-likelihood of

$$-\frac{1}{2}(\mathbf{t}_l^T \mathbf{K}_l^{-1} \mathbf{t}_l) - \frac{1}{2} \log(|\mathbf{K}_l|) - \frac{n}{2} \log(2\pi). \quad (5.7)$$

Once the GP models are trained, their predictions are mapped back to the original d -dimensional observable space via the inverse PCA transformation.

5.2.4 Classical and Neural-Network-Powered Posterior Generation

Equation (5.3) is in practically all relevant cases analytically untrackable. However, thanks to steadily increasing computational power, this is no major obstacle. Markov Chain Monte Carlo (MCMC) techniques aim at constructing a sequence of points in parameter space whose density emulates the density of the posterior probability distribution function. This chain is a Markov chain, which is a sequence of random variables such that the probability of the $(t+1)$ -th element in the chain only depends on the directly preceding element, and that it converges to a stationary state, in the sense that from a certain t on, the samples are from the target distribution. This target distribution is in our case $\mathcal{P}(\mathbf{y}_{\text{exp}} | \boldsymbol{\theta})$ [425–427].

5.2.4.1 Traditional MCMC Algorithms

There are several implementations of MCMC algorithms. We want to outline some of the most used algorithms for MCMC in the field of heavy-ion physics.

THE METROPOLIS-HASTINGS ALGORITHM The Metropolis-Hastings algorithm [428, 429] is one of the earliest MCMC algorithms and operates as follows:

1. Initialize the Markov chain with a starting value $\boldsymbol{\theta}_0$.
2. For each iteration t , given the current state $\boldsymbol{\theta}_t$:
 - a) Propose a new state $\boldsymbol{\theta}'$ from a proposal distribution $q(\boldsymbol{\theta}' | \boldsymbol{\theta}_t)$.
 - b) Compute the acceptance probability
$$\alpha = \min \left(1, \frac{\mathcal{P}(\mathbf{y}_{\text{exp}} | \boldsymbol{\theta}') q(\boldsymbol{\theta}_t | \boldsymbol{\theta}')}{\mathcal{P}(\mathbf{y}_{\text{exp}} | \boldsymbol{\theta}_t) q(\boldsymbol{\theta}' | \boldsymbol{\theta}_t)} \right). \quad (5.8)$$
 - c) Accept the proposed state with probability α , setting $\boldsymbol{\theta}_{t+1} = \boldsymbol{\theta}'$. Otherwise, retain the current state, $\boldsymbol{\theta}_{t+1} = \boldsymbol{\theta}_t$.
3. Repetition of step 2 for a large number of iterations to generate samples.

The proposal distribution $q(\boldsymbol{\theta}' | \boldsymbol{\theta}_t)$ is a key component of the algorithm. It determines how candidate states are generated and can significantly impact the efficiency of the sampling process. Common choices include symmetric distributions, such as a Gaussian centered at $\boldsymbol{\theta}_t$, where the ratio $q(\boldsymbol{\theta}_t | \boldsymbol{\theta}')/q(\boldsymbol{\theta}' | \boldsymbol{\theta}_t)$ simplifies to 1.

AFFINE-INVARIANT ENSEMBLE SAMPLERS In an N -dimensional parameter space, standard Metropolis–Hastings MCMC can be inefficient if the posterior exhibits strong covariances or anisotropies [430–432]. To mitigate this, [433] introduced the affine-invariant ensemble sampler, which has proved very effective in practice. Its defining property is that it performs equally well under any linear (affine) transformation of the parameter space. At each step, the position of a particular walker θ_k is updated by choosing another walker θ_j (with $j \neq k$) from the ensemble and drawing a scalar z from a proposal distribution $g(z)$ satisfying $g(z) \propto z^{-1}$ on an interval $[1/a, a]$. The new position \mathbf{Y} of walker k is

$$\mathbf{Y} = \theta_k + z [\theta_k - \theta_j]. \quad (5.9)$$

In this way, the direction and scale of the update are informed by the separation between θ_k and θ_j , making the sampler invariant to affine transformations. One accepts this proposed move with the same method as for Metropolis–Hastings. An efficient implementation of this algorithm was provided with the emcee package, which is widely used for Bayesian Inference [434].

PARALLEL TEMPERING MCMC When a posterior density is strongly multimodal or exhibits numerous local maxima, MCMC chains may stick in sub-dominant modes. This cannot be mitigated by affine transformations alone. A powerful strategy to overcome such modes is parallel tempering (also known as replica exchange MCMC) [431, 435, 436]. One introduces a ladder of N_β parallel chains $\{\theta^{(i)}\}$, each targeting a tempered density:

$$p_i(\theta) \propto [p(\theta)]^{\beta_i}, \quad (5.10)$$

where $0 < \beta_1 < \beta_2 < \dots < \beta_{N_\beta} = 1$. For small β_i , the chain explores a flatter version of the posterior, enabling large jumps that more easily escape local maxima. This can be intuitively seen as multiple gases with different temperatures. In hot gases, the particles rapidly fluctuate through space, whereas in cool ones, the particles are slower and become more and more localized. Periodically, one attempts to swap the states $\theta^{(i)}$ and $\theta^{(i+1)}$ of adjacent temperatures i and $i+1$ with probability

$$r = \min\left[1, \frac{p_i(\theta^{(i+1)}) p_{i+1}(\theta^{(i)})}{p_i(\theta^{(i)}) p_{i+1}(\theta^{(i+1)})}\right]. \quad (5.11)$$

After sufficient mixing, the coldest chain ($\beta_{N_\beta} = 1$) samples from the true posterior, but has benefited from global exploration by the hotter chains. Parallel tempering thus greatly reduces the risk of getting stuck in local modes.

5.2.4.2 *Neurally Preconditioned MCMC*

If the posterior is even more multimodal or faces complex structures in its multidimensional space, even parallel tempering can fail. State-of-the-art approaches to mitigate this involves preconditioning. In general, preconditioning involves defining a variable transformation which maps arbitrarily complex probability distributions isomorphically to simpler ones. An especially successful approach for this is realized by normalizing flows. Normalizing flows are a neural-network-powered approach capable of learning complex distributions [437–442]. They achieve this by generating complex probability

distribution functions from simpler ones using parametric changes of variables that can be learned to approximate a target distribution. Their crucial advantage is that normalizing flows are diffeomorphisms: invertible, (nearly-everywhere) differentiable mappings with a differentiable inverse.

Indeed, if $u \sim p(u)$, then $T(u) = x \sim q(x)$ where

$$q(x = T(u)) = p(u) |J_T(u)|^{-1}, \quad (5.12)$$

where J_T is the Jacobian determinant of T :

$$J_T(u) = \det \frac{\partial T_i}{\partial u_j}(u). \quad (5.13)$$

In machine learning, the transformation T is referred to as a normalizing flow, commonly chosen from a parametric family of diffeomorphisms $\{T(\cdot, \theta)\}$ for which gradients $\nabla_\theta J_T$ are tractable to compute.

Coupling cell mappings offer a suitable implementation of this idea [443–445]: they are bijections parameterized by neural networks, and their Jacobian factors can be derived in closed-form without requiring backpropagation or computationally intensive determinant evaluations.

Coupling cells use a neural network (NN) not to learn probability distributions directly—this is challenging due to tails—but to learn parameters of the normalizing flows. This element was developed for the NICE (Non-linear independent component analysis) algorithm [443, 444]. A coupling cell takes the incoming vector x and splits it in two parts, x^A and x^B . This process is referred to as masking. A and B mark a collection of indices a and b . The coupling cell defines a mapping; for the first set of indices, this is the identity: $x^A = y^A$. The vector y^B will be defined as the output of a set of separable, invertible functions $C^b(v^b, x^b)$, one per element of x^B . These v^b are crucial: They are determined by the NN m , which takes x^A as input data. The NN tries to learn the probability density of x^b depending on the values of x^A , but without any knowledge of the other values in x^B . Multiple coupling cells which transform different dimensions form together a coupling layer. This process is also drawn schematically in fig. 5.13. As mentioned, we desire to have an invertible transformation. Therefore, we demand that the coupling transform C is an invertible map. This gives:

$$\begin{aligned} y^A &= x^A \\ y^{b_1} &= C^{b_1}(m(x^A), x^{b_1}) \\ &\vdots \\ y^{|B|} &= C^{|B|}(m(x^A), x^{|B|}) \end{aligned} \quad (5.14)$$

and its inverse

$$\begin{aligned} x^A &= y^A \\ x^B &= C^B -1(m(y^A), y^B). \end{aligned} \quad (5.15)$$

Naively, this can result in a slowdown—as a part of the data is not mapped, it will be necessary to use multiple coupling layers and train multiple instances of the neural

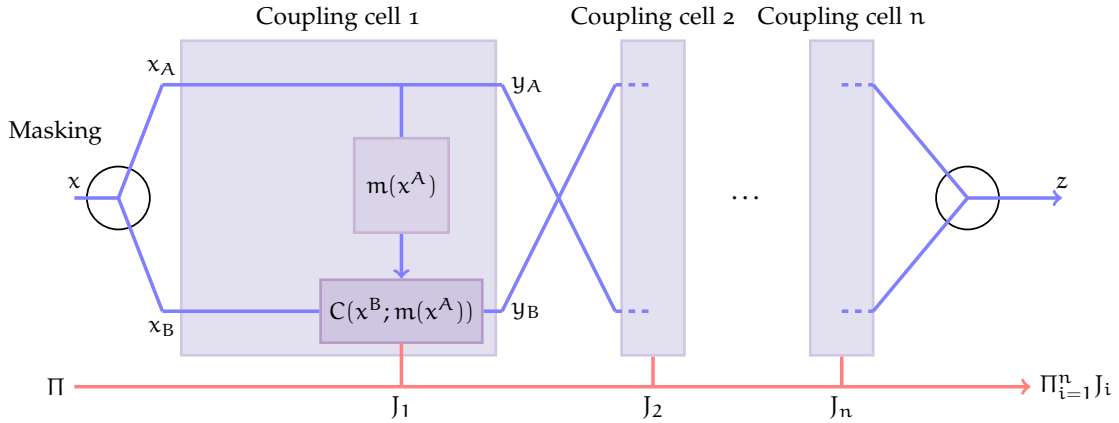


FIGURE 5.13: Schematic structure of a coupling layer. From [446].

network. However, this comes with a great advantage: The Jacobian of the coupling layer has an especially simple structure:

$$\begin{pmatrix} 1 & 0 & & & \\ & \ddots & & & \\ 0 & 1 & & & \\ \hline & \frac{\partial C^{b_1}(\mathbf{v}^{b_1}, x^{b_1})}{\partial x^{b_1}} & & & 0 \\ \frac{\partial C^B(\mathbf{v}^B, x^B)}{\partial x^A} & & & \ddots & \\ & 0 & & & \frac{\partial C^{b_B}(\mathbf{v}^{b_B}, x^{b_B})}{\partial x^{b_B}} \end{pmatrix} \quad (5.16)$$

This saves us from determining the complex derivatives of the NN, as they do not contribute to the determinant of the Jacobian:

$$\det J = \prod_{b \in B} \frac{\partial C^b(\mathbf{v}^b, x^b)}{\partial x^b}. \quad (5.17)$$

Therefore, the determinant of the Jacobian of each of the coupling cells is efficient to evaluate and can be passed on to the next coupling cell, in order to generate a Jacobian of the complete transformation. This reduction of the computation cost for the determinant is the key feature of the coupling cells. Without this, the algorithm would be very expensive for high dimensions. Now, it is also possible to include complex coupling transformations and NN without suffering from difficulties during the computation of the Jacobian. Looking at the definition in the last section, we see that each of the C^b together with id^A form a normalizing flow, as they are diffeomorphisms. They can be composed and define the change in the transformation from a uniform one to the desired approximation of f . As we act on a hypercube, the derivatives of C can be seen as probability distributions, whereas C itself is a cumulative probability distribution. The reason for this is that C , in order to be invertible, has to be monotone, which is the property of a cumulative distribution. The distribution itself, as seen earlier, transforms proportional to the Jacobian.

Normalizing flows have been successfully applied for many problems involving probability distributions inside and outside of physics, including importance sampling for cross section calculations [447, 448], jet measurements [449] and image processing [445]. For this work, its application in the MCMC framework pocoMC [450, 451] is relevant.

5.2.4.3 pocoMC: A Python Implementation of Preconditioned MCMC

A practical and efficient realization of the neurally preconditioned MCMC approach is provided by the pocoMC package [450, 451]. This open-source Python code implements the Preconditioned Monte Carlo (PMC) algorithm by integrating normalizing-flow-based transformations and Sequential Monte Carlo (SMC) sampling [442, 444, 452]. Preconditioning means here performing a suitable change of variables in order to provide a more sufficient posterior generation. Generally, this reduces correlations and multimodal features. The PMC method underlying pocoMC proceeds by first training a normalizing flow to learn a diffeomorphic mapping $T : \theta \rightarrow \mathbf{u}$ that reparameterizes the target posterior to a simpler (approximately) uncorrelated distribution in the latent space \mathbf{u} . In this latent space, one can then apply simple MCMC kernels (e.g., Metropolis–Hastings with isotropic Gaussian proposals) to execute the MCMC. The acceptance probability in the original parameter space θ follows

$$\alpha = \min\left[1, \frac{\mathcal{P}(T^{-1}(\mathbf{u}')) q(\mathbf{u}) \left| \det \frac{\partial T^{-1}(\mathbf{u}')}{\partial \mathbf{u}'} \right|}{\mathcal{P}(T^{-1}(\mathbf{u})) q(\mathbf{u}') \left| \det \frac{\partial T^{-1}(\mathbf{u})}{\partial \mathbf{u}} \right|}\right], \quad (5.18)$$

where $q(\cdot)$ is an isotropic proposal density and $\mathcal{P}(\theta) = \mathcal{P}(\mathbf{y}_{\text{exp}} | \theta)$ denotes the unnormalized posterior.

Sequential Monte Carlo (SMC) draws samples from a difficult target distribution by defining a sequence of intermediate densities $p_t(\theta)$ that gradually transition from a simpler distribution (often the prior) to the posterior [425, 427, 452]. A typical construction is temperature annealing:

$$p_t(\theta) = \pi(\theta) \mathcal{P}(\mathbf{y}_{\text{exp}} | \theta)^{\beta_t}, \quad 0 = \beta_1 < \dots < \beta_T = 1, \quad (5.19)$$

where $\pi(\theta)$ is the prior probability distribution. Note that this is different to parallel tempering—whereas for parallel tempering, all chains with different temperatures coexist, here, the temperature iteratively decreases. Starting with $p_1(\theta) = \pi(\theta)$, one proceeds step by step in time (i.e. $t = 1 \rightarrow 2 \rightarrow \dots \rightarrow t_{\text{max}}$) to increment β_t . Each step involves:

1. Updating the importance weights of N particles to reflect the change from $p_{t-1} \rightarrow p_t$.
2. Resampling the particles if needed to eliminate low-weight particles.
3. Performing a short MCMC "mutation" under $p_t(\theta)$ to diversify the particle set.

Eventually at ($t = t_{\text{max}}$), the population approximates the full posterior. Because SMC reweights, resamples, and mutates particles as β_t increases, it can track the target distribution reliably through successive stages. This procedure also delivers an unbiased estimate of the Bayesian evidence, which is a measure (also called the marginal likelihood)

of how well a model explains the observed data, by accumulating the normalizing constant ratios at each stage.

By training T , or in other words, coupling layers, at each stage t of the annealing schedule, pocoMC preconditions the target distribution to reduce non-Gaussian features such as strong covariances or complicated multimodality. With these powerful tools, pocoMC can deal with highly complex multidimensional posteriors.

Additionally, a major practical advantage of pocoMC is the nearly linear speed-up across parallel resources. Since the algorithm allows evaluating the posterior and flow transformations for each of the N ensemble particles independently, typical MPI-based parallelization can scale effectively up to thousands of cores. Thus, for computationally demanding likelihoods in high-dimensional parameter spaces, pocoMC yields significant gains in wall-clock time. Furthermore, in addition to generating posterior samples, pocoMC computes the Bayesian model evidence Z via the SMC weights, allowing users to perform both parameter estimation and model comparison.

The aptitude of pocoMC to deal with complex distributions while being highly parallelisable motivated its use in this work. With all necessary technical components in place, it is time to proceed with presenting the application of Bayesian Inference on SMASH-vHLLE-Hybrid.

5.3 Investigation of Temperature and Baryochemical Potential Dependent Viscosities

The aim is to leverage the power of Bayesian Inference to gain insights from the SMASH-vHLLE-Hybrid approach. On the one hand, we want to refine the existing tuning, which was done in a qualitative way. On the other hand, we want to get quantitative insight into the predictions of the temperature and baryochemical potential dependence predicted by SMASH-vHLLE-Hybrid. In a first step, we want to give a short overview of prior existing research in performing Bayesian Inference for the purpose of gaining insight into viscosities.

5.3.1 Prior Research

This section gives an overview of the past advances in Bayesian Inference for heavy-ion physics. More details can be found in Ref. [453].

5.3.1.1 *Historical Development of Bayesian Inference in Heavy-Ion Physics*

Over the past decade, Bayesian Inference has been increasingly adopted in the heavy-ion community to confront quantitative models of relativistic nucleus–nucleus collisions with an ever-growing body of experimental data. Early precursors of comprehensive Bayesian analyses in this field can be found in Refs. [454–456], which introduced emulators (surrogate models) and Gaussian-process-based uncertainty quantification for relativistic hydrodynamic simulations. These efforts demonstrated the viability of systematically exploring a large parameter space of hydrodynamic and hadronic observables, effectively shifting the computational bottleneck from high-statistics event-by-event simulations to low-cost statistical emulators.

FOUNDATIONAL WORKS. Inspired by the above pioneering efforts, Ref. [457] explored the sensitivity of various heavy-ion observables to the equation of state. Following that, a series of influential studies by the Duke group [309, 310, 349, 458–460] refined these Bayesian methods. They incorporated multi-stage collision models (including initial conditions, relativistic viscous hydrodynamics, hadronic afterburners), performed dimensionality reduction of large experimental data sets, and deployed Gaussian process emulators trained on systematic model calculations with Latin hypercube sampling of the parameter space. This framework eventually became a standard blueprint for contemporary Bayesian studies of quark-gluon plasma (QGP) properties.

TOWARD MULTI-OBSERVABLE CONSTRAINTS. Subsequent investigations expanded the breadth of data sets and models under Bayesian scrutiny. For instance, the JETSCAPE Collaboration studies [53, 54] presented a multi-system and multi-observable framework, simultaneously analyzing soft hadronic observables at RHIC and LHC energies in a Bayesian Inference. Similarly, Refs. [57, 66, 67, 421, 461–464] extended the scope by including sub-nucleonic initial structure, anisotropic hydrodynamics, improved statistical tools, refined treatments of viscous corrections in the Cooper-Frye transition and many other features. Such works emphasize that new stages in the collision model or additional observables can significantly shift the posterior constraints on e.g., the shear and bulk viscosities.

EXTENSION TO 3D AND ADVANCED VISCOSITY INFERENCE. Increased computational budgets greatly improved the quality and complexity of Bayesian Inference. One big step was the extension to 3-dimensional modeling, which requires substantially more computational power but gives access to the full collision dynamics. While earlier 3D studies were very restricted in size of experimental data set and parameter space [331, 465], full studies can now be performed [312, 466–468]. Along similar lines, whereas early studies only included constant specific viscosities or only shear viscosity, parameterizations became increasingly complex. The latest advancement is the inclusion of baryochemical potential dependence in the viscosities [467, 468].

5.3.1.2 *Status of Constraints on Viscosities*

Figure 1.5 shows a selection of existing results from Bayesian Inference and other methods for the temperature dependence of shear and bulk viscosity, and vanishing baryochemical potential, including results from Duke [309], JETSCAPE [53] and Trajectum [469], the viscous blastwave (BW) [470], Chapman-Enskog (Chap-Ensk) method [471], hadron resonance gas (HRG) model with Hagedorn states (HS) [472], FRG [473], lQCD (Lattice1 [333, 474], Lattice2 [475], Lattice3 [334] and Lattice4 [476]), T-matrix [477], and next-to-leading order pQCD [55] for shear viscosity and Duke [309], JETSCAPE [53] and Trajectum [469], lQCD (Lattice1 [478], Lattice3 [479] and Lattice5 [69]), hybrid model (McGill) [323], holographic model (Holo) [480], HRG model with HS [472] and SMASH [70] for bulk viscosity.

For the shear viscosity, there is for many approaches a trend to have a small value near the crossover temperature. There is roughly consistent agreement for increasing shear viscosity for lower temperature. Although many approaches support increasing values

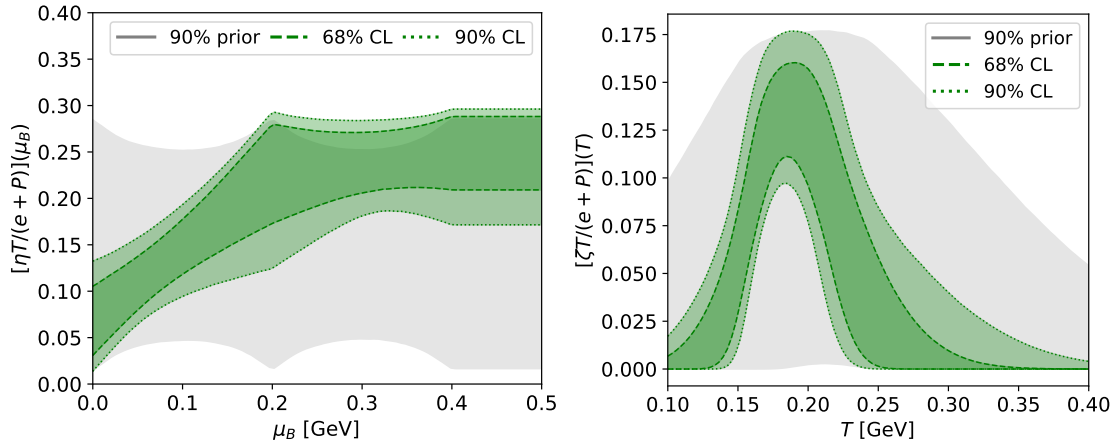


FIGURE 5.14: Posterior for the μ_B -dependence of the shear viscosity and T -dependence of the bulk viscosity from [468].

for high temperatures, some do slightly decrease or have no clear preference due to high uncertainties. For many studies, a constant value of η/s is not ruled out. There are considerably higher disagreements for the bulk viscosity. Lattice data and some hybrid model calculations support substantial peaks in the bulk viscosity, whereas other studies observe rather small values and give no clear preference for a peak.

Recent 3D studies for a wide range of collision energies include also μ_B -dependence of the shear viscosity. In [468], a μ_B -dependence was studied, while the T -dependence was omitted as a constant η/s is in agreement with most studies. As can be seen in fig. 5.14, it was observed that a non-vanishing baryochemical potential dependence is significantly preferred. However, due to the omitted temperature dependence, this could also be attributed to the fact that collisions at low energies realize both on average lower temperatures and higher baryochemical potentials, and lower temperatures are associated with higher shear viscosity in many predictions. The same study also investigated bulk viscosity, albeit without baryochemical potential, and observed a significant peak around the transition temperature.

With this overview of existing works, the setup of the present study is introduced now.

5.3.2 Choice of Viscosity Parameterizations

The choice of parameterizations is one of the core design choices of a Bayesian Analysis, and is due to this the starting point for our study. Although with the right parameter ranges, many different parameterizations can cover the same values of the viscosities (referring to the same region covered by the confidence intervals in the earlier figures), the inherent functional form results in different evolution trajectories. Therefore, we want to choose a plausible structure of the dependency. On the other hand, we have to minimize the number of parameters as an increasing parameter space weakens the predictive strength.

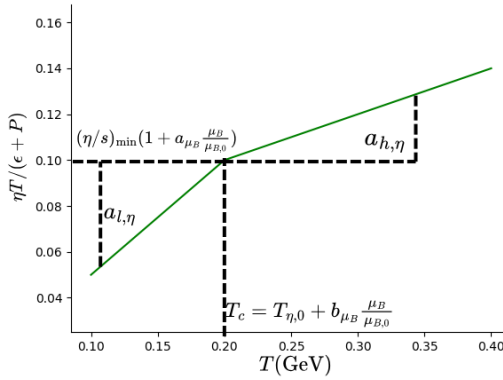


FIGURE 5.15: Illustration of the shear viscosity parameterization.

5.3.2.1 Shear Viscosity

In this project, we want to not only restrict ourselves to a pure temperature or pure baryochemical potential dependence. Instead, we want to investigate both. This is due to the fact that as all but systems at very high collision energies are subject to effects of both. We choose the following parameterization:

$$\frac{\eta T}{\epsilon + P} = \max \left(0, (\eta/s)_{\text{kink}} + \begin{cases} a_{l,\eta}(T - T_c) & T < T_c, \\ a_{h,\eta}(T - T_c) & T > T_c \end{cases} \right) \times \left(1 + a_{\mu_B} \frac{\mu_B}{\mu_{B,0}} \right), \quad (5.20)$$

$$T_c = T_{\eta,0} + b_{\mu_B} \frac{\mu_B}{\mu_{B,0}}. \quad (5.21)$$

The parameters are illustrated in fig. 5.15. The parameter $(\eta/s)_{\text{min}}$ sets the shear viscosity at T_c for $\mu_B = 0$, with $a_{l,\eta}$ and $a_{h,\eta}$ controlling the slopes in the low- and high-temperature regions, respectively. This mirrors the common piecewise-linear structure for the temperature in many studies. The critical temperature T_c varies however with μ_B , governed by $T_{\eta,0}$ and b_{μ_B} . The overall viscosity is scaled by a_{μ_B} to reflect μ_B -dependent effects not just for the position of the kink, but also for the value itself.

This flexible structure accommodates a temperature dependence consistent with earlier studies [53, 54], while explicitly incorporating μ_B effects. Here, a temperature and baryochemical potential dependence was chosen instead of the energy density to allow for better comparisons with earlier studies. We allow for an explicit temperature dependence, greatly increasing the flexibility with respect to [467, 468] which featured no explicit temperature dependence. This allows us to test whether earlier agreements with constant, temperature independent shear viscosity holds in our model as well [54], and if we indeed find substantial baryochemical potential dependence in the presence of temperature dependence.

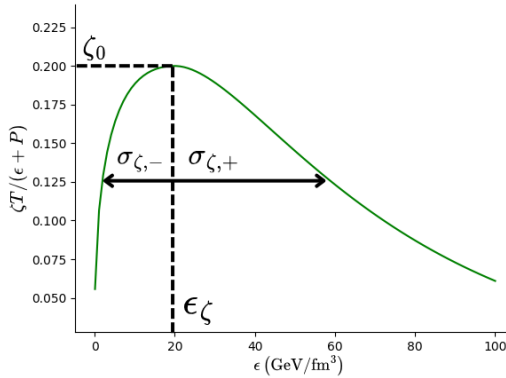


FIGURE 5.16: Illustration of the bulk viscosity parameterization.

5.3.2.2 Bulk Viscosity

In contrast to recent studies [68] we choose one bulk viscosity parameterization for all collision energies. The bulk viscosity parameterization incorporates μ_B implicitly by depending on the energy density ϵ . This approach assumes that the bulk viscosity peak follows a line of constant ϵ , potentially aligning with the QCD phase crossover at finite μ_B . This is a similar line of reasoning as for the shear viscosity earlier in this chapter. Such a simplification of the bulk viscosity reduces the number of parameters to determine, while naturally incorporating a critical peak of the bulk viscosity. The parameterization is:

$$\frac{\zeta T}{\epsilon + P} = \zeta_0 \begin{cases} \exp\left(-\beta \frac{(\epsilon^{1/4} - \epsilon_{\zeta}^{1/4})^2}{2\sigma_{\zeta,-}^2}\right), & \epsilon < \epsilon_{\zeta}, \\ \exp\left(-\beta \frac{(\epsilon^{1/4} - \epsilon_{\zeta}^{1/4})^2}{2\sigma_{\zeta,+}^2}\right), & \epsilon > \epsilon_{\zeta}, \end{cases} \quad (5.22)$$

where ζ_0 controls the peak amplitude, ϵ_{ζ} sets the location of the peak, and $\sigma_{\zeta,-}$ and $\sigma_{\zeta,+}$ define the widths below and above ϵ_{ζ} , respectively. As we want to have a similar shape than a comparable parameterization in the temperature, we take the fourth root of the energy density and scale it by a conversion factor. Figure 5.16 illustrates this parameterization.

5.3.3 Selection of Priors

The correct choice of priors is of crucial relevance when performing a Bayesian Analysis. Indeed, the probability distribution of the posterior is highly dependent on the initial prior beliefs. As demonstrated in [426], the same data and model can lead to strongly diverging results depending on the initial assumptions. Therefore, there is a substantial trade-off—allowing a wide, low informing prior reduces the likelihood of finding a local optimum, whereas a narrow prior gives stronger preference to prior knowledge and increases constraints. As this is a first explorative study of the SMASH-vHLL-E-Hybrid approach, we choose wide priors which constrain only within the boundaries of applicability of the approaches.

For the shear viscosity, the prior ranges in table 5.1 are broad enough to include both μ_B -independent and constant shear viscosities, as well as a wide range of values at all relevant regions of the phase diagram. The KSS-bound [47] of 0.08 is not enforced, allowing the analysis to explore the parameter space freely.

Parameter	Prior Range
$a_{l,\eta}$	[-15, 1]
$a_{h,\eta}$	[-15, 1.75]
T_0	[0.09, 0.25] GeV
$(\eta/s)_{\min}$	[0.001, 0.35]
a_{μ_B}	[-0.8, 7]
b_{μ_B}	[-0.3, 0.8]

TABLE 5.1: Priors for shear viscosity parameters.

In a similar fashion, table 5.2 lists the prior ranges for the bulk viscosity, which allows for vanishing bulk viscosity as well as a pronounced, potentially asymmetric peak in wide ranges of the phase diagram.

Parameter	Prior Range
ζ_0	[0, 0.2]
ϵ_ζ	[0.5, 40] $\frac{\text{GeV}}{\text{fm}^3}$
$\sigma_{\zeta,-}$	[0.005, 0.1]
$\sigma_{\zeta,+}$	[0.01, 0.15]

TABLE 5.2: Priors for bulk viscosity parameters.

Lastly, we also need priors for several technical parameters. They govern the interaction between the initial hadronic transport stage and the subsequent hydrodynamic evolution and were mostly introduced in chapter 2. These include two smearing parameters: R_\perp , for transverse smearing, and R_η , for longitudinal smearing. For the original definition of SMASH-vHLLE-Hybrid, these parameters were energy-dependent to match experimental data. However, in this study, we absorb the collision energy dependence into the temperature and baryochemical potential dependencies of the viscosities. As such, R_\perp and R_η are treated as constants within the range [0.2, 2.2] fm and [0.2, 3.0] fm, respectively. The lower limit reflects finite grid resolution constraints, while the upper limit avoids excessive smoothing, which could erase essential fluctuations.

The initialization time, τ_0 , is chosen proportional to the passing time of the nuclei. We assume that hydrodynamic evolution should begin only after the nuclei have passed to prevent far-from-equilibrium conditions. However, τ_0 must remain significantly shorter than the system's evolution time to capture relevant dynamics. Accordingly, a proportionality factor $\tau_{\text{IC, scale}}$ is selected within the range [0.8, 2.5]. The initial hadronic transport is then performed until a hypersurface of constant eigentime of $\tau_{\text{IC, scale}}$ times the passing time of this collision energy is reached.

The switching or particlization energy density, ϵ_{switch} , marks the transition from hydrodynamics to transport. It must represent a regime where both descriptions are approximately valid—neither too dilute for hydrodynamics nor too dense for transport. This parameter is constrained to $[0.25, 0.75]$ $\frac{\text{GeV}}{\text{fm}^3}$. Furthermore, the impact of late stage rescattering is investigated by scaling the cross-sections in the final state hadronic transport. Table 5.3 summarizes the prior ranges for all technical parameters. Note that we use the convention $c = 1$ here.

Parameter	Prior Range	
R_{\perp}	[0.2, 2.2]	fm
R_{η}	[0.2, 3.0]	fm
$\tau_{\text{IC,scale}}$	[0.8, 2.5]	
ϵ_{switch}	[0.25, 0.75]	$\frac{\text{GeV}}{\text{fm}^3}$
$\sigma_{\text{AB,scale}}$	[0.8, 1.2]	

TABLE 5.3: Priors for technical parameters.

Flat priors are chosen, which means a uniform distribution in parameter space, as none of these values is a priori to be preferred over another. With this broad set of priors, the procedure can find the optimal set of parameters to describe experimental data, at the cost of limiting the constraining power of the Bayesian Inference. The constraining power is however also affected by the set of observables that used for the comparison, which is presented in the following.

5.3.4 Choice of Observables

Table 5.4 summarizes the experimental observables which we use to tune our model. They consist of STAR RHIC BES integrated bulk observables and flows, enriched with $dN/d\eta$ data from PHOBOS at $\sqrt{s_{\text{NN}}} = 200$ GeV. For 19.6 GeV, there is a choice between $dN/d\eta$ data from PHOBOS and STAR, which show substantial differences [481]. We chose the more recent STAR data for our tuning. η -differential data is included until a cutoff of 3 in forward and backwards-rapidity, as uncertainty here is more substantial and we expect our model to perform worse at high rapidities. The total data set size is 168 data points.

For the identified particle observables, we have excluded antiprotons due to the high statistical uncertainties. Additionally, the initialization with hadronic transport leads to excess baryon charge at 200 GeV, due to which we have excluded protons at 200 GeV [482].

The choice of these observables is motivated by the fact that we want to cover a wide range of centralities, which we approximate by restricting ourselves to two distinct centrality classes in order to reduce the amount of data. An exception of this is 200 GeV, where we include a third centrality class in order to add rapidity-dependent data. The choice of three different collision energies is motivated by our aim to cover wide ranges of the phase diagram, both in the cold and dense region and the hot and dilute phase. This way, we aim at constraining the transport coefficients over a wide range of T and μ_B .

$\sqrt{s_{NN}}$	0-5%	15-25%	20-30%
200 GeV	$dN/dy _{y=0}(\pi^{+,-}, K^{+,-})$ [483] $\langle p_T \rangle _{y=0}(\pi^{+,-}, K^{+,-})$ [483] $v_2^{\text{ch}}[2] _{y=0}$ [412], $v_3^{\text{ch}}[2] _{y=0}$ [484] $dN^{\text{ch}}/d\eta$ [486]	$v_2^{\text{ch}}(\eta)$ [485] $dN^{\text{ch}}/d\eta$ [486]	$dN/dy _{y=0}(\pi^{+,-}, K^{+,-})$ [483] $\langle p_T \rangle _{y=0}(\pi^{+,-}, K^{+,-})$ [483] $v_2^{\text{ch}}[2] _{y=0}$ [412] $v_3^{\text{ch}}[2] _{y=0}$ [484]
19.6 GeV	$dN/dy _{y=0}(\pi^{+,-}, K^{+,-}, p)$ [411] $\langle p_T \rangle _{y=0}(\pi^{+,-}, K^{+,-}, p)$ [411] $dN^{\text{ch}}/d\eta$ [481] $v_2^{\text{ch}}[2] _{y=0}$ [412], $v_3^{\text{ch}}[2] _{y=0}$ [484]	-	$dN/dy _{y=0}(\pi^{+,-}, K^{+,-}, p)$ [411] $\langle p_T \rangle _{y=0}(\pi^{+,-}, K^{+,-}, p)$ [411] $dN^{\text{ch}}/d\eta$ [481] $v_2^{\text{ch}}[2] _{y=0}$ [412], $v_3^{\text{ch}}[2] _{y=0}$ [484]
7.7 GeV	$dN/dy _{y=0}(\pi^{+,-}, K^{+,-}, p)$ [411] $\langle p_T \rangle _{y=0}(\pi^{+,-}, K^{+,-}, p)$ [411] $v_2^{\text{ch}}[2] _{y=0}$ [412], $v_3^{\text{ch}}[2] _{y=0}$ [484]	-	$dN/dy _{y=0}(\pi^{+,-}, K^{+,-}, p)$ [411] $\langle p_T \rangle _{y=0}(\pi^{+,-}, K^{+,-}, p)$ [411] $v_2^{\text{ch}}[2] _{y=0}$ [412], $v_3^{\text{ch}}[2] _{y=0}$ [484]

TABLE 5.4: The experimental measurements in Au–Au collisions used in this Bayesian Inference study.

Indeed, fig. 5.17 shows that both values vary strongly between both collision energies shortly after fluidization. Taking into account constraints from multiple energies therefore greatly improves our insights. These systems provide a wide μ_B coverage of mean values of around 0 to 400 MeV at freeze-out [106, 411, 487]. Furthermore, we want to study the core properties of collisions and extend our investigation in the longitudinal direction, which also improves the coverage of the phase diagram, as explained in section 3.2.

The observables are calculated from the event data using SPARKX-2.0.2, as outlined in section 3.4.

5.3.5 Setup

To explore the 14-dimensional parameter space, we employ Latin Hypercube Sampling (LHS), implemented via pyDOE [488, 489] and included in SMASH-vHLLE-Hybrid. This method ensures an efficient and uniform coverage of the prior space. This can be achieved by defining a Latin square in the hyperparameter space, which is a $n \times n$ -array. Latin Hypercube sampling ensures that every row and column has at least one sample, which guarantees high coverage of the parameter space. For random sampling, on the other hand, configurations are possible which exclude subregions of the parameter space. A total of 750 parameter points are sampled, and for each, we generate 250 events per centrality class. We use SMASH-vHLLE-Hybrid in the version 2.0, and SMASH in the version 3.1.

The centrality classes are selected by generating 5000 initial state events, sorting them by energy content, and selecting events accordingly. As we aim for equal statistics for all centrality classes, only half of the events are chosen for the wider classes. The initial events are propagated through all stages of the hybrid approach. We improve statistical accuracy and maintain charge conservation by oversampling, which is performed at different magnitudes depending on the collision energy: 4000, 2000, and 500 events for $\sqrt{s_{NN}} = 7.7, 19.6$, and 200 GeV, respectively.

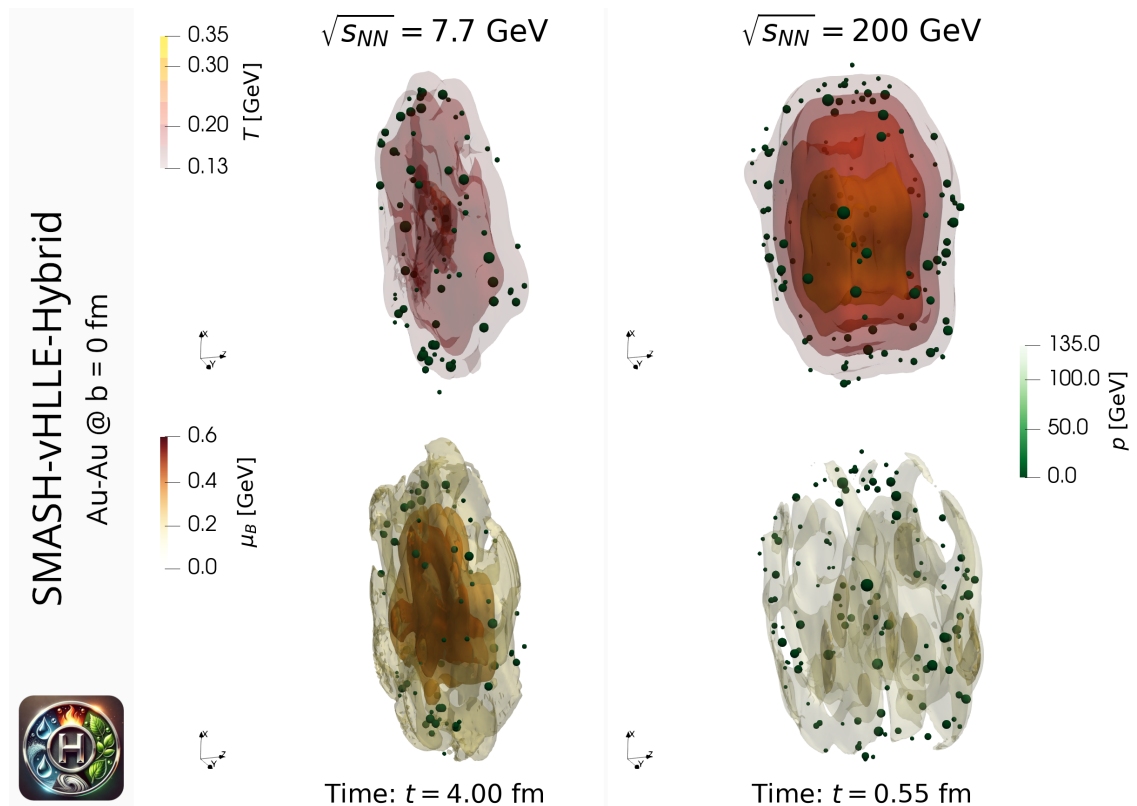


FIGURE 5.17: Temperature (top) and net baryochemical potential (bottom) shortly after fluidization in central Au–Au collisions at $\sqrt{s_{NN}} = 7.7$ GeV (left, fluidization at 3.29 fm) and 200 GeV (right, fluidization at 0.5 fm) [107].

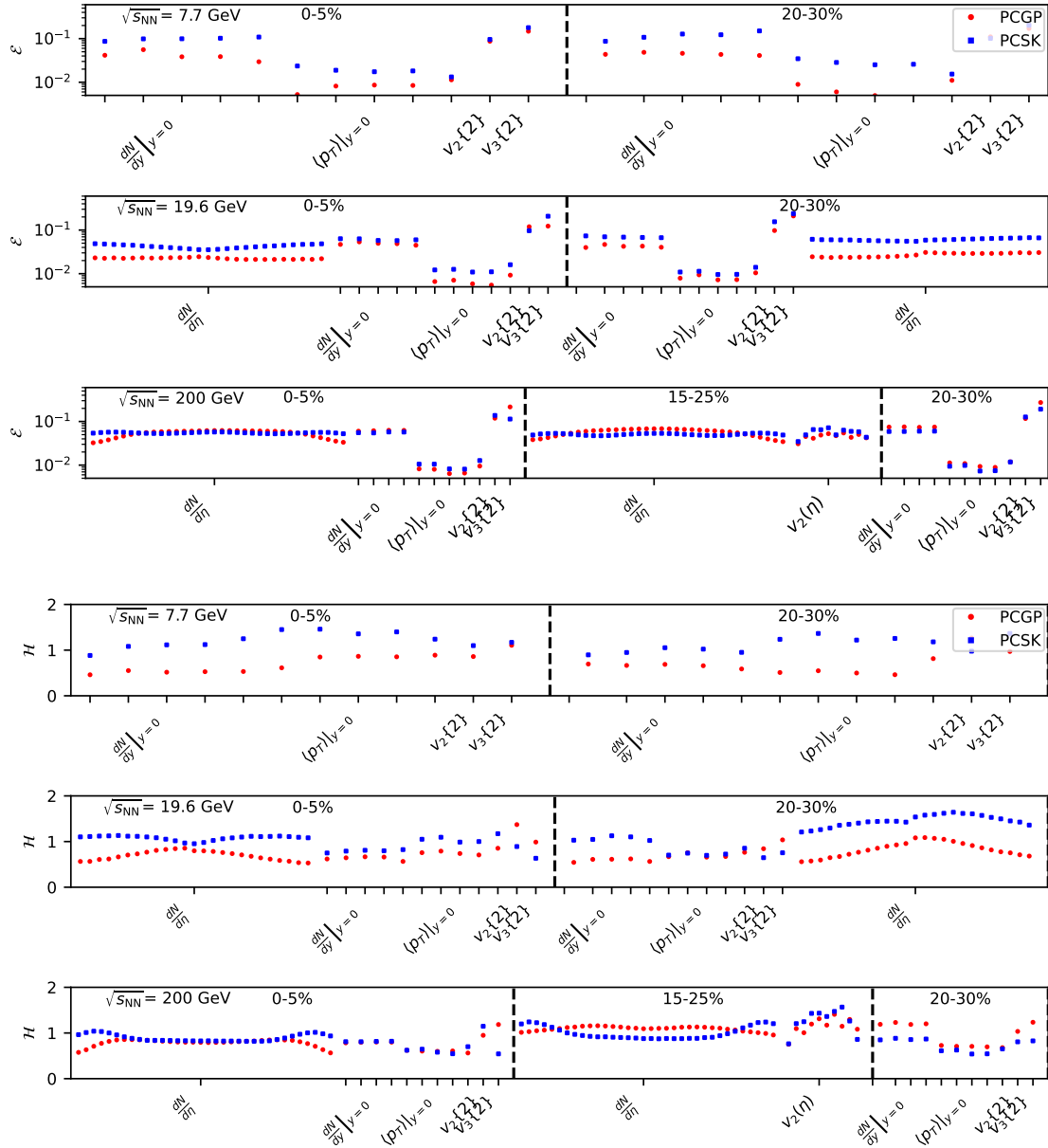


FIGURE 5.18: The averaged root-mean-square error \mathcal{E} (top) and the uncertainty estimation metric \mathcal{H} (bottom) for both emulation strategies for all observables.

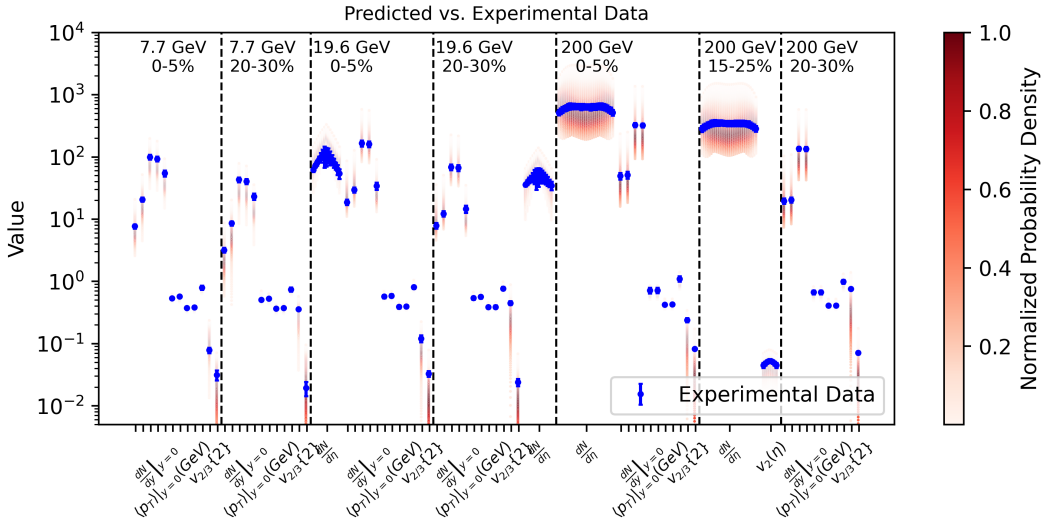


FIGURE 5.19: Probability distribution of the posterior observables for the full prior range, compared to the experimental data points used in this study. For mean transverse momenta, the width of the distribution is comparable to the size of the data markers.

5.3.6 Validation

Validation is a crucial process when performing a Bayesian analysis, as it ensures trustworthy results and spots potential issues in the parameter estimation. Additionally, it helps to determine the confidence in the results we obtain, and gives access to various strategies to improve upon our prediction.

5.3.6.1 Emulator Validation

In a first step, we want to validate our emulation process. This allows us to optimize the emulation strategy on the model at hand. On the other hand, we can also ensure that we have chosen enough parameter sets to efficiently cover the prior. If we were to sample less points from the prior, we would expect to observe substantially lower performing emulators.

We use the test metric for benchmarking proposed in [490] to choose the most accurate Gaussian Process (GP) configuration in our setup. This test metric allows an easy interpretable way to quantify the quality of the emulation. To quantify the prediction error of the GP emulators, one defines

$$\mathcal{E} \equiv \sqrt{\left\langle \left(\frac{\text{prediction} - \text{truth}}{\text{truth}} \right)^2 \right\rangle} \quad (5.23)$$

for each observable in the analysis, whereas the emulator's uncertainty is quantified as

$$\mathcal{H} \equiv \ln \left(\sqrt{\left\langle \left(\frac{\text{prediction} - \text{truth}}{\text{prediction uncertainty}} \right)^2 \right\rangle} \right). \quad (5.24)$$

For an accurate prediction, we expect the values of $\mathcal{E} \rightarrow 0$ and $\mathcal{H} \rightarrow 0$.

In the case where $\mathcal{H} > 0$, the emulator gives uncertainties that are too small compared to the actual error away from the true values; when $\mathcal{H} < 0$, the returned uncertainty estimates are too conservative. To determine prediction and truth, 15 parameter sets were excluded from the training of the GP. Then, the prediction for the value and its uncertainty at the excluded parameter sets are compared to the simulation results at these values. The values of the benchmarking metric for each observable can be found in fig. 5.18. Two prescriptions of GP emulation are presented, which were found in Ref. [490] to perform well: PCGP and PCSK, which were introduced earlier in section 5.2.3. The top three panels show \mathcal{E} , and the bottom three panels show \mathcal{H} . From top to bottom, the energy increases, whereas the centrality decreases from left to right, with centrality classes separated by a dashed vertical line. Each x-tick represents a different observable.

We observe that for both prescriptions, errors remain within acceptable bounds. The biggest deviations occur for the integrated flow, probably due to the higher impact of fluctuations. In comparison to [490], we observe basically no rapidity dependence of the errors. Additionally, for the majority of data points, PCGP outperforms PCSK substantially. A similar picture emerges for the uncertainty metric. It is for most data points considerably closer to zero than for PCSK, and therefore underestimates the uncertainty less. This is remarkable as PCSK takes the standard deviation of the training data into account, whereas PCGP does not. However, such behavior can also be observed for several observables in [490]. Therefore, there is still space for improvement of the uncertainty estimation of the emulators. There are several further preprocessing methods which could affect the quality of emulation: for example, one could logscale the observables to reduce issues of different orders of magnitude, or perform a PCA on the viscosity parameters in order to reduce the parameter space. However, neither could improve the performance in these metrics. Therefore, they were not employed. As PCGP outperforms PCSK in most metrics, we continue using this approach for the rest of this work.

5.3.6.2 *Prior Validation*

A further validation is the consideration if the prior range chosen is sufficient to fit experimental data. Figure 5.19 shows the probability distribution for values of the observables to be fitted to experimental data. In simple words, it shows the likelihood for each observable to be predicted if a random point were to be chosen from prior space. We see that the experimental data points lie all within this range. However, we see that certain experimental data points lie closer to the edges of the range, especially flows at higher collision energies and $\frac{dN}{dn}$ at 19.6 GeV. It is important to note however that this alone does not guarantee that experimental data can be precisely fitted, as not necessarily all data points can be fitted correctly simultaneously. Nevertheless, we can confirm that we have in principle a sufficient range of prior values.

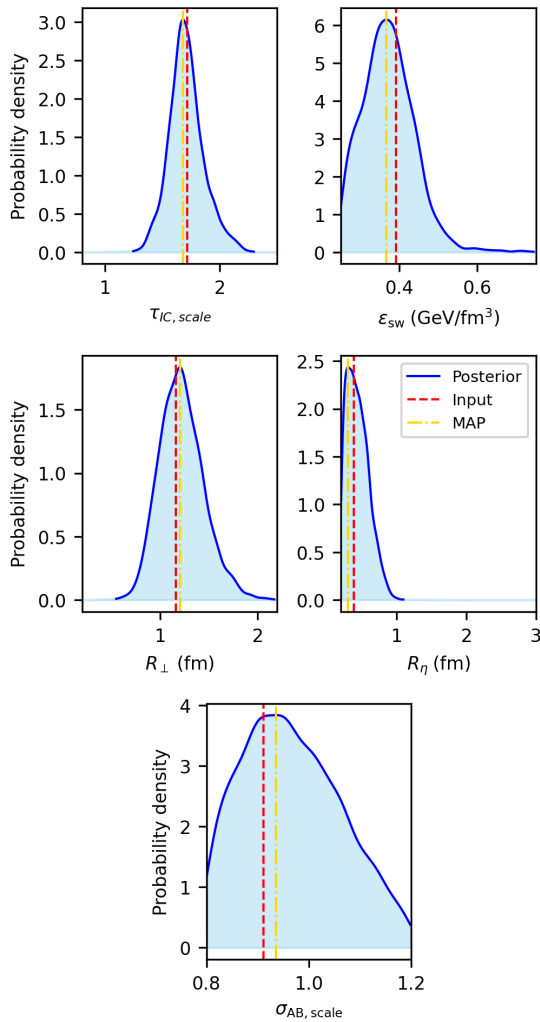


FIGURE 5.20: Posterior of the technical parameters in the closure test. The red vertical line is the value of the parameter generating the pseudo-experimental data, whereas the golden vertical line represents the maximum-a-posteriori value.

5.3.6.3 Closure Test

As a next step, we perform a closure test. Closure tests are crucial in validating that model parameters can be successfully constrained. They can, for example, detect if the number of points in prior space is too low, if data is insensitive to a parameter or if there are degeneracies in a model, allowing disjunct regions of the parameter space to result in the same predictions. Conducting a closure test follows a similar idea than the emulator validation before. Again, one of the training points is separated out. However, this time the predictions of this training point are considered as pseudo-experimental data. Now, the whole tool chain, starting from the Gaussian process emulation and continuing to the construction of the posterior using MCMC, is performed under the assumption of this pseudo-experimental data. In an ideal case, the original input parameters are reproduced, and the peaks of the posterior are close to these values. If the data is sufficient to constrain a parameter well, one expects strongly pronounced peaks.

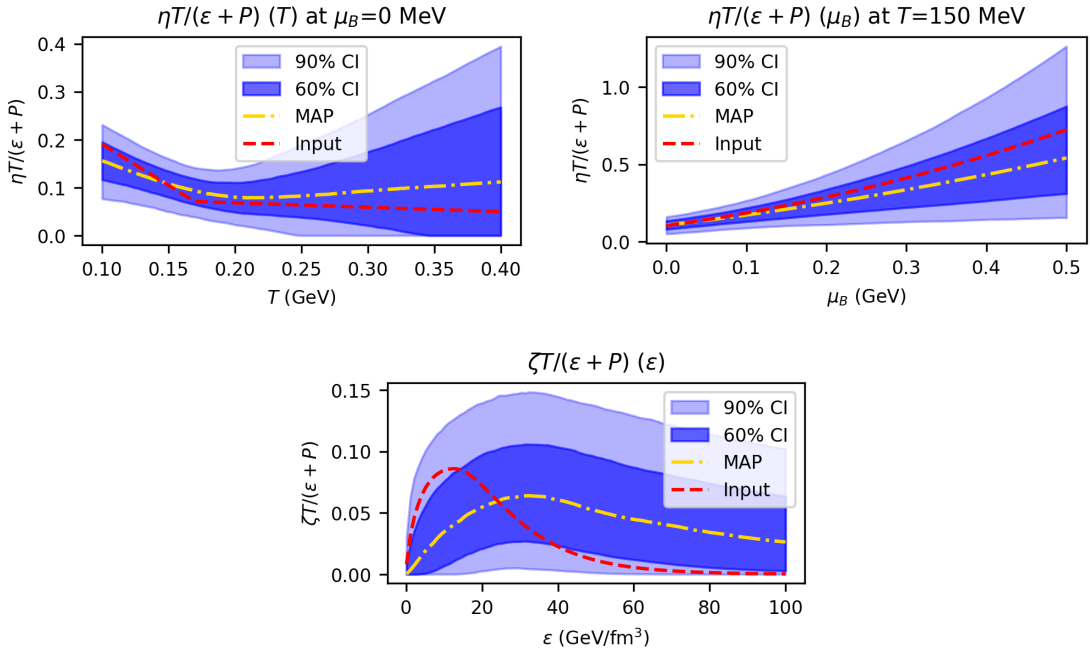


FIGURE 5.21: Posterior of the viscosities in the closure test. From top to bottom: the shear viscosity as a function of temperature for vanishing baryo-chemical potential, the shear viscosity as a function of baryo-chemical potential at fixed temperature, and the bulk viscosity as a function of the energy density. The red line is the input parameterization, and the golden line represents the maximum-a-posteriori. The bands represent the 60% and 90% confidence interval of the posterior.

Figure 5.20 shows the posterior distributions of the technical parameters. Especially the scaling factor for the fluidization time and the smearing parameters are well constrained. The distribution is wider for the particlization energy density and especially for the late stage rescattering cross section scaling $\sigma_{AB, \text{scale}}$. Indeed, although for the latter, the MAP (maximum-a-posteriori) estimate agrees quite well with the original parameter, the distribution is very wide, showing only weak constraints.

Continuing to the viscosities in fig. 5.21, we see good constraints for the shear viscosity. Both as a function of temperature and as a function of baryochemical potential, the original parameterization lies comfortably in the 60% confidence interval. This means that the Bayesian Inference could extract the correct functional dependence. For the bulk viscosity, this holds in general, too. However, the quality of the posterior is here decreased and the original parameterization lies at the boundaries between the more strict 60% confidence interval and the 90% confidence interval. This is however still in the statistically acceptable range.

With this successful validation of our approach, we can now move on to the results on applying this setup to experimental data.

5.3.7 Results

In the following, we aim to answer the questions which parameters affect observables the strongest, what the preferred parameters are and how strongly they depend on the

choice of data used for tuning. This will provide deeper insights into the dynamics of heavy-ion collisions.

5.3.7.1 *Sensitivity Analysis*

In this initial step, we seek a preliminary understanding of how different model parameters influence key observables. One straightforward approach is the construction of a response matrix, which consists of the partial derivatives of observables with respect to the model parameters, computed using the centered finite difference method. Notably, this technique is independent of the posterior, as it can be carried out directly on the emulated prior. However, it should be emphasized that the response matrix is a local, linearized measure of sensitivity and may vary throughout the parameter space, especially if nonlinear parameter interactions are present. Such interactions are more comprehensively captured by advanced methods, for instance the Sobol indices [491].

Figure 5.22 shows the averaged, normalized response matrix over many prior points. For each prior point, it can be defined as

$$R_{ij}(\theta) = \frac{1}{2h} \left(\mathcal{O}_i(\theta + h \mathbf{e}_j) - \mathcal{O}_i(\theta - h \mathbf{e}_j) \right), \quad (5.25)$$

where i labels the observables, j labels the parameters, θ is the parameter vector, h is a small step size, and \mathbf{e}_j is the unit vector along the direction of parameter j .

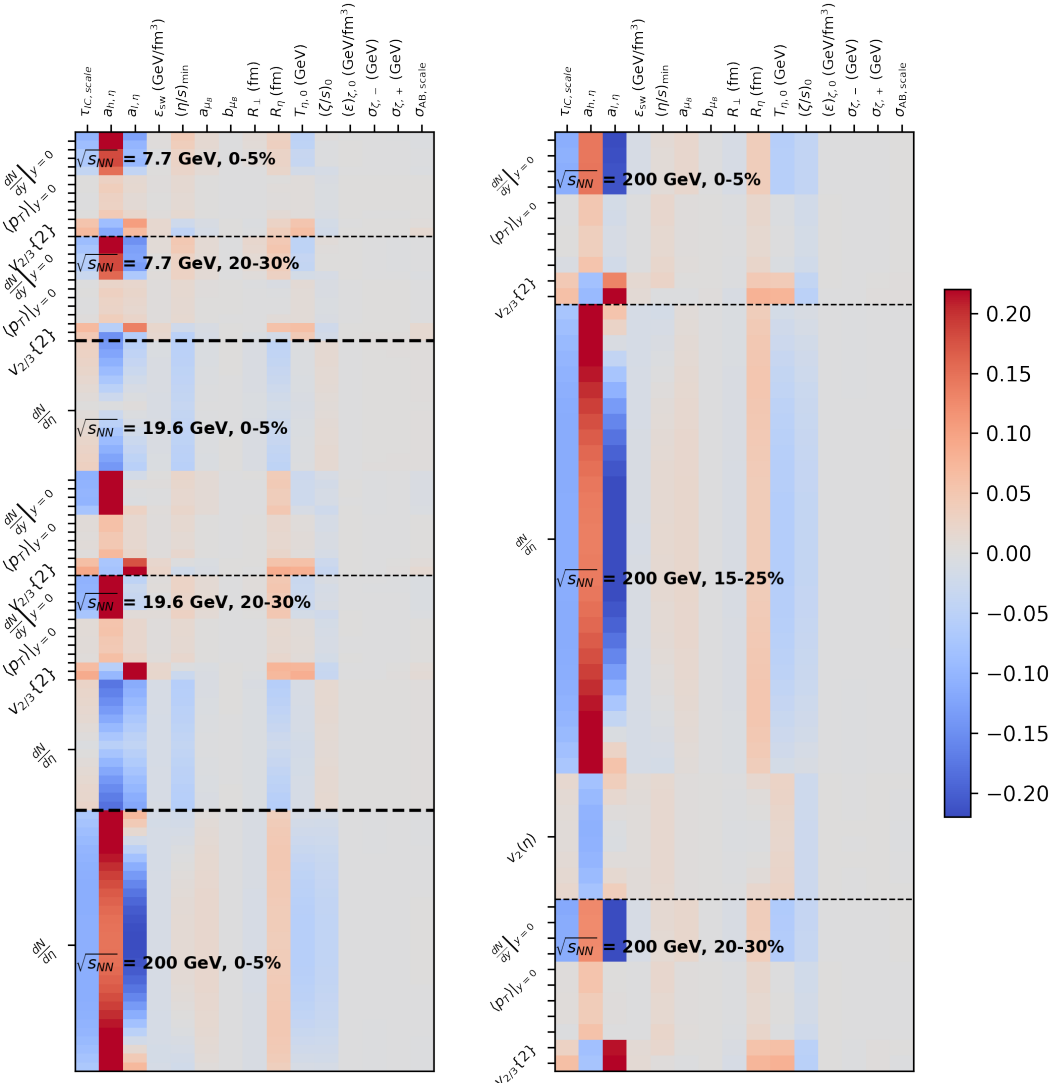


FIGURE 5.22: Normalized partial derivatives of observables with respect to parameters of the simulation (response matrix) averaged over multiple prior points. Positive values (red) mark an increase in the observable with the value of the parameter, negative values (blue) mark a decrease.

Positive (red) regions signify a positive correlation between parameter and observable, while negative (blue) regions imply that decreasing the parameter increases the observable. From this, we highlight some noteworthy features.

The fluidization time scale, $\tau_{\text{IC},\text{scale}}$, exhibits a pronounced sensitivity to numerous observables, in particular flow coefficients and particle multiplicities. Whereas midrapidity regions consistently reveal a negative correlation, higher rapidities at intermediate energies display a positive correlation between $\tau_{\text{IC},\text{scale}}$ and particle yields. This underscores the intricate role played by extended initial scatterings. A plausible explanation emerges from the distinct treatments of particle formation in SMASH across different energies: at high energies, particles typically remain unformed following the first collision and thus

cannot undergo secondary interactions, while at lower energies secondary collisions are more likely.

Furthermore, we observe a positive correlation between the fluidization time scale and the flow coefficients, contrasting with the behavior reported in [177]. This suggests, also in the light of the earlier studies, that while early-stage transport does not generate momentum anisotropies which are present in the final state, it may produce pressure gradients in the early stages of the collision more effectively than the subsequent hydrodynamic phase. In addition, longitudinal smearing enhances multiplicities at high energies, but reduces them in the high-rapidity regions at intermediate energies, thereby refining previous observations [177].

Another key parameter is the kink temperature of the shear viscosity, $T_{\eta,0}$. It generally exhibits a similar trend to the fluidization time scale but reduces the overall multiplicities at intermediate energies over the entire rapidity range. The steepnesses of the linear temperature dependence of the shear viscosity show strong impacts on a wide range of observables, with a substantial presence of rapidity dependence. Note that the correlations are of opposite sign due to the additional minus sign for low temperatures in eq. (5.20). Decreasing the coefficient at temperatures lower than T_c increases the steepness, but as we have a negative coefficient and a negative multiplicand, this increased steepness reduces the shear viscosity. For temperatures higher than T_c , the missing minus sign inverts this behavior. In general, the expected behavior is realized that increasing the shear viscosity decreases anisotropic flows. By contrast, parameters associated with the baryochemical potential exhibit only a marginal effect. Regarding bulk viscosity, only its overall magnitude is relevant, while other viscous parameters, including the density dependence of shear viscosity and rescattering cross section scaling, induce comparatively minor signals. Consequently, these latter parameters are subject to weaker constraints. It is also evident that bulk viscosity has sizeable effects only at high collision energies, although it is often disregarded in this range.

5.3.7.2 Posterior Predictions

In a next step, we want to investigate which regions of the parameter space optimize agreement with experimental data. First, we take a look at the posterior distribution of technical parameters again, which can be found in fig. 5.23. We observe a preference for slightly increased fluidization time, which contrasts with the results of Ref. [331] preferring a minimal fluidization time.

Both the present study and the earlier one identify an optimal particlization energy density of roughly 0.5 GeV/fm^3 , although there is considerable uncertainty in this determination. In contrast to the previous work, the current model indicates that minimal smearing is preferred in the transverse plane, while a substantial amount of longitudinal smearing is favored. For the late-stage rescattering cross section scaling, the result is statistically consistent with a value of unity, reflecting the high degree of uncertainty in this parameter.

Turning to the viscosities, and referring to fig. 5.24, the patterns noted earlier in the sensitivity analysis reemerge. The bulk viscosity and the possible dependence on baryochemical potential of the shear viscosity are only weakly constrained, allowing for a broad range of values to be consistent with the data.

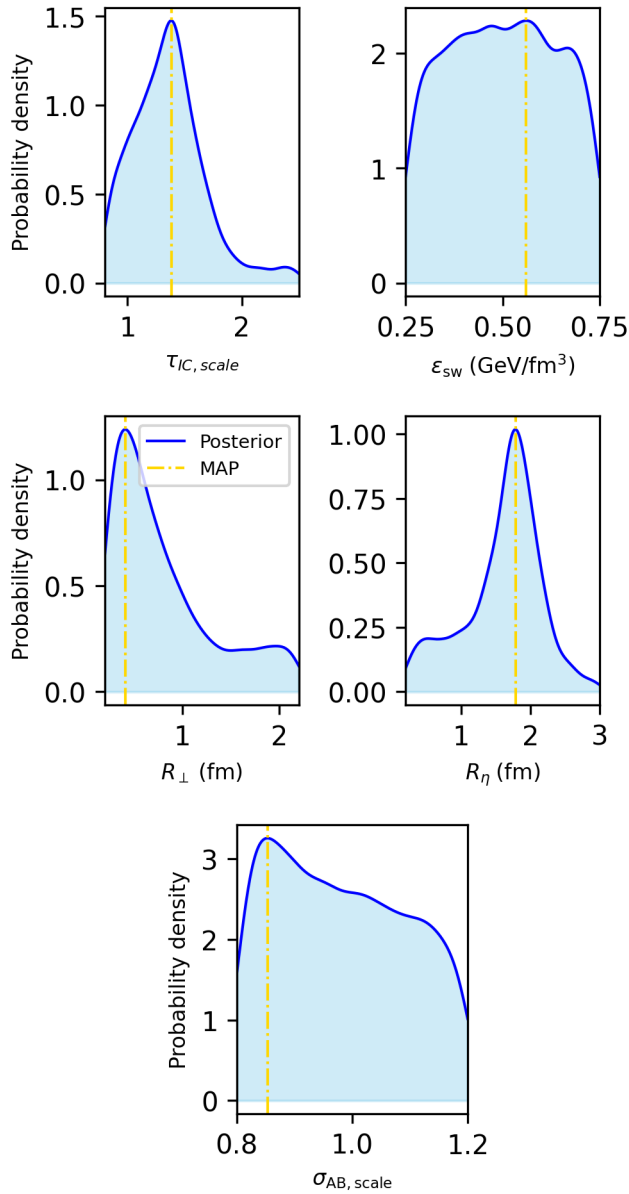


FIGURE 5.23: Posterior of the technical parameters. The golden vertical line represents the maximum-a-posteriori value.

The situation changes when considering the temperature dependence of the shear viscosity. A rapid decrease at higher temperatures is preferred, with the viscosity effectively reaching zero from about 150 to 250 MeV. The full posterior shown in fig. 5.25 clarifies this behavior. Although there is a finite kink value $(\eta/s)_{\min}$ at intermediate temperatures, the slopes on both sides of this kink are nearly the same, so any negative slope beyond a certain temperature pushes the shear viscosity toward zero for high temperatures. Interestingly, this effect can be viewed as a degenerate scenario in which a kink with $(\eta/s)_{\min} = 0$ and a negative slope would yield an equivalent configuration. The reasoning behind why such a solution is favored remains unclear, but the outcome suggests that

the model strongly prefers a vanishing shear viscosity in the high-temperature phase of the quark-gluon plasma, combined with a substantial viscosity near particlization.

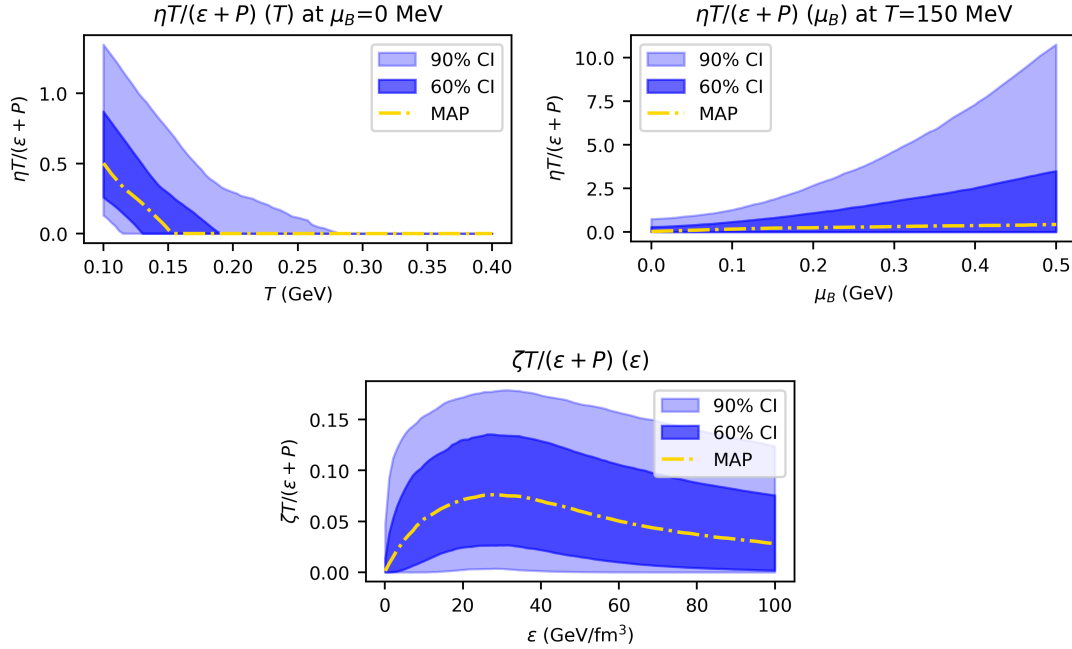


FIGURE 5.24: Posterior of the viscosities. From top to bottom and left to right: the shear viscosity as a function of temperature for vanishing baryo-chemical potential, the shear viscosity as a function of baryo-chemical potential at fixed temperature, and the bulk viscosity as a function of the energy density. The golden line represents the maximum-a-posteriori. The bands represent the 60% and 90% confidence interval of the posterior.

Further insights arise from fig. 5.25, which reveals that b_{μ_B} is tightly peaked at zero, causing much of the uncertainty in baryochemical potential dependence to stem from the coefficient a_{μ_B} , which remains poorly constrained. There are also only limited correlations among the parameters, easily spotted by diagonal trends in the triangle plot. One notable trace of such a relationship appears for the fluidization time scale $\tau_{IC, scale}$ and the transverse radius parameter R_{\perp} . The maximum-a-posteriori value for all parameters marked here in a golden line can also be found in table A.13.

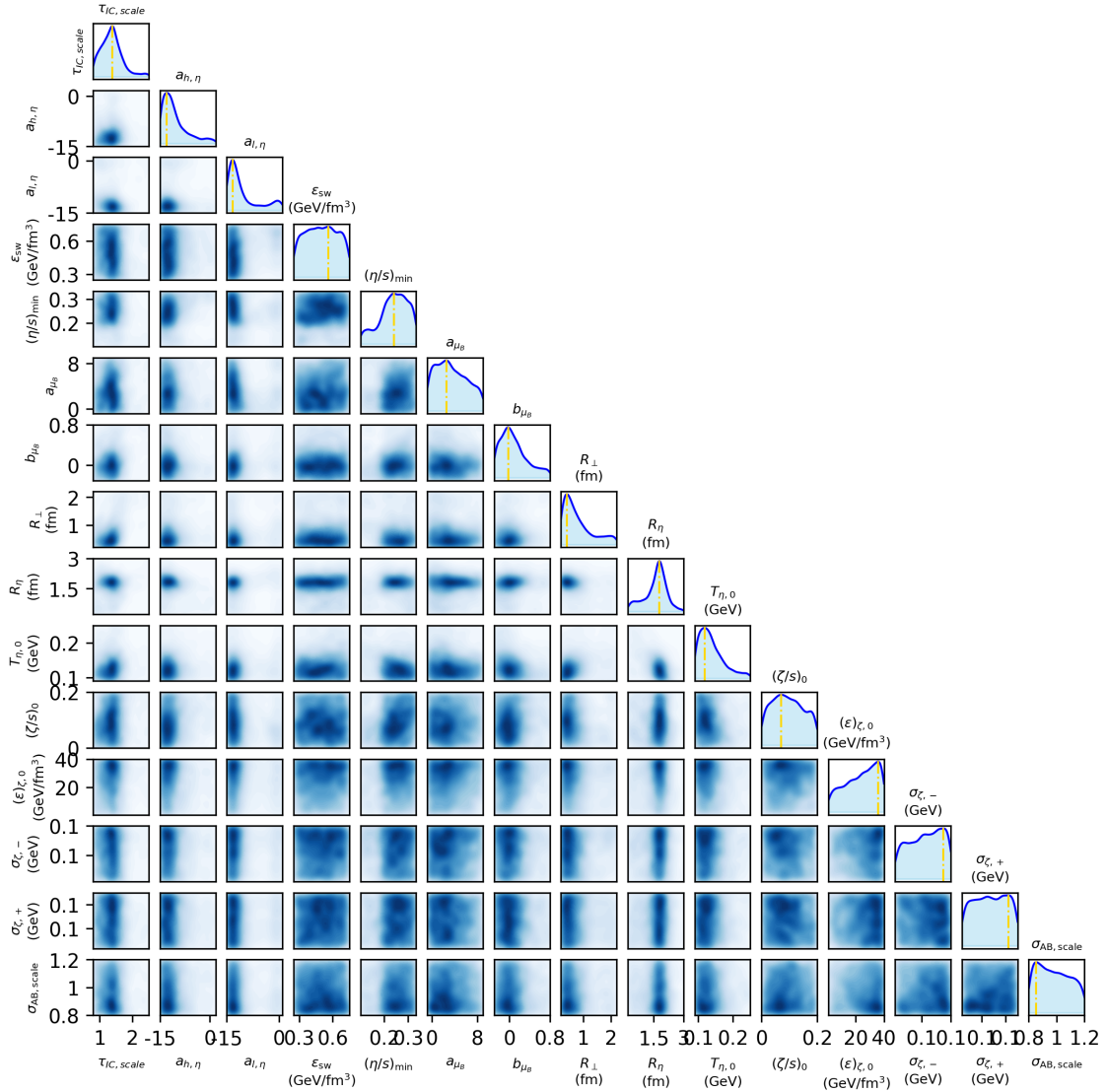


FIGURE 5.25: Full posterior for all parameters. The diagonal shows the distribution for each parameter, whereas the off-diagonal shows the probability distribution for a combination of two parameters.

Figure 5.26 shows our results for the shear viscosity in comparison with known and estimated values for other media. One can see that our agreement with the meson gas is good, confirming again the preference for continuity between hydrodynamics and hadronic transport. Around the critical temperature, we observe very small values, as suggested by data from RHIC [492]. However, we do not find the kink structure observed in other media, or as suggested from flow at LHC energies. Our fit might be dominated by data from lower energies. In future studies, it might be worthwhile to observe if a kink structure can be found when including LHC energies as well.

The tune achieved here matches experimental data to a consistently high degree, as shown in fig. 5.27, where all points remain within roughly two standard deviations of the measurements. Notably, for collisions at high energies, the model reproduces

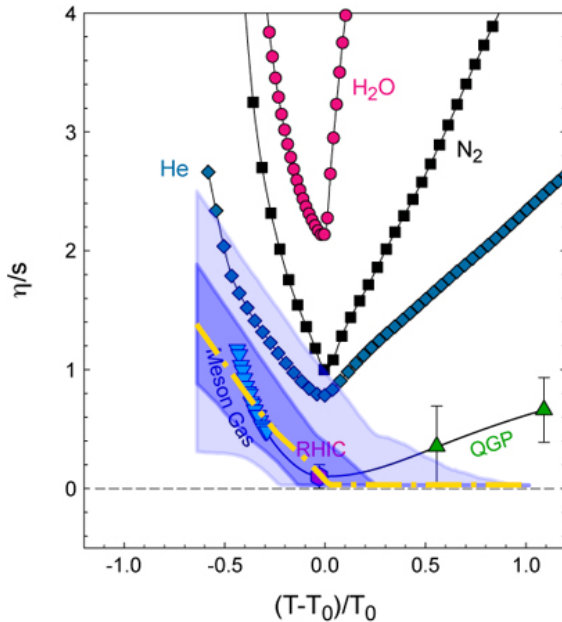


FIGURE 5.26: Shear viscosity over entropy ratio as a function of the critical temperature of $T_0 = 155$ MeV for different substances, with an overlay of the presented results as blue confidence bands. Adapted from [493].

midrapidity multiplicities more accurately than those at forward or backward rapidity, whereas at intermediate energies, the situation is reversed. This observation highlights a more general limitation in fully describing the longitudinal dynamics across different collision energies. A comparison of the different observables with the experimental values is also shown in linear scale in the appendix in fig. A.1, fig. A.2, and fig. A.3.

5.3.7.3 Hydrodynamic evolution time

The parameters $\tau_{\text{IC, scale}}$ and ϵ_{switch} jointly determine the overall duration of the hydrodynamic evolution by defining its beginning and ending points. This observation naturally motivates the introduction of τ_{Hydro} , which represents the time interval during which the system is in a hydrodynamic regime. Here, it is defined as the difference between the time when the last fluid element is particlized and the eigentime of the hypersurface which is fluidized. This interval is crucial for tuning the viscosity, since it covers the phase of the evolution during which viscous effects are most directly controlled. The maximum-a-posteriori (MAP) estimates for τ_{Hydro} in different systems are presented in fig. 5.28. As expected, the hydrodynamic duration increases with collision energy and centrality. These values align reasonably well with those reported in Ref. [221] for a default setup.

The reason for examining τ_{Hydro} more closely is its pronounced influence on the primary observables of interest. Figure 5.29 shows the Pearson correlation coefficients between various observables and the hydrodynamic evolution time. The strongest correlations occur for yields and for flow observables at low energies. One explanation for this finding is that lower-energy systems typically have lower temperatures and higher

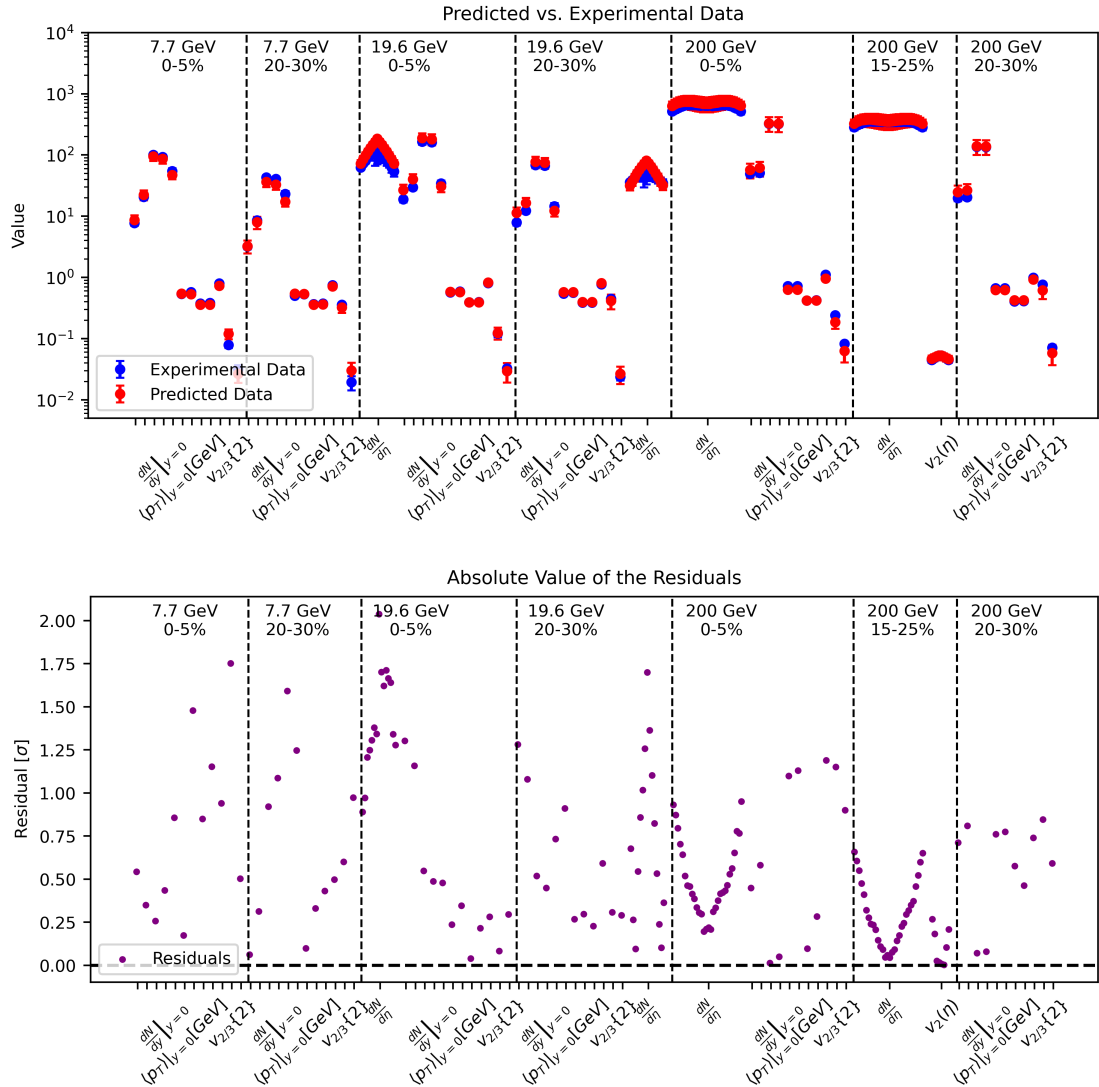


FIGURE 5.27: Comparison of predictions of observables from the posterior with experimental values (top). Residuals between predictions and experimental data in multiples of standard deviations (bottom).

baryochemical potentials, leading to higher viscosities and therefore a more pronounced role for the hydrodynamic phase in shaping the flow.

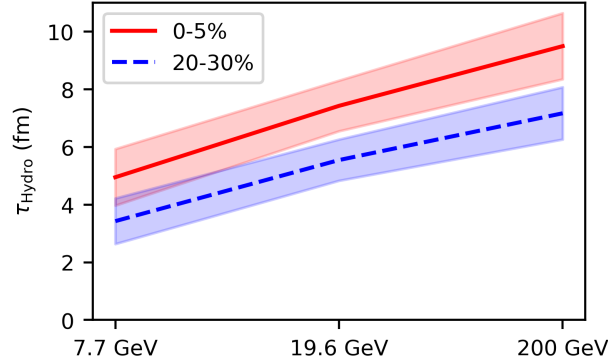


FIGURE 5.28: MAP of the duration of the hydrodynamic evolution in the posterior.

It is important to note, however, that τ_{Hydro} cannot replace $\tau_{\text{IC, scale}}$ and ϵ_{switch} as a fundamental parameter in this framework. Although one could hypothetically increase both $\tau_{\text{IC, scale}}$ and ϵ_{switch} to obtain a similar average value of τ_{Hydro} , this would not produce identical observables. The early and late stages of the system's evolution are qualitatively different, so merely shifting the entire hydrodynamic window in time is not sufficient to recover the same dynamical behavior. This distinction is also supported by the absence of diagonal structures between $\tau_{\text{IC, scale}}$ and ϵ_{switch} in fig. 5.25, indicating that there are no pairs of values for these two parameters that yield comparable results.

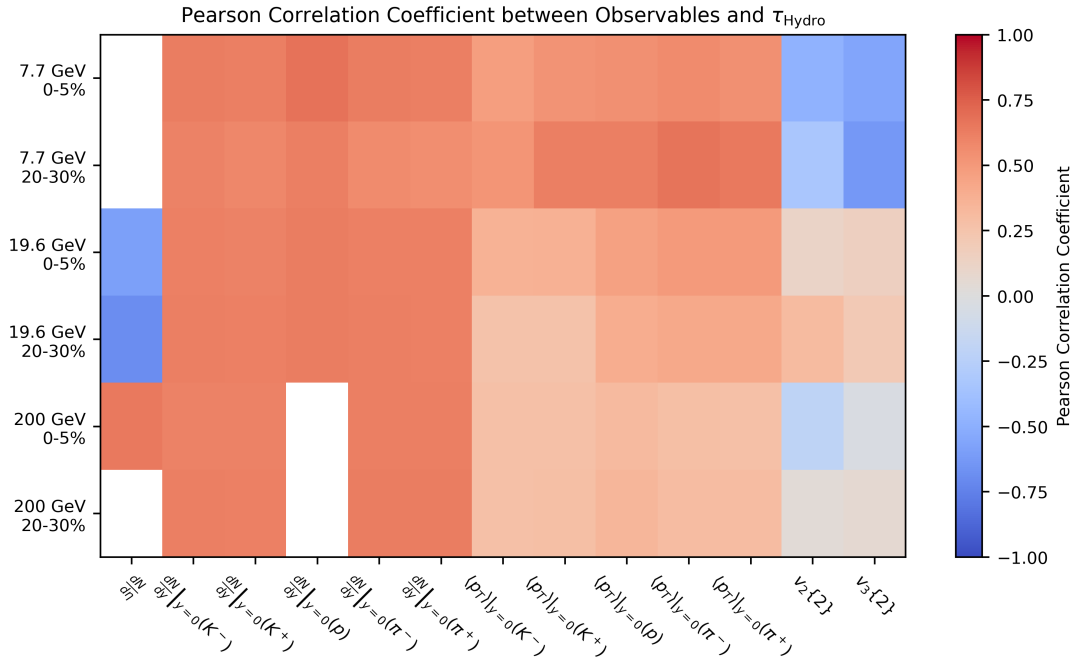


FIGURE 5.29: Pearson correlation coefficients between the hydrodynamic evolution duration and observables used to train the fit. White squares signify observables which were not used at the respective energies/centralities. For spectra, the average over the data points is displayed.

5.3.7.4 *Impact of data selection*

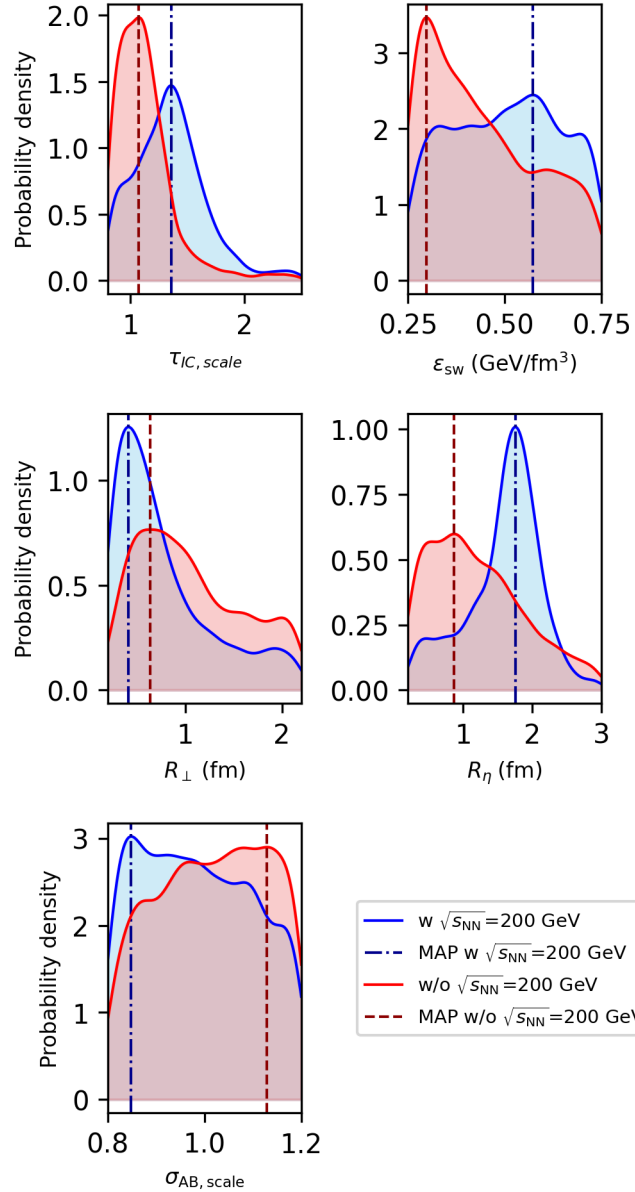


FIGURE 5.30: Posterior of the technical parameters when including and excluding data at $\sqrt{s_{NN}} = 200$ GeV.

We now explore the impact of longitudinal data and different collision energies in more detail. As a first step, we remove the data at $\sqrt{s_{NN}} = 200$ GeV and investigate the changes in the posterior distributions of the model parameters.

In fig. 5.30, we observe only minor deviations for the cross section scaling and the transverse smearing, whereas other technical parameters shift significantly. In particular, the initial stage scaling becomes centered around unity, and there is a pronounced preference for both a longer hydrodynamic lifetime and reduced longitudinal smearing.

The default of the passing time for the initial transport is therefore appropriate for intermediate energies but too small at high energies, where the current setup of the hybrid approach lacks a dedicated pre-equilibrium treatment. Changes in parameters is likely driven also driven by the multiplicity residuals that were substantial at intermediate energies but balanced by high-rapidity residuals at higher energies in the full fit. Further examination of the viscosities, shown in fig. 5.31, confirms that data at higher energies plays an essential role.

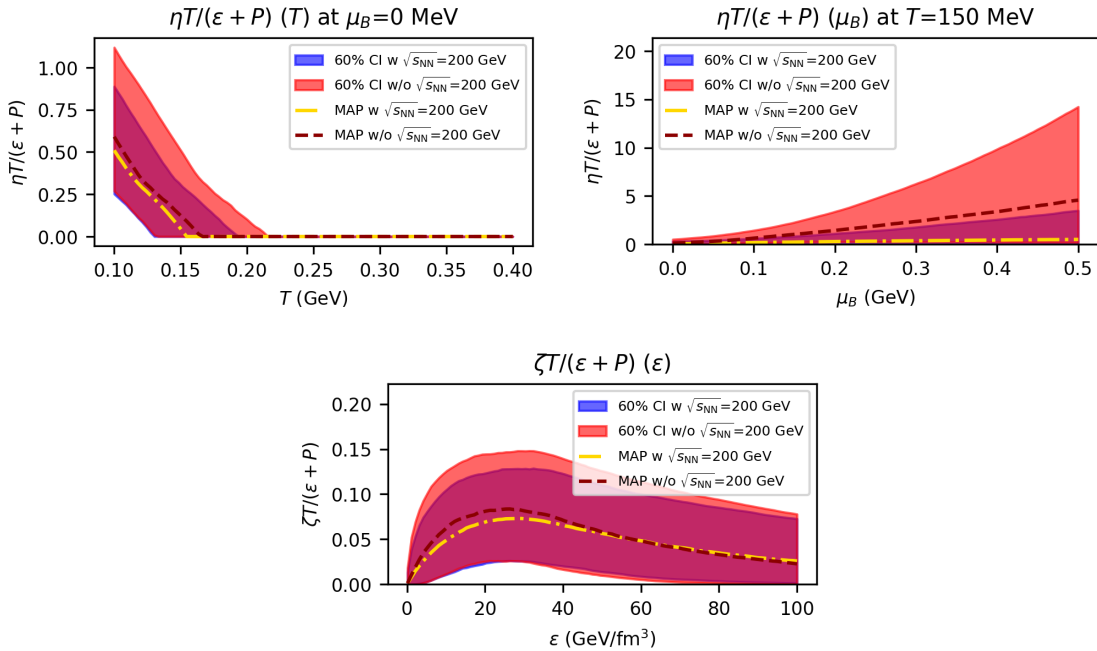


FIGURE 5.31: Posterior of the viscosities when including and excluding data at $\sqrt{s_{NN}} = 200$ GeV. From top to bottom and left to right: the shear viscosity as a function of temperature for vanishing baryo-chemical potential, the shear viscosity as a function of baryo-chemical potential at fixed temperature, and the bulk viscosity as a function of the energy density. The bands represent the 60% confidence interval of the posterior.

Although the shear viscosity as a function of baryochemical potential is stronger constrained, this is a combination of two contributions: on the one hand, the additional rapidity-dependent data at 200 GeV contributes to the constraints. On the other hand, the additional data also constraints the temperature dependence, leading to a more constrained viscosity at $T = 150$ MeV at vanishing baryochemical potential. As this is scaled in proportion to the baryochemical potential, a more peaked temperature dependence also gives a less wide distribution as a function of μ_B .

The significance of longitudinal data becomes clearer in fig. 5.32 and fig. 5.33, where we compare the complete data set against variants with a tighter or looser rapidity cut. Most of the technical parameters remain largely unchanged when the rapidity range is decreased, although a slight increase in transverse smearing becomes evident. If the rapidity cut is relaxed and data from higher rapidity regions is included, some technical

parameters tend to hit the boundaries of the prior ranges, indicating that the model struggles to accurately describe such high-rapidity data within the current framework.

From a viscosity standpoint, high-rapidity data adds further constraints on the baryochemical potential dependence, but it also amplifies the uncertainties of the bulk viscosity. This is illustrated in fig. 5.33, which shows that while the high-rapidity information refines one aspect of the viscosity parameterization, it simultaneously broadens the allowed range of another.

We can therefore conclude that high-rapidity regions are still a challenge for this model and that the inclusion of high-energy data improves constraints on baryochemical potential dependence.

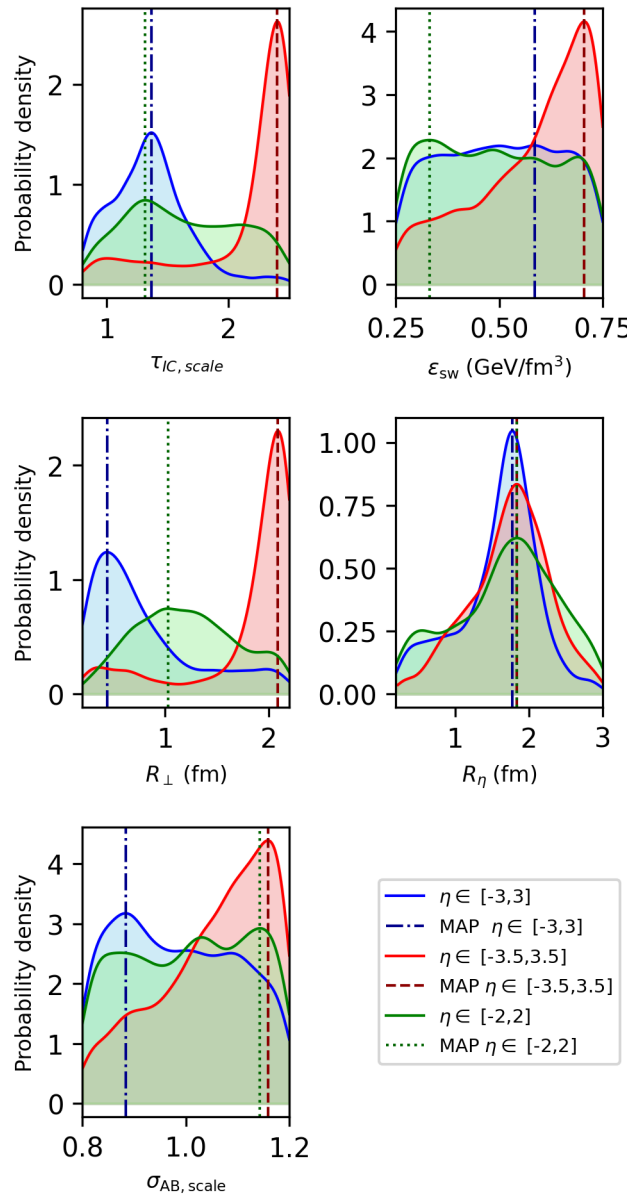


FIGURE 5.32: Posterior of the technical parameters depending on the rapidity cut.

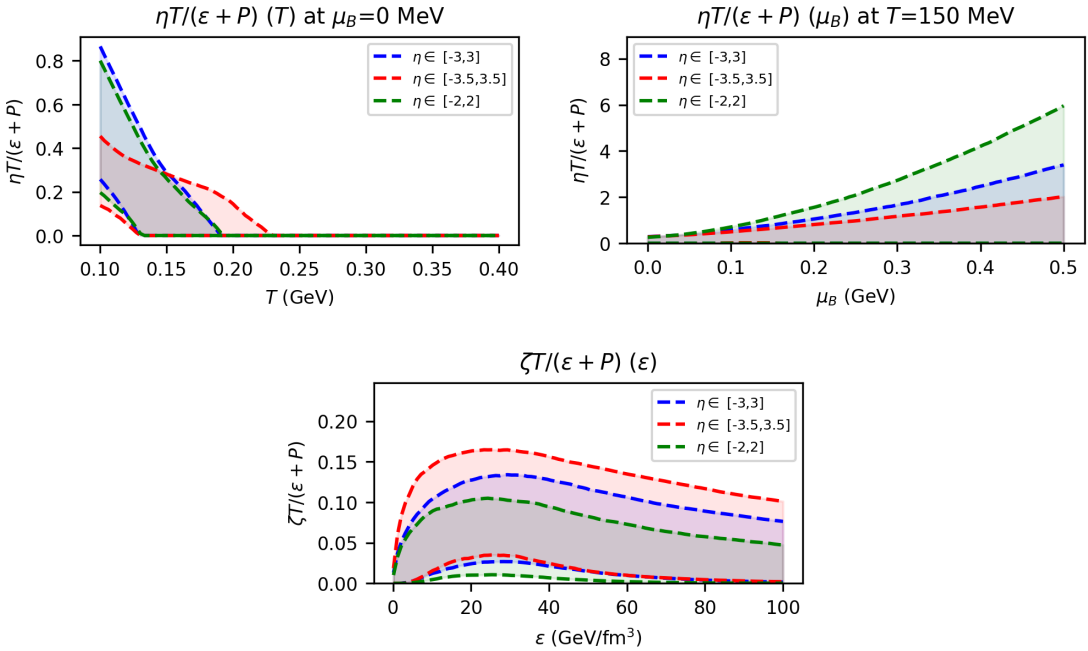


FIGURE 5.33: Posterior of the viscosities depending on the rapidity cut. From top to bottom and left to right: the shear viscosity as a function of temperature for vanishing baryochemical potential, the shear viscosity as a function of baryochemical potential at fixed temperature, and the bulk viscosity as a function of the energy density. The bands represent the 60% confidence interval of the posterior.

5.4 Summary

This chapter examined the role of viscosities in a multi-stage model of heavy-ion collisions, where an initial hadronic transport phase evolves into relativistic viscous hydrodynamics and eventually returns to a microscopic description below a certain energy density. Throughout, particular attention was paid to the importance of baryochemical potential and temperature dependencies of the shear viscosity, as described in section 5.1.

In section 5.1, the motivation for including a non-constant (and possibly μ_B -dependent) shear viscosity was laid out, underpinned by theoretical arguments and prior lattice as well as effective-model results suggesting that shear viscosity may be smallest around the crossover region. A practical parameterization in energy density and baryon density was discussed, along with a more conventional constant or temperature-dependent η/s . These different approaches were then compared in numerical simulations to assess their effect on yields, mean transverse momenta, and anisotropic flow.

While yield observables at intermediate collision energies were shown to be sensitive to the baryochemical-potential dependence of the shear viscosity, it emerged that integrated elliptic flow often displayed only moderate or, in certain cases, negligible dependence. This pattern was further evidenced by analyzing the effective, density-averaged viscosity throughout the space-time evolution. Within a hybrid model, it was also found that increasing the transport-to-hydrodynamics particlization/switching energy density sometimes had a large impact on observables—but only for certain functional forms of the

viscosity. When the shear viscosity was chosen to match the hadronic transport value near the transition, including a baryochemical potential dependence, the flow became less sensitive to the choice of the point of switching the description between hydrodynamics and hadronic transport, which makes the modeling more robust against small variations in switching criteria.

In order to achieve a more quantitative statement on the baryochemical potential dependence of the shear viscosity, a Bayesian analysis was performed. As part of that approach, Gaussian Process emulators were introduced to overcome the computational cost of running extensive event-by-event simulations for large parameter scans. These emulators, trained on systematically chosen parameter points, can efficiently predict observables and their uncertainties, thereby enabling global fits to large data sets. We validated the ideal setup for training such Gaussian Emulators to achieve maximal performance. The combined fit revealed that while the temperature dependence of shear viscosity is moderately constrained by data, the net baryon density dependence is less so, implying that additional experimental observables or improved precision would be needed to further restrict this sector of the parameter space. Similarly, the location and height of the proposed bulk-viscous peak were only loosely fixed in the posterior, reflecting limited current sensitivity of inclusive flow and yield measurements to the details of bulk viscosity.

Putting these findings together clarifies how each transport coefficient and model parameter can influence the evolution of the fireball. Results suggest that future work on, for instance, higher-order flow harmonics or more differential rapidity-dependent measurements could enhance sensitivity, especially at intermediate energies where μ_B is substantial.

The findings for the transport coefficients, especially regarding the nearly vanishing specific shear viscosity at higher temperatures, have tension with several existing Bayesian analyses [53, 309, 464], which generally support a non-zero minimal shear viscosity in the QGP phase. This discrepancy can be partly attributed to the reduced freedom in the initial state provided by the hadronic transport model, which lowers the degrees of freedom for tuning geometric fluctuations and thus pushes certain parameters, such as the hydrodynamic onset time, into especially sensitive roles. While this analysis accommodates key beam energies and rapidity-dependent observables, even higher-statistics data would be needed for more definitive conclusions.

SUMMARY, CONCLUSIONS, AND PERSPECTIVES

Science condemns itself to failure when, yielding to the infatuation of the serious, it aspires to attain being, to contain it, and to possess it; but it finds its truth if it considers itself as a free engagement of thought in the given, aiming, at each discovery, not at fusion with the thing, but at the possibility of new discoveries; what the mind then projects is the concrete accomplishment of its freedom.

— Simone de Beauvoir, *Pour une morale de l'ambiguité*

The study of the QCD phase diagram from the phenomenological perspective using hybrid approaches has remained one of the most dynamic fields in heavy-ion physics. Its success has been greatly enhanced by steadily increasing computational power, advances in methods, and improving access to precise experimental data.

The main goal of this thesis was to contribute to the understanding of transport coefficients across the phase diagram of QCD. To achieve this objective, the necessary groundwork was laid by describing the SMASH-vHLLE-Hybrid approach in detail in chapter 2, thereby demonstrating the capabilities of the hadronic transport approach SMASH and of the viscous (3+1)D hydrodynamics code vHLLE. In this context, the origin and role of transport coefficients in hydrodynamics were outlined, along with the different models available for initializing the hydrodynamic simulation. Since hybrid simulations require substantial computational effort, specific measures were presented to build an efficient and practical framework for multi-stage hybrid calculations.

The study of transport coefficients demands an understanding of the signatures of their presence. In chapter 3, the most important observables of heavy-ion collisions were summarized, with special emphasis on harmonic flows. These momentum anisotropies in the final state are strongly affected by the isotropizing effect of transport coefficients and are intimately connected to the spatial anisotropies of the initial state, known as eccentricities.

The influence of both eccentricities and transport coefficients on flow motivated the study in chapter 4. An investigation was conducted to determine how strongly results depend on the choice of initial state models. For this purpose, IP-Glasma, T_RENTo, and initial states generated by SMASH were compared. It was found that the choice of initial states has a substantial effect beyond a mere modification of the eccentricities. Instead, the additional momentum in both IP-Glasma and SMASH partly explains the differences in the medium's response to the initial state eccentricities. This analysis allowed one substantial source of model uncertainty in hybrid approach predictions to be identified and quantified.

Chapter 5 presents the core contribution of this work to the understanding of transport coefficients across the full phase diagram. First, the basic assumption of constant shear viscosity was compared with a temperature dependence and with a parameterization based on energy density and net baryon density. It was observed that the net baryon

density dependence affects bulk observables mainly during the early stages of the evolution, while harmonic flows are more strongly influenced by the late stages of the hydrodynamic phase. Additionally, non-linear effects emerged upon including a net baryon density dependence, highlighting the complexity of such studies. An especially noteworthy result was that a purely energy-density-based shear viscosity, with the chosen constraints, removed the dependence of the elliptic flow on the hadronization energy density. This finding suggests that the proposed shear viscosity parameterization closely tracks the shear viscosity from the afterburner stage.

In the second part of chapter 5, the power of statistical learning was harnessed by employing Bayesian inference on the SMASH-vHLLE-Hybrid approach. This is the first application of Bayesian inference to a (3+1)D simulation featuring both a hadronic initial state and a temperature- and baryochemical-potential-dependent shear viscosity. The choices of priors, experimental data, and parameterizations were outlined, and the approach was carefully validated. The analysis yielded weak constraints on the bulk viscosity, indicating non-vanishing values for energy densities from 5–50 GeV/fm³. While a dependency of the shear viscosity on the baryochemical potential could neither be ruled out nor definitively confirmed, strong constraints were found for the shear viscosity at high temperatures, where it was observed to vanish. At low temperatures, by contrast, substantial shear viscosities were identified. Furthermore, a considerable correlation between the hydrodynamic simulation time and most observables was highlighted, and the impact of data selection was discussed. Data at $\sqrt{s_{NN}} = 200$ GeV was shown to significantly increase the constraints, underscoring the importance of including wide ranges of collision energies, even if the core region of interest pertains to lower collision energies where the net density does not vanish. In addition, the amount of longitudinal data employed was found to play a critical role. Including more longitudinal data both weakened and strengthened some constraints, and an overall collapse of predictions occurred upon including data at very forward and backward rapidities, exposing limitations in the model.

Outlook

The investigations presented here serve as a starting point for many possible further studies. Among numerous other research directions, correct initial state modeling remains a key challenge. On the one hand, an expanded survey of the response function and possible independent variables in the initial state could help clarify which properties of the initial state affect which final-state observables. On the other hand, comparing different initial-state models in isobaric collisions could help disentangle the influence of tuning models to specific experimental data from a true description of the physical system.

Regarding our results from the Bayesian Inference, a natural next step is to simplify the modeling assumptions by removing the presently unconstrained baryochemical potential dependence in order to reduce the dimensionality of the parameter space and isolate the most dominant effects. Similarly, it is a worthwhile study to investigate how much of the strong constraints on the high temperature shear viscosity can be attributed to the presence of bulk viscosity. One can also envision direct comparisons to other initial-state

scenarios, such as TRENTo, UrQMD, or McDIPPER, to examine the interplay between initial conditions and viscosity extractions.

More precise constraints on the baryochemical potential dependence of transport coefficients will require the extension of the hybrid approach to lower energies. However, the picture of a strictly sequential description begins to break down at such energies, since not all regions of the collision zone reach sufficient densities. Dynamic initialization offers a promising way forward: hadronic transport and hydrodynamics run in parallel, allowing particles to leave the medium and others to enter it.

Besides lower energies, small systems such as O–O collisions can also contribute to this effort, as they permit a more comprehensive model-to-data comparison across a broad range of system sizes within a single model. To fully realize the benefits of Bayesian inference and achieve comparability between different studies, additional work is needed. As discussed in the introduction, corrections during the particlization procedure can influence constraints on transport coefficients, especially at low energies where the hydrodynamic evolution time is short. A formalism motivated by the non-equilibrium model itself is needed, ideally including a parameterization of these corrections based on the distribution functions in SMASH. Such a procedure would enable a smoother transition from hydrodynamics to transport.

Lastly, an important next step is to discard strictly parametric forms of viscosities in favor of non-parametric priors. This approach would eliminate many assumptions underlying the present work. Although the computational cost of such endeavors would be substantial, ongoing advances in hardware and software performance make them more and more feasible. The insights gained here can guide future efforts to uncover the true nature of transport coefficients across the QCD phase diagram.

APPENDIX

Regression tables

The following section contains the regression results for the different models and dependent variables, as well as different choices for the set of independent variables. Each row is an independent regression. For each independent variable, the coefficient with error as well as the p-value is given. As a p-value smaller than 0.05 is seen as statistically significant, it is printed in bold. If a value is present in the column of a row, the respective independent variable was used in the regression. The final column contains the r^2 -value for the regression.

The concept of the p-value can be illustrated with a simple regression problem involving one dependent variable, y , and one independent variable, x . Assume a model of the form:

$$y_i = \beta_0 + \beta_1 x_i + \varepsilon_i,$$

with

- β_0 the intercept (the value of y when $x = 0$),
- β_1 the slope,
- ε_i the error term, capturing everything not explained by the model.

The p-value signifies the likelihood that the slope differs from zero, and therefore contains an estimate of the probability that the independent variable affects the system. This leads to the hypothesis:

$$H_0 : \beta_1 = 0 \quad \text{versus} \quad H_a : \beta_1 \neq 0.$$

If $\beta_1 = 0$, it means x has no effect on y . To see if this is true, we compute a test statistic t :

$$t = \frac{\hat{\beta}_1}{\sigma(\hat{\beta}_1)},$$

where

- $\hat{\beta}_1$ is our estimate of the slope,
- $\sigma(\hat{\beta}_1)$ is the standard error of the slope estimate.

The statistic t follows a t-distribution (also known as Student's distribution) with $n - 2$ degrees of freedom (n = number of data points). The two-sided p-value is:

$$\text{p-value} = 2 \left[1 - F_{t(n-2)}(|t|) \right],$$

where $F_{t(n-2)}$ is the cumulative distribution function (CDF) of a t-distribution with $n - 2$ degrees of freedom. A small p-value suggests β_1 is likely not zero, indicating x has a real effect on y [494].

In addition, we report r^2 . It tells us what fraction of the total variation in y is explained by our regression line. Mathematically:

$$r^2 = 1 - \frac{\sum_{i=1}^n (y_i - \hat{y}_i)^2}{\sum_{i=1}^n (y_i - \bar{y})^2},$$

where:

- \hat{y}_i is the predicted value from the regression line for the i th observation.
- \bar{y} is the average of the observed y values.
- $\sum (y_i - \hat{y}_i)^2$ is called the *sum of squared errors* (SSE).
- $\sum (y_i - \bar{y})^2$ is called the *total sum of squares* (SST).

If r^2 is close to 1, it means the regression line explains practically all changes in y . If r^2 is close to 0, it means the line does not explain much of the variability in y at all.

We observe throughout all models, independent variables, and centralities for $\sqrt{s_{NN}} = 200$ GeV that the most significant increase in predictive power, measured by r^2 , is gained by adding $\langle p_T^{IC} \rangle$ as a second independent variable. Adding further variables is either not statistically significant, leading to greater p-values, or only negligibly improves r^2 , which is always expected to stay constant or improve upon adding further independent variables. Using other independent variables apart from ϵ_n and $\langle p_T^{IC} \rangle$ fails to consistently reach improvements greater or equal to the combination of ϵ_n and $\langle p_T^{IC} \rangle$.

coeff ϵ_2	p- value ϵ_2	coeff ϵ_3	p- value ϵ_3	coeff $\langle p_T^{IC} \rangle$	p- value $\langle p_T^{IC} \rangle$	coeff v_2^{IC}	p- value v_2^{IC}	coeff v_3^{IC}	p- value v_3^{IC}	r^2
2.86	0.00	-	-	-	-	-	-	-	-	0.763
\times										
10^{-1}										
± 5.8										
\times										
10^{-3}										
2.26	0.00	8.09	0.00	-	-	-	-	-	-	0.783
\times		\times								
10^{-1}		10^{-2}								
± 9.1		± 9.7								
\times		\times								
10^{-3}		10^{-3}								
1.72	0.00	-	-	3.65	0.00	-	-	-	-	0.804
\times				\times						
10^{-1}				10^{-6}						
± 1.1				± 2.9						
\times				\times						
10^{-2}				10^{-7}						
2.29	0.00	-	-	-	-	4.94	0.00	-	-	0.781
\times						\times				
10^{-1}						10^{-1}				
± 9.1						± 6.2				
\times						\times				
10^{-3}						10^{-2}				
1.93	0.00	4.50	0.00	-	-	2.45	0.00	3.14	0.00	0.794
\times		\times				\times		\times		
10^{-1}		10^{-2}				10^{-1}		10^{-1}		
± 1.0		± 1.1				± 7.1		± 7.8		
\times		\times				\times		\times		
10^{-2}		10^{-2}				10^{-2}		10^{-2}		
1.70	0.00	1.12	3.57	3.21	0.00	2.10	7.89	4.77	5.87	0.804
\times		\times	\times	\times		\times	\times	\times	\times	
10^{-1}		10^{-2}	10^{-1}	10^{-6}		10^{-2}	10^{-1}	10^{-2}	10^{-1}	
± 1.1		± 1.2		± 5.3		± 7.8		± 8.8		
\times		\times		\times		\times		\times		
10^{-2}		10^{-2}		10^{-7}		10^{-2}		10^{-2}		

TABLE A.1: Regression results for v_2 with SMASH IC at 0-5% centrality, $\sqrt{s_{NN}} = 200$ GeV.

coeff ϵ_2	p- value ϵ_2	coeff ϵ_3	p- value ϵ_3	coeff $\langle p_T^{IC} \rangle$	p- value $\langle p_T^{IC} \rangle$	coeff v_2^{IC}	p- value v_2^{IC}	coeff v_3^{IC}	p- value v_3^{IC}	r^2
-	-	1.93	0.00	-	-	-	-	-	-	0.688
		\times								
		10^{-1}								
		± 4.7								
		\times								
		10^{-3}								
5.28	0.00	1.48	0.00	-	-	-	-	-	-	0.711
\times		\times								
10^{-2}		10^{-1}								
± 7.0		± 7.5								
\times		\times								
10^{-3}		10^{-3}								
-	-	1.06	0.00	2.54	0.00	-	-	-	-	0.728
		\times		\times						
		10^{-1}		10^{-6}						
		± 9.4		± 2.4						
		\times		\times						
		10^{-3}		10^{-7}						
-	-	1.54	0.00	-	-	3.11	0.00	-	-	0.705
		\times				\times				
		10^{-1}				10^{-1}				
		± 7.5				± 4.8				
		\times				\times				
		10^{-3}				10^{-2}				
2.98	0.00	1.23	0.00	-	-	1.09	4.50	2.92	0.00	0.724
\times		\times				\times	\times	\times		
10^{-2}		10^{-1}				10^{-1}	10^{-2}	10^{-1}		
± 7.9		± 8.5				± 5.4		± 6.0		
\times		\times				\times		\times		
10^{-3}		10^{-3}				10^{-2}		10^{-2}		
1.66	4.75	1.04	0.00	1.81	0.00	-1.79	7.68	1.41	3.80	0.731
\times	\times	\times		\times		\times	\times	\times	\times	
10^{-2}	10^{-2}	10^{-1}		10^{-6}		10^{-2}	10^{-1}	10^{-1}	10^{-2}	
± 8.4		± 9.4		± 4.1		± 6.1		± 6.8		
\times		\times		\times		\times		\times		
10^{-3}		10^{-3}		10^{-7}		10^{-2}		10^{-2}		

TABLE A.2: Regression results for v_3 with SMASH IC at 0-5% centrality, $\sqrt{s_{NN}} = 200$ GeV.

coeff ϵ_2	p- value ϵ_2	coeff ϵ_3	p- value ϵ_3	coeff $\langle p_T^{IC} \rangle$	p- value $\langle p_T^{IC} \rangle$	coeff v_2^{IC}	p- value v_2^{IC}	coeff v_3^{IC}	p- value v_3^{IC}	r^2
2.53	0.00	-	-	-	-	-	-	-	-	0.869
\times										
10^{-1}										
± 3.6										
\times										
10^{-3}										
2.28	0.00	5.51	0.00	-	-	-	-	-	-	0.872
\times		\times								
10^{-1}		10^{-2}								
± 6.5		± 1.2								
\times		\times								
10^{-3}		10^{-2}								
1.60	0.00	-	-	1.91	0.00	-	-	-	-	0.885
\times				\times						
10^{-1}				10^{-5}						
± 9.6				± 1.9						
\times				\times						
10^{-3}				10^{-6}						
2.28	0.00	-	-	-	-	4.01	0.00	-	-	0.872
\times						\times				
10^{-1}						10^{-1}				
± 6.5						± 8.8				
\times						\times				
10^{-3}						10^{-2}				
2.03	0.00	3.37	0.01	-	-	2.61	0.00	3.30	0.00	0.876
\times		\times				\times		\times		
10^{-1}		10^{-2}				10^{-1}		10^{-1}		
± 8.4		± 1.3				± 9.3		± 1.1		
\times		\times				\times		\times		
10^{-3}		10^{-2}				10^{-2}		10^{-1}		
1.57	0.00	1.31	9.20	1.81	0.00	-7.09	9.41	1.26	2.38	0.885
\times		\times	\times	\times		\times	\times	\times	\times	
10^{-1}		10^{-3}	10^{-1}	10^{-5}		10^{-3}	10^{-1}	10^{-1}	10^{-1}	
± 1.0		± 1.3		± 2.3		± 9.5		± 1.1		
\times		\times		\times		\times		\times		
10^{-2}		10^{-2}		10^{-6}		10^{-2}		10^{-1}		

TABLE A.3: Regression results for v_3 with SMASH IC at 20-30% centrality, $\sqrt{s_{NN}} = 200$ GeV.

coeff ϵ_2	p- value ϵ_2	coeff ϵ_3	p- value ϵ_3	coeff $\langle p_T^{IC} \rangle$	p- value $\langle p_T^{IC} \rangle$	coeff v_2^{IC}	p- value v_2^{IC}	coeff v_3^{IC}	p- value v_3^{IC}	r^2
-	-	1.33	0.00	-	-	-	-	-	-	0.617
		\times								
		10^{-1}								
		± 3.8								
		\times								
		10^{-3}								
3.76	0.00	7.41	0.00	-	-	-	-	-	-	0.668
\times		\times								
10^{-2}		10^{-2}								
± 3.5		± 6.6								
\times		\times								
10^{-3}		10^{-3}								
-	-	4.64	0.00	1.03	0.00	-	-	-	-	0.700
		\times		\times						
		10^{-2}		10^{-5}						
		± 6.9		± 7.1						
		\times		\times						
		10^{-3}		10^{-7}						
-	-	9.11	0.00	-	-	3.85	0.00	-	-	0.654
		\times				\times				
		10^{-2}				10^{-1}				
		± 5.9				± 4.3				
		\times				\times				
		10^{-3}				10^{-2}				
2.31	0.00	6.16	0.00	-	-	1.79	0.00	1.61	0.01	0.678
\times		\times				\times		\times		
10^{-2}		10^{-2}				10^{-1}		10^{-1}		
± 4.6		± 6.9				± 5.0		± 5.8		
\times		\times				\times		\times		
10^{-3}		10^{-3}				10^{-2}		10^{-2}		
-7.00	8.97	4.48	0.00	9.44	0.00	3.91	4.49	5.52	3.40	0.701
\times	\times	\times		\times		\times	\times	\times	\times	
10^{-4}	10^{-1}	10^{-2}		10^{-6}		10^{-2}	10^{-1}	10^{-2}	10^{-1}	
± 5.4		± 7.1		± 1.3		± 5.2		± 5.8		
\times		\times		\times		\times		\times		
10^{-3}		10^{-3}		10^{-6}		10^{-2}		10^{-2}		

TABLE A.4: Regression results for v_3 with SMASH IC at 20-30% centrality, $\sqrt{s_{NN}} = 200$ GeV.

coeff ϵ_2	p-value ϵ_2	coeff ϵ_3	p-value ϵ_3	coeff $\langle p_T^{IC} \rangle$	p-value $\langle p_T^{IC} \rangle$	coeff ϵ_p	p-value ϵ_p	r^2
$4.39 \times 10^{-1} \pm 9.4 \times 10^{-3}$	0.00	-	-	-	-	-	-	0.745
$2.47 \times 10^{-1} \pm 1.2 \times 10^{-2}$	0.00	$2.68 \times 10^{-1} \pm 1.3 \times 10^{-2}$	0.00	-	-	-	-	0.838
$3.55 \times 10^{-2} \pm 1.0 \times 10^{-2}$	0.00	-	-	$5.99 \times 10^{-6} \pm 1.3 \times 10^{-7}$	0.00	-	-	0.930
$2.41 \times 10^{-1} \pm 1.2 \times 10^{-2}$	0.00	-	-	-	-	$4.02 \pm 2.0 \times 10^{-1}$	0.00	0.833
$1.67 \times 10^{-1} \pm 1.2 \times 10^{-2}$	0.00	$1.90 \times 10^{-1} \pm 1.3 \times 10^{-2}$	0.00	-	-	$2.74 \pm 2.0 \times 10^{-1}$	0.00	0.872
$3.36 \times 10^{-2} \pm 1.0 \times 10^{-2}$	0.00	$3.32 \times 10^{-2} \pm 1.1 \times 10^{-2}$	0.00	$5.37 \times 10^{-6} \pm 2.1 \times 10^{-7}$	0.00	$4.07 \times 10^{-1} \pm 1.7 \times 10^{-1}$	1.73×10^{-2}	0.931

TABLE A.5: Regression results for v_2 with IP-Glasma at 0-5% centrality, $\sqrt{s_{NN}} = 200$ GeV.

coeff ϵ_2	p-value	coeff ϵ_3	p-value	coeff $\langle p_T^{IC} \rangle$	p-value	coeff ϵ_p	p-value	r^2
		ϵ_2	ϵ_3	$\langle p_T^{IC} \rangle$	$\langle p_T^{IC} \rangle$	ϵ_p	ϵ_p	
-	-	$1.39 \times 10^{-1} \pm 3.5 \times 10^{-3}$	0.00	-	-	-	-	0.680
$5.60 \times 10^{-2} \pm 4.7 \times 10^{-3}$	0.00	$9.19 \times 10^{-2} \pm 5.1 \times 10^{-3}$	0.00	-	-	-	-	0.732
-	-	$3.53 \times 10^{-2} \pm 6.0 \times 10^{-3}$	0.00	$1.42 \times 10^{-6} \pm 7.2 \times 10^{-8}$	0.00	-	-	0.789
-	-	$8.84 \times 10^{-2} \pm 5.1 \times 10^{-3}$	0.00	-	-	$9.64 \times 10^{-1} \pm 7.6 \times 10^{-2}$	0.00	0.737
$3.62 \times 10^{-2} \pm 5.1 \times 10^{-3}$	0.00	$7.26 \times 10^{-2} \pm 5.4 \times 10^{-3}$	0.00	-	-	$6.84 \times 10^{-1} \pm 8.3 \times 10^{-2}$	0.00	0.754
$4.33 \times 10^{-3} \pm 5.5 \times 10^{-3}$	4.30×10^{-1}	$3.52 \times 10^{-2} \pm 6.0 \times 10^{-3}$	0.00	$1.28 \times 10^{-6} \pm 1.1 \times 10^{-7}$	0.00	$1.29 \times 10^{-1} \pm 9.1 \times 10^{-2}$	1.58×10^{-1}	0.790

TABLE A.6: Regression results for v_3 with IP-Glasma at 0-5% centrality, $\sqrt{s_{NN}} = 200$ GeV.

coeff ϵ_2	p-value ϵ_2	coeff ϵ_3	p-value ϵ_3	coeff $\langle p_T^{IC} \rangle$	p-value $\langle p_T^{IC} \rangle$	coeff ϵ_p	p-value ϵ_p	r^2
$2.77 \times 10^{-1} \pm 3.8 \times 10^{-3}$	0.00	-	-	-	-	-	-	0.879
$2.21 \times 10^{-1} \pm 6.6 \times 10^{-3}$	0.00	$1.08 \times 10^{-1} \pm 1.1 \times 10^{-2}$	0.00	-	-	-	-	0.894
$1.26 \times 10^{-1} \pm 7.8 \times 10^{-3}$	0.00	-	-	$1.17 \times 10^{-5} \pm 5.6 \times 10^{-7}$	0.00	-	-	0.924
$2.26 \times 10^{-1} \pm 6.5 \times 10^{-3}$	0.00	-	-	-	-	$1.84 \pm 2.0 \times 10^{-1}$	0.00	0.892
$1.92 \times 10^{-1} \pm 7.5 \times 10^{-3}$	0.00	$8.79 \times 10^{-2} \pm 1.1 \times 10^{-2}$	0.00	-	-	$1.43 \pm 1.9 \times 10^{-1}$	0.00	0.901
$1.19 \times 10^{-1} \pm 8.1 \times 10^{-3}$	0.00	$2.47 \times 10^{-2} \pm 1.0 \times 10^{-2}$	1.57×10^{-2}	$1.04 \times 10^{-5} \pm 6.8 \times 10^{-7}$	0.00	$3.97 \times 10^{-1} \pm 1.8 \times 10^{-1}$	2.98×10^{-2}	0.925

TABLE A.7: Regression results for ν_2 with IP-Glasma at 20-30% centrality, $\sqrt{s_{NN}} = 200$ GeV.

coeff ϵ_2	p-value ϵ_2	coeff ϵ_3	p-value ϵ_3	coeff $\langle p_T^{IC} \rangle$	p-value $\langle p_T^{IC} \rangle$	coeff ϵ_p	p-value ϵ_p	r^2
-	-	$1.45 \times 10^{-1} \pm 3.3 \times 10^{-3}$	0.00	-	-	-	-	0.725
$5.47 \times 10^{-2} \pm 3.2 \times 10^{-3}$	0.00	$7.04 \times 10^{-2} \pm 5.2 \times 10^{-3}$	0.00	-	-	-	-	0.801
-	-	$5.06 \times 10^{-2} \pm 5.5 \times 10^{-3}$	0.00	$4.78 \times 10^{-6} \pm 2.4 \times 10^{-7}$	0.00	-	-	0.818
-	-	$9.84 \times 10^{-2} \pm 4.8 \times 10^{-3}$	0.00	-	-	$1.12 \pm 8.9 \times 10^{-2}$	0.00	0.773
$4.41 \times 10^{-2} \pm 3.7 \times 10^{-3}$	0.00	$6.31 \times 10^{-2} \pm 5.3 \times 10^{-3}$	0.00	-	-	$5.19 \times 10^{-1} \pm 9.7 \times 10^{-2}$	0.00	0.808
$2.19 \times 10^{-2} \pm 4.4 \times 10^{-3}$	0.00	$4.38 \times 10^{-2} \pm 5.5 \times 10^{-3}$	0.00	$3.18 \times 10^{-6} \pm 3.7 \times 10^{-7}$	0.00	$2.03 \times 10^{-1} \pm 9.9 \times 10^{-2}$	4.02×10^{-2}	0.826

TABLE A.8: Regression results for v_3 with IP-Glasma at 20-30% centrality, $\sqrt{s_{NN}} = 200$ GeV.

coeff ϵ_2	p-value ϵ_2	coeff ϵ_3	p-value ϵ_3	coeff $\langle p_T^{IC} \rangle$	p-value $\langle p_T^{IC} \rangle$	coeff v_2^{IC}	p-value v_2^{IC}	coeff v_3^{IC}	p-value v_3^{IC}	r^2
2.52	0.00	-	-	-	-	-	-	-	-	0.616
$\times 10^{-1}$										
$\pm 7.3 \times 10^{-3}$										
1.96	0.00	7.88	0.00	-	-	-	-	-	-	0.636
$\times 10^{-1}$		$\times 10^{-2}$								
$\pm 1.1 \times 10^{-2}$		$\pm 1.2 \times 10^{-2}$								
1.67	0.00	-	-	9.01	0.00	-	-	-	-	0.638
$\times 10^{-1}$				$\times 10^{-6}$						
$\pm 1.4 \times 10^{-2}$				$\pm 1.3 \times 10^{-6}$						
2.04	0.00	-	-	-	-	1.85	0.00	-	-	0.630
$\times 10^{-1}$						$\times 10^{-1}$				
$\pm 1.1 \times 10^{-2}$						$\pm 3.4 \times 10^{-2}$				
1.75	0.00	5.44	0.00	-	-	9.14	2.18	6.02	1.98	0.640
$\times 10^{-1}$		$\times 10^{-2}$				$\times 10^{-2}$	$\times 10^{-2}$	$\times 10^{-2}$	$\times 10^{-1}$	
$\pm 1.3 \times 10^{-2}$		$\pm 1.5 \times 10^{-2}$				$\pm 4.0 \times 10^{-2}$		$\pm 4.7 \times 10^{-2}$		
1.65	0.00	4.13	1.22	4.32	7.07	4.98	2.79	1.70	7.46	0.642
$\times 10^{-1}$		$\times 10^{-2}$	$\times 10^{-2}$	$\times 10^{-6}$	$\times 10^{-2}$	$\times 10^{-2}$	$\times 10^{-1}$	$\times 10^{-2}$	$\times 10^{-1}$	
$\pm 1.5 \times 10^{-2}$		$\pm 1.6 \times 10^{-2}$		$\pm 2.4 \times 10^{-6}$		$\pm 4.6 \times 10^{-2}$		$\pm 5.2 \times 10^{-2}$		

TABLE A.9: Regression results for v_2 with SMASH IC at 0-5% centrality, $\sqrt{s_{NN}} = 17.3$ GeV.

coeff ϵ_2	p- value ϵ_2	coeff ϵ_3	p- value ϵ_3	coeff $\langle p_T^{IC} \rangle$	p- value $\langle p_T^{IC} \rangle$	coeff v_2^{IC}	p- value v_2^{IC}	coeff v_3^{IC}	p- value v_3^{IC}	r^2
-	-	1.01	0.00	-	-	-	-	-	-	0.097
		\times								
		10^{-1}								
		± 1.1								
		\times								
		10^{-2}								
2.78	8.83	7.71	0.00	-	-	-	-	-	-	0.101
\times	\times	\times								
10^{-2}	10^{-2}	10^{-2}								
± 1.6		± 1.8								
\times		\times								
10^{-2}		10^{-2}								
-	-	5.42	2.29	4.44	2.73	-	-	-	-	0.103
		\times	\times	\times	\times					
		10^{-2}	10^{-2}	10^{-6}	10^{-2}					
		± 2.4		± 2.0						
		\times		\times						
		10^{-2}		10^{-6}						
-	-	7.33	0.00	-	-	9.44	6.25	-	-	0.102
		\times				\times	\times			
		10^{-2}				10^{-2}	10^{-2}			
		± 1.8				± 5.1				
		\times				\times				
		10^{-2}				10^{-2}				
8.21	6.73	5.53	0.01	-	-	5.11	3.76	9.06	1.81	0.105
\times	\times	\times				\times	\times	\times	\times	
10^{-3}	10^{-1}	10^{-2}				10^{-2}	10^{-1}	10^{-2}	10^{-1}	
± 1.9		± 2.1				± 5.8		± 6.8		
\times		\times				\times		\times		
10^{-2}		10^{-2}				10^{-2}		10^{-2}		
5.26	8.04	5.16	3.09	1.22	7.25	3.93	5.56	7.85	3.03	0.105
\times	\times	\times	\times	\times	\times	\times	\times	\times	\times	
10^{-3}	10^{-1}	10^{-2}	10^{-2}	10^{-6}	10^{-1}	10^{-2}	10^{-1}	10^{-2}	10^{-1}	
± 2.1		± 2.4		± 3.5		± 6.7		± 7.6		
\times		\times		\times		\times		\times		
10^{-2}		10^{-2}		10^{-6}		10^{-2}		10^{-2}		

TABLE A.10: Regression results for v_3 with SMASH IC at 0-5% centrality, $\sqrt{s_{NN}} = 17.3$ GeV.

coeff ϵ_2	p- value ϵ_2	coeff ϵ_3	p- value ϵ_3	coeff $\langle p_T^{IC} \rangle$	p- value $\langle p_T^{IC} \rangle$	coeff v_2^{IC}	p- value v_2^{IC}	coeff v_3^{IC}	p- value v_3^{IC}	r^2
2.11	0.00	-	-	-	-	-	-	-	-	0.922
\times										
10^{-1}										
± 2.2										
\times										
10^{-3}										
1.94	0.00	3.92	0.00	-	-	-	-	-	-	0.925
\times		\times								
10^{-1}		10^{-2}								
± 3.9		± 7.6								
\times		\times								
10^{-3}		10^{-3}								
1.63	0.00	-	-	3.09	0.00	-	-	-	-	0.930
\times				\times						
10^{-1}				10^{-5}						
± 5.6				± 3.3						
\times				\times						
10^{-3}				10^{-6}						
1.94	0.00	-	-	-	-	1.23	0.00	-	-	0.925
\times						\times				
10^{-1}						10^{-1}				
± 4.0						± 2.5				
\times						\times				
10^{-3}						10^{-2}				
1.82	0.00	2.73	0.00	-	-	8.37	0.00	4.83	8.62	0.927
\times		\times				\times		\times	\times	
10^{-1}		10^{-2}				10^{-2}		10^{-2}	10^{-2}	
± 5.0		± 8.1				± 2.6		± 2.8		
\times		\times				\times		\times		
10^{-3}		10^{-3}				10^{-2}		10^{-2}	10^{-2}	
1.62	0.00	7.30	3.88	2.96	0.00	1.37	6.20	-2.11	4.73	0.931
\times		\times	\times	\times		\times	\times	\times	\times	
10^{-1}		10^{-3}	10^{-1}	10^{-5}		10^{-2}	10^{-1}	10^{-2}	10^{-1}	
± 5.7		± 8.5		± 4.5		± 2.8		± 2.9		
\times		\times		\times		\times		\times		
10^{-3}		10^{-3}		10^{-6}		10^{-2}		10^{-2}		

TABLE A.11: Regression results for v_2 with SMASH IC at 20-30% centrality, $\sqrt{s_{NN}} = 17.3$ GeV.

coeff ϵ_2	p- value ϵ_2	coeff ϵ_3	p- value ϵ_3	coeff $\langle p_T^{IC} \rangle$	p- value $\langle p_T^{IC} \rangle$	coeff v_2^{IC}	p- value v_2^{IC}	coeff v_3^{IC}	p- value v_3^{IC}	r^2
-	-	6.38	0.00	-	-	-	-	-	-	0.184
		\times								
		10^{-2}								
		± 4.9								
		\times								
		10^{-3}								
1.09	1.34	4.62	0.00	-	-	-	-	-	-	0.190
\times	\times	\times								
10^{-2}	10^{-2}	10^{-2}								
± 4.4		± 8.6								
\times		\times								
10^{-3}		10^{-3}								
-	-	3.57	0.00	9.79	0.00	-	-	-	-	0.195
		\times		\times						
		10^{-2}		10^{-6}						
		± 9.8		± 3.0						
		\times		\times						
		10^{-3}		10^{-6}						
-	-	5.36	0.00	-	-	4.03	1.06	-	-	0.187
		\times				\times	\times			
		10^{-2}				10^{-2}	10^{-1}			
		± 8.0				± 2.5				
		\times				\times				
		10^{-3}				10^{-2}				
7.93	1.70	4.34	0.00	-	-	4.53	8.81	2.80	3.86	0.191
\times	\times	\times				\times	\times	\times	\times	
10^{-3}	10^{-1}	10^{-2}				10^{-3}	10^{-1}	10^{-2}	10^{-1}	
± 5.8		± 9.3				± 3.0		± 3.2		
\times		\times				\times		\times		
10^{-3}		10^{-3}				10^{-2}		10^{-2}		
8.43	9.01	3.62	0.00	1.08	4.19	-2.09	5.22	2.79	9.36	0.196
\times	\times	\times		\times	\times	\times	\times	\times	\times	
10^{-4}	10^{-1}	10^{-2}		10^{-5}	10^{-2}	10^{-2}	10^{-1}	10^{-3}	10^{-1}	
± 6.7		± 1.0		± 5.3		± 3.3		± 3.5		
\times		\times		\times		\times		\times		
10^{-3}		10^{-2}		10^{-6}		10^{-2}		10^{-2}		

TABLE A.12: Regression results for v_3 with SMASH IC at 20-30% centrality, $\sqrt{s_{NN}} = 17.3$ GeV.

MAP of Parameters

The following table shows the maximum-a-posteriori of the parameters, equivalent to the golden lines in fig. 5.25, with 1σ -confidence interval.

Parameter	MAP	
R_\perp	$0.6321^{+0.7465}_{-0.3018}$	fm
R_η	$1.6955^{+0.3611}_{-0.6767}$	fm
$\tau_{\text{IC},\text{scale}}$	$1.3405^{+0.2889}_{-0.3019}$	
ϵ_{switch}	$0.5029^{+0.1612}_{-0.1668}$	$\frac{\text{GeV}}{\text{fm}^3}$
$a_{l,\eta}$	$-12.5323^{+7.8258}_{-1.6009}$	
$a_{h,\eta}$	$-11.7024^{+4.6039}_{-2.2125}$	
$T_{\eta,0}$	$0.1313^{+0.0395}_{-0.0267}$	GeV
$(\eta/s)_{\text{min}}$	$0.2185^{+0.0832}_{-0.0994}$	
a_{μ_B}	$3.2318^{+3.3766}_{-2.7164}$	
b_{μ_B}	$0.0373^{+0.3290}_{-0.2110}$	
ζ_0	$0.0916^{+0.0675}_{-0.0582}$	
ϵ_ζ	$25.7295^{+10.2582}_{-15.2152}$	$\frac{\text{GeV}}{\text{fm}^3}$
$\sigma_{\zeta,-}$	$0.0589^{+0.0289}_{-0.0344}$	
$\sigma_{\zeta,+}$	$0.0824^{+0.0457}_{-0.0480}$	
$\sigma_{\text{AB},\text{scale}}$	$0.9769^{+0.1451}_{-0.1240}$	

TABLE A.13: MAP of all parameters of the model.

MAP Observable Predictions

In the following, we show the maximum a posterior observable predictions in comparison to experimental data. These are in fact the data points from fig. 5.27 in linear scale. References for the experimental values can be found in table 5.4.

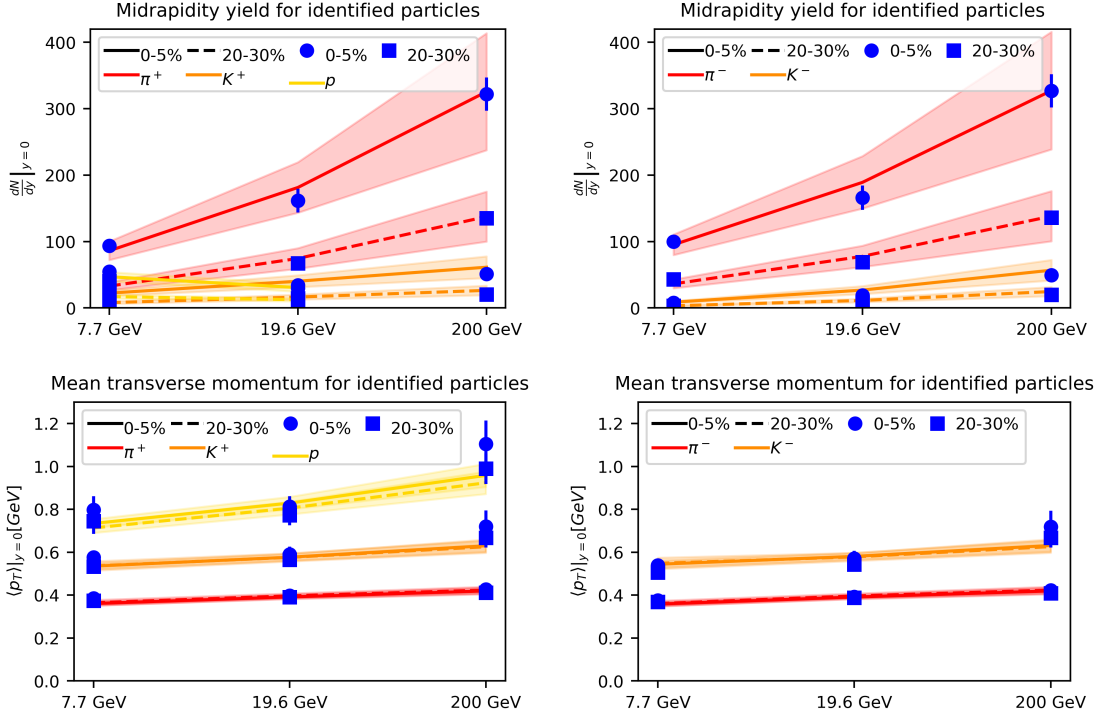


FIGURE A.1: Comparison of predictions of observables from the posterior with experimental values for bulk observables.

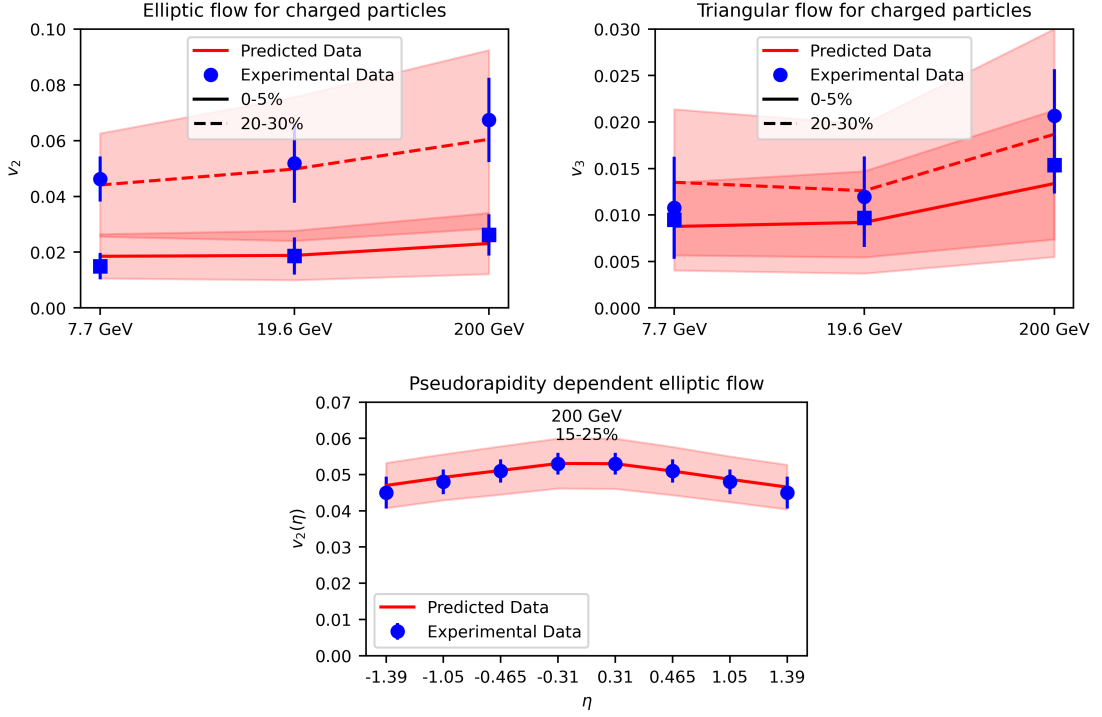


FIGURE A.2: Comparison of predictions of observables from the posterior with experimental values for flow data.

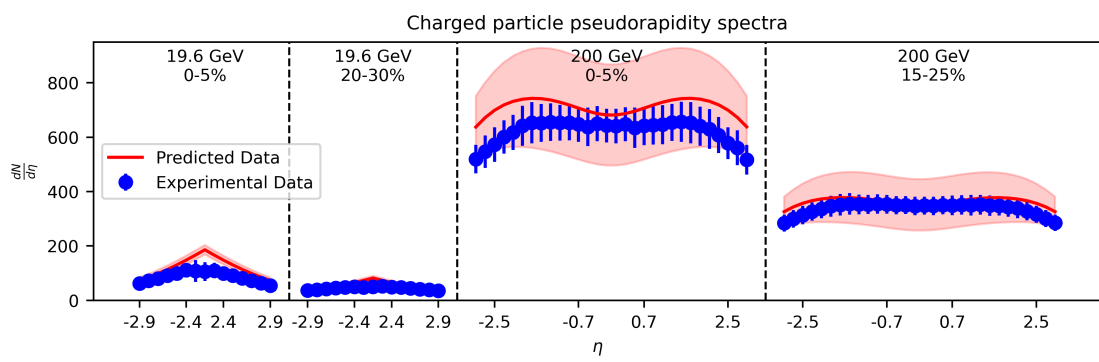


FIGURE A.3: Comparison of predictions of observables from the posterior with experimental values for pseudorapidity yields.

BIBLIOGRAPHY

1. Götz, N. & Elfner, H. Temperature and net baryochemical potential dependence of η/s in a hybrid approach. *Phys. Rev. C* **106**, 054904 (2022).
2. Götz, N., Constantin, L. & Elfner, H. Role of initial transverse momentum in a hybrid approach. *Phys. Rev. C* **110**, 034901 (2024).
3. Sass, N., Roch, H., Götz, N., Krupczak, R. & Rosenkvist, C. B. SPARKX: A Software Package for Analyzing Relativistic Kinematics in Collision Experiments (2025).
4. Götz, N., Karpenko, I. & Elfner, H. Bayesian analysis of a (3+1)D hybrid approach with initial conditions from hadronic transport (2025).
5. Goethe, J. *Faust. Der Tragödie erster Teil. Textausgabe mit editorischer Notiz: Goethe, Johann Wolfgang – Deutsch-Lektüre, Deutsche Klassiker der Literatur – 1* (Reclam Verlag, 2012).
6. Maxwell, J. C. A Dynamical Theory of the Electromagnetic Field. *Philosophical Transactions of the Royal Society of London* **155**, 459 (1865).
7. Planck, M. Über das Gesetz der Energieverteilung im Normalspectrum. *Annalen der Physik* **309**, 553 (1901).
8. Einstein, A. Über einen die Erzeugung und Verwandlung des Lichtes betreffenden heuristischen Gesichtspunkt. *Annalen der Physik* **322**, 132 (1905).
9. Einstein, A. Zur Elektrodynamik bewegter Körper. *Annalen der Physik* **322**, 891 (1905).
10. Einstein, A. Die Feldgleichungen der Gravitation. *Sitzungsberichte der Königlich Preußischen Akademie der Wissenschaften zu Berlin*, 844 (1915).
11. Wulf, A. *The Invention of Nature: Alexander von Humboldt's New World* (Knopf Doubleday Publishing Group, 2016).
12. Strano, G. *Galileo's Telescope: The Instrument that Changed the World* (Giunti, 2008).
13. Clark, R. *The Life of Bertrand Russell* (Bloomsbury Publishing, 2011).
14. Weinberg, S. A Model of Leptons. *Phys. Rev. Lett.* **19**, 1264 (21 1967).
15. Maldacena, J. M. The Large N limit of superconformal field theories and supergravity. *Adv. Theor. Math. Phys.* **2**, 231 (1998).
16. Henrich, D. & Pacini, D. *Between Kant and Hegel: Lectures on German Idealism* (Harvard University Press, 2009).
17. Brüning, O., Burkhardt, H. & Myers, S. The large hadron collider. *Progress in Particle and Nuclear Physics* **67**, 705 (2012).
18. Collier, P. The technical challenges of the Large Hadron Collider. *Philosophical Transactions of the Royal Society A: Mathematical, Physical and Engineering Sciences* **373**, 20140044 (2015).

19. Aad, G. *et al.* Observation of a new particle in the search for the Standard Model Higgs boson with the ATLAS detector at the LHC. *Phys. Lett. B* **716**, 1 (2012).
20. Chatrchyan, S. *et al.* Observation of a New Boson at a Mass of 125 GeV with the CMS Experiment at the LHC. *Phys. Lett. B* **716**, 30 (2012).
21. Popper, K. *The Logic of Scientific Discovery* (Harper & Row Publishers, 1968).
22. Brock, D. *Understanding Moore's Law: Four Decades of Innovation* (Chemical Heritage Foundation, 2006).
23. MissMJ, C. *Elementary particles included in the Standard Model* https://en.wikipedia.org/wiki/Elementary_particle. [Online; accessed 2024-Dec-15].
24. Gross, D. J. & Wilczek, F. Ultraviolet Behavior of Nonabelian Gauge Theories. *Phys. Rev. Lett.* **30** (ed Taylor, J. C.) 1343 (1973).
25. Politzer, H. D. Reliable Perturbative Results for Strong Interactions? *Phys. Rev. Lett.* **30** (ed Taylor, J. C.) 1346 (1973).
26. Bethke, S. α_s at Zinnowitz 2004. *Nucl. Phys. B Proc. Suppl.* **135** (eds Blumlein, J., Moch, S. O. & Riemann, T.) 345 (2004).
27. Gell-Mann, M. Symmetries of baryons and mesons. *Phys. Rev.* **125**, 1067 (1962).
28. Rapp, R., Wambach, J. & van Hees, H. The Chiral Restoration Transition of QCD and Low Mass Dileptons. *Landolt-Bornstein* **23**, 134 (2010).
29. Nambu, Y. & Jona-Lasinio, G. Dynamical model of elementary particles based on an analogy with superconductivity. II. *Phys. Rev.* **124** (ed Eguchi, T.) 246 (1961).
30. Wilson, K. G. Confinement of Quarks. *Phys. Rev.* **D10**, 2445 (1974).
31. Aoki, Y., Endrodi, G., Fodor, Z., Katz, S. D. & Szabo, K. K. The Order of the quantum chromodynamics transition predicted by the standard model of particle physics. *Nature* **443**, 675 (2006).
32. Bazavov, A. *et al.* The chiral and deconfinement aspects of the QCD transition. *Phys. Rev. D* **85**, 054503 (2012).
33. Bazavov, A. *et al.* Equation of state in (2+1)-flavor QCD. *Phys. Rev. D* **90**, 094503 (2014).
34. Borsanyi, S., Endrodi, G., Fodor, Z., Jakovac, A., Katz, S. D., Krieg, S., Ratti, C. & Szabo, K. K. The QCD equation of state with dynamical quarks. *JHEP* **11**, 077 (2010).
35. Borsanyi, S., Fodor, Z., Hoelbling, C., Katz, S. D., Krieg, S. & Szabo, K. K. Full result for the QCD equation of state with 2+1 flavors. *Phys. Lett. B* **730**, 99 (2014).
36. Philipsen, O. Lattice calculations at non zero chemical potential. *PoS*, 011 (2012).
37. Ratti, C. Lattice QCD and heavy ion collisions: a review of recent progress. *Rept. Prog. Phys.* **81**, 084301 (2018).
38. Nambu, Y. & Jona-Lasinio, G. Dynamical Model of Elementary Particles Based on an Analogy with Superconductivity. I. *Phys. Rev.* **122**, 345 (1961).
39. Nambu, Y. & Jona-Lasinio, G. Dynamical Model of Elementary Particles Based on an Analogy with Superconductivity. II. *Phys. Rev.* **124**, 246 (1961).

40. Machleidt, R. & Entem, D. R. Chiral effective field theory and nuclear forces. *Phys. Rept.* **503**, 1 (2011).
41. Gelis, F., Iancu, E., Jalilian-Marian, J. & Venugopalan, R. The Color Glass Condensate. *Ann. Rev. Nucl. Part. Sci.* **60**, 463 (2010).
42. Costa, P., de Sousa, C. A., Ruivo, M. C. & Kalinovsky, Y. L. The QCD critical end point in the SU(3) Nambu-Jona-Lasinio model. *Phys. Lett. B* **647**, 431 (2007).
43. Berges, J., Tetradis, N. & Wetterich, C. Nonperturbative renormalization flow in quantum field theory and statistical physics. *Phys. Rept.* **363**, 223 (2002).
44. Alkofer, R. & von Smekal, L. The Infrared behavior of QCD Green's functions: Confinement dynamical symmetry breaking, and hadrons as relativistic bound states. *Phys. Rept.* **353**, 281 (2001).
45. Alford, M. G., Schmitt, A., Rajagopal, K. & Schäfer, T. Color superconductivity in dense quark matter. *Rev. Mod. Phys.* **80**, 1455 (2008).
46. Gyulassy, M., Vitev, I., Wang, X.-N. & Zhang, B.-W. Jet quenching and radiative energy loss in dense nuclear matter (eds Hwa, R. C. & Wang, X. N.) (2003).
47. Kovtun, P., Son, D. T. & Starinets, A. O. Viscosity in strongly interacting quantum field theories from black hole physics. *Phys. Rev. Lett.* **94**, 111601 (2005).
48. Halasz, A. M., Jackson, A. D., Shrock, R. E., Stephanov, M. A. & Verbaarschot, J. J. M. On the phase diagram of QCD. *Phys. Rev. D* **58**, 096007 (1998).
49. Stephanov, M. A., Rajagopal, K. & Shuryak, E. V. Signatures of the tricritical point in QCD. *Phys. Rev. Lett.* **81**, 4816 (1998).
50. Berges, J. & Rajagopal, K. Color superconductivity and chiral symmetry restoration at nonzero baryon density and temperature. *Nucl. Phys. B* **538**, 215 (1999).
51. Rapp, R., Schäfer, T., Shuryak, E. V. & Velkovsky, M. High density QCD and instantons. *Annals Phys.* **280**, 35 (2000).
52. Yang, Z. & Chen, L.-W. Bayesian inference of the specific shear and bulk viscosities of the quark-gluon plasma at crossover from ϕ and Ω observables. *Phys. Rev. C* **107**, 064910 (2023).
53. Everett, D. *et al.* Phenomenological constraints on the transport properties of QCD matter with data-driven model averaging. *Phys. Rev. Lett.* **126**, 242301 (2021).
54. Everett, D. *et al.* Multisystem Bayesian constraints on the transport coefficients of QCD matter. *Phys. Rev. C* **103**, 054904 (2021).
55. Ghiglieri, J., Moore, G. D. & Teaney, D. QCD Shear Viscosity at (almost) NLO. *JHEP* **03**, 179 (2018).
56. Auvinen, J., Eskola, K. J., Huovinen, P., Niemi, H., Paatelainen, R. & Petreczky, P. Temperature dependence of η/s of strongly interacting matter: Effects of the equation of state and the parametric form of $(\eta/s)(T)$. *Phys. Rev. C* **102**, 044911 (2020).
57. Nijs, G., van der Schee, W., Gürsoy, U. & Snellings, R. Transverse Momentum Differential Global Analysis of Heavy-Ion Collisions. *Phys. Rev. Lett.* **126**, 202301 (2021).

58. Nijs, G., van der Schee, W., Gürsoy, U. & Snellings, R. Bayesian analysis of heavy ion collisions with the heavy ion computational framework Trajectum. *Phys. Rev. C* **103**, 054909 (2021).
59. Greiner, C., Noronha-Hostler, J. & Noronha, J. *Hagedorn States and Thermalization in Heavy Ion Collisions* 2011.
60. Gorenstein, M. I., Hauer, M. & Moroz, O. N. Viscosity in the excluded volume hadron gas model. *Phys. Rev. C* **77**, 024911 (2008).
61. Csernai, L. P., Kapusta, J. I. & McLerran, L. D. On the Strongly-Interacting Low-Viscosity Matter Created in Relativistic Nuclear Collisions. *Phys. Rev. Lett.* **97**, 152303 (2006).
62. Denicol, G. S., Gale, C., Jeon, S. & Noronha, J. Fluid behavior of a baryon-rich hadron resonance gas. *Phys. Rev. C* **88**, 064901 (2013).
63. Itakura, K., Morimatsu, O. & Otomo, H. Shear viscosity of a hadronic gas mixture. *Phys. Rev. D* **77**, 014014 (2008).
64. Kadam, G. P. & Mishra, H. Dissipative properties of hot and dense hadronic matter in an excluded-volume hadron resonance gas model. *Phys. Rev. C* **92**, 035203 (2015).
65. Demir, N. & Bass, S. A. Shear-Viscosity to Entropy-Density Ratio of a Relativistic Hadron Gas. *Phys. Rev. Lett.* **102**, 172302 (2009).
66. Heffernan, M. R., Gale, C., Jeon, S. & Paquet, J.-F. Early-Times Yang-Mills Dynamics and the Characterization of Strongly Interacting Matter with Statistical Learning. *Phys. Rev. Lett.* **132**, 252301 (2024).
67. Heffernan, M. R., Gale, C., Jeon, S. & Paquet, J.-F. Bayesian quantification of strongly interacting matter with color glass condensate initial conditions. *Phys. Rev. C* **109**, 065207 (2024).
68. Shen, C., Schenke, B. & Zhao, W. Viscosities of the Baryon-Rich Quark-Gluon Plasma from Beam Energy Scan Data. *Phys. Rev. Lett.* **132**, 072301 (2024).
69. Karsch, F., Kharzeev, D. & Tuchin, K. Universal properties of bulk viscosity near the QCD phase transition. *Phys. Lett. B* **663**, 217 (2008).
70. Rose, J. B., Torres-Rincon, J. M. & Elfner, H. Inclusive and effective bulk viscosities in the hadron gas. *J. Phys. G* **48**, 015005 (2020).
71. Shuryak, E. Physics of Strongly coupled Quark-Gluon Plasma. *Prog. Part. Nucl. Phys.* **62**, 48 (2009).
72. Baym, G., Hatsuda, T., Kojo, T., Powell, P. D., Song, Y. & Takatsuka, T. From hadrons to quarks in neutron stars: a review. *Rept. Prog. Phys.* **81**, 056902 (2018).
73. Bauswein, A., Bastian, N.-U. F., Blaschke, D. B., Chatzioannou, K., Clark, J. A., Fischer, T. & Oertel, M. Identifying a first-order phase transition in neutron star mergers through gravitational waves. *Phys. Rev. Lett.* **122**, 061102 (2019).
74. Friman, B., Hohne, C., Knoll, J., Leupold, S., Randrup, J., Rapp, R. & Senger, P. The CBM physics book: Compressed baryonic matter in laboratory experiments. *Lect. Notes Phys.* **814**, pp.1 (2011).

75. Spiller, P. & Franchetti, G. The FAIR accelerator project at GSI. *Nucl. Instrum. Meth. A* **561**, 305 (2006).

76. Turko, L. Looking for the Phase Transition—Recent NA61/SHINE Results. *Universe* **4** (eds Blaschke, D., Ayriyan, A., Friesen, A. & Grigorian, H.) 52 (2018).

77. Gazdzicki, M. Onset of Deconfinement and Critical Point: NA49 and NA61/SHINE at the CERN SPS. *Eur. Phys. J. ST* **155**, 37 (2008).

78. Agakishiev, G. *et al.* The High-Acceptance Dielectron Spectrometer HADES. *Eur. Phys. J. A* **41**, 243 (2009).

79. Ablyazimov, T. *et al.* Challenges in QCD matter physics –The scientific programme of the Compressed Baryonic Matter experiment at FAIR. *Eur. Phys. J. A* **53**, 60 (2017).

80. Armesto, N. & Scomparin, E. Heavy-ion collisions at the Large Hadron Collider: a review of the results from Run 1. *Eur. Phys. J. Plus* **131**, 52 (2016).

81. Adams, J. *et al.* Experimental and theoretical challenges in the search for the quark gluon plasma: The STAR Collaboration’s critical assessment of the evidence from RHIC collisions. *Nucl. Phys. A* **757**, 102 (2005).

82. Adcox, K. *et al.* Formation of dense partonic matter in relativistic nucleus-nucleus collisions at RHIC: Experimental evaluation by the PHENIX collaboration. *Nucl. Phys. A* **757**, 184 (2005).

83. Aamodt, K. *et al.* The ALICE experiment at the CERN LHC. *JINST* **3**, S08002 (2008).

84. Adler, C. *et al.* Disappearance of back-to-back high p_T hadron correlations in central Au+Au collisions at $\sqrt{s_{NN}} = 200$ GeV. *Phys. Rev. Lett.* **90**, 082302 (2003).

85. Muller, B. & Nagle, J. L. Results from the relativistic heavy ion collider. *Ann. Rev. Nucl. Part. Sci.* **56**, 93 (2006).

86. Back, B. B. *et al.* The PHOBOS perspective on discoveries at RHIC. *Nucl. Phys. A* **757**, 28 (2005).

87. Arsene, I. *et al.* Quark gluon plasma and color glass condensate at RHIC? The Perspective from the BRAHMS experiment. *Nucl. Phys. A* **757**, 1 (2005).

88. Kumar, L. Review of Recent Results from the RHIC Beam Energy Scan. *Mod. Phys. Lett. A* **28**, 1330033 (2013).

89. Barale, J. Performance of the Bevalac. *IEEE Trans. Nucl. Sci.* **22** (ed Mills, F. E.) 1672 (1975).

90. Alonso, J. R., Avery, R. T., Elioff, T., Force, R. J., Grunder, H. A., Lancaster, H. D., Meneghetti, J. R., Selph, F. B., Stevenson, R. R. & Yourd, R. B. Acceleration of Uranium at the Bevalac. *Science* **217**, 1135 (1982).

91. Malakhov, A. I. *The Main Physical Results at the Dubna Synchrophasotron in 11th International Workshop on Relativistic Nuclear Physics: from Hundreds of MeV to TeV* (2013), 6.

92. Kovalenko, A. *et al.* *Nuclotron at JINR: Operation Experience and Recent Development* in *13th International Conference on Heavy Ion Accelerator Technology* (2016), MOPA19.

93. Kuznetsov, A. B., Tuzikov, A. V. & Philippov, A. V. Gold ion beams induced desorption studies for Booster Nuclotron. *Phys. Part. Nucl. Lett.* **13**, 982 (2016).
94. Friman, B., Höhne, C., Knoll, J., Leupold, S., Randrup, J., Rapp, R. & Senger, P. *The CBM Physics Book: Compressed Baryonic Matter in Laboratory Experiments* (Springer Berlin Heidelberg, 2011).
95. *RHIC website* <https://www.osti.gov/scitech/servlets/purl/6955779>. [Online; accessed 2024-Dec-15].
96. *RHIC website* <http://www.rhichome.bnl.gov/RHIC/Runs/>. [Online; accessed 2024-Dec-15].
97. Pugh, H. G. Search for the Quark-Gluon Plasma (1989): The NA35 experiment at the CERN SPS. *Phys. Scripta T* **32**, 208 (1990).
98. Acharya, S. *et al.* Production of charged pions, kaons, and (anti-)protons in Pb-Pb and inelastic pp collisions at $\sqrt{s_{NN}} = 5.02$ TeV. *Phys. Rev. C* **101**, 044907 (2020).
99. Acharya, S. *et al.* Centrality and pseudorapidity dependence of the charged-particle multiplicity density in Xe–Xe collisions at $\sqrt{s_{NN}} = 5.44$ TeV. *Phys. Lett. B* **790**, 35 (2019).
100. Brewer, J., Mazeliauskas, A. & van der Schee, W. *Opportunities of OO and pO collisions at the LHC in Opportunities of OO and pO collisions at the LHC* (2021).
101. Schlichting, S. & Teaney, D. The First fm/c of Heavy-Ion Collisions. *Ann. Rev. Nucl. Part. Sci.* **69**, 447 (2019).
102. Heinz, U. & Snellings, R. Collective flow and viscosity in relativistic heavy-ion collisions. *Ann. Rev. Nucl. Part. Sci.* **63**, 123 (2013).
103. Andronic, A., Braun-Munzinger, P., Redlich, K. & Stachel, J. Decoding the phase structure of QCD via particle production at high energy. *Nature* **561**, 321 (2018).
104. Heinz, U. W. *Concepts of heavy ion physics* in *2nd CERN-CLAF School of High Energy Physics* (2004), 165.
105. Busza, W. & Goldhaber, A. S. Nuclear stopping power. *Phys. Lett. B* **139**, 235 (1984).
106. Cleymans, J., Oeschler, H., Redlich, K. & Wheaton, S. Comparison of chemical freeze-out criteria in heavy-ion collisions. *Phys. Rev. C* **73**, 034905 (2006).
107. Sattler, R. *Private communication* 2025.
108. Harris, S. *An Introduction to the Theory of the Boltzmann Equation* (Dover Publications, 2012).
109. Weil, J. *et al.* Particle production and equilibrium properties within a new hadron transport approach for heavy-ion collisions. *Phys. Rev. C* **94**, 054905 (2016).
110. Buss, O., Gaitanos, T., Gallmeister, K., van Hees, H., Kaskulov, M., Lalakulich, O., Larionov, A. B., Leitner, T., Weil, J. & Mosel, U. Transport-theoretical Description of Nuclear Reactions. *Phys. Rept.* **512**, 1 (2012).
111. Ehehalt, W. & Cassing, W. Relativistic transport approach for nucleus nucleus collisions from SIS to SPS energies. *Nucl. Phys. A* **602**, 449 (1996).

112. Danielewicz, P. Determination of the mean field momentum dependence using elliptic flow. *Nucl. Phys. A* **673**, 375 (2000).
113. Danielewicz, P. & Bertsch, G. Production of deuterons and pions in a transport model of energetic heavy ion reactions. *Nucl. Phys. A* **533**, 712 (1991).
114. Bass, S. A. *et al.* Microscopic models for ultrarelativistic heavy ion collisions. *Prog. Part. Nucl. Phys.* **41**, 255 (1998).
115. Hartnack, C., Li, Z. X., Neise, L., Peilert, G., Rosenhauer, A., Sorge, H., Stoecker, H., Greiner, W. & Aichelin, J. Quantum Molecular Dynamics: A Microscopic Model From Unilac to CERN Energies. *Nucl. Phys. A* **495**, 303C (1989).
116. Nara, Y., Otuka, N., Ohnishi, A., Niita, K. & Chiba, S. Study of relativistic nuclear collisions at AGS energies from p + Be to Au + Au with hadronic cascade model. *Phys. Rev. C* **61**, 024901 (2000).
117. Ono, A., Horiuchi, H., Maruyama, T. & Ohnishi, A. Antisymmetrized version of molecular dynamics with two nucleon collisions and its application to heavy ion reactions. *Prog. Theor. Phys.* **87**, 1185 (1992).
118. Sorge, H., Stoecker, H. & Greiner, W. Relativistic Quantum Molecular Dynamics approach to nuclear collisions at ultrarelativistic energies. *Nucl. Phys. A* **498** (eds Baym, G. A., Braun-Munzinger, P. & Nagamiya, S.) 567C (1989).
119. Cassing, W. & Bratkovskaya, E. L. Parton transport and hadronization from the dynamical quasiparticle point of view. *Phys. Rev. C* **78**, 034919 (2008).
120. Lin, Z.-W., Ko, C. M., Li, B.-A., Zhang, B. & Pal, S. A Multi-phase transport model for relativistic heavy ion collisions. *Phys. Rev. C* **72**, 064901 (2005).
121. Xu, Z. & Greiner, C. Thermalization of gluons in ultrarelativistic heavy ion collisions by including three-body interactions in a parton cascade. *Phys. Rev. C* **71**, 064901 (2005).
122. Zhang, B. ZPC 1.0.1: A Parton cascade for ultrarelativistic heavy ion collisions. *Comput. Phys. Commun.* **109**, 193 (1998).
123. Cugnon, J. Monte Carlo calculation of high-energy heavy-ion interactions. *Phys. Rev. C* **22**, 1885 (1980).
124. Yariv, Y. & Fraenkel, Z. Intranuclear cascade calculation of high-energy heavy-ion interactions. *Phys. Rev. C* **20**. [Erratum: Phys. Rev. C **21**, 2139–2139 (1980)], 2227 (1979).
125. Stoecker, H. & Greiner, W. High-Energy Heavy Ion Collisions: Probing the Equation of State of Highly Excited Hadronic Matter. *Phys. Rept.* **137**, 277 (1986).
126. Bertsch, G. F. & Das Gupta, S. A Guide to microscopic models for intermediate-energy heavy ion collisions. *Phys. Rept.* **160**, 189 (1988).
127. Mattiello, R., Sorge, H., Stoecker, H. & Greiner, W. K/π Ratios in Relativistic Nuclear Collisions: A Signature for the Quark - Gluon Plasma? *Phys. Rev. Lett.* **63**, 1459 (1989).
128. Kahana, S. H., Kahana, D. E., Pang, Y. & Schlagel, T. J. Modeling relativistic heavy ion collisions at the AGS. *Ann. Rev. Nucl. Part. Sci.* **46**, 31 (1996).

129. Bratkovskaya, E. L., Bleicher, M., Cassing, W., van Leeuwen, M., Reiter, M., Soff, S., Stoecker, H. & Weber, H. Strangeness dynamics in relativistic nucleus nucleus collision. *Prog. Part. Nucl. Phys.* **53** (ed Faessler, A.) 225 (2004).
130. Luzum, M. & Romatschke, P. Conformal Relativistic Viscous Hydrodynamics: Applications to RHIC results at $s(\text{NN})^{**}(1/2) = 200 \text{ GeV}$. *Phys. Rev. C* **78**. [Erratum: *Phys. Rev. C* **79**, 039903 (2009)], 034915 (2008).
131. Kolb, P. F. & Heinz, U. W. Hydrodynamic description of ultrarelativistic heavy ion collisions (eds Hwa, R. C. & Wang, X.-N.) 634 (2003).
132. Khachatryan, V. *et al.* Evidence for collectivity in pp collisions at the LHC. *Phys. Lett. B* **765**, 193 (2017).
133. Aad, G. *et al.* Observation of Long-Range Elliptic Azimuthal Anisotropies in $\sqrt{s} = 13$ and 2.76 TeV pp Collisions with the ATLAS Detector. *Phys. Rev. Lett.* **116**, 172301 (2016).
134. Shuryak, E. & Zahed, I. High-multiplicity pp and pA collisions: Hydrodynamics at its edge. *Phys. Rev. C* **88**, 044915 (2013).
135. Ollitrault, J.-Y. Relativistic hydrodynamics for heavy-ion collisions. *Eur. J. Phys.* **29**, 275 (2008).
136. Schukraft, J. QM2017: Status and Key open Questions in Ultra-Relativistic Heavy-Ion Physics. *Nucl. Phys. A* **967** (eds Heinz, U., Evdokimov, O. & Jacobs, P.) 1 (2017).
137. Rezzolla, L. & Zanotti, O. *Relativistic Hydrodynamics* (OUP Oxford, 2013).
138. Landau, L. D. On the multiparticle production in high-energy collisions. *Izv. Akad. Nauk Ser. Fiz.* **17**, 51 (1953).
139. Belenkij, S. Z. & Landau, L. D. Hydrodynamic theory of multiple production of particles. *Nuovo Cim. Suppl. S* **310**, 15 (1956).
140. Pang, L.-G., Zhou, K., Su, N., Petersen, H., Stoecker, H. & Wang, X.-N. An EoS-meter of QCD transition from deep learning (2016).
141. Huovinen, P. & Petreczky, P. QCD Equation of State and Hadron Resonance Gas. *Nucl. Phys. A* **837**, 26 (2010).
142. Allton, C. R., Ejiri, S., Hands, S. J., Kaczmarek, O., Karsch, F., Laermann, E., Schmidt, C. & Scorzato, L. The QCD thermal phase transition in the presence of a small chemical potential. *Phys. Rev. D* **66**, 074507 (2002).
143. Borsanyi, S., Endrodi, G., Fodor, Z., Katz, S. D., Krieg, S., Ratti, C. & Szabo, K. K. QCD equation of state at nonzero chemical potential: continuum results with physical quark masses at order μ^2 . *JHEP* **08**, 053 (2012).
144. Bellwied, R., Borsanyi, S., Fodor, Z., Katz, S. D., Pasztor, A., Ratti, C. & Szabo, K. K. Fluctuations and correlations in high temperature QCD. *Phys. Rev. D* **92**, 114505 (2015).
145. Fodor, Z. & Katz, S. D. A New method to study lattice QCD at finite temperature and chemical potential. *Phys. Lett. B* **534**, 87 (2002).

146. Giordano, M., Kapas, K., Katz, S. D., Nogradi, D. & Pasztor, A. Radius of convergence in lattice QCD at finite μ_B with rooted staggered fermions. *Phys. Rev. D* **101**, 074511 (2020).
147. Vovchenko, V., Pasztor, A., Fodor, Z., Katz, S. D. & Stoecker, H. Repulsive baryonic interactions and lattice QCD observables at imaginary chemical potential. *Phys. Lett. B* **775**, 71 (2017).
148. Guenther, J. N., Bellwied, R., Borsanyi, S., Fodor, Z., Katz, S. D., Pasztor, A., Ratti, C. & Szabó, K. K. The QCD equation of state at finite density from analytical continuation. *Nucl. Phys. A* **967** (eds Heinz, U., Evdokimov, O. & Jacobs, P.) 720 (2017).
149. Giordano, M., Kapas, K., Katz, S. D., Nogradi, D. & Pasztor, A. New approach to lattice QCD at finite density; results for the critical end point on coarse lattices. *JHEP* **05**, 088 (2020).
150. Steinheimer, J., Schramm, S. & Stocker, H. An Effective chiral Hadron-Quark Equation of State. *J. Phys. G* **38**, 035001 (2011).
151. Torres-Rincon, J. M. & Aichelin, J. Equation of state of a quark-meson mixture in the improved Polyakov–Nambu–Jona-Lasinio model at finite chemical potential. *Phys. Rev. C* **96**, 045205 (2017).
152. Peshier, A., Kampfer, B. & Soff, G. The Equation of state of deconfined matter at finite chemical potential in a quasiparticle description. *Phys. Rev. C* **61**, 045203 (2000).
153. Karthein, J. M., Mrocze, D., Nava Acuna, A. R., Noronha-Hostler, J., Parotto, P., Price, D. R. P. & Ratti, C. Strangeness-neutral equation of state for QCD with a critical point. *Eur. Phys. J. Plus* **136**, 621 (2021).
154. Sorensen, A. & Koch, V. Phase transitions and critical behavior in hadronic transport with a relativistic density functional equation of state (2020).
155. Vovchenko, V., Gorenstein, M. I. & Stoecker, H. Monte Carlo approach to the excluded-volume hadron resonance gas in grand canonical and canonical ensembles. *Phys. Rev. C* **98**, 064909 (2018).
156. Albright, M., Kapusta, J. & Young, C. Matching Excluded Volume Hadron Resonance Gas Models and Perturbative QCD to Lattice Calculations. *Phys. Rev. C* **90**, 024915 (2014).
157. Satarov, L. M., Dmitriev, M. N. & Mishustin, I. N. Equation of state of hadron resonance gas and the phase diagram of strongly interacting matter. *Phys. Atom. Nucl.* **72**, 1390 (2009).
158. Rischke, D. H., Gorenstein, M. I., Stoecker, H. & Greiner, W. Excluded volume effect for the nuclear matter equation of state. *Z. Phys. C* **51**, 485 (1991).
159. Noronha-Hostler, J., Noronha, J. & Greiner, C. Hadron Mass Spectrum and the Shear Viscosity to Entropy Density Ratio of Hot Hadronic Matter. *Phys. Rev. C* **86**, 024913 (2012).
160. Majumder, A. & Muller, B. Hadron Mass Spectrum from Lattice QCD. *Phys. Rev. Lett.* **105**, 252002 (2010).

161. Noronha-Hostler, J., Beitel, M., Greiner, C. & Shovkovy, I. Dynamics of Chemical Equilibrium of Hadronic Matter Close to T(c). *Phys. Rev. C* **81**, 054909 (2010).
162. Vovchenko, V., Anchishkin, D. V. & Gorenstein, M. I. Hadron Resonance Gas Equation of State from Lattice QCD. *Phys. Rev. C* **91**, 024905 (2015).
163. Kim, K.-Y., Sin, S.-J. & Zahed, I. The Chiral Model of Sakai-Sugimoto at Finite Baryon Density. *JHEP* **01**, 002 (2008).
164. Lope-Oter, E. & Llanes-Estrada, F. J. Unbiased interpolated neutron-star EoS at finite T for modified gravity studies (2021).
165. Motornenko, A., Steinheimer, J., Vovchenko, V., Schramm, S. & Stoecker, H. Equation of state for hot QCD and compact stars from a mean field approach. *Phys. Rev. C* **101**, 034904 (2020).
166. Israel, W. & Stewart, J. M. Transient relativistic thermodynamics and kinetic theory. *Annals Phys.* **118**, 341 (1979).
167. Denicol, G. S., Molnár, E., Niemi, H. & Rischke, D. H. Derivation of fluid dynamics from kinetic theory with the 14-moment approximation. *Eur. Phys. J. A* **48**, 170 (2012).
168. Teaney, D. The Effects of viscosity on spectra, elliptic flow, and HBT radii. *Phys. Rev. C* **68**, 034913 (2003).
169. Romatschke, P. & Romatschke, U. Viscosity Information from Relativistic Nuclear Collisions: How Perfect is the Fluid Observed at RHIC? *Phys. Rev. Lett.* **99**, 172301 (2007).
170. Schenke, B., Jeon, S. & Gale, C. Elliptic and triangular flow in event-by-event (3+1)D viscous hydrodynamics. *Phys. Rev. Lett.* **106**, 042301 (2011).
171. Song, H. & Heinz, U. W. Suppression of elliptic flow in a minimally viscous quark-gluon plasma. *Phys. Lett. B* **658**, 279 (2008).
172. Eckart, C. The Thermodynamics of irreversible processes. 3.. Relativistic theory of the simple fluid. *Phys. Rev.* **58**, 919 (1940).
173. Landau, L. D. & Lifshitz, E. M. *Fluid Mechanics* (Pergamon Press, 1959).
174. Denicol, G. S., Niemi, H., Molnar, E. & Rischke, D. H. Derivation of transient relativistic fluid dynamics from the Boltzmann equation. *Phys. Rev. D* **85**. [Erratum: *Phys. Rev.D91,no.3,039902(2015)*], 114047 (2012).
175. Molnar, E., Holopainen, H., Huovinen, P. & Niemi, H. Influence of temperature-dependent shear viscosity on elliptic flow at backward and forward rapidities in ultrarelativistic heavy-ion collisions. *Phys. Rev. C* **90**, 044904 (2014).
176. Niemi, H., Eskola, K. J., Paatelainen, R. & Tuominen, K. Pinning down QCD-matter shear viscosity in A + A collisions via EbyE fluctuations using pQCD + saturation + hydrodynamics. *Nucl. Phys. A* **956**, 312 (2016).
177. Karpenko, I. A., Huovinen, P., Petersen, H. & Bleicher, M. Estimation of the shear viscosity at finite net-baryon density from A + A collision data at $\sqrt{s_{NN}} = 7.7 - 200$ GeV. *Phys. Rev. C* **91**, 064901 (2015).

178. Strickland, M. Anisotropic Hydrodynamics: Three lectures. *Acta Phys. Polon. B* **45**, 2355 (2014).

179. Bazow, D., Heinz, U. W. & Strickland, M. Second-order (2+1)-dimensional anisotropic hydrodynamics. *Phys. Rev. C* **90**, 054910 (2014).

180. Shen, C. & Yan, L. Recent development of hydrodynamic modeling in heavy-ion collisions. *Nucl. Sci. Tech.* **31**, 122 (2020).

181. An, X., Başar, G., Stephanov, M. & Yee, H.-U. Fluctuation dynamics in a relativistic fluid with a critical point. *Phys. Rev. C* **102**, 034901 (2020).

182. Derradi de Souza, R., Koide, T. & Kodama, T. Hydrodynamic Approaches in Relativistic Heavy Ion Reactions. *Prog. Part. Nucl. Phys.* **86**, 35 (2016).

183. Bjorken, J. D. Highly Relativistic Nucleus-Nucleus Collisions: The Central Rapidity Region. *Phys. Rev. D* **27**, 140 (1983).

184. Gale, C., Jeon, S. & Schenke, B. Hydrodynamic Modeling of Heavy-Ion Collisions. *Int. J. Mod. Phys. A* **28**, 1340011 (2013).

185. Coleman-Smith, C. E., Petersen, H. & Wolpert, R. L. Classification of initial state granularity via 2d Fourier Expansion. *J. Phys. G* **40**, 095103 (2013).

186. Glauber, R. J. Cross-sections in deuterium at high-energies. *Phys. Rev.* **100**, 242 (1955).

187. Miller, M. L., Reygers, K., Sanders, S. J. & Steinberg, P. Glauber modeling in high energy nuclear collisions. *Ann. Rev. Nucl. Part. Sci.* **57**, 205 (2007).

188. Loizides, C., Nagle, J. & Steinberg, P. Improved version of the PHOBOS Glauber Monte Carlo. *SoftwareX* **1-2**, 13 (2015).

189. Schenke, B., Tribedy, P. & Venugopalan, R. Event-by-event gluon multiplicity, energy density, and eccentricities in ultrarelativistic heavy-ion collisions. *Phys. Rev. C* **86**, 034908 (2012).

190. Schenke, B., Tribedy, P. & Venugopalan, R. Fluctuating Glasma initial conditions and flow in heavy ion collisions. *Phys. Rev. Lett.* **108**, 252301 (2012).

191. Kharzeev, D. & Levin, E. Manifestations of high density QCD in the first RHIC data. *Phys. Lett. B* **523**, 79 (2001).

192. Drescher, H. J. & Nara, Y. Effects of fluctuations on the initial eccentricity from the Color Glass Condensate in heavy ion collisions. *Phys. Rev. C* **75**, 034905 (2007).

193. Lappi, T. & Venugopalan, R. Universality of the saturation scale and the initial eccentricity in heavy ion collisions. *Phys. Rev. C* **74**, 054905 (2006).

194. Weil, J., van Hees, H. & Mosel, U. Dilepton production in proton-induced reactions at SIS energies with the GiBUU transport model. *Eur. Phys. J. A* **48**. [Erratum: *Eur. Phys. J. A* **48**, 150 (2012)], 111 (2012).

195. Petersen, H., Qin, G.-Y., Bass, S. A. & Muller, B. Triangular flow in event-by-event ideal hydrodynamics in Au+Au collisions at $\sqrt{s_{NN}} = 200$ A GeV. *Phys. Rev. C* **82**, 041901 (2010).

196. Werner, K., Karpenko, I., Bleicher, M., Pierog, T. & Porteboeuf-Houssais, S. Jets, Bulk Matter, and their Interaction in Heavy Ion Collisions at Several TeV. *Phys. Rev. C* **85**, 064907 (2012).
197. Pang, L., Wang, Q. & Wang, X.-N. Effects of initial flow velocity fluctuation in event-by-event (3+1)D hydrodynamics. *Phys. Rev. C* **86**, 024911 (2012).
198. Gardim, F. G., Grassi, F., Luzum, M. & Ollitrault, J.-Y. Mapping the hydrodynamic response to the initial geometry in heavy-ion collisions. *Phys. Rev. C* **85**, 024908 (2012).
199. Auvinen, J. & Petersen, H. Evolution of elliptic and triangular flow as a function of $\sqrt{s_{NN}}$ in a hybrid model. *Phys. Rev. C* **88**, 064908 (2013).
200. Noronha-Hostler, J. *Resolving the R_{AA} to v_n puzzle in 8th International Conference on Hard and Electromagnetic Probes of High-energy Nuclear Collisions: Hard Probes 2016 (HP2016) Wuhan, Hubei, China, September 23-27, 2016* (2016).
201. Ivanov, Y. B. & Russkikh, V. N. What we have learned from 3-fluid hydrodynamics up to now. *PoS CPOD07*, 008 (2007).
202. Cimerman, J., Karpenko, I., Tomaszik, B. & Huovinen, P. Next-generation multifluid hydrodynamic model for nuclear collisions at sNN from a few GeV to a hundred GeV. *Phys. Rev. C* **107**, 044902 (2023).
203. Ivanov, Y. B., Russkikh, V. N. & Toneev, V. D. Relativistic heavy-ion collisions within 3-fluid hydrodynamics: Hadronic scenario. *Phys. Rev. C* **73**, 044904 (2006).
204. Ivanov, Y. B. Baryon Stopping as a Probe of Deconfinement Onset in Relativistic Heavy-Ion Collisions. *Phys. Lett. B* **721**, 123 (2013).
205. Ivanov, Y. B. Alternative Scenarios of Relativistic Heavy-Ion Collisions: III. Transverse Momentum Spectra. *Phys. Rev. C* **89**, 024903 (2014).
206. Ivanov, Y. B. Phase Evolution and Freeze-out within Alternative Scenarios of Relativistic Heavy-Ion Collisions. *Phys. Lett. B* **726**, 422 (2013).
207. Konchakovski, V. P., Cassing, W., Ivanov, Y. B. & Toneev, V. D. Examination of the directed flow puzzle in heavy-ion collisions. *Phys. Rev. C* **90**, 014903 (2014).
208. Harten, A., Lax, P. & van Leer, B. On Upstream Differencing and Godunov-Type Schemes for Hyperbolic Conservation Laws. *SIAM Rev* **25**, 35 (1983).
209. Einfeldt, B. On Godunov-Type Methods for Gas Dynamics. *Siam Journal on Numerical Analysis - SIAM J NUMER ANAL* **25**, 294 (1988).
210. Schneider, V., Katscher, U., Rischke, D. H., Waldhauser, B., Maruhn, J. A. & Munz, C. D. New algorithms for ultrarelativistic numerical hydrodynamics. *J. Comput. Phys.* **105**, 92 (1993).
211. Karpenko, I., Huovinen, P. & Bleicher, M. A 3+1 dimensional viscous hydrodynamic code for relativistic heavy ion collisions. *Comput. Phys. Commun.* **185**, 3016 (2014).
212. Okamoto, K., Akamatsu, Y. & Nonaka, C. A new relativistic hydrodynamics code for high-energy heavy-ion collisions. *Eur. Phys. J. C* **76**, 579 (2016).
213. Boris, J. P. & Book, D. L. Flux-corrected transport. I. SHASTA, a fluid transport algorithm that works. *Journal of Computational Physics* **11**, 38 (1973).

214. Book, D., Boris, J. & Hain, K. Flux-corrected transport II: Generalizations of the method. *Journal of Computational Physics* **18**, 248 (1975).

215. Boris, J. & Book, D. Flux-corrected transport. III. Minimal-error FCT algorithms. *Journal of Computational Physics* **20**, 397 (1976).

216. Kuzmin, D., Löhner, R. & Turek, S. *Flux-Corrected Transport* (Springer, 2005).

217. Pang, L.-G., Petersen, H. & Wang, X.-N. Pseudorapidity distribution and decorrelation of anisotropic flow within the open-computing-language implementation CLVisc hydrodynamics. *Phys. Rev. C* **97**, 064918 (2018).

218. Kurganov, A. & Tadmor, E. New High-Resolution Central Schemes for Nonlinear Conservation Laws and Convection–Diffusion Equations. *Journal of Computational Physics* **160**, 241 (2000).

219. Schenke, B., Jeon, S. & Gale, C. (3+1)D hydrodynamic simulation of relativistic heavy-ion collisions. *Phys. Rev. C* **82**, 014903 (2010).

220. Schenke, B., Jeon, S. & Gale, C. Higher flow harmonics from (3+1)D event-by-event viscous hydrodynamics. *Phys. Rev. C* **85**, 024901 (2012).

221. Schäfer, A., Karpenko, I., Wu, X.-Y., Hammelmann, J. & Elfner, H. Particle production in a hybrid approach for a beam energy scan of Au+Au/Pb+Pb collisions between $\sqrt{s_{NN}} = 4.3$ GeV and $\sqrt{s_{NN}} = 200.0$ GeV (2021).

222. Schäfer, A., Garcia-Montero, O., Paquet, J.-F., Elfner, H. & Gale, C. Out-of-Equilibrium Photon Production in the Late Stages of Relativistic Heavy-Ion Collisions (2021).

223. Cooper, F. & Frye, G. Comment on the Single Particle Distribution in the Hydrodynamic and Statistical Thermodynamic Models of Multiparticle Production. *Phys. Rev. D* **10**, 186 (1974).

224. Huovinen, P. & Petersen, H. Particlization in hybrid models. *Eur. Phys. J. A* **48**, 171 (2012).

225. Shen, C., Qiu, Z., Song, H., Bernhard, J., Bass, S. & Heinz, U. The iEBE-VISHNU code package for relativistic heavy-ion collisions. *Comput. Phys. Commun.* **199**, 61 (2016).

226. Chojnacki, M., Kisiel, A., Florkowski, W. & Broniowski, W. THERMINATOR 2: THERMal heavy IoN generATOR 2. *Comput. Phys. Commun.* **183**, 746 (2012).

227. Schwarz, C., Oliinychenko, D., Pang, L. .-, Ryu, S. & Petersen, H. Different Realizations of Cooper-Frye Sampling with Conservation Laws (2017).

228. Oliinychenko, D. & Koch, V. Microcanonical Particlization with Local Conservation Laws. *Phys. Rev. Lett.* **123**, 182302 (2019).

229. Vovchenko, V. Cooper-Frye sampling with short-range repulsion. *Phys. Rev. C* **106**, 064906 (2022).

230. Bass, S. A. & Dumitru, A. Dynamics of hot bulk QCD matter: From the quark gluon plasma to hadronic freezeout. *Phys. Rev. C* **61**, 064909 (2000).

231. Teaney, D., Lauret, J. & Shuryak, E. V. Flow at the SPS and RHIC as a quark gluon plasma signature. *Phys. Rev. Lett.* **86**, 4783 (2001).

232. Hirano, T., Huovinen, P., Murase, K. & Nara, Y. Integrated Dynamical Approach to Relativistic Heavy Ion Collisions. *Prog. Part. Nucl. Phys.* **70**, 108 (2013).

233. Petersen, H. Anisotropic flow in transport + hydrodynamics hybrid approaches. *J. Phys.* **G41**, 124005 (2014).

234. Teaney, D., Lauret, J. & Shuryak, E. V. A Hydrodynamic description of heavy ion collisions at the SPS and RHIC (2001).

235. Hirano, T., Heinz, U. W., Kharzeev, D., Lacey, R. & Nara, Y. Hadronic dissipative effects on elliptic flow in ultrarelativistic heavy-ion collisions. *Phys. Lett. B* **636**, 299 (2006).

236. Nonaka, C. & Bass, S. A. Space-time evolution of bulk QCD matter. *Phys. Rev. C* **75**, 014902 (2007).

237. Petersen, H., Steinheimer, J., Burau, G., Bleicher, M. & Stöcker, H. A Fully Integrated Transport Approach to Heavy Ion Reactions with an Intermediate Hydrodynamic Stage. *Phys. Rev. C* **78**, 044901 (2008).

238. Werner, K., Karpenko, I., Pierog, T., Bleicher, M. & Mikhailov, K. Event-by-Event Simulation of the Three-Dimensional Hydrodynamic Evolution from Flux Tube Initial Conditions in Ultrarelativistic Heavy Ion Collisions. *Phys. Rev. C* **82**, 044904 (2010).

239. Song, H., Bass, S. A., Heinz, U., Hirano, T. & Shen, C. 200 A GeV Au+Au collisions serve a nearly perfect quark-gluon liquid. *Phys. Rev. Lett.* **106**. [Erratum: *Phys. Rev. Lett.* **109**, 139904 (2012)], 192301 (2011).

240. Karpenko, I. A., Sinyukov, Y. M. & Werner, K. Uniform description of bulk observables in the hydrokinetic model of A + A collisions at the BNL Relativistic Heavy Ion Collider and the CERN Large Hadron Collider. *Phys. Rev. C* **87**, 024914 (2013).

241. Shen, C. *Dynamic modeling for heavy-ion collisions* in *19th International Conference on Strangeness in Quark Matter* (2021).

242. Schenke, B., Shen, C. & Tribedy, P. Running the gamut of high energy nuclear collisions. *Phys. Rev. C* **102**, 044905 (2020).

243. Auvinen, J., Redlich, K. & Bass, S. A. Multi-strange hadrons and the precision extraction of QGP properties in the RHIC-BES domain. *J. Phys. Conf. Ser.* **779**, 012045 (2017).

244. Bugaev, K. A. Relativistic kinetic equations for finite domains and freezeout problem. *Phys. Rev. Lett.* **90**, 252301 (2003).

245. Csernai, L. P., Magas, V. K., Molnar, E., Nyiri, A. & Tamosiunas, K. Freeze out and the Boltzmann transport equation (2004).

246. Molnar, E., Csernai, L. P., Magas, V. K., Nyiri, A. & Tamosiunas, K. Covariant description of kinetic freeze out through a finite space-like layer. *Phys. Rev. C* **74**, 024907 (2006).

247. Sinyukov, Y. M., Akkelin, S. V. & Hama, Y. On freezeout problem in hydro kinetic approach to A+A collisions. *Phys. Rev. Lett.* **89**, 052301 (2002).

248. Akkelin, S. V., Hama, Y., Karpenko, I. A. & Sinyukov, Y. M. Hydro-kinetic approach to relativistic heavy ion collisions. *Phys. Rev. C* **78**, 034906 (2008).

249. S. Tiwari, A. K. & Hardt, S. A particle–particle hybrid method for kinetic and continuum equations. *Journal of Computational Physics* **228**, 7109 (2009).

250. F.H. Harlow, A. A. & Nix, J. Relativistic fluid dynamics calculations with the particle-in-cell technique. *J. Comp. Phys.* **20**, 119 (1976).

251. Oliinychenko, D. & Petersen, H. Forced canonical thermalization in a hadronic transport approach at high density. *J. Phys. G* **44**, 034001 (2017).

252. Steinheimer, J. & Bleicher, M. Core-corona separation in the UrQMD hybrid model. *Phys. Rev. C* **84**, 024905 (2011).

253. Akamatsu, Y., Asakawa, M., Hirano, T., Kitazawa, M., Morita, K., Murase, K., Nara, Y., Nonaka, C. & Ohnishi, A. Dynamically integrated transport approach for heavy-ion collisions at high baryon density. *Phys. Rev. C* **98**, 024909 (2018).

254. SMASH source code <https://github.com/smash-transport/smash>. [Online; accessed 2025-Dec-16].

255. SMASH Analysis Suite <https://github.com/smash-transport/smash-analysis>. [Online; accessed 2025-Dec-16].

256. SMASH documentation <http://theory.gsi.de/~smash/doc/current/>. [Online; accessed 2025-Dec-16].

257. Cassing, W. & Bratkovskaya, E. L. Hadronic and electromagnetic probes of hot and dense nuclear matter. *Phys. Rept.* **308**, 65 (1999).

258. Mohs, J., Ege, M., Elfner, H. & Mayer, M. Collective flow at SIS energies within a hadronic transport approach: Influence of light nuclei formation and equation of state (2020).

259. Steinberg, V., Staudenmaier, J., Oliinychenko, D., Li, F., Erkiner, Ö. & Elfner, H. Strangeness production via resonances in heavy-ion collisions at energies available at the GSI Schwerionensynchrotron. *Phys. Rev. C* **99**, 064908 (2019).

260. Steinberg, V., Steinheimer, J., Elfner, H. & Bleicher, M. Constraining resonance properties through kaon production in pion–nucleus collisions at low energies. *J. Phys. G* **48**, 025109 (2021).

261. Mohs, J., Ryu, S. & Elfner, H. Particle Production via Strings and Baryon Stopping within a Hadronic Transport Approach. *J. Phys. G* **47**, 065101 (2020).

262. Oliinychenko, D., Pang, L.-G., Elfner, H. & Koch, V. Centrality dependence of deuteron production in Pb+Pb collisions at 2.76 TeV via hydrodynamics and hadronic afterburner. *MDPI Proc.* **10** (eds Albacete, J., Bielcikova, J., Grelli, A., Jia, J., Noronha, J., Elfner (nee Petersen), H., Ruan, L., Salur, S., Schenke, B. & Timmins, A.) 6 (2019).

263. Oliinychenko, D., Shen, C. & Koch, V. Deuteron production in AuAu collisions at $\sqrt{s_{NN}} = 7\text{--}200$ GeV via pion catalysis. *Phys. Rev. C* **103**, 034913 (2021).

264. Schäfer, A., Torres-Rincon, J. M., Rothermel, J., Ehlert, N., Gale, C. & Elfner, H. Benchmarking a nonequilibrium approach to photon emission in relativistic heavy-ion collisions. *Phys. Rev. D* **99**, 114021 (2019).

265. Oliinychenko, D. & Shen, C. Resonance production in PbPb collisions at 5.02 TeV via hydrodynamics and hadronic afterburner (2021).

266. Rose, J. B., Torres-Rincon, J. M., Schäfer, A., Oliinychenko, D. R. & Petersen, H. Shear viscosity of a hadron gas and influence of resonance lifetimes on relaxation time. *Phys. Rev. C* **97**, 055204 (2018).

267. Hammelmann, J., Staudenmaier, J. & Elfner, H. Collision term dependence of the hadronic shear viscosity and diffusion coefficients (2023).

268. Hammelmann, J., Torres-Rincon, J. M., Rose, J.-B., Greif, M. & Elfner, H. Electrical conductivity and relaxation via colored noise in a hadronic gas. *Phys. Rev. D* **99**, 076015 (2019).

269. Rose, J.-B., Greif, M., Hammelmann, J., Fotakis, J. A., Denicol, G. S., Elfner, H. & Greiner, C. Cross-conductivity: novel transport coefficients to constrain the hadronic degrees of freedom of nuclear matter. *Phys. Rev. D* **101**, 114028 (2020).

270. Hammelmann, J., Bluhm, M., Nahrgang, M. & Elfner, H. Fate of critical fluctuations in an interacting hadronic medium using maximum-entropy distributions. *Phys. Rev. C* **110**, 054910 (2024).

271. Zhang, Y.-X. *et al.* Comparison of heavy-ion transport simulations: Collision integral in a box. *Phys. Rev. C* **97**, 034625 (2018).

272. Ono, A. *et al.* Comparison of heavy-ion transport simulations: Collision integral with pions and Δ resonances in a box. *Phys. Rev. C* **100**, 044617 (2019).

273. Colonna, M. *et al.* Comparison of heavy-ion transport simulations: Mean-field dynamics in a box. *Phys. Rev. C* **104**, 024603 (2021).

274. Zyla, P. *et al.* Review of Particle Physics. *PTEP* **2020**, 083C01 (2020).

275. Wergieluk, A., Weil, J., Tindall, J., Steinberg, V., Staudenmaier, J., Sorensen, A., Sciarra, A., Schäfer, A., Sattler, R., Ryu, S., Rothermel, J., Rose, J.-B., Roch, H., Prinz, L., Petersen, H., Paulinyova, Z., Pang, L.-G., Oliinychenko, D., Mohs, J., Mitrovic, D., Mayer, M., Li, F., Kübler, N., Kretz, M., Kehrenberg, T., Inghirami, G., Hirayama, R., Hammelmann, J., Götz, N., Groebel, J., Goldschmidt, A., Geiger, L., Garcia-Montero, O., Elfner, H., Ehlert, N., Christensen, C. H., Bäuchle, B., Auvinen, J. & Attems, M. *smash-transport/smash: SMASH-3.1* version SMASH-3.1. 2024.

276. Rosenkvist, C. & Elfner, H. (in preparation).

277. Ege, M., Mohs, J., Staudenmaier, J. & Elfner, H. Deuteron, triton, helium-3 and hypertriton production in relativistic heavy-ion collisions via stochastic multi-particle reactions (2024).

278. Staudenmaier, J., Weil, J., Steinberg, V., Endres, S. & Petersen, H. Dilepton production and resonance properties within a new hadronic transport approach in the context of the GSI-HADES experimental data. *Phys. Rev. C* **98**, 054908 (2018).

279. Manley, D. M. & Saleski, E. M. Multichannel resonance parametrization of π N scattering amplitudes. *Phys. Rev. D* **45**, 4002 (1992).

280. Blatt, J. M. & Weisskopf, V. F. *Theoretical Nuclear Physics* (Wiley, 1958).

281. Post, M., Leupold, S. & Mosel, U. Hadronic spectral functions in nuclear matter. *Nucl. Phys. A* **741**, 81 (2004).

282. Tindall, J., Torres-Rincon, J. M., Rose, J. B. & Petersen, H. Equilibration and freeze-out of an expanding gas in a transport approach in a Friedmann–Robertson–Walker metric. *Phys. Lett. B* **770**, 532 (2017).

283. Xu, J. *et al.* Understanding transport simulations of heavy-ion collisions at 100A and 400A MeV: Comparison of heavy-ion transport codes under controlled conditions. *Phys. Rev. C* **93**, 044609 (2016).

284. Weil, J. *Vector Mesons in Medium in a Transport Approach* PhD thesis (Justus-Liebig-Universität, Gießen, 2013).

285. San Martin, J. S., Hirayama, R., Hammelmann, J., Karthein, J. M., Parotto, P., Noronha-Hostler, J., Ratti, C. & Elfner, H. Thermodynamics of an updated hadronic resonance list and influence on hadronic transport (2023).

286. *SMASH cross section results* http://theory.gsi.de/~smash/analysis_suite/SMASH-3.1/cross_sections/. Accessed: 2025-Dec-12.

287. Goulianos, K. A. Diffractive Interactions of Hadrons at High-Energies. *Phys. Rept.* **101**, 169 (1983).

288. Balinovic, B., Hirayama, R. & Elfner, H. Collisional Broadening within a Hadronic Transport Approach. *Universe* **9**, 414 (2023).

289. Cugnon, J., Vandermeulen, J. & L'Hote, D. Simple parametrization of cross-sections for nuclear transport studies up to the GeV range. *Nucl. Instrum. Meth. B* **111**, 215 (1996).

290. Andersson, B., Gustafson, G., Ingelman, G. & Sjostrand, T. Parton Fragmentation and String Dynamics. *Phys. Rept.* **97**, 31 (1983).

291. Sjöstrand, T., Ask, S., Christiansen, J. R., Corke, R., Desai, N., Ilten, P., Mrenna, S., Prestel, S., Rasmussen, C. O. & Skands, P. Z. An introduction to PYTHIA 8.2. *Comput. Phys. Commun.* **191**, 159 (2015).

292. Bleicher, M. *et al.* Relativistic hadron hadron collisions in the ultrarelativistic quantum molecular dynamics model. *J. Phys. G* **25**, 1859 (1999).

293. *SMASH detailed balance results* http://theory.gsi.de/~smash/analysis_suite/SMASH-3.1/detailed_balance/. Accessed: 2025-Dec-12.

294. Hirano, T. & Nara, Y. Dynamical modeling of high energy heavy ion collisions. *PTEP* **2012**, 01A203 (2012).

295. Staudenmaier, J. *Multi-particle interactions in hadronic transport approaches* PhD thesis (Goethe U., Frankfurt (main), Goethe U., Frankfurt (main), 2021).

296. Prinz, L. *Exzentrizitäten im Anfangszustand von Schwerionenkollisionen deformierter Kerne* B.Sc. Thesis, Goethe-Universität, Frankfurt am Main. 2020.

297. Sass, N., Müller, M., Garcia-Montero, O. & Elfner, H. Global angular momentum generation in heavy-ion reactions within a hadronic transport approach. *Phys. Rev. C* **108**, 044903 (2023).

298. Dorau, P., Rose, J.-B., Pablos, D. & Elfner, H. Jet Quenching in the Hadron Gas: An Exploratory Study. *Phys. Rev. C* **101**, 035208 (2020).

299. *vHLL input file collection* https://github.com/yukarpenko/vhll_params. [Online; accessed 2025-Dec-16].

300. Israel, W. Nonstationary irreversible thermodynamics: A Causal relativistic theory. *Annals Phys.* **100**, 310 (1976).

301. Takamoto, M. & Inutsuka, S.-i. A Fast Numerical Scheme for Causal Relativistic Hydrodynamics with Dissipation. *J. Comput. Phys.* **230**, 7002 (2011).

302. Amiram, H., Peter D., L. & Bram van, L. On Upstream Differencing and Godunov-Type Schemes for Hyperbolic Conservation Laws. *SIAM Rev.* **25**, 35 (2006).

303. Godunov, S. K. & Bohachevsky, I. Finite difference method for numerical computation of discontinuous solutions of the equations of fluid dynamics. *Matematicheskij sbornik* **47**, 271 (1959).

304. Courant, R., Friedrichs, K. & Lewy, H. Über die partiellen Differenzengleichungen der mathematischen Physik. *Math. Ann.* **100**, 32 (1928).

305. Rischke, D. H., Bernard, S. & Maruhn, J. A. Relativistic hydrodynamics for heavy ion collisions. 1. General aspects and expansion into vacuum. *Nucl. Phys. A* **595**, 346 (1995).

306. Constantin, L. *Vergleich von Anfangszustandsmodellen zur hydrodynamischen Beschreibung von Schwerionenkollisionen* B.Sc. Thesis, Goethe-Universität, Frankfurt am Main. 2022.

307. Moreland, J. S., Bernhard, J. E. & Bass, S. A. Alternative ansatz to wounded nucleon and binary collision scaling in high-energy nuclear collisions. *Phys. Rev. C* **92**, 011901 (2015).

308. Everett, D. *et al.* Role of bulk viscosity in deuteron production in ultrarelativistic nuclear collisions. *Phys. Rev. C* **106**, 064901 (2022).

309. Bernhard, J. E., Moreland, J. S. & Bass, S. A. Bayesian estimation of the specific shear and bulk viscosity of quark–gluon plasma. *Nature Phys.* **15**, 1113 (2019).

310. Bernhard, J. E., Moreland, J. S., Bass, S. A., Liu, J. & Heinz, U. Applying Bayesian parameter estimation to relativistic heavy-ion collisions: simultaneous characterization of the initial state and quark-gluon plasma medium. *Phys. Rev. C* **94**, 024907 (2016).

311. Niemi, H., Eskola, K. J. & Paatelainen, R. Event-by-event fluctuations in a perturbative QCD + saturation + hydrodynamics model: Determining QCD matter shear viscosity in ultrarelativistic heavy-ion collisions. *Phys. Rev. C* **93**, 024907 (2016).

312. Soeder, D., Ke, W., Paquet, J. F. & Bass, S. A. Bayesian parameter estimation with a new three-dimensional initial-conditions model for ultrarelativistic heavy-ion collisions (2023).

313. Kowalski, H. & Teaney, D. An Impact parameter dipole saturation model. *Phys. Rev. D* **68**, 114005 (2003).

314. Bartels, J., Golec-Biernat, K. J. & Kowalski, H. A modification of the saturation model: DGLAP evolution. *Phys. Rev. D* **66**, 014001 (2002).

315. Krasnitz, A. & Venugopalan, R. Nonperturbative computation of gluon minijet production in nuclear collisions at very high-energies. *Nucl. Phys. B* **557**, 237 (1999).

316. Kovner, A., McLerran, L. D. & Weigert, H. Gluon production from nonAbelian Weizsäcker-Williams fields in nucleus-nucleus collisions. *Phys. Rev. D* **52**, 6231 (1995).

317. Lappi, T., Srednyak, S. & Venugopalan, R. Non-perturbative computation of double inclusive gluon production in the Glasma. *JHEP* **01**, 066 (2010).

318. Gelis, F., Lappi, T. & McLerran, L. Glittering Glasma. *Nucl. Phys. A* **828**, 149 (2009).

319. Hirayama, R., Paulinyová, Z. & Elfner, H. *A dynamically initialized hybrid approach with varying equations of state* https://indico.cern.ch/event/1043736/contributions/5363945/attachments/2690904/4669564/Poster_IS23_Hirayama.pdf. Accessed: 2025-Dec-12.

320. Steinheimer, J., Schramm, S. & Stocker, H. The hadronic SU(3) Parity Doublet Model for Dense Matter, its extension to quarks and the strange equation of state. *Phys. Rev. C* **84**, 045208 (2011).

321. Most, E. R., Motornenko, A., Steinheimer, J., Dexheimer, V., Hanuske, M., Rezzolla, L. & Stoecker, H. Probing neutron-star matter in the lab: Similarities and differences between binary mergers and heavy-ion collisions. *Phys. Rev. D* **107**, 043034 (2023).

322. Denicol, G. S., Jeon, S. & Gale, C. Transport Coefficients of Bulk Viscous Pressure in the 14-moment approximation. *Phys. Rev. C* **90**, 024912 (2014).

323. Ryu, S., Paquet, J. F., Shen, C., Denicol, G. S., Schenke, B., Jeon, S. & Gale, C. Importance of the Bulk Viscosity of QCD in Ultrarelativistic Heavy-Ion Collisions. *Phys. Rev. Lett.* **115**, 132301 (2015).

324. Denicol, G. S., Koide, T. & Rischke, D. H. Dissipative relativistic fluid dynamics: a new way to derive the equations of motion from kinetic theory. *Phys. Rev. Lett.* **105**, 162501 (2010).

325. Chapman, S., Cowling, T., Burnett, D. & Cercignani, C. *The Mathematical Theory of Non-uniform Gases: An Account of the Kinetic Theory of Viscosity, Thermal Conduction and Diffusion in Gases* (Cambridge University Press, 1990).

326. Lacey, R. A., Ajitanand, N. N., Alexander, J. M., Chung, P., Holzmann, W. G., Issah, M., Taranenko, A., Danielewicz, P. & Stoecker, H. Has the QCD Critical Point been Signaled by Observations at RHIC? *Phys. Rev. Lett.* **98**, 092301 (2007).

327. He, W.-b., Shao, G.-y., Xie, C.-l. & Xu, R.-x. Shear viscosity of quark-gluon plasma at finite temperature and chemical potential and QCD phase transitions (2024).

328. Petreczky, P. & Teaney, D. Heavy quark diffusion from the lattice. *Phys. Rev. D* **73**, 014508 (2006).

329. Aarts, G. & Resco, J. M. M. Transport coefficients, spectral functions and the lattice. *Journal of High Energy Physics* **2002**, 053 (2002).

330. Moore, G. D. *Shear viscosity in QCD and why it's hard to calculate in Criticality in QCD and the Hadron Resonance Gas* (2020).

331. Auvinen, J., Bernhard, J. E., Bass, S. A. & Karpenko, I. Investigating the collision energy dependence of η/s in the beam energy scan at the BNL Relativistic Heavy Ion Collider using Bayesian statistics. *Phys. Rev. C* **97**, 044905 (2018).

332. Nakamura, A. & Sakai, S. Transport coefficients of gluon plasma. *Phys. Rev. Lett.* **94**, 072305 (2005).

333. Meyer, H. B. A Calculation of the shear viscosity in SU(3) gluodynamics. *Phys. Rev. D* **76**, 101701 (2007).

334. Astrakhantsev, N., Braguta, V. & Kotov, A. Temperature dependence of shear viscosity of SU(3)-gluodynamics within lattice simulation. *JHEP* **04**, 101 (2017).

335. Altenkort, L., Eller, A. M., Francis, A., Kaczmarek, O., Mazur, L., Moore, G. D. & Shu, H.-T. Viscosity of pure-glue QCD from the lattice. *Phys. Rev. D* **108**, 014503 (2023).

336. Shen, C. & Heinz, U. The road to precision: Extraction of the specific shear viscosity of the quark-gluon plasma. *Nucl. Phys. News* **25**, 6 (2015).

337. Schenke, B., Shen, C. & Tribedy, P. Multi-particle and charge-dependent azimuthal correlations in heavy-ion collisions at the Relativistic Heavy-Ion Collider. *Phys. Rev. C* **99**, 044908 (2019).

338. Ryu, S., Paquet, J.-F., Shen, C., Denicol, G., Schenke, B., Jeon, S. & Gale, C. Effects of bulk viscosity and hadronic rescattering in heavy ion collisions at energies available at the BNL Relativistic Heavy Ion Collider and at the CERN Large Hadron Collider. *Phys. Rev. C* **97**, 034910 (2018).

339. Gardim, F. G. & Ollitrault, J.-Y. Effective shear and bulk viscosities for anisotropic flow. *Phys. Rev. C* **103**, 044907 (2021).

340. *SMASH-hadron-sampler* <https://github.com/smash-transport/smash-hadron-sampler>. Accessed: 2025-Dec-12.

341. Mc Nelis, M., Everett, D. & Heinz, U. Particilization in fluid dynamical simulations of heavy-ion collisions: The i S3D module. *Comput. Phys. Commun.* **258**, 107604 (2021).

342. Dusling, K., Moore, G. D. & Teaney, D. Radiative energy loss and $v(2)$ spectra for viscous hydrodynamics. *Phys. Rev. C* **81**, 034907 (2010).

343. Monnai, A. & Hirano, T. Effects of Bulk Viscosity at Freezeout. *Phys. Rev. C* **80**, 054906 (2009).

344. Dusling, K. & Schäfer, T. Bulk viscosity, particle spectra and flow in heavy-ion collisions. *Phys. Rev. C* **85**, 044909 (2012).

345. Bhatnagar, P. L., Gross, E. P. & Krook, M. A Model for Collision Processes in Gases. 1. Small Amplitude Processes in Charged and Neutral One-Component Systems. *Phys. Rev.* **94**, 511 (1954).

346. Anderson, J. & Witting, H. A relativistic relaxation-time model for the Boltzmann equation. *Physica* **74**, 466 (1974).

347. Jaiswal, A., Ryblewski, R. & Strickland, M. Transport coefficients for bulk viscous evolution in the relaxation time approximation. *Phys. Rev. C* **90**, 044908 (2014).

348. Pratt, S. & Torrieri, G. Coupling Relativistic Viscous Hydrodynamics to Boltzmann Descriptions. *Phys. Rev. C* **82**, 044901 (2010).

349. Bernhard, J. E. *Bayesian parameter estimation for relativistic heavy-ion collisions* PhD thesis (Duke U., 2018).

350. Wolff, Z. & Molnar, D. Flow harmonics from self-consistent particlization of a viscous fluid. *Phys. Rev. C* **96**, 044909 (2017).

351. Paquet, J.-F., Shen, C., Denicol, G. S., Luzum, M., Schenke, B., Jeon, S. & Gale, C. Production of photons in relativistic heavy-ion collisions. *Phys. Rev. C* **93**, 044906 (2016).

352. SMASH-vHLL-E-Hybrid User Guide <https://smash-transport.github.io/smash-vhll-e-hybrid/latest/user/>.

353. Martin, R. C. *The clean coder: a code of conduct for professional programmers* (Pearson Education, 2011).

354. Vovchenko, V., Koch, V. & Shen, C. Proton number cumulants and correlation functions in Au-Au collisions at 7.7–200 GeV from hydrodynamics. *Physical Review C* **105** (2022).

355. Patrignani, C. *et al.* Review of Particle Physics. *Chin. Phys. C* **40**, 100001 (2016).

356. Elfner, H. & Müller, B. The exploration of hot and dense nuclear matter: introduction to relativistic heavy-ion physics. *J. Phys. G* **50**, 103001 (2023).

357. Neff, D. *Recent Highlights from STAR BES Phase II in 58th Rencontres de Moriond on QCD and High Energy Interactions* (2024).

358. Jacak, B. V. & Müller, B. The Exploration of Hot Nuclear Matter. *Science* **337**, 310 (2012).

359. Poskanzer, A. M. & Voloshin, S. A. Methods for analyzing anisotropic flow in relativistic nuclear collisions. *Phys. Rev. C* **58**, 1671 (1998).

360. Holopainen, H., Niemi, H. & Eskola, K. J. Elliptic flow from event-by-event hydrodynamics with fluctuating initial state. *Nucl. Phys. A* **855** (eds Tserruya, I., Milov, A., d'Enterria, D., Jacobs, P. & Wiedemann, U.) 486 (2011).

361. Ollitrault, J.-Y. On the measurement of azimuthal anisotropies in nucleus-nucleus collisions (1997).

362. Adler, C. *et al.* Elliptic flow from two and four particle correlations in Au+Au collisions at $s(\text{NN})^{**}(1/2) = 130\text{-GeV}$. *Phys. Rev. C* **66**, 034904 (2002).

363. Borghini, N., Dinh, P. M. & Ollitrault, J.-Y. A New method for measuring azimuthal distributions in nucleus-nucleus collisions. *Phys. Rev. C* **63**, 054906 (2001).

364. Borghini, N., Dinh, P. M. & Ollitrault, J.-Y. Flow analysis from multiparticle azimuthal correlations. *Phys. Rev. C* **64**, 054901 (2001).

365. Bilandzic, A., Snellings, R. & Voloshin, S. Flow analysis with cumulants: Direct calculations. *Phys. Rev. C* **83**, 044913 (2011).

366. Alver, B. *et al.* System size, energy, pseudorapidity, and centrality dependence of elliptic flow. *Phys. Rev. Lett.* **98**, 242302 (2007).
367. Alver, B. & Roland, G. Collision geometry fluctuations and triangular flow in heavy-ion collisions. *Phys. Rev. C* **81**. [Erratum: *Phys. Rev. C* **82**, 039903 (2010)], 054905 (2010).
368. Teaney, D. & Yan, L. Triangularity and Dipole Asymmetry in Heavy Ion Collisions. *Phys. Rev. C* **83**, 064904 (2011).
369. Floerchinger, S. & Wiedemann, U. A. Mode-by-mode fluid dynamics for relativistic heavy ion collisions. *Phys. Lett. B* **728**, 407 (2014).
370. Niemi, H., Denicol, G. S., Holopainen, H. & Huovinen, P. Event-by-event distributions of azimuthal asymmetries in ultrarelativistic heavy-ion collisions. *Phys. Rev. C* **87**, 054901 (2013).
371. Gardim, F. G., Noronha-Hostler, J., Luzum, M. & Grassi, F. Effects of viscosity on the mapping of initial to final state in heavy ion collisions. *Phys. Rev. C* **91**, 034902 (2015).
372. Bhalerao, R. S., Blaizot, J.-P., Borghini, N. & Ollitrault, J.-Y. Elliptic flow and incomplete equilibration at RHIC. *Phys. Lett. B* **627**, 49 (2005).
373. Schenke, B., Tribedy, P. & Venugopalan, R. Gluon field fluctuations in nuclear collisions: Multiplicity and eccentricity distributions. *Nucl. Phys. A* **926** (eds Armesto, N., McLerran, L., Pajares, C. & Salgado, C.) 102 (2014).
374. Yan, L., Ollitrault, J.-Y. & Poskanzer, A. M. Azimuthal Anisotropy Distributions in High-Energy Collisions. *Phys. Lett. B* **742**, 290 (2015).
375. Teaney, D. & Yan, L. Non linearities in the harmonic spectrum of heavy ion collisions with ideal and viscous hydrodynamics. *Phys. Rev. C* **86**, 044908 (2012).
376. Gardim, F. G., Grassi, F., Luzum, M. & Ollitrault, J.-Y. Mapping the hydrodynamic response to the initial geometry in heavy-ion collisions. *Physical Review C* **85** (2012).
377. Roch, H., Götz, N., Saß, N. & Krupczak, R. *smash-transport/sparkx: v2.0.2-Chatelet* version v2.0.2. 2025.
378. Martin, R. C. Design principles and design patterns. *Object Mentor* **1**, 597 (2000).
379. Bilandzic, A. *Anisotropic flow measurements in ALICE at the large hadron collider* PhD thesis (Utrecht U., 2012).
380. Voloshin, S. & Zhang, Y. Flow study in relativistic nuclear collisions by Fourier expansion of Azimuthal particle distributions. *Z. Phys. C* **70**, 665 (1996).
381. Bhalerao, R. S., Borghini, N. & Ollitrault, J. Y. Genuine collective flow from Lee-Yang zeroes. *Phys. Lett. B* **580**, 157 (2004).
382. Bhalerao, R. S., Borghini, N. & Ollitrault, J. Y. Analysis of anisotropic flow with Lee-Yang zeroes. *Nucl. Phys. A* **727**, 373 (2003).
383. SPARKX Documentation Accessed: 2025-02-05.

384. Bierlich, C., Buckley, A., Butterworth, J., Christensen, C. H., Corpe, L., Grellscheid, D., Grosse-Oetringhaus, J. F., Gutschow, C., Karczmarczyk, P., Klein, J., Lönnblad, L., Pollard, C. S., Richardson, P., Schulz, H. & Siegert, F. Robust Independent Validation of Experiment and Theory: Rivet version 3. *SciPost Physics* **8** (2020).

385. *IP-Glasma* <https://github.com/schenke/ipglasma/>.

386. Schenke, B., Shen, C. & Tribedy, P. Hybrid Color Glass Condensate and hydrodynamic description of the Relativistic Heavy Ion Collider small system scan. *Phys. Lett. B* **803**, 135322 (2020).

387. Bozek, P. & Broniowski, W. Transverse-momentum fluctuations in relativistic heavy-ion collisions from event-by-event viscous hydrodynamics. *Phys. Rev. C* **85**, 044910 (2012).

388. Bożek, P., Broniowski, W. & Olszewski, A. Hydrodynamic modeling of pseudorapidity flow correlations in relativistic heavy-ion collisions and the torque effect. *Phys. Rev. C* **91**, 054912 (2015).

389. Cimerman, J., Karpenko, I., Tomášik, B. & Trzeciak, B. A. A benchmark of initial state models for heavy-ion collisions at $\sqrt{s_{NN}} = 27$ and 62 GeV. *Phys. Rev. C* **103**, 034902 (2021).

390. Chatterjee, S. & Bozek, P. Pseudorapidity profile of transverse momentum fluctuations in heavy ion collisions. *Phys. Rev. C* **96**, 014906 (2017).

391. Bozek, P. Collective flow in p-Pb and d-Pd collisions at TeV energies. *Phys. Rev. C* **85**, 014911 (2012).

392. Bozek, P. & Broniowski, W. Longitudinal decorrelation measures of flow magnitude and event-plane angles in ultrarelativistic nuclear collisions. *Phys. Rev. C* **97**, 034913 (2018).

393. Alvioli, M., Drescher, H. .- & Strikman, M. A Monte Carlo generator of nucleon configurations in complex nuclei including Nucleon-Nucleon correlations. *Phys. Lett. B* **680**, 225 (2009).

394. Eyyubova, G. K., Korotkikh, V. L., Snigirev, A. M. & Zabrodin, E. E. Eccentricities, fluctuations and A-dependence of elliptic and triangular flows in heavy-ion collisions. *Journal of Physics G: Nuclear and Particle Physics* **48**, 095101 (2021).

395. Broniowski, W., Bozek, P. & Rybczynski, M. Fluctuating initial conditions in heavy-ion collisions from the Glauber approach. *Phys. Rev. C* **76**, 054905 (2007).

396. Borghini, N., Borrell, M., Feld, N., Roch, H., Schlichting, S. & Werthmann, C. Statistical analysis of initial-state and final-state response in heavy-ion collisions. *Phys. Rev. C* **107**, 034905 (2023).

397. Kurkela, A., Mazeliauskas, A., Paquet, J.-F., Schlichting, S. & Teaney, D. Effective kinetic description of event-by-event pre-equilibrium dynamics in high-energy heavy-ion collisions. *Phys. Rev. C* **99**, 034910 (2019).

398. Schlichting, S. Early time dynamics and hard probes in heavy-ion collisions. *PoS* (eds d'Enterria, D., Morsch, A. & Crochet, P.) 033 (2019).

399. Heinz, U. W. & Liu, J. Pre-equilibrium dynamics and heavy-ion observables. *Nucl. Phys. A* **956** (eds Akiba, Y., Esumi, S., Fukushima, K., Hamagaki, H., Hatsuda, T., Hirano, T. & Shigaki, K.) 549 (2016).

400. Liu, J., Shen, C. & Heinz, U. Pre-equilibrium evolution effects on heavy-ion collision observables. *Phys. Rev. C* **91**. [Erratum: Phys. Rev.C92,no.4,049904(2015)], 064906 (2015).

401. McNelis, M., Bazow, D. & Heinz, U. Anisotropic fluid dynamical simulations of heavy-ion collisions. *Computer Physics Communications* **267**, 108077 (2021).

402. Friedman, J. The elements of statistical learning: Data mining, inference, and prediction (2009).

403. McLaughlin, E., Rose, J., Dore, T., Parotto, P., Ratti, C. & Noronha-Hostler, J. Building a testable shear viscosity across the QCD phase diagram. *Phys. Rev. C* **105**, 024903 (2022).

404. Magdy, N., Parfenov, P., Taranenko, A., Karpenko, I. & Lacey, R. A. Model study of the energy dependence of the correlation between anisotropic flow and the mean transverse momentum in Au+Au collisions. *Phys. Rev. C* **105**, 044901 (2022).

405. Dubla, A., Masciocchi, S., Pawłowski, J. M., Schenke, B., Shen, C. & Stachel, J. Towards QCD-assisted hydrodynamics for heavy-ion collision phenomenology. *Nucl. Phys. A* **979**, 251 (2018).

406. Bazavov, A. *et al.* The QCD Equation of State to $\mathcal{O}(\mu_B^6)$ from Lattice QCD. *Phys. Rev. D* **95**, 054504 (2017).

407. Liao, J. & Koch, V. On the Fluidity and Super-Criticality of the QCD matter at RHIC. *Phys. Rev. C* **81**, 014902 (2010).

408. Cleymans, J., Oeschler, H., Redlich, K. & Wheaton, S. Status of chemical freeze-out. *J. Phys. G* **32**, S165 (2006).

409. Critelli, R., Finazzo, S. I., Zaniboni, M. & Noronha, J. Anisotropic shear viscosity of a strongly coupled non-Abelian plasma from magnetic branes. *Phys. Rev. D* **90**, 066006 (2014).

410. Alt, C. *et al.* Energy and centrality dependence of antiproton and proton production in relativistic Pb + Pb collisions at the CERN SPS (2005).

411. Adamczyk, L. *et al.* Bulk Properties of the Medium Produced in Relativistic Heavy-Ion Collisions from the Beam Energy Scan Program. *Phys. Rev. C* **96**, 044904 (2017).

412. Adamczyk, L. *et al.* Harmonic decomposition of three-particle azimuthal correlations at energies available at the BNL Relativistic Heavy Ion Collider. *Phys. Rev. C* **98**, 034918 (2018).

413. Cox, D. R. *Principles of Statistical Inference* (Cambridge University Press, 2006).

414. Sivia, D. & Skilling, J. *Data analysis: a Bayesian tutorial* (OUP Oxford, 2006).

415. Kennedy, M. C. & O'Hagan, A. Bayesian Calibration of Computer Models. *Journal of the Royal Statistical Society. Series B* **63**, 425 (2001).

416. Gramacy, R. B. in. <http://bobby.gramacy.com/surrogates/> (Chapman Hall/CRC, Boca Raton, Florida, 2020).

417. Rasmussen, C. E. in *Advanced Lectures on Machine Learning* (eds Bousquet, O., von Luxburg, U. & Rätsch, G.) 63 (Springer Berlin Heidelberg, Berlin, Heidelberg, 2004).

418. Ramsay, J. & Silverman, B. *Functional Data Analysis* (Springer, 1997).

419. Higdon, D., McDonnell, J. D., Schunck, N., Sarich, J. & Wild, S. M. A Bayesian Approach for Parameter Estimation and Prediction using a Computationally Intensive Model. *J. Phys. G* **42**, 034009 (2015).

420. Sürer, Ö., Nunes, F. M., Plumlee, M. & Wild, S. M. Uncertainty quantification in breakup reactions. *Phys. Rev. C* **106**, 024607 (2022).

421. Liyanage, D., Sürer, Ö., Plumlee, M., Wild, S. M. & Heinz, U. Bayesian calibration of viscous anisotropic hydrodynamic simulations of heavy-ion collisions. *Phys. Rev. C* **108**, 054905 (2023).

422. Moses Y.-H. Chan, M. P. & Wild, S. M. Constructing a Simulation Surrogate with Partially Observed Output. *Technometrics* **66**, 1 (2024).

423. Ankenman, B., Nelson, B. & Staum, J. Stochastic kriging for simulation metamodeling. *Operations Research* **58**, 371 (2010).

424. Plumlee, M., Sürer, Ö., Wild, S. M. & Chan, M. Y.-H. *surmise 0.2.1 Users Manual* tech. rep. Version 0.2.1 (NAISE, 2023).

425. Brooks, S., Gelman, A., Jones, G. & Meng, X. *Handbook of Markov Chain Monte Carlo* (CRC Press, 2011).

426. Trotta, R. Bayes in the sky: Bayesian inference and model selection in cosmology. *Contemporary Physics* **49**, 71 (2008).

427. Robert, C. & Casella, G. *Monte Carlo Statistical Methods* (Springer New York, 2013).

428. Metropolis, N., Rosenbluth, A. W., Rosenbluth, M. N., Teller, A. H. & Teller, E. Equation of state calculations by fast computing machines. *The journal of chemical physics* **21**, 1087 (1953).

429. Hastings, W. K. Monte Carlo sampling methods using Markov chains and their applications (1970).

430. MacKay, D. J. *Information theory, inference and learning algorithms* (Cambridge university press, 2003).

431. Gregory, P. *Bayesian Logical Data Analysis for the Physical Sciences: A Comparative Approach with Mathematica® Support* (Cambridge University Press, 2005).

432. Hogg, D. W., Bovy, J. & Lang, D. Data analysis recipes: Fitting a model to data (2010).

433. Goodman, J. & Weare, J. Ensemble samplers with affine invariance. *Communications in applied mathematics and computational science* **5**, 65 (2010).

434. Foreman-Mackey, D., Hogg, D. W., Lang, D. & Goodman, J. emcee: The MCMC Hammer. *Publications of the Astronomical Society of the Pacific* **125**, 306 (2013).

435. Geyer, C. J. & Thompson, E. A. Annealing Markov chain Monte Carlo with applications to ancestral inference. *Journal of the American Statistical Association* **90**, 909 (1995).

436. Liu, J. S. & Liu, J. S. *Monte Carlo strategies in scientific computing* (Springer, 2001).

437. Tabak, E. G. & Vanden-Eijnden, E. Density estimation by dual ascent of the log-likelihood (2010).

438. Tabak, E. G. & Turner, C. V. A family of nonparametric density estimation algorithms. *Communications on Pure and Applied Mathematics* **66**, 145 (2013).

439. Rippel, O. & Adams, R. P. High-dimensional probability estimation with deep density models. *arXiv preprint arXiv:1302.5125* (2013).

440. Rezende, D. & Mohamed, S. *Variational inference with normalizing flows* in *International conference on machine learning* (2015), 1530.

441. Papamakarios, G., Pavlakou, T. & Murray, I. Masked autoregressive flow for density estimation. *Advances in neural information processing systems* **30** (2017).

442. Papamakarios, G., Nalisnick, E., Rezende, D. J., Mohamed, S. & Lakshminarayanan, B. Normalizing flows for probabilistic modeling and inference. *Journal of Machine Learning Research* **22**, 1 (2021).

443. Dinh, L., Krueger, D. & Bengio, Y. *NICE: Non-linear Independent Components Estimation* 2014.

444. Dinh, L., Sohl-Dickstein, J. & Bengio, S. *Density estimation using Real NVP* 2016.

445. Müller, T., McWilliams, B., Rousselle, F., Gross, M. & Novák, J. *Neural Importance Sampling* 2018.

446. Götz, N. Machine learning techniques applied to Monte Carlo integration. M.Sc. Thesis (2020).

447. Deutschmann, N. & Götz, N. Accelerating HEP simulations with Neural Importance Sampling. *JHEP* **03**, 083 (2024).

448. Heimel, T., Mattelaer, O., Plehn, T. & Winterhalder, R. Differentiable MadNIS-Lite. *SciPost Phys.* **18**, 017 (2025).

449. Butter, A., Charton, F., Villadamigo, J. M., Ore, A., Plehn, T. & Spinner, J. Extrapolating Jet Radiation with Autoregressive Transformers (2024).

450. Karamanis, M., Beutler, F., Peacock, J. A., Nabergoj, D. & Seljak, U. Accelerating astronomical and cosmological inference with preconditioned Monte Carlo. *Mon. Not. Roy. Astron. Soc.* **516**, 1644 (2022).

451. Karamanis, M., Nabergoj, D., Beutler, F., Peacock, J. A. & Seljak, U. pocoMC: A Python package for accelerated Bayesian inference in astronomy and cosmology. *J. Open Source Softw.* **7**, 4634 (2022).

452. Del Moral, P., Doucet, A. & Jasra, A. Sequential monte carlo samplers. *Journal of the Royal Statistical Society Series B: Statistical Methodology* **68**, 411 (2006).

453. Paquet, J.-F. *Applications of emulation and Bayesian methods in heavy-ion physics* 2023.

454. Petersen, H., Coleman-Smith, C., Bass, S. A. & Wolpert, R. Constraining the initial state granularity with bulk observables in Au+Au collisions at $\sqrt{s_{\text{NN}}} = 200$ GeV. *J. Phys. G* **38**, 045102 (2011).

455. Bass, S. A., Petersen, H., Quammen, C., Canary, H., Healey, C. G. & Taylor II, R. M. Probing the QCD Critical Point with Relativistic Heavy-Ion Collisions. *Central Eur. J. Phys.* **10**, 1278 (2012).

456. Novak, J., Novak, K., Pratt, S., Vredevoogd, J., Coleman-Smith, C. & Wolpert, R. Determining Fundamental Properties of Matter Created in Ultrarelativistic Heavy-Ion Collisions. *Phys. Rev. C* **89**, 034917 (2014).

457. Sangaline, E. & Pratt, S. Toward a deeper understanding of how experiments constrain the underlying physics of heavy-ion collisions. *Phys. Rev. C* **93**, 024908 (2016).

458. Pratt, S., Sangaline, E., Sorensen, P. & Wang, H. Constraining the Eq. of State of Super-Hadronic Matter from Heavy-Ion Collisions. *Phys. Rev. Lett.* **114**, 202301 (2015).

459. Bernhard, J. E., Marcy, P. W., Coleman-Smith, C. E., Huzurbazar, S., Wolpert, R. L. & Bass, S. A. Quantifying properties of hot and dense QCD matter through systematic model-to-data comparison. *Phys. Rev. C* **91**, 054910 (2015).

460. Ke, W., Xu, Y. & Bass, S. A. Linearized Boltzmann-Langevin model for heavy quark transport in hot and dense QCD matter. *Phys. Rev. C* **98**, 064901 (2018).

461. Moreland, J. S., Bernhard, J. E. & Bass, S. A. Bayesian calibration of a hybrid nuclear collision model using p-Pb and Pb-Pb data at energies available at the CERN Large Hadron Collider. *Phys. Rev. C* **101**, 024911 (2020).

462. Parkkila, J. E., Onnerstad, A. & Kim, D. J. Bayesian estimation of the specific shear and bulk viscosity of the quark-gluon plasma with additional flow harmonic observables. *Phys. Rev. C* **104**, 054904 (2021).

463. Phillips, D. R. *et al.* Get on the BAND Wagon: A Bayesian Framework for Quantifying Model Uncertainties in Nuclear Dynamics. *J. Phys. G* **48**, 072001 (2021).

464. Parkkila, J. E., Onnerstad, A., Taghavi, S. F., Mordasini, C., Bilandzic, A., Virta, M. & Kim, D. J. New constraints for QCD matter from improved Bayesian parameter estimation in heavy-ion collisions at LHC. *Phys. Lett. B* **835**, 137485 (2022).

465. Ke, W., Moreland, J. S., Bernhard, J. E. & Bass, S. A. Constraints on rapidity-dependent initial conditions from charged particle pseudorapidity densities and two-particle correlations. *Phys. Rev. C* **96**, 044912 (2017).

466. Mankolli, A. *et al.* 3D multi-system Bayesian calibration with energy conservation to study rapidity-dependent dynamics of nuclear collisions. *EPJ Web Conf.* **296**, 05010 (2024).

467. Shen, C., Schenke, B. & Zhao, W. The effects of pseudorapidity-dependent observables on (3+1)D Bayesian Inference of relativistic heavy-ion collisions. *EPJ Web Conf.* **296**, 14001 (2024).

468. Jahan, S. A., Roch, H. & Shen, C. Bayesian analysis of (3+1)D relativistic nuclear dynamics with the RHIC beam energy scan data. *Phys. Rev. C* **110**, 054905 (2024).

469. Nijs, G. & van der Schee, W. Hadronic Nucleus-Nucleus Cross Section and the Nucleon Size. *Phys. Rev. Lett.* **129**, 232301 (2022).

470. Yang, Z. & Fries, R. J. Shear stress tensor and specific shear viscosity of hot hadron gas in nuclear collisions. *Phys. Rev. C* **105**, 014910 (2022).

471. Dash, A., Samanta, S. & Mohanty, B. Transport coefficients for multicomponent gas of hadrons using Chapman-Enskog method. *Phys. Rev. D* **100**, 014025 (2019).

472. Noronha-Hostler, J., Noronha, J. & Greiner, C. Transport Coefficients of Hadronic Matter near T(c). *Phys. Rev. Lett.* **103**, 172302 (2009).

473. Christiansen, N., Haas, M., Pawłowski, J. M. & Strodthoff, N. Transport Coefficients in Yang–Mills Theory and QCD. *Phys. Rev. Lett.* **115**, 112002 (2015).

474. Meyer, H. B. Transport properties of the quark-gluon plasma from lattice QCD. *Nucl. Phys. A* **830** (eds Stankus, P., Silvermyr, D., Sorensen, S. & Greene, V.) 641C (2009).

475. Mages, S. W., Borsányi, S., Fodor, Z., Schäfer, A. & Szabó, K. Shear Viscosity from Lattice QCD. *PoS LATTICE2014*, 232 (2015).

476. Borsanyi, S., Fodor, Z., Giordano, M., Katz, S. D., Pasztor, A., Ratti, C., Schäfer, A., Szabo, K. K. & Toth Balint, C. High statistics lattice study of stress tensor correlators in pure SU(3) gauge theory. *Phys. Rev. D* **98**, 014512 (2018).

477. Liu, S. Y. F. & Rapp, R. Spectral and transport properties of quark-gluon plasma in a nonperturbative approach. *Eur. Phys. J. A* **56**, 44 (2020).

478. Meyer, H. B. A Calculation of the bulk viscosity in SU(3) gluodynamics. *Phys. Rev. Lett.* **100**, 162001 (2008).

479. Astrakhantsev, N. Y., Braguta, V. V. & Kotov, A. Y. Temperature dependence of the bulk viscosity within lattice simulation of SU(3) gluodynamics. *Phys. Rev. D* **98**, 054515 (2018).

480. Rougemont, R., Critelli, R., Noronha-Hostler, J., Noronha, J. & Ratti, C. Dynamical versus equilibrium properties of the QCD phase transition: A holographic perspective. *Phys. Rev. D* **96**, 014032 (2017).

481. Molnár, M. Charged Particle Pseudorapidity Distributions Measured with the STAR EPD. *Universe* **9**, 335 (2023).

482. Garcia-Montero, O., Staudenmaier, J., Schäfer, A., Torres-Rincon, J. M. & Elfner, H. Role of proton-antiproton regeneration in the late stages of heavy-ion collisions. *Phys. Rev. C* **105**, 064906 (2022).

483. Abelev, B. I. *et al.* Systematic Measurements of Identified Particle Spectra in pp, d⁺ Au and Au+Au Collisions from STAR. *Phys. Rev. C* **79**, 034909 (2009).

484. Adamczyk, L. *et al.* Beam Energy Dependence of the Third Harmonic of Azimuthal Correlations in Au+Au Collisions at RHIC. *Phys. Rev. Lett.* **116**, 112302 (2016).

485. Back, B. B. *et al.* Centrality and pseudorapidity dependence of elliptic flow for charged hadrons in Au+Au collisions at s(NN)**(1/2) = 200-GeV. *Phys. Rev. C* **72**, 051901 (2005).

486. Back, B. B. *et al.* Centrality and energy dependence of charged-particle multiplicities in heavy ion collisions in the context of elementary reactions. *Phys. Rev. C* **74**, 021902 (2006).

487. Andronic, A., Braun-Munzinger, P. & Stachel, J. The Horn, the hadron mass spectrum and the QCD phase diagram: The Statistical model of hadron production in central nucleus-nucleus collisions. *Nucl. Phys. A* **834** (eds Zhang, H.-Q., Zhu, S.-Y., Zhao, Z.-X., Liu, W.-P., Yuan, D.-Q. & Wang, Y.-B.) 237C (2010).

488. *PyDoe Repository* <https://github.com/tisimst/pyDOE>.

489. Deutsch, J. L. & Deutsch, C. V. Latin hypercube sampling with multidimensional uniformity. *Journal of Statistical Planning and Inference* **142**, 763 (2012).

490. Roch, H., Jahan, S. A. & Shen, C. Model emulation and closure tests for (3+1)D relativistic heavy-ion collisions. *Phys. Rev. C* **110**, 044904 (2024).

491. Sobol, I. Global sensitivity indices for nonlinear mathematical models and their Monte Carlo estimates. *Mathematics and Computers in Simulation* **55**. The Second IMACS Seminar on Monte Carlo Methods, 271 (2001).

492. Lacey, R. A. Is there a sonic boom in the little bang at RHIC? *Nucl. Phys. A* **785** (eds Karsch, F., Kharzeev, D. & Venugopalan, R.) 122 (2007).

493. Bhalerao, R. S. *Relativistic heavy-ion collisions* 2014.

494. Montgomery, D. C., Peck, E. A. & Vining, G. G. *Introduction to linear regression analysis* (John Wiley & Sons, 2021).

ACKNOWLEDGEMENTS

Like many significant endeavors in life, a dissertation is never the work of one individual but rather the collective achievement of many. First and foremost, I would like to thank Prof. Hannah Elfner, who guided me through a pandemic, scientific impasses, and countless other challenges. I could not have hoped for a better mentor or a more supportive group leader. You have built an extraordinary team, and I hope it will remain as outstanding as it is today. I would also like to thank Carsten Greiner for agreeing to review my dissertation. This involves a considerable amount of effort, which deserves great recognition.

This PhD project would not have been possible without the support by the Studienstiftung des deutschen Volkes, which funded me from the beginning of my Bachelor's till now and made me gain many unique experiences and friends, as well as the Stiftung Polytechnische Gesellschaft Frankfurt am Main, and the Helmholtz Graduate School for Hadron and Ion Research. All the computations performed for this work used resources which have been provided by the GreenCube at GSI. I would also like to thank my HGS-HIRe PhD committee members Prof. Lorenz von Smekal and Prof. Volker Koch for fruitful discussions, valuable input and ideas, curiosity regarding my projects and encouragement to finalize this PhD work.

I am also deeply grateful to the wonderful colleagues with whom I have worked over the years: Lucas, not only my first student but also brave enough to return for a second project; Timo, whose vast knowledge I had the privilege to guide; Nils, Hendrik, and Renata, who joined me in countless hours of building something lasting; and Oscar, whose wide expertise continues to amaze me.

I will forever cherish the SMASHies, a group whose warmth made me feel part of something more than just a research team. It is truly the most excelling example of collective dynamics in the field. From retreats to social gatherings, you have all been both colleagues and friends. I would like to especially acknowledge a few individuals who were pivotal to my work: Renan, who was always there to answer any physics question imaginable; Nils, who shared an office with me for so long that it is hard to picture a week without him; and Alessandro, the best software developer I have encountered inside or outside of academia, who inspired me to strive for software that endures beyond a PhD. I know reviewing my pull requests was sometimes a challenge, but I hope it became smoother over time! I also want to give special thanks to everybody who proofread this work and helped me to polish this text. Your efforts truly transformed this work.

Although this is a work of physics, two people outside the field contributed more than they might realize. My thanks go to Paul, who made me feel at home in Frankfurt, listened to my ideas and anxieties, always encouraged me to find my own solutions and gave some of the best advise I ever received. And, of course, I am profoundly thankful to my wife, Radha, my steadfast companion on this journey through life. She graciously endured my years of deep thought and occasional frustration—and she will soon have to

endure the fact that I have finally finished. I would have never made it this far without you.

CURRICULUM VITAE

Personal data

Name	Niklas Götz
Date of Birth	July 22, 1995
Place of Birth	Schweinfurt, Germany
Citizen of	Germany

Education

2019 – 2020	ETH, Zürich, Switzerland <i>Master Thesis:</i> Machine learning techniques applied to Monte Carlo integration
2018 – 2019	École Polytechnique, Palaiseau, France <i>Research internship:</i> Kinetic theory for momentum-dependent scattering
2014 – 2017	Julius-Maximilians-Universität, Würzburg, Germany <i>Bachelor Thesis:</i> Positivitätserhaltende Methoden hoher Konvergenzordnung für die eindimensionalen Eulergleichungen
2006 – 2014	Jack-Steinberger-Gymnasium Bad Kissingen, Germany

Publications

- **Niklas Götz**, Iurii Karpenko, Hannah Elfner, *Bayesian analysis of a (3+1)D hybrid approach with initial conditions from hadronic transport*, arXiv: 2503.10181 [nucl-th].
- Nils Sass, Hendrik Roch, **Niklas Götz**, Renata Krupczak und Carl B. Rosenkvist, *SPARKX: A Software Package for Analyzing Relativistic Kinematics in Collision Experiments*, arXiv: 2503.09415 [physics.data-an].
- Nicolas Deutschmann and **Niklas Götz**, *Accelerating HEP simulations with Neural Importance Sampling*, JHEP **03** (2024), 083.
- **Niklas Götz**, Lucas Constantin and Hannah Elfner, *Role of initial transverse momentum in a hybrid approach*, Phys. Rev. C **110** (2024) no.3, 034901.
- **Niklas Götz**, Lucas Constantin and Hannah Elfner, *Momentum anisotropy generation in a hybrid approach*, arXiv:2312.03557 [hep-ph].

- Hannah Elfner, **Niklas Götz**, Oscar Garcia-Montero, Jean-François Paquet and Charles Gale, *Photon momentum anisotropies from the late stages of relativistic heavy-ion collisions*, PoS Hard Probes 2023 (2024), 070
- **Niklas Götz** and Hannah Elfner, *Temperature and Net Baryochemical Potential Dependence of η/s in a Hybrid Approach*, Acta Phys. Polon. Supp. **16** (2023) no.1, 1-A133-A133
- **Niklas Götz** and Hannah Elfner, *Temperature and Net Baryochemical Potential Dependence of η/s in a Hybrid Approach*, Phys. Rev. C **106** (2022) no.5, 054904
- Anna Schäfer, **Niklas Götz**, Oscar Garcia-Montero, Jean-François Paquet Hannah Elfner and Charles Gale, *Out-of-equilibrium photon production in the late stages of relativistic heavy-ion collisions*, Phys. Rev. C **105** (2022) no.4, 044910 [Erratum: Phys. Rev. C **109** (2024) no.4, 049901]

Presentations

2025	31th Quark Matter, Frankfurt am Main: <i>Bayesian analysis of a (3+1)D hybrid approach with initial conditions from hadronic transport in the BES energy range</i> , poster
2024	Workshop Hydrodynamics and related observables in heavy-ion collisions, Nantes: <i>(3+1)D Bayesian analysis with initial conditions from hadronic transport</i> , talk
2024	CP3 Seminar, Louvain-la-Neuve: <i>Neural Importance Sampling: Accelerating Phase Space Integrals in High-Energy Physics with Generative AI</i> , talk
2024	TP2 Theory Seminar, Würzburg: <i>Generative Models for High-Energy-Physics Phase Space Integrals</i> , talk
2024	DPG Frühjahrstagung, Gießen: <i>Role of initial transverse momentum in a hybrid approach</i> , talk
2023	MU days, Karlsruhe: <i>Event-by-event correlations of anisotropic flow generation in a hybrid approach</i> , poster
2023	30th Quark Matter, Houston: <i>Event-by-event correlations of anisotropic flow generation in a hybrid approach</i> , poster
2023	DPG Frühjahrstagung, Dresden: <i>Anisotropic flow generation with $\eta/s(T, \mu_B)$ in a hybrid approach</i> , talk
2023	Magic 23 Workshop, Kovalam: <i>Investigation of shear viscosity and the generation of anisotropic flow in a hybrid approach</i> , talk
2022	Hot Quarks 2022, Estes Park: <i>Anisotropic flow generation with $\eta/s(T, \mu_B)$ in a hybrid approach</i> , talk
2022	CRC-TR211 collaboration meeting, Bielefeld: <i>Temperature and net baryochemical potential dependence of η/s in a hybrid approach</i> , talk
2022	29th Quark Matter, Krakau: <i>Temperature and net baryochemical potential dependence of η/s in a hybrid approach</i> , talk
2022	DPG Frühjahrstagung, Mainz: <i>Temperature and net baryochemical potential dependence of η/s in a hybrid approach</i> , talk

Teaching

- Theoretical Physics 5: Statistical Mechanics and Thermodynamics, winter term 2024/2025, Prof. Dr. Dirk Rischke
- Theoretical Physics 4: Quantum Mechanics, summer term 2024, Prof. Dr. Dirk Rischke
- Theoretical Physics 3: Electrodynamics, winter term 2023/2024, Prof. Dr. Dirk Rischke
- Theoretical Physics 2: Classical Mechanics, summer term 2023, Prof. Dr. Dirk Rischke
- Theoretical Physics 1: Mathematical Methods, winter term 2022/2023, Prof. Dr. Dirk Rischke
- Introduction into Programming, summer term 2022, Dr. Matthias Hanauske
- Introduction into Programming, winter term 2021/2022, Prof. Dr. Francesca Cuteri
- Theoretical Physics 2: Classical Mechanics, summer term 2021, Prof. Dr. Carsten Greiner

Employment

since 2021 Goethe-Universität Frankfurt am Main, Teaching assistant/PhD student
2019 Institute de Physique Théorique Saclay, Research Intern
2018 Heidelberg Engineering, Research Intern
2018 d-fine, Risk Analysis Intern
2017 Senacor, Software Development Intern



Publiziert unter der Creative Commons-Lizenz Namensnennung - Nicht kommerziell (CC BY-NC) 4.0 International.

Published under a Creative Commons Attribution-NonCommercial (CC BY-NC) 4.0 International License.
<https://creativecommons.org/licenses/by-nc/4.0/>